รายงานวิจัยฉบับสมบูรณ์

Fabrication of Graphene/PP composites filaments for Fused Deposition Modeling (FDM) 3D Printing

โดย

ดร.ชวนชม อ่วมเนตร

พฤษภาคม 2563

สัญญาเลขที่ TRG6180009

รายงานวิจัยฉบับสมบูรณ์

โครงการ

Fabrication of Graphene/PP composites filaments for Fused Deposition Modeling (FDM) 3D Printing

ผู้วิจัย

ดร.ชวนชม อ่วมเนตร

สังกัด

สถาบันวิจัยโลหะและวัสดุ จุฬาลงกรณ์มหาวิทยาลัย

สนับสนุนโดยสำนักงานคณะกรรมการการอุดมศึกษา และสำนักงานกองทุนสนับสนุนการวิจัย

Table of Contents

List of Figures

List of Tables

Fabrication of Graphene/PP composites filaments for Fused Deposition Modeling (FDM) 3D Printing

บทคัดย่อ

วัสดุฐานแกรฟีนมีคุณสมบัติเด่นหลายประการ อาทิ มีความแข็งแรงเชิงกลสูง มีความสามารในการนำไฟฟ้าและความร้อน ส่งผลให้ได้รับความนิยมในการนำมาใช้เป็นวัสดุตัวเติมในวัสดุพอลิเมอร์ เนื่องจากเส้นฟิลาเมนต์ กระบวนการพิมพ์สามมิติ เป็นเทคโนโลยีการขึ้นรูปที่กำลังได้รับความนิยมสูง ด้วยข้อได้เปรียบหลายประการ เช่น สามารถผลิตชิ้นงานที่มีรูปร่างซับซ้อนได้ง่าย เกิดของเสียจากกระบวนการผลิตน้อย เป็นต้น อย่างไรก็ตาม ปัจจุบันมีวัสดุเพียงไม่กี่ประเภทที่สามารภนำมาใช้กับกระบวนการพิมพ์สามมิติได้ โดยส่วนมากเป็นวัสดุที่มีความเป็นผลึกต่ำ หรือมีโครงสร้างอสัณฐานเป็นหลัก เช่น พอลิแลคติกแอซิด และ เอบีเอส เป็นต้น ส่งผลให้เกิดข้อจำกัดในการนำไปผลิตชิ้นงานเพื่อใช้จริง เนื่องจากชิ้นงานส่วนใหญ่ที่ได้จากการพิมพ์สามมิติยังมีความแข็งแรงเชิงกลต่ำ รวมถึงไม่มีสมบัติเฉพาะทางอื่นๆ ที่เหมาะสมต่อการนำไปใช้งานจริงในวัตถุประสงค์ต่างๆ นอกจากนี้เส้นฟิลาเมนต์ที่มีจำหน่ายทางการค้ายังมีราคาสูงอีกด้วย งานวิจัยนี้จึงมีความสนใจที่จะพัฒนาเส้นฟิลาเมนต์จากวัสดุคอมโพสิตฐานแกรฟีนร่วมกับพอลิโพรพิลีน เพื่อเป็นทางเลือกวัสดุชนิดใหม่สำหรับใช้ในกระบวนการพิมพสามมิติ โดยทำการศึกษาสมบัติต่างๆของวัสดุคอมโพสิตที่พัฒนาขึ้น ได้แก่ พฤติกรรมการไหล สมบัติเชิงความร้อน และสมบัติเชิงกลของวัสดุ รวมทั้งปัจจัยอื่นๆ ที่ส่งผลต่อความสามารถในการพิมพ์สามมิติ เพื่อเป็นแนวทางในการผลิตและทดสอบคุณภาพของเส้นฟิลาเมนต์และชิ้นงานที่ผลิตจากกระบวนการพิมพ์สามมิติต่อไป

คำสำคัญ วัสดุคอมโพสิตฐานแกรฟีน การพิมพ์สามมิติ พอลิโพรพิลีน แกรฟีน

Abstract

Graphene-based materials have very high performances due to high mechanical strength, electrical, and thermal conductivities, making them the best candidates for nanofillers. Since there is still a lack of the standard information of FDM filament available for either pure or composite material, this study aims to achieve a methodology of fabricating good-quality composite filaments, in particular, G/PP and GO/PP composites for the FDM 3D printing process. To produce a good quality filament for the FDM process, critical melt extrusion process parameters need to be examined. The processability of graphene-based/polymer composites are further investigated in term of thermal properties, rheological properties, and morphology. Also, 3D objects are printed to explore the printability as well as the mechanical properties of the obtained graphene-based/ polymer composites filaments.

In this study, new graphene-based and PP-based composites filaments were successfully prepared as feedstock for FDM 3D printing process.

Keywords: graphene-based composite, 3D printing, polypropylene, graphene

1. Executive Summary

This study arrived at a methodology of fabricating good-quality composite materials, including ABS/GO, PP/organoclay and PP/graphene nanocomposite filaments for material extrusion 3D printing. The critical parameters, thermal, mechanical, rheological, and morphological were examined. For ***ABS/GO composites,*** the solvent system improved the GO dispersion capability in ABS matrix and had no significant effect on the thermal properties of the ABS/GO composite. However, the aggregation of GO could lead to the die clogging and failed the extrusion process. The tensile strength and Young's modulus of ABS were enhanced naturally by GO. For ***PP/organoclay nanocomposites,*** D18 was successfully used to modify the clay surfaces, providing a better dispersion and wetting of the clay particles in the hydrophobic polymer matrix such as PP. The developed PP/organoclay nanocomposites could be 3D printed using a conventional 3D printer. For ***PP/graphene nanocomposites***, the graphene exfoliation seems to be playing an important role on the mechanical performance of the nanocomposites.

From this study, the filament fabrication methodology as well as the testing protocol can be further used as a standard method for the development of new composites filaments for Fused Deposition Modeling (FDM) 3D printing.

2. Final Report

2.1 Objectives:

1. To achieve good-quality composite filaments from G/PP and GO/PP composites as well as the properly print conditions for the FDM 3D printing.
2. To fabricate the new G/polymer and GO/polymer composites and use them as a feed stock filament for FDM 3D printing
3. To optimize the nanocomposite compositions and fabrication conditions that are practical for melt extrusion technique.
4. To create standard properties that of the development of polymer composite for 3D printing filament applications

2.2 The expected outputs

Detail	Month																	
	1	2	3	4	5	6	7	8	9	10	11	12	13	14	15	16	17	18
1. Basic knowledge of FDM 3D printing technologies and commercial filaments																		
2. An appropriate solvent for PP and graphene dispersion																		
3. Progress report for TRF																		
4. G/PP and GO/PP nanocomposites and filaments																		
5. Progress report for TRF																		
6. FDM 3D print conditions for G/PP and GO/PP composite filaments																		
7. Progress report to TRF																		

2.3 Results and Discussion

2.3.1. Graphene and graphene oxide synthesis

2.3.1.1. Graphite and graphene

In the last decades, graphene is getting a lot of attention. Graphene is an allotrope of carbon as shown in **Figure 1**. It is obtained from graphite. In graphene, each atoms of carbon has three **σ-**bonds with each fits three neighbors and one π-

bond, responsible for graphene's electrical properties. Graphene, the two-dimensional material attracts more and more in recent years owing to its extraordinary electrical, optical, magnetic, thermal and mechanical properties. A single square-meter sheet of graphene would weight just 0.0077g while it could support up to 4 kg [1]. Besides the incredibly strong, graphene is also flexible and has large specific surface area. These extraordinary properties make graphene one of the perfect materials for composite fabrication.

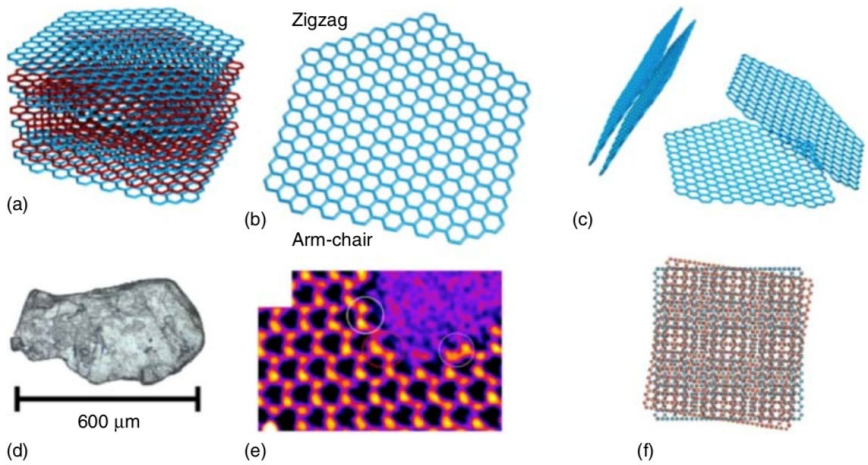

Figure 1. (a) Chemical structure motive of AB stack graphite, (b) Graphene with zigzag and arm-chair edges, (c) Restacked layers of graphene and few-layer graphene, (d) a flake of natural graphite [1].

There are different methods to generate graphene. One of the most used methods is the Hummer's method, which offers high efficiency and satisfying reaction safety. The graphene is obtained by reducing graphene oxide as shown in

Figure 2. The principle of Hummer's method is based on the oxidation and reduction reactions. First, the graphite oxide is synthesized by inserting large alkali ions between graphite layers to reduce the interlayers Van Der Waals forces. Then, the single or few layers graphene oxide are exfoliated by rapid heating or sonication. The last step is the reduction of the graphene oxide to obtain graphene. Thus, the graphene is often called "reduce graphene oxide" (rGO).

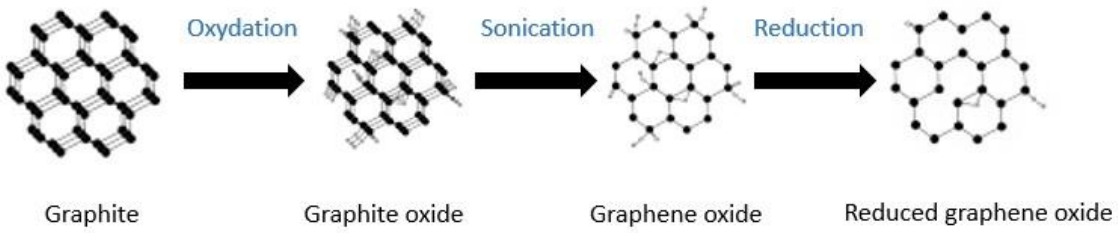

Figure 2. Change of the graphite's structure during the Hummer's method.

2.3.1.2 Preparation of graphene oxide (GO)

The GO was prepared using Hummers' method. Briefly, the graphite powder was first oxidized into graphite oxide using $KMnO_4$/ H_2SO_4 and then the graphite oxide was exfoliated into GO sheets by ultrasonication in water. Concentrated H_2SO_4 was added to a mixture of graphite flakes (1 wt% equiv.), and $NaNO_3$ (0.5 wt% equiv.). Then, the mixture was cooled to 0 ^oC, and $KMnO_4$ (3 wt% equiv.) was added slowly in portions to keep the reaction temperature below 20 ^oC. After that, the reaction was warmed to 35 ^oC and stirred for 30 minutes, at which time water

was added slowly to produce a sizable exothermic reaction to 98°C. The external heating was also introduced to maintain the reaction temperature at 98 °C for 15 minutes. Then the heat was removed, and the reaction was cooled down in a water bath for 10 minutes. From this step, additional water (420 ml) and 30% H_2O_2 (3ml) were added and then cooled the mixture down to room temperature, followed by multiple washing, and dispersed in water.

2.3.1.3. Preparation of graphene or reduced graphene oxide (rGO)

In order to prepare graphene, the graphene oxide (GO) is reduced by removing oxygen-containing functional groups. In general, the chemical reduction of GO was conducted by using hydrazine or hydrazine hydrate. However, because both reducing agents are highly poisonous and explosive, a new approach for converting GO into stable graphene sheets (rGO) is introduced by using L-Ascorbic acid, which provide a nontoxic and mild reductive ability. Thus, after the sonication, L-Ascorbic acid is added to the aqueous solution of GO in a ratio of 0.1 mg GO: 1ml L-Ascorbic acid. After 48h, most oxygen functionalities in the GO are removed [2].

2.3.2. Polymer Matrix

2.3.2.1. Polypropylene (PP)

The main problem of using PP in 3D printing process came from its high crystallinity. During the 3D printing process, the filament is heated and extruded from the nozzle to build up the item on the platform or printed bed. Once the extruded material contacted the printed bed, some parts of printed sample are cooled. Thus, the recrystallization occurred and led to a heavy warping. Moreover, a huge thermal contraction stresses could be observed because of the high thermal dilatation coefficient of PP. A decrease of crystalline ratio would be able to reduce the shrinkage and make PP more practical for the 3D printing process.

The PP used in this study is the Clyrell RC6049 (HMC Polymers), with the MFR of 7.0 g/10min (230^{o}C/2.16 kg) and the density of 0.90 g/cm^{3}.

2.3.2.2. Acrylonitrile butadiene styrene (ABS)

ABS is one of the most used materials in the FFF process [3]. The relatively low glass transition temperature (T_g) and excellent processing properties of ABS, lead to the ease of filament extrusion and 3D printing. Moreover, it is an amorphous polymer, which means there is no crystallite. Accordingly, the shrinkage ratio during the cooling process is small, offering the high printing

accuracy as well as the dimensional constancy. All of the characteristics stated above make ABS as an outstanding material for FFF 3D printing. Incorporation of graphene-based materials will potentially enlarge the applications and functionalities of the 3D printed ABS, in particular, some practical applications such as auto parts, conceptual prototypes, and jigs. However, the use of ABS/graphene-based composites in 3D printing application is still rarely demonstrated. Wei et al. [4] successfully demonstrated one of the first attempts to 3D print ABS/graphene composites using solution-based process. However, there was no report regarding the properties investigation for such 3D printed composites.

2.3.3. Selection of an appropriate solvent for polymer matrix and graphene dispersion

At elevated temperature, PP can be dissolved in nonpolar solvents such as xylene, ethylbenzene, chlorobenzene. In this study, the xylene and toluene are of interested solvents because of their high boiling points, modest toxicity and availability for purchasing.

2.3.3.1. Xylene

Xylene or dimethylbenzene with the formula $(CH_3)_2C_6H_4$, has three isomers, which are 1,2-dimethylbenzene (ortho-xylene), 1,3-dimethylbenzene (meta-

xylene) and 1,4-dimetylbenzene (para-xylene) as shown in **Figure 3**. It is colorless, flammable liquids, and great industrial value [5]. Xylene is flammable but of the modest acute toxicity.

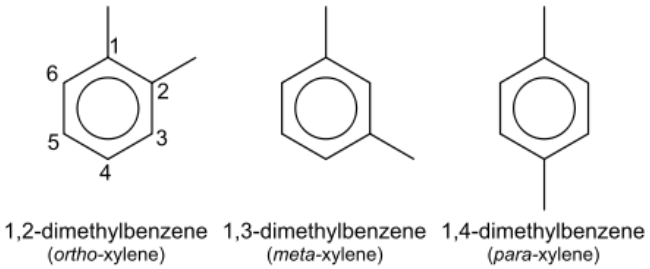

Figure 3. The three possible xylene isomers [5].

2.3.3.2. Toluene

Toluene is an aromatic hydrocarbon, which is colorless. It is a mono-substituted benzene derivative with the structure shown in **Figure 4**.

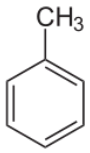

Figure 4. Chemical structure of toluene [6].

Table 1: Properties of xylene and toluene

Properties	**Xylene**	**Toluene**
Chemical formula	$(CH_3)_2C_6H_4$	$C_6H_5CH_3$

Chemical structure	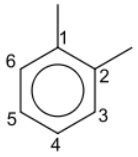 1,2-dimethylbenzene (*ortho*-xylene) 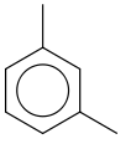 1,3-dimethylbenzene (*meta*-xylene)  1,4-dimethylbenzene (*para*-xylene)	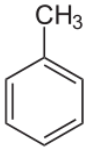
Boiling point	~140°C	~110°C
Main hazards	Highly flammable	Highly flammable

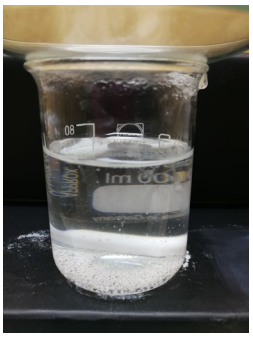

(a) Xylene

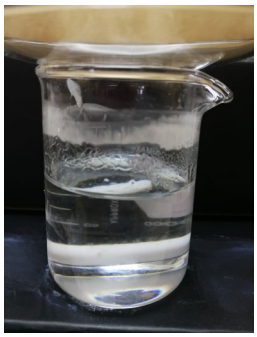

(b) Toluene

Figure 5. PP solution in (a) Xylene and (b) Toluene after heated at 100°C for 2 hours.

Figure 5 shows the dissolution of 10 wt% of PP in xylene and toluene at 100°C (for 2 hours). It is found that the PP can be dissolved well in both xylene and toluene. Because of the higher boiling point and modest toxicity of xylene, it is selected as the most suitable solvent for the dissolution of PP and the dispersion of G and GO in this study.

2.3.4. Graphene-based/polymer composite filaments fabrication

2.3.4.1. Solution Mixing

In this method, for G/PP and GO/PP composites, the dissolved PP and dispersed G (or GO) are mixed (solvent: xylene). The G/PP and GO/PP composites will be obtained after the coagulation in methanol, and dried out the solvent. The G/PP and GO/PP will be further combined with pure PP and extruded to produce G/PP and GO/PP filaments for FFF 3D printing.

GO/ABS was prepared using the same procedure used for the GO/PP, however, the DMF was used as a solvent instead of xylene.

G/PLA/PP was prepared using the same procedure used for the GO/PP and GO/ABS, but the G and PLA were dissolved and mixed together using chloroform as a solvent. The obtained G/PLA masterbatch was further mixed with neat PP to prepare G/PLA/PP filament in the next step.

2.3.4.2. Dry Mixing

PP is mixed mechanically with G powder (or GO), and then melt compounded using the twin-screw extruder to avoid the use of the solvent system. This method is widely used for preparing thermoplastic nanocomposite. GO/ABS was prepared using the same procedure used for the GO/PP.

2.3.4.3. Composite filament extrusion

For the filament extrusion process, the graphene-based composites with 10wt% of G and GO contents (masterbatch) were diluted to 0.1- 5 wt% of G and GO by mixing with the neat PP granules. The extrusion temperatures will be set from 160 °C to 210 °C from the hopper to die. Thus, the 1.75 mm diameter filament was produced and collected for 3D printing test. **Figure 6** demonstrates the equipment set up for preparing the graphene-based/polymer composite filaments by the melt extrusion process.

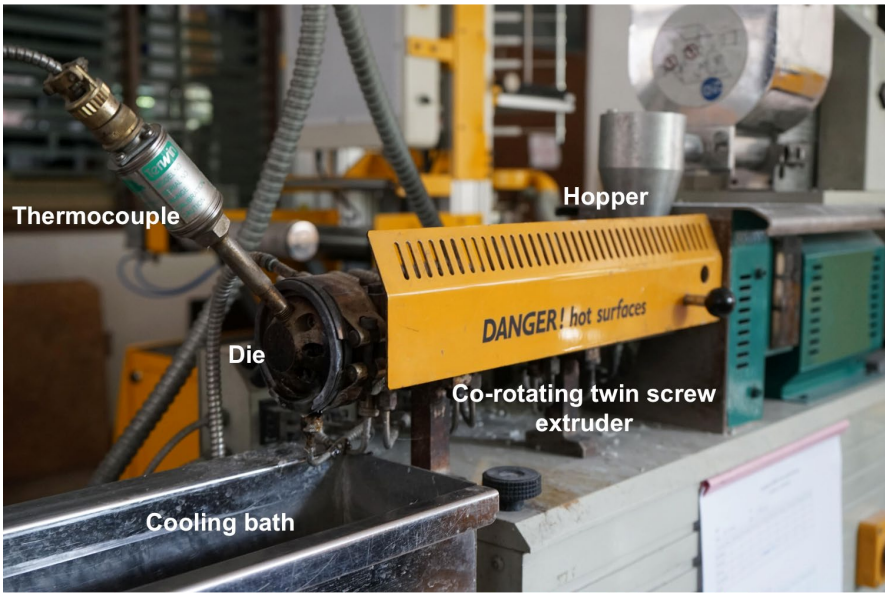

Figure 6. Melt extrusion process set up for graphene-based/polymer composite filaments fabrication.

However, the extruded G/PP and GO/PP filaments (with 1wt% of G and GO) prepared from the method mentioned in 4.1 and 4.2 did not come out well.

PP and graphene-based additives were found as an agglomerated and phase separated structure. A more pronounced in phase separation was found in the case of GO/PP. Since ABS and PP has the processing temperature at almost the same range, from this point, G/ABS and GO/ABS were prepared as alternative system. Moreover, for the PP-based composites, PLA was used to prepared graphene masterbatch instead of directly using PP. The characteristic of the obtained graphene-based/polymer composites from different masterbatch systems was shown in **Table 2**.

Table 2: Graphene-based/polymer composites filaments from different masterbatch system.

System	**Filaments**	**Practicable**
G/PP	Non-uniform size, naked-eye detected agglomeration and phase separation	X
GO/PP	Non-uniform size, naked-eye detected agglomeration and phase separation	X
G/ABS	Uniform size and smooth surface filament	/
GO/ABS	Uniform size and smooth surface filament	/
G/PLA/PP	Uniform size and smooth surface filament	/

2.3.5 GO/ABS composite filaments

According to the agglomeration and phase separation occurred between PP and graphene-based materials (G and GO), the ABS was selected as an alternative material because of its good mechanical performance, chemical resistance and high processing temperature (almost the same range of PP). As mentioned before, the apparent graphene aggregation and the phase separation between graphene and polymer matrix are significant problems, for ABS system, graphene oxide (GO) was selected as an alternative form to improve the graphene's dispersion in ABS matrix.

2.3.5.1. Differential Scanning Calorimetry (DSC)

The measurements were carried out using a Netzsch DSC 3500 Sirius, under the nitrogen atmosphere. The samples were heated from room temperature to 250 °C. After an isothermal step for 2 minutes, the samples were cooled down to 30 °C and finally heated up to 250 °C after another isothermal step for 2 min. Scanning temperature ramps of 10 K/min were used for all dynamic steps.

Figure 7 shows the representative DSC curves of ABS, ABS/GO (Dry Mixing), and ABS/GO (Solvent Mixing) composite filaments. In general, the variation in the melting temperature (T_m) indicated the change in crystal structures of material. The T_m of nanocomposites could be changed upon filler loading. ABS

has no exact melting point because of its amorphous characteristic. However, no significant difference between the T_g of the neat ABS filament and the ABS/GO composite filaments from both dry mixing and solvent mixing methods was found. The glass transition temperatures (T_g) were observed at 105.72 °C, 104.77 °C and 105.69 °C for ABS, ABS/GO (Dry Mixing), and ABS/GO (Solvent Mixing) filaments, respectively. The maintained T_g subsequently revealed the thermal stability of ABS/GO composite even though the composite experienced the solvent system before the extrusion process. Furthermore, ABS/GO composite could be softened and possibly 3D printed using the same temperature setup used for the pure and conventional ABS filaments.

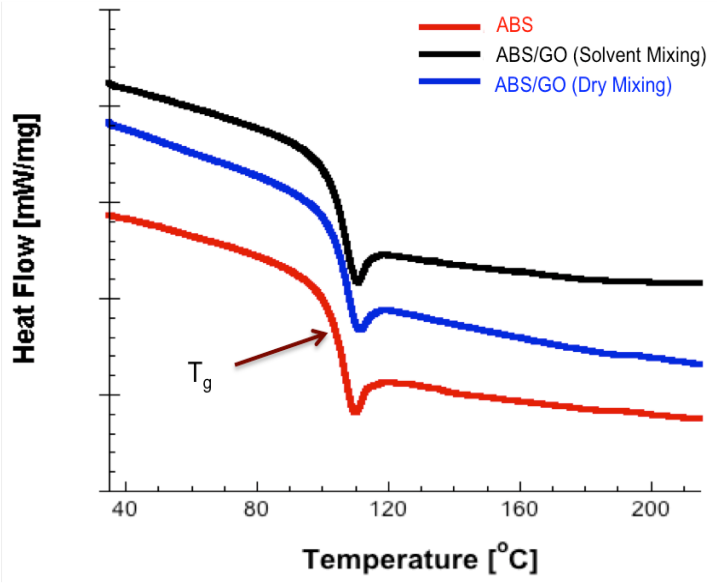

Figure 7. Melting temperature of ABS filament, ABS/GO (Solvent Mixing) and ABS/GO (Dry Mixing) composite filaments from the DSC second heating scan.

2.3.5.2. Themogravimetric Analysis (TGA)

The measurements were carried out using a Netzsch STA 2500. The samples were heated from room temperature to 600 °C, under the nitrogen atmosphere. Scanning temperature ramps of 10 K/min were used for the dynamic steps.

To explore the effect of GO on thermal stability of the ABS and ABS/GO composite filaments, thermal gravimetric analysis (TGA) was conducted. **Figure 8** shows the TGA thermogram of neat ABS and ABS/GO composite (2wt% GO) filaments. All materials started to decompose at the temperature around 400°C, which was higher than the typical temperature for 3D printing the conventional ABS filament (220-240°C). At 240°C, the highest temperature used for the 3D printing the conventional ABS filament, the ABS/GO (Solvent Mixing) showed a more mass drop (~3%) as compared to the pure ABS (~1.3%), and ABS/GO (Dry Mixing). These results could be due to the volatile compounds and the solvent molecules that might still be trapped in the composite filaments.

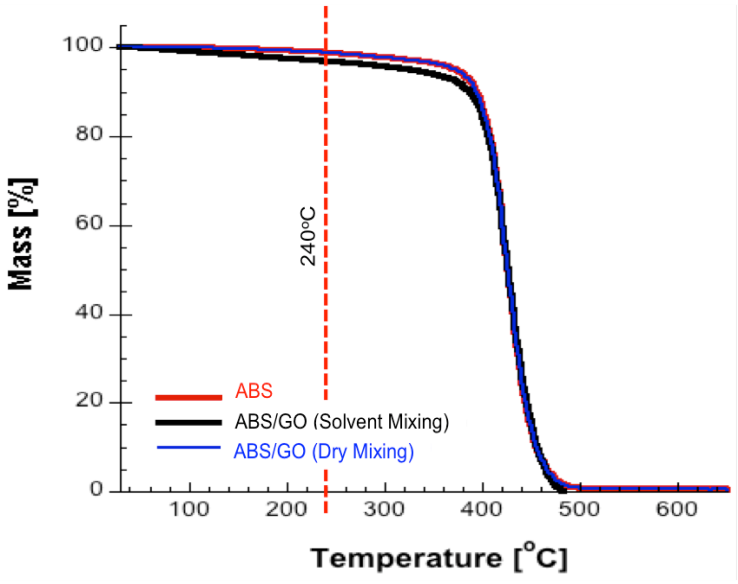

Figure 8. TGA thermogram of ABS filament, ABS/GO (Solvent Mixing) and ABS/GO (Dry Mixing) composite filaments.

2.3.5.3. Melt Flow Rate

The melt flow rate (MFR) is a common rheological measurement in which the molten polymer is pushed through a capillary die under a specific load, and the mass of extruded polymer is measured and reported in the unit of the extruded mass/10 minutes. The MFR measurements were carried out according to ASTM D1238 standard (Procedure A), at a temperature range of 220-240 °C with an applied load of 2.16 kg [7].

A pseudo-MFR measurement was performed using the FFF 3D printer with the nozzle diameter of 0.4 mm in order to determine the proper printing temperature. The extruded material through the nozzle in a 30-second time frame was weighed as a function of temperature. The flowability of the ABS/GO

composite was investigated via the melt flow rate (MFR) measurement. The MFR represented the flowability of the material and was inversely proportional to its viscosity. It could be used to evaluate how the presence of GO affected the processability of the ABS/GO composite. As shown in Figure 6, the MFR values of both ABS and ABS/GO composite filaments increased with the temperatures, which meant the materials flew easier upon the temperature increased. The MFR values of the ABS/GO were lower than those of pure ABS filament at all measured temperatures, which might be attributed to the solid GO flakes restricted the mobility and disturbed the flowability of the ABS chains.

For FFF 3D printing processes, with knowing the extrusion temperatures and flowability of the printed materials led to the more accuracy and precision of the printing process. The MFR information can be used as a guideline for setting up the printing parameters [8]. In this study, a pseudo-MFR measurement was conducted by measuring the extruded mass of the filaments through the printer nozzle. The pure ABS and ABS/GO filaments displayed clear plateau values at all temperatures (see **Figure 9**). As a result, the edge of the plateau was reflected the lower bound of acceptable temperature for the corresponded extrusion rate. Theoretically, below this temperature, the mass of polymer extruded cannot be accurately achieved at the given feed rate.

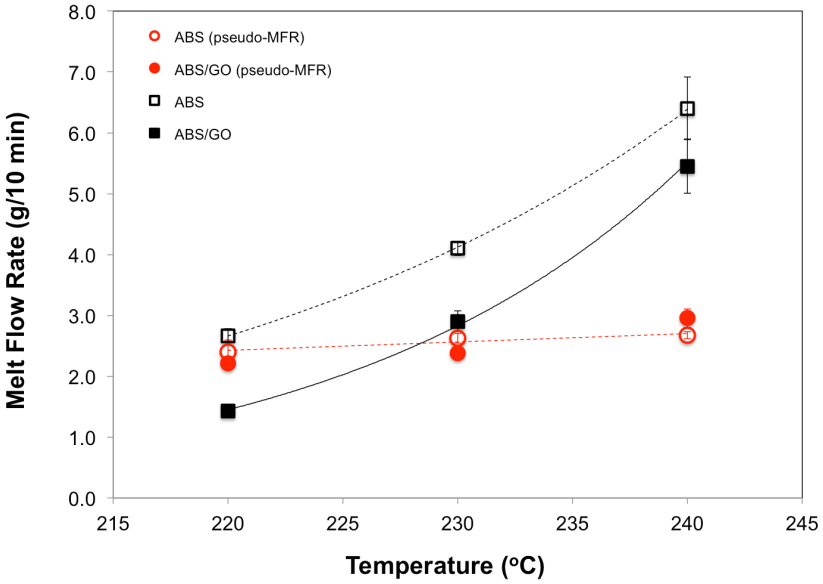

Figure 9. Melt flow rate (MFR) of ABS filament and ABS/GO composite filament in dependent of temperature (220-240°C). The black color represented the results from the conventional MRF measurement, and the red color represented the results from the pseudo-MFR measurement using 3D printer.

On the other hand, extruding at a higher temperature than the lower bound is undesirable since it would lead to slower solidification of the extruded bead on the printed part. It was found that the ABS/GO composite filament exhibited the similar behavior as compared to the pure ABS. Thus, the ABS/GO could be printed using the same temperature range (220 - 240 °C) used for the pure or conventional ABS filaments.

2.3.5.4. Rheology Test

The linear viscoelasticity responses of the materials were measured using a parallel plate rheometer (ARES G2000). A frequency sweep between 0.0628 and 628 rad/s was performed at a temperature of 210 °C. Based on the result of the strain sweep test, a constant strain was fixed as 5 % where the linear viscoelastic behavior maintained. Also, the steady shear measurements were conducted at 220 °C, from the shear rate range of 0.01 to 1000 s^{-1}. The two parallel plates were set up at 1 mm gap for all measurements.

The average shear rate in typical twin-screw extrusion ranges between 1 and 1,000 s^{-1} [9] [10]. For the FFF 3D printer, the shear rates in the nozzle are commonly in the range of 0.1 - 200 s^{-1} [11]. **Figure 10** shows the shear rate dependence of viscosity for ABS and ABS/GO at 220 ^{o}C. At the shear rate of 0.1 to 1 s^{-1}, ABS and ABS/GO filaments showed almost similar viscosity values, which confirmed that the ABS/GO could be 3D printed with the same temperatures set up for pure ABS. Incorporating with the MFR results, it was concluded that the ABS/GO and pure ABS could be 3D printed using the same printing parameters (nozzle temperature and print speed).

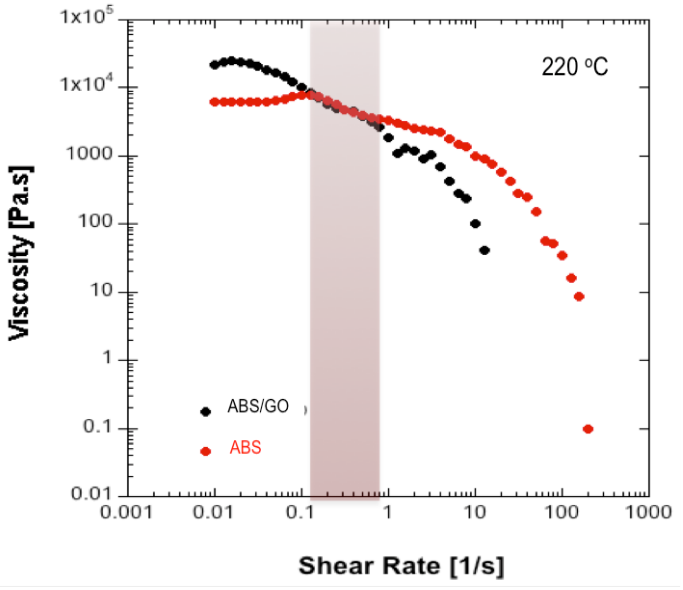

Figure 10. Shear rate dependence of viscosity for ABS and ABS/GO composite filaments.

Interfacial interaction between GO and ABS is a crucial role for enhancing the mechanical performance of the composite. Generally, the opposition between particle-particle interaction and particle-polymer interaction can be used to determine the particle dispersion or aggregation in nanocomposites. Thus, rheological behavior becomes a useful tool to evaluate the dispersion and distribution of the GO in ABS. Since rheological behaviors deliver the relation between molecular structure and mesoscale properties (such as phase structure and filler dispersion), at the same time, providing the processing properties [12], [13]. From the dynamic frequency sweep measurements, it was noticed that the rheological behaviors of ABS and ABS/GO were almost similar as shown in **Figure**

11, **Figure 12**, and **Figure 13**, respectively.

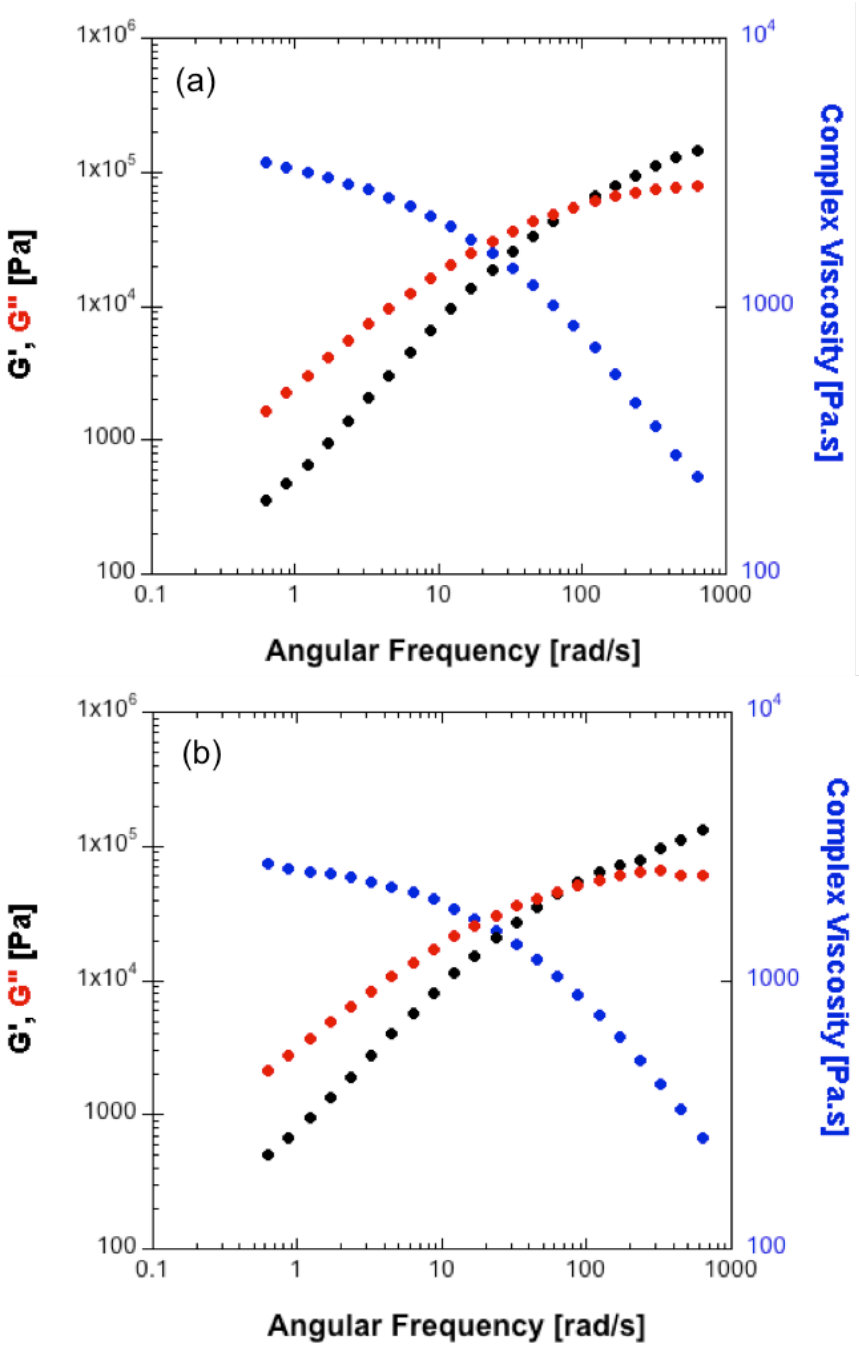

Figure 11. Rheological properties from the dynamic frequency sweep test: (a) ABS filament; (b) ABS/GO composite filament.

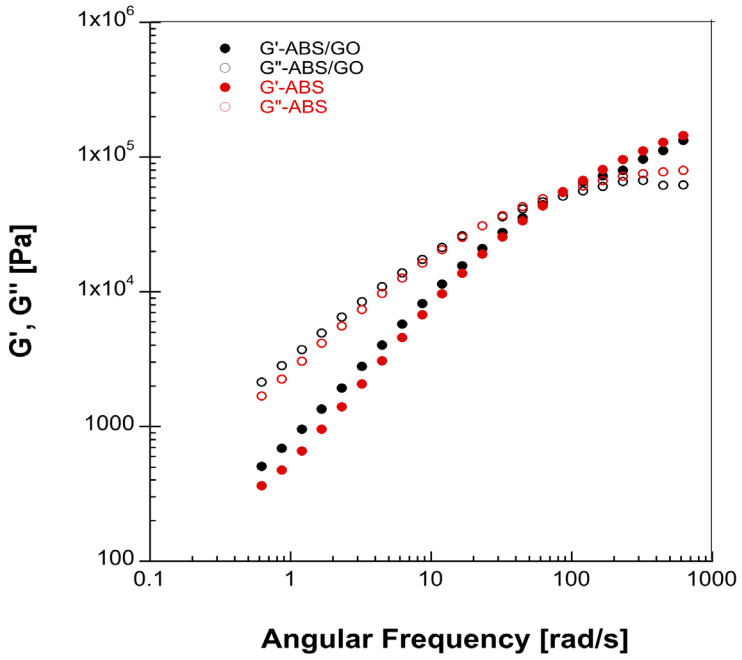

Figure 12. Storage modulus (G′) and loss modulus (G″) versus the angular frequency for ABS filament and ABS/GO composite filament.

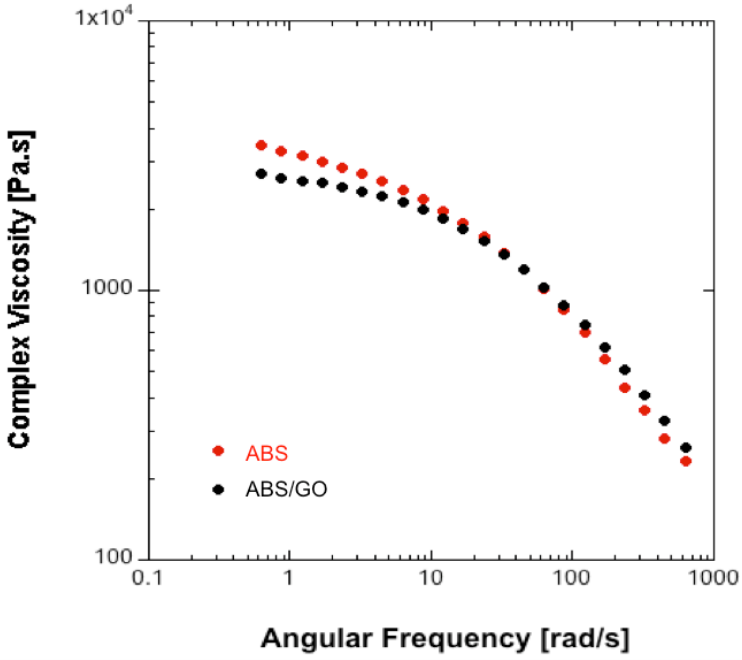

Figure 13. Complex viscosity versus the angular frequency for ABS filament and ABS/GO composite filament.

Figure 12 presents the storage and loss moduli of ABS and ABS/GO filaments. Only a small deviation of the G′ and G″ values were observed between the ABS and ABS/GO filaments. Even though the increase in complex viscosities at low frequencies due to the effect of GO fillers was found, the complex viscosities of ABS and ABS/GO filament remained almost the same values at higher rates as shown in **Figure 13**. This is again confirmed that the GO loading did not affect the viscosity or flowability of the ABS.

Furthermore, we created the G′- G″ plot for predicting the dispersion of GO in ABS as presented in **Figure 14**. The G′- G″ pattern of pure ABS and ABS/GO were close together, suggested the well distributed of GO in the composite.

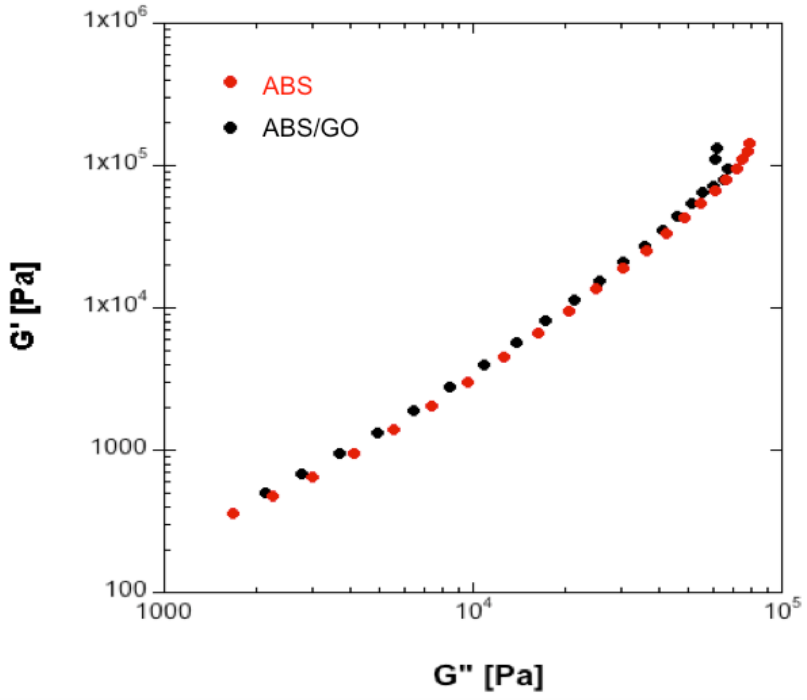

Figure 14. G′ versus G″ plot for (red): ABS filament, and (black): ABS/GO composite filament.

2.3.5.5. FDM 3D Printability

Figure 15 and **Figure 16** present the WANHAO Duplicator 6, the 3D printer based on the FDM principle and the printed ABS/GO tensile specimens, respectively. With the same printing conditions using for pure ABS, the ABS/GO composite has been successfully printed. However, the clogged nozzle was sometimes observed, which further led to the print failure (**Figure 16 (a)**).

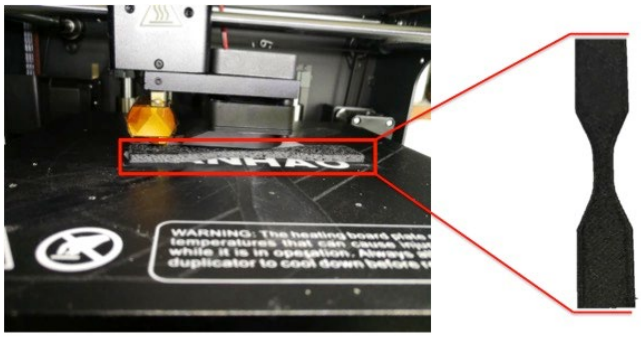

Figure 15. FDM 3D printed specimen from ABS/GO composite filament

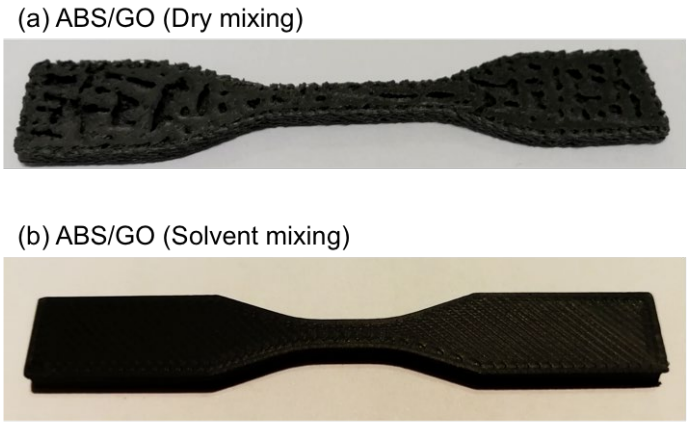

Figure 16. FDM 3D printed specimen from (a) ABS/GO (Dry Mixing) and (b) ABS/GO (Solvent Mixing) composite filaments.

2.3.5.6. Tensile Test

To study the mechanical properties, the tensile test specimens were printed based on ASTM D638 Type-V geometry [14]. The crosshead speed was set as 5mm/min. Ultimate tensile strength; Young's modulus and elongation at break were evaluated as an average value of at least three replicates.

The tensile properties at room temperature of ABS and ABS/GO were investigated and presented in **Figure 17**. From the typical stress-strain tensile curves and corresponding statistical data, the elongation at break value decreased with the GO loading. The elongation at break value of pure ABS was determined as 5.8%, while the value of ABS/GO composite was 2.9%. However, by adding 2 wt% GO, the tensile strength and Young's modulus of ABS were enhanced. This might be due to the interlayer crosslinks of GO sheets under loads, led to the ordering of the hierarchical structures, resulting in the great significant enhancing of the mechanical properties [15].

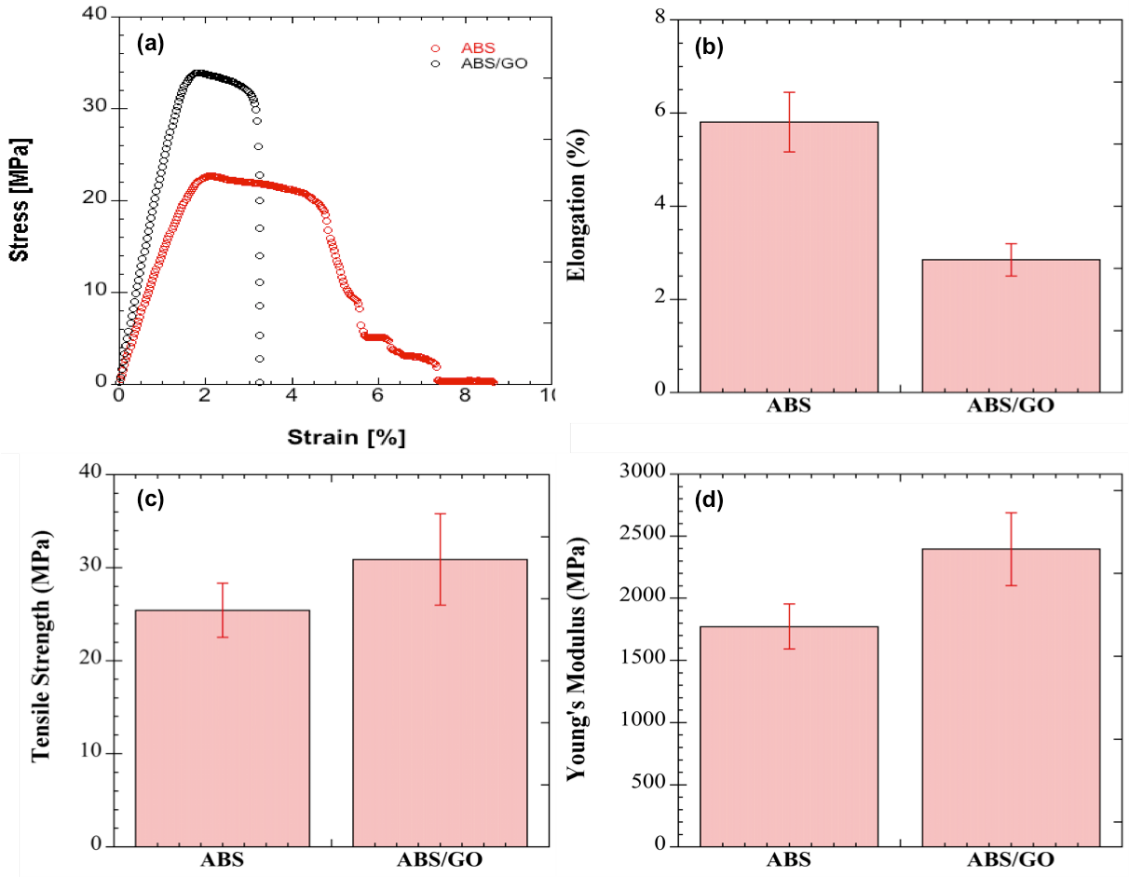

Figure 17. Typical stress-strain curves (a), value of elongation at break (b), tensile strength (c), and Young's modulus (d) of ABS and ABS/GO printed specimens.

2.3.5.7. Morphology

The alternative performance of graphene-based nanofiller reinforced composites depends on the dispersion and distribution of graphene-based materials in the polymer matrix as well as the interfacial bonding between these two phases [16]. The microstructures of the cryo-fractured sections of ABS, ABS/GO (Dry Mixing), and ABS/GO (Solvent Mixing) on cross-section are shown in **Figure 18**. Pure ABS showed a denser microstructure, while ABS/GO

demonstrated a higher-porous surface with the presence of dispersed GO flakes embedded in the ABS matrix.

For ABS/GO, GO flakes with dimensions around 10 μm were noticed for the ABS/GO (Dry Mixing), while they were ranged from 1-3 μm for the ABS/GO (Solvent Mixing). The smaller size and more uniform distribution of GO were the critical keys for enhancing the mechanical behavior and for the thermal diffusivity of the composite.

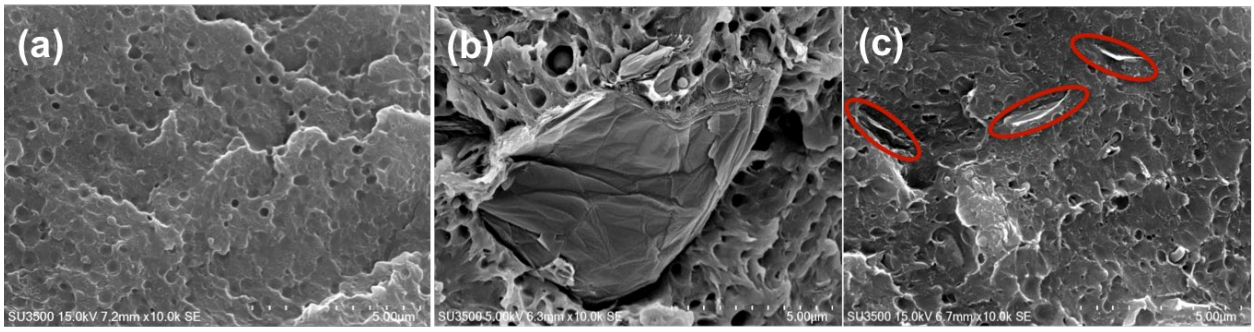

Figure 18. SEM images of (a) ABS; (b) ABS/GO (Dry Mixing); and (c) ABS/GO (Solvent Mixing) composite filaments.

2.3.6. PP/organoclay nanocomposite filaments

Polypropylene (PP) pellets were ground into powder form. PP powder with 30 wt% of organoclay was extruded first as a master batch using a co-rotating twin-screw extruder. The extrusion temperature profiles ramped from 180 up to 220 °C (from the hopper to the die). The amount of the organoclay used in all the nanocomposites was kept constant as 3 wt% concerning total PP, according to the

good mechanical performance improvement resulting from our previous study [17]. Thus, the PP/organoclay master batch was then diluted to obtain 3 wt% of organoclay using the same melt extrusion parameters.

2.3.6.1. Nonisothermal DSC

Figure 19 shows the representative DSC curves of the PP and the PP/organoclay nanocomposites. In general, the variation in the melting temperature (T_m) indicates the change of crystal structures of material. The T_m of nanocomposites could be changed upon filler loading. However, there is no significant difference between T_m for the PP and the PP/organoclay nanocomposites. Since the amount of organoclay loading in all of the PP/organoclay nanocomposites in this study were kept constant at 3wt%, this justified that the concentration of D18 does not considerably affect the thermal stability of the PP.

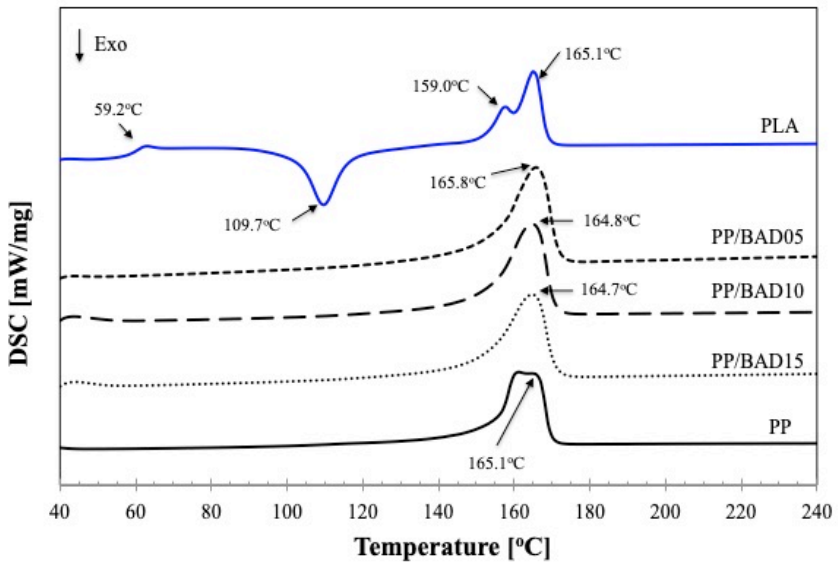

Figure 19. Melting temperatures of PP and PP/organoclay nanocomposites in comparison with PLA, the conventional material used for FFF 3D printing.

A relative broad melting peak at 165 °C is characteristic of the α −phase of iPP [18]. In comparison with the conventional PLA filament, the PP and the PP/organoclay nanocomposites could be softened at the nearly same temperature (T_m ~165 °C). It could be implied that the PP and the PP nanocomposites could be possibly 3D printed using the same temperature setup for the conventional PLA filament. Hence, the developed PP and PP/organoclay nanocomposite filaments can be 3D printed using the conventional FDM 3D printers.

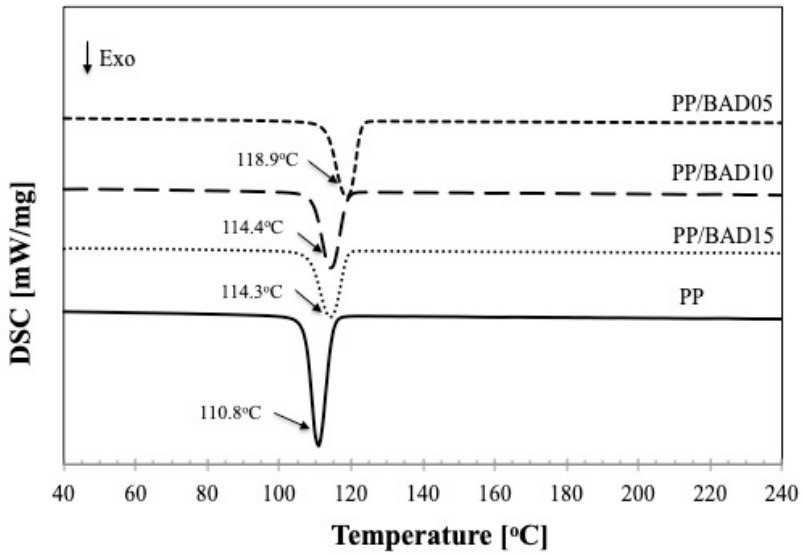

Figure 20. Crystallization temperature of PP and its composites; PP/BAD05, PP/BAD10 and PP/BAD15.

Figure 20 shows the crystallization temperature (T_c) for the PP and the PP/organoclay nanocomposites. The crystallization temperatures of all the PP/organoclay nanocomposites were found to be higher than that of pure PP. The PP/BAD10 and PP/BAD15 presented a nearly similar crystallization behavior whereas the PP/BAD05 showed the highest crystallization temperature. The shifts of both the onset and peak toward higher temperatures for all the PP/organoclay nanocomposites were observed as compared to pure PP.

2.3.6.2. Isothermal DSC

The crystallization of PP significantly affected by both the presence of D18 and the clay. These effects on the crystallization were in agreement with the

importance of the spherulite size reduction. Organoclay acted as nucleating sites and induced crystallization of the PP matrix. The degree of crystallization for materials with short molecules was high since they could crystallize faster and more accessible [19]. The addition of D18 delayed the crystallization process as shown in **Figure 21**.

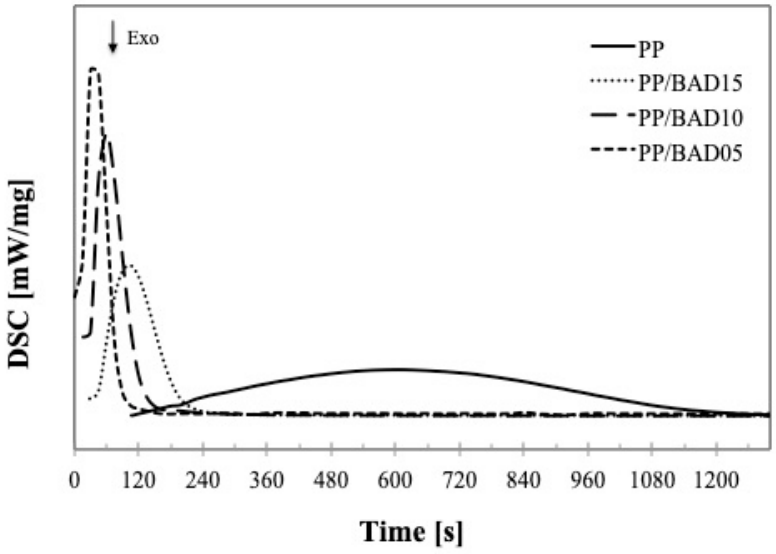

Figure 21. Isothermal segments of the crystallization process at 125 °C of PP its composites; PP/BAD05, PP/BAD10 and PP/BAD15.

When the higher content of D18 was added into the nanocomposites, the crystallization behavior tended to be much more similar to the PP, in agreement again with the weaker reductions in spherulite size compared to the pure PP. However, for the small amount of D18 (PP/BAD05), the significant shift of T_m to the higher temperature was observed, indicating the substantial reduction in spherulite size as well as the faster crystallization of the composite. These results

thus suggested that the amount of D18 played an essential role in the crystallization behavior and also the degree of crystallinity. Furthermore, the enthalpy tended to drop with an increase in D18 content. This phenomenon may also attribute to a decrease of the thermodynamically stable alpha phase content in favor of a mesomorphic structure [20].

2.3.6.3. Rheological Behaviors

The viscosity of the polymer melt usually plays an important role in the processability of materials. Understanding rheological properties is of great importance to achieve an overview of the material's structures and also the determination of processing conditions for real polymer processing, such as extrusion and injection molding. The crucial challenge is to find the optimum balance between improvements in properties, at the same time being able to process the materials. Polymer composites are mainly processed under high temperatures and high shear rates. There are several drawbacks resulted from mixing hard particles with polymers, principally due to the considerable difference in densities. Adding solid particles into a molten polymer changes the viscoelastic behavior, the viscosity and the elasticity of the system.

The dynamic strain sweep test was first applied to the neat PP and PP/organoclay nanocomposites to determine the linear viscoelastic region. **Figure**

22 presents the storage modulus (G′), which is a sensitive rheological function related to the structural changes of the nanocomposites [21]. Storage modulus (G′) of all samples exhibits a linear region (Newtonian plateau) at low strain and the non-linear region at high strain amplitudes. The addition of organoclay increased the plateau modulus. The transition point, which appeared at the deviation region from the linear to non-linear viscoelastic behavior, is defined as a critical strain (γ_c). It was observed that the critical strain (γ_c) for the PP/organoclay nanocomposites varies with the D18 content. However, at the strain less than 10%, all samples exhibit linear viscoelastic behavior. Therefore, all further rheological measurements in this study were done in the linear regime at 2% strain.

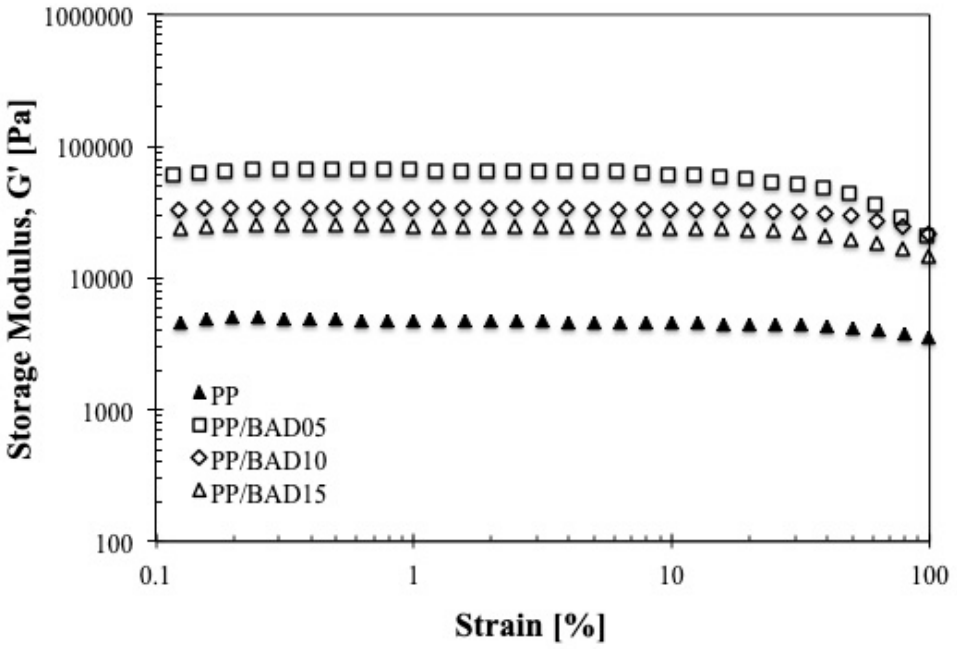

Figure 22. Storage modulus (G′) versus strain (γ) curves for neat PP and its organoclay nanocomposites at the temperature of 230 °C.

Frequency sweep tests for the PP/organoclay nanocomposites in the linear viscoelastic domain are shown in **Figure 23**. The storage modulus (G′) was increased by the incorporation of the organoclay into the PP matrix. The enhancement in the dynamic modulus was significant, in particular, at low frequencies regime. Also, G′ becomes nearly independent on the frequency at low frequencies, which is an evidence of the exfoliation or partial exfoliation [22]. It can be explained that the diffusion of the organoclay molecules is favored by making the galleries chemically compatible with the PP matrix. The compatibility occurs by exchanging interlayers inorganic clay cations with D18 cations. Therefore, layer distance (gallery distance) of organoclay increases due to the modifier. With the same loading of organoclay, G′ value is molder with higher D18 content. This reflects the less effective development of the physical interaction between the PP chains and the layer of organoclay at higher D18 content.

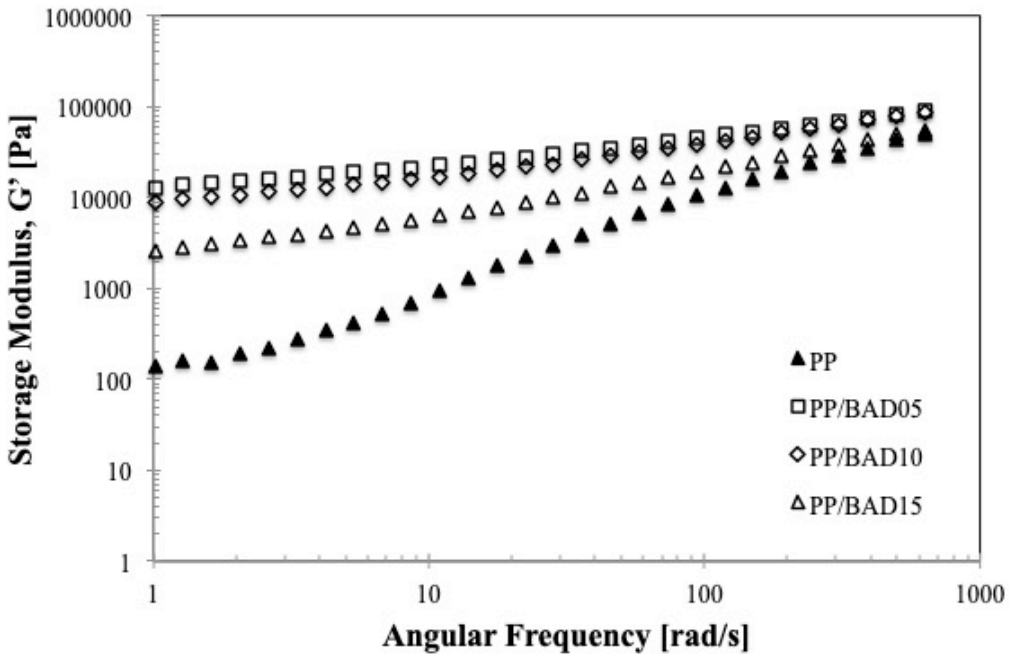

Figure 23. Frequency variations of the storage modulus, G' curves for neat PP and its organoclay nanocomposites at the temperature of 230 ^{o}C.

Figure 24 shows the variation of the complex viscosity for the neat PP, PP/BAD05, PP/BAD10, and PP/BAD15 nanocomposites. It was well established that the addition of nanofillers into the polymer matrix increased the viscosity of the system. When solid particles were added into a polymer matrix, they might disturb the flow lines and restricted the mobility of the polymer chains. The increase of the viscosity values also proves the physical network-like structure developed in the PP/organoclay nanocomposites. Furthermore, it should be noted that all the PP/organoclay nanocomposites exhibited shear-thinning behavior for the complex viscosity without any plateau region at low frequencies. Pronounced

shear thinning has also been reflected the nanodispersion which is another evidence of the exfoliation morphology [23].

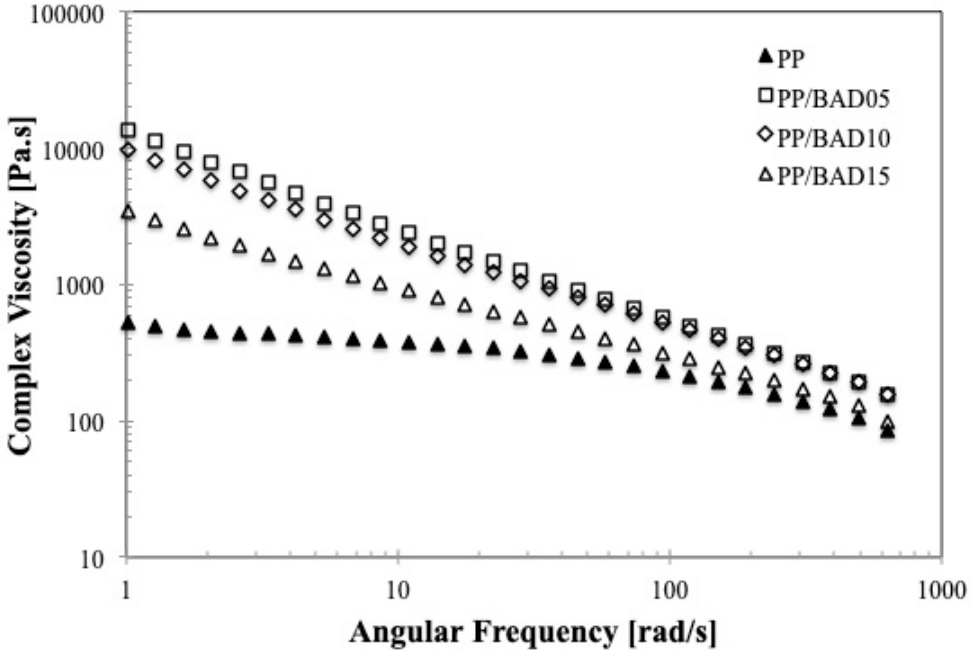

Figure 25. Complex viscosity curves for neat PP and its organoclay nanocomposites at the temperature of 230 ^{o}C.

For the FFF 3D printer, the relatively low shear rate is expected near the liquefier entrance and the print nozzle. Shear rates in the nozzle are commonly in the range of 100-200 s^{-1} [10]. Table 3 illustrates the viscosities of the PP and the PP/organoclay nanocomposites at the shear rate of 100, 200 and 1,000 s^{-1}. As expected, PP/BAD15, the nanocomposites with the highest degree of D18 loading displayed the lowest viscosity among the PP/organoclay nanocomposites at all shear rates. This can be attributed to the effect of the shorter molecule of D18,

which flow easier than the longer molecules, PP. Addition of D18 led to the improvement of the flowability of the nanocomposites. The less amount of D18 resulted in the higher degree of exfoliation/intercalation.

Table 3: Shear thinning exponent and viscosities of neat PP and PP/organoclay composites.

Samples	η (@100s^{-1})	η (@200s^{-1})	η (@1000s^{-1})
PP	235.56	176.42	80.73
PP/BAD05	581.77	360.43	117.64
PP/BAD10	578.87	369.49	128.98
PP/BAD15	339.90	230.17	90.50

2.3.6.4. Morphology

The homogeneity of organoclay dispersion directly affected the composite's printing ability and other physical properties. **Figure 26** shows the SEM images for fracture surface of the PP/clay composites filaments. With low D18 content, the PP/BAD05, the matrix coverage was not sufficient. It can be seen from many voids appeared as some evidences of the organoclay pullout from the PP matrix. This indicated the weak interfacial bonding between the organoclay and the PP matrix. With increasing the D18 content, the matrix coverage was improved. This could

be explained by the fact that the high mobility of the low molecular weight coupling agent, D18, allowed the PP matrix to interact actively with a large number of clay platelets during compounding.

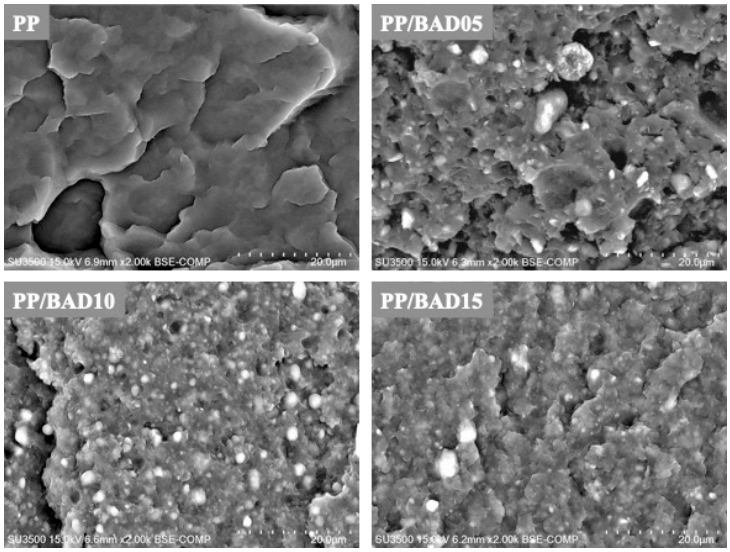

Figure 26. SEM images of fracture surfaces for neat PP and its organoclay nanocomposites at 2000x magnification.

The morphology of the PP/organoclay nanocomposites reported in this section were in good agreement with the rheological properties, confirming the capability of dispersion as well as the consequent formation of interfacial adhesion between the modified clay and the PP matrix.

Furthermore, to verify the dispersion of the organoclay and its microstructure in the PP matrix, the TEM images of the printed PP/BAD05 and PP/BAD15 were presented in **Figure 27**. At the same magnification (5,000x), the organoclay modified with higher D18 content (PP/BAD159) showed a smaller size

and better dispersion in the PP matrix than the PP/BAD05. Both the PP/BAD05 and the PP/BAD15 seem to a combination of exfoliation and intercalation morphologies as anticipated by the XRD analysis. However, it is observed that the PP/BAD15 sample has larger clay tactoids which correspond to the more likely intercalated morphology [21].

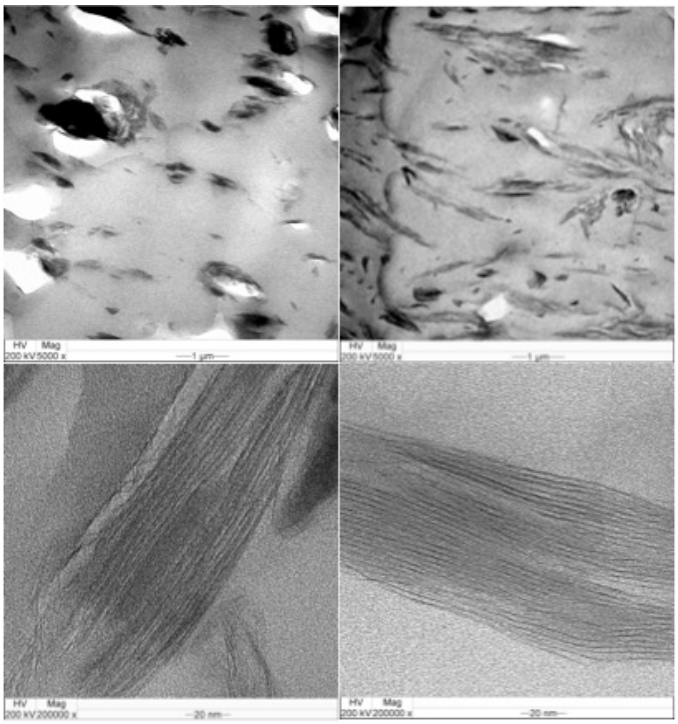

Figure 27. TEM images of the 3D printed PP/BAD05 and PP/BAD15 at 5,000x (top) and 200,000x (bottom) magnifications.

2.3.6.5. 3D Printing Optimization

For FFF 3D printing, with the extrusion temperature known, the accuracy of machine's motions can be explored [24], [25]. **Figure 28** shows the extruded mass

as a function of temperature for the PP/BAD05 in comparison with the conventional PLA filament.

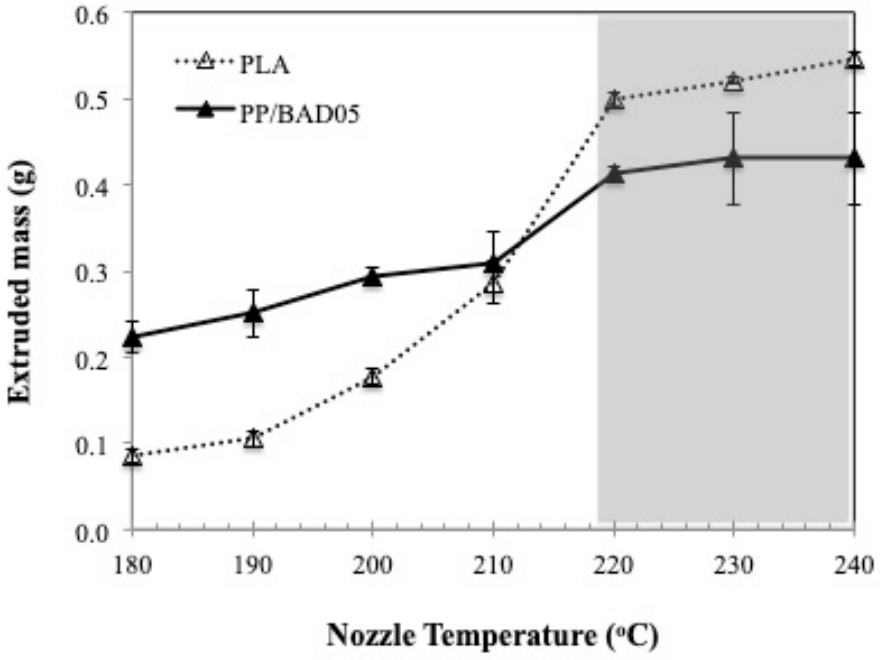

Figure 28. Extruded mass as a function of nozzle temperatures for PP/BAD05 and PLA filaments.

Both materials tended to display a plateau at the temperatures higher than 220 °C. The edge of the plateau region is considered the lower bound of acceptable temperatures for the extrusion rate. Below this temperature, the theoretical amount of polymer extruded cannot be accurately achieved at the given feed rate. Furthermore, extruding at the higher temperature than this lower bound would cause the slower solidification of the extruded bead on the printed part. From the

results, it could be concluded that PP/BAD05 could be 3D printed at the temperature range of 220 - 240 °C.

In this study, an open source 3D printer, WANHAO Duplicator 6, was used to 3D print the tensile test specimens based on ASTM D638-14 [14]. It is noted that all prepared PP/organoclay nanocomposites can be 3D printed using the same printing parameters listed in Table 4. However, the neat PP cannot be successfully 3D printed because of its semi-crystalline characteristic, which leads to the high shrinkage and warpage during printing.

Table 4: Parameters used for 3D printing of PP/organoclay nanocomposites.

Parameters	Value
Print nozzle diameter [mm]	0.4
Nozzle temperature [°C]	220
Bed temperature [°C]	110
Layer height [mm]	0.2
Print infill [%]	30
Print speed [mm·s^{-1}]	20

2.3.7. PP/graphene nanocomposite filaments

2.3.7.1. Nonisothermal DSC

In FFF 3D printing, the nozzle temperature selection, guided by thermal properties, is crucial to printing flawless. To print, semi-crystalline materials must therefore be heated above their T_m, but below their degradation points. **Figure 29** shows our calorimetry on PP/graphene nanocomposite filaments. We find that the T_m of our nanocomposites thus increases with filler loading.

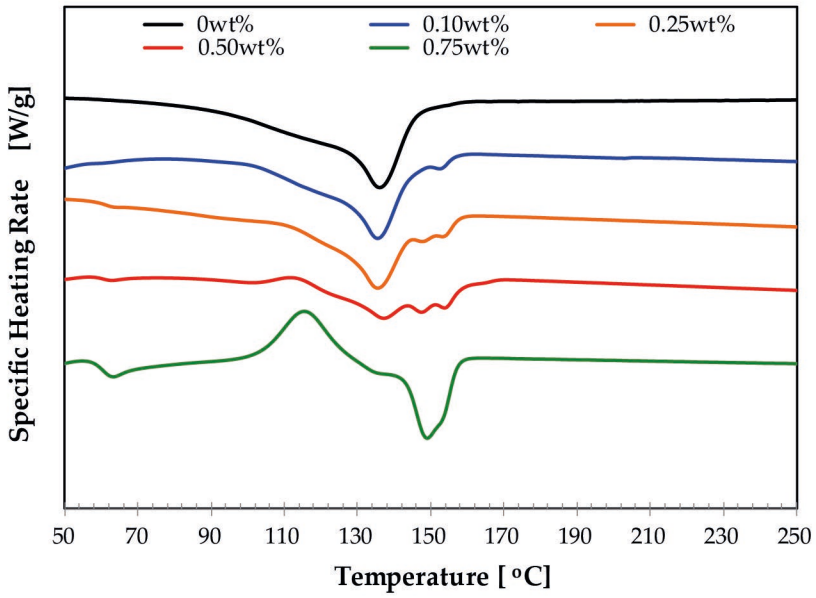

Figure 29. Melting temperature of neat PP and PP/graphene nanocomposite filament from the DSC second heating scan.

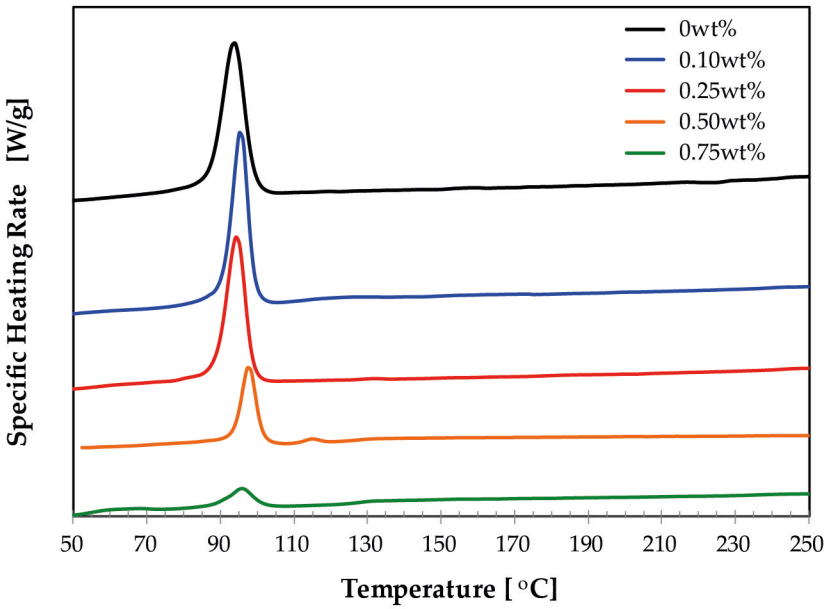

Figure 30. Crystallization temperature of neat PP and PP/graphene nanocomposite filament from the DSC first cooling scan.

Figure 30 elucidates the crystallization of our PP and PP/graphene nanocomposite filaments. The crystallization temperature of the nanocomposites increased with the graphene loading. The graphene nanoparticles are thus nucleating crystallization of the PP.

2.3.7.2. Isothermal DSC

Figure 31 shows isothermal crystallization curves of PP and PP/graphene nanocomposites. We find that the peak rates descend monotonically with graphene content. However, both the times at peak rate and the halfwidths for compositions between 0.1 and 0.25wt% match. Outside this composition range,

both the times at peak rate and the halfwidths ascend monotonically with graphene content.

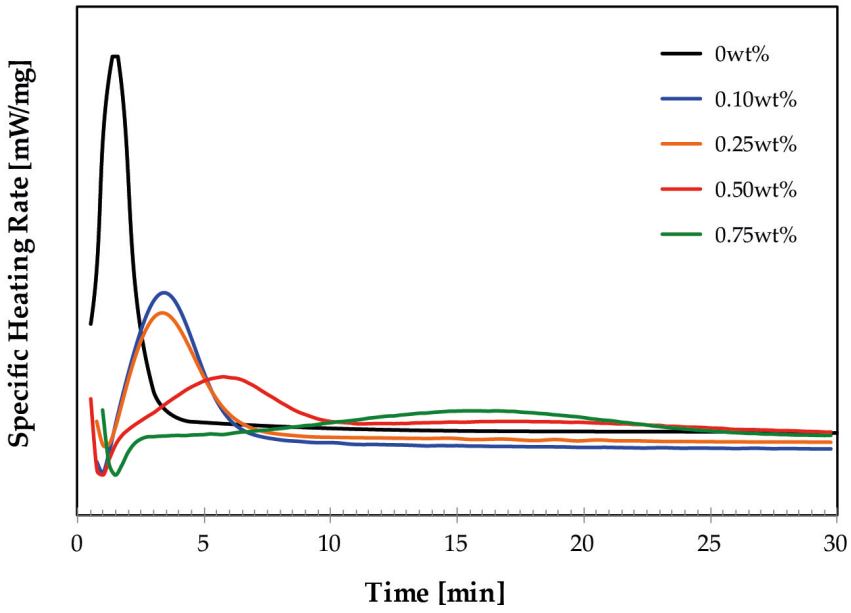

Figure 31. Isothermal crystallization of neat PP and PP/graphene nanocomposites at 110 °C.

2.3.7.3. 3D Printing Optimization

Melt extrusion based additive manufacturing is attractive and promising, potentially providing solutions for current industrial challenges. The most important parameters to achieve high interfacial bonding between printed layers are high extrusion temperature, and maintaining this temperature in the most recently deposited layers. In melt extrusion based 3D printing, knowing the extrusion temperature and flowability of the printed materials leads to more accurate and precise printing. The melt viscosity should be adequate to allow

extrusion, yet sufficient to provide structural support [25], [26]. Also, high cooling rate leads to a higher and more uniform mechanical performance. Thus, tuning the cooling rates also matters.

Figure 32 shows the low bound for the extrusion temperature by comparing nanocomposite crystallization with its viscosity behavior. The material is both fully melted and soft enough to be extruded so long as temperature exceeds 110°C. Exceeding 110°C will thus prevent solidification at the nozzle. Further, for our material extrusion 3D printing, we thus use a build plate temperature of 110°C, below which we may get dimensional instability. Specifically, instead of a smooth interface, a build plate temperature below 110°C may cause shrinkage and warpage.

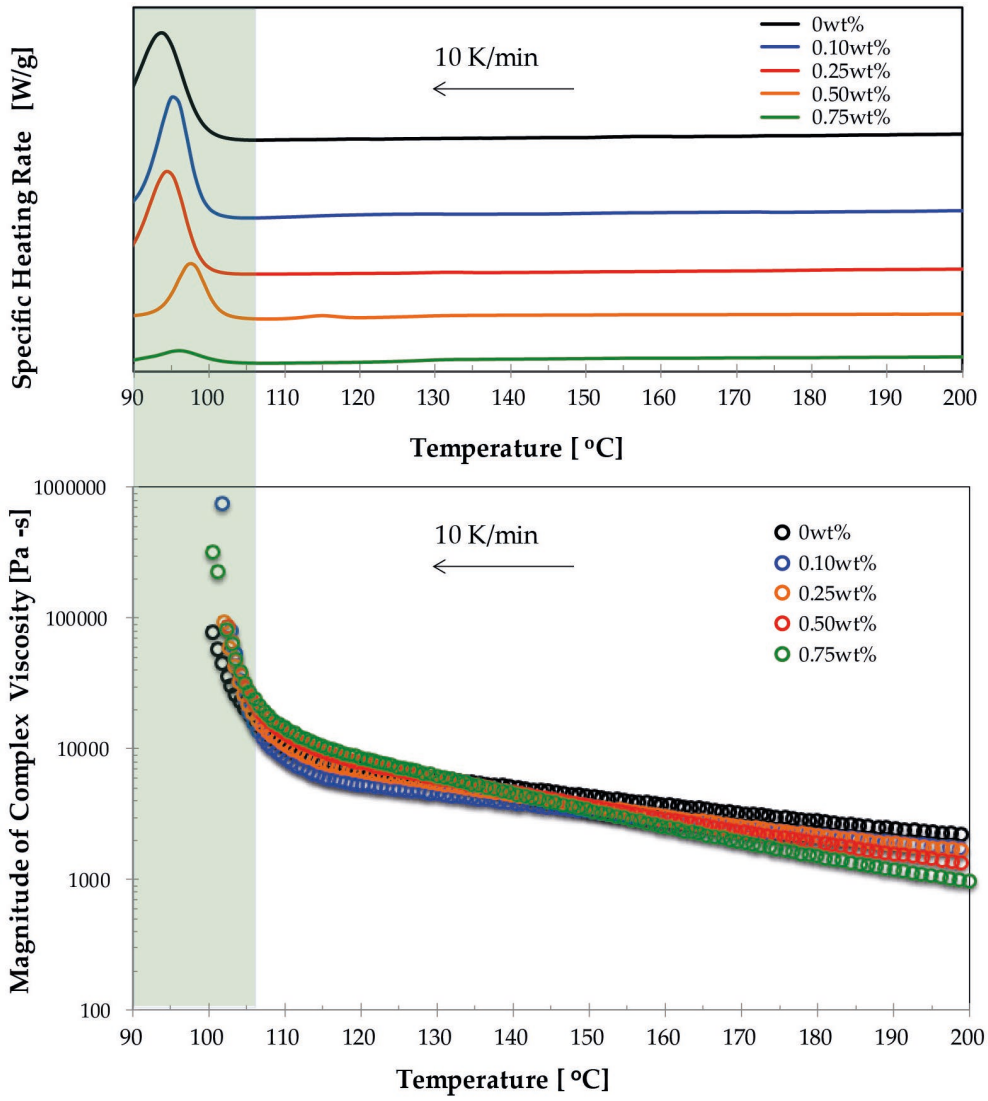

Figure 32. Specific heating rate and the magnitude of complex viscosity versus temperature of neat PP and PP/graphene nanocomposites.

For the melt extrusion-based 3D printing, we expect shear rates of 100 to 200 s^{-1} [27]–[29]. **Figure 33** shows steady shear viscosity as a function of shear rate for the neat PP and its nanocomposites, spanning this important range. Whereas, compositions 0.10 and 0.25wt% overlap, otherwise the viscosity decreases with graphene content. The reduction in viscosity can be attributed to poor interfacial

adhesion between the graphene platelets and the PP matrix, leading to discontinuous phases in the melt [30]. Of course, competing with this mechanism is the effect of graphene sheet orientation, which itself is a source of shear thinning. According to the steady shear viscosity data, over the range 100 to 200 s^{-1} shown in Figure 10, we might expect the nanocomposite with 0.75 wt% of graphene to flow most easily in our material extrusion 3D printing.

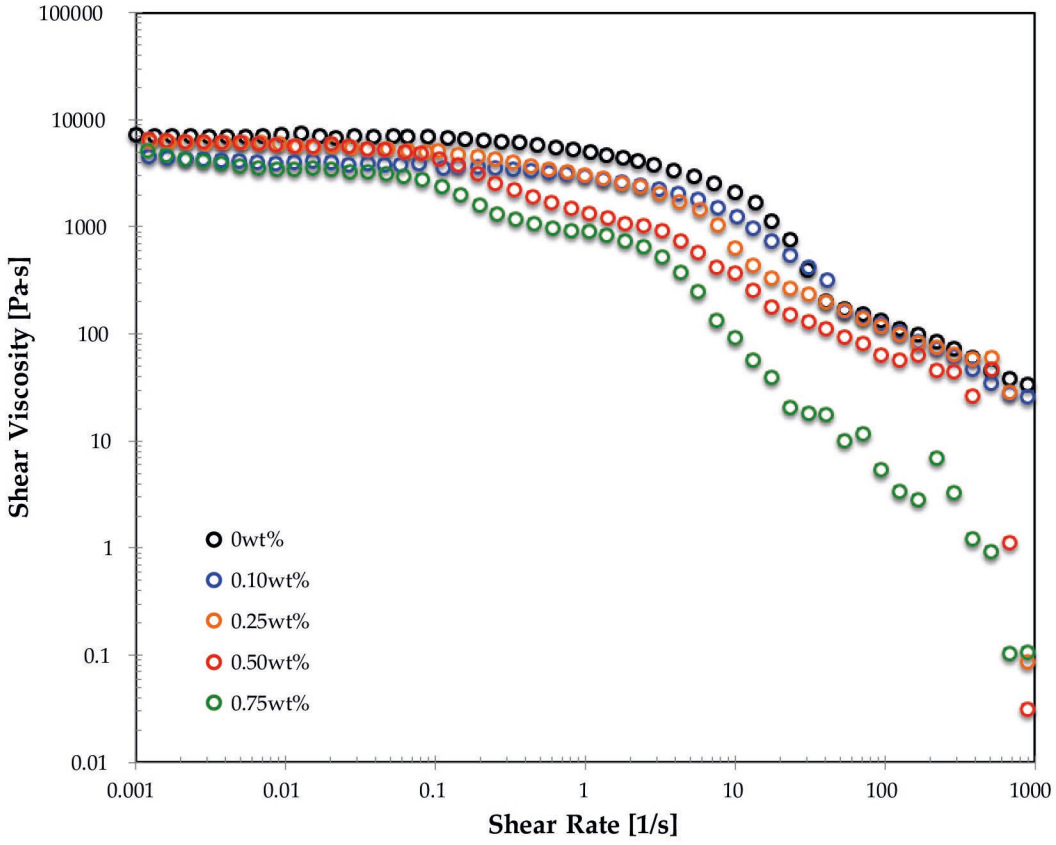

Figure 33. Shear shear viscosity of neat PP and PP/graphene nanocomposites at 200 °C.

2.3.7.4. Transmission Electron Microscopy (TEM)

Well controlled morphology of multiphase polymer blends is important for blends with the best mechanical properties. Figure 34 shows TEM images of PP/graphene nanocomposites with 0.10 wt% and 0.75 wt% of graphene. The graphene nanosheets (black lines) are visible in these micrographs. Graphene nanosheets are less visible in the nanocomposite with low graphene loading, which may be attributed to the low concentration as well as the better exfoliation.

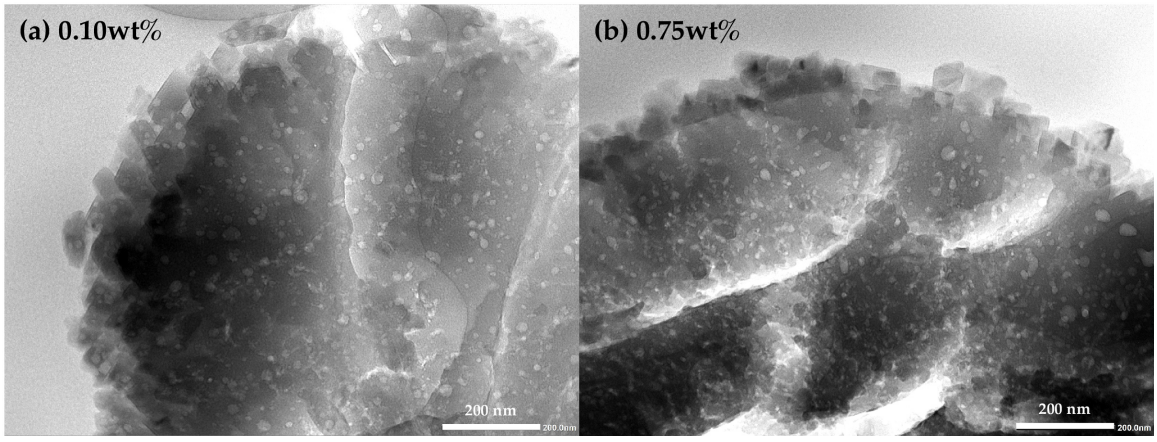

Figure 34. TEM images of PP/graphene nanocomposite containing (a) 0.10wt% and (b) 0.75wt%.

2.3.7.5. Mechanical Properties

In this study, an extrusion-based 3D printer, Cubicon 210F (3D Printing Studios, Sydney) was used to prepare the tensile test specimens following the ASTM standard, D638-14 [25]. All PP/graphene nanocomposites were printed using the same printing conditions, listed in Table 5.

Table 5. Parameters setup for 3D printing of PP/graphene nanocomposites.

Parameters		Values
Print nozzle diameter	[mm]	0.4
Nozzle temperature	[°C]	200
Building plate temperature	[°C]	110
Layer height	[mm]	0.2
Infill density	[%]	30
Printing speed	[mm/s]	20

As expected, Figure 35(a) [and Figure 35(c)] show the Young's modulus [and elongation at break] increasing [decreasing] with graphene loading. By contrast, Figure 35(b) records a nonmonotonic tensile strength behavior with graphene loading. As a result, graphene exfoliation seems to be playing an important role on the mechanical performance of the nanocomposites.

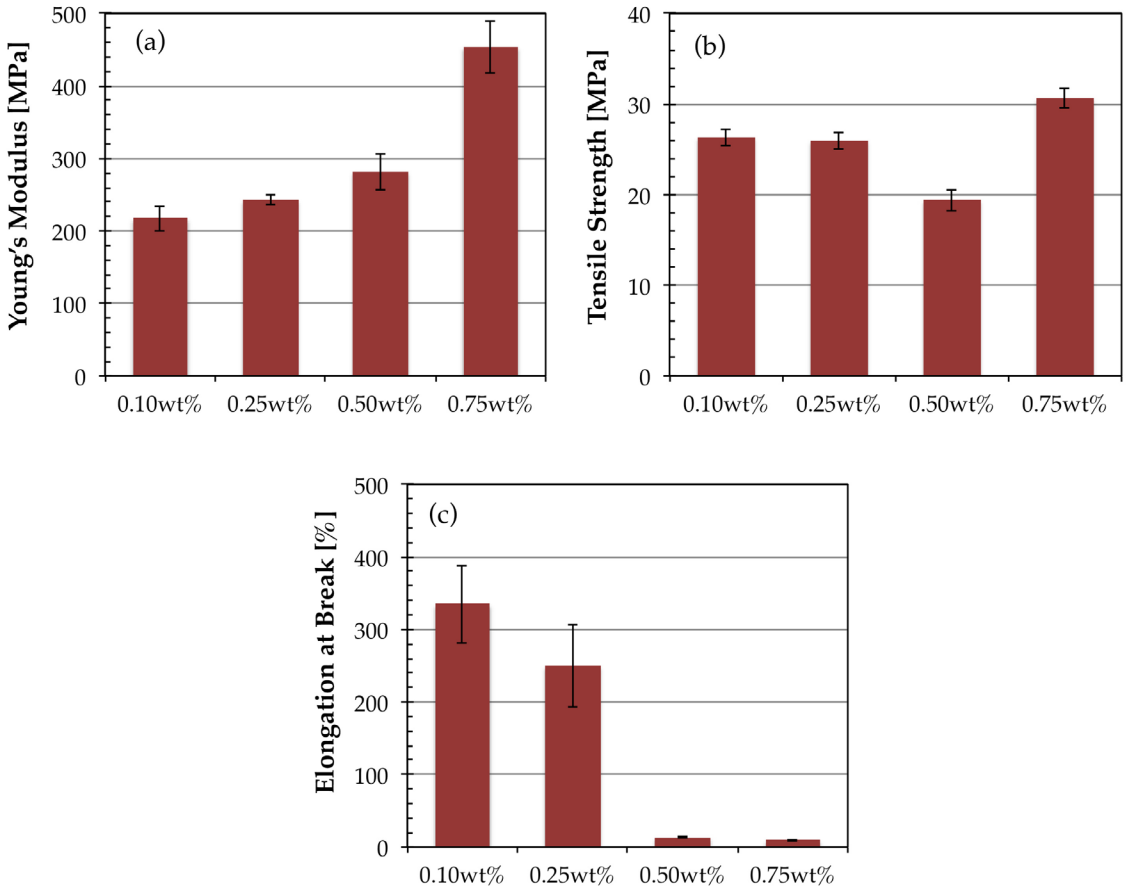

Figure 35. Young's modulus (a), tensile strength (b) and elongation at break (c) with increasing graphene content for PP/graphene nanocomposites.

2.3.8 Conclusion

This study arrived at a methodology of fabricating good-quality ABS/GO, PP/organoclay and PP/graphene nanocomposite filaments for material extrusion 3D printing. The critical parameters, thermal, mechanical, rheological, and morphological were examined.

For ***ABS/GO composites,*** the solvent system improved the GO dispersion capability in ABS matrix and had no significant effect on the thermal properties of the ABS/GO composite. However, the aggregation of GO could lead to the die clogging and failed the extrusion process. The tensile strength and Young's modulus of ABS were enhanced naturally by GO. Besides, the elongation at break decreased and needed to be further improved. Improving mechanical properties verified the feasibility of 3D printed ABS/GO for potential use in engineering applications.

For ***PP/organoclay nanocomposites,*** the linear viscoelasticity responses showed the significant effect of the clay addition. D18 was successfully used to modify the clay surfaces, providing a better dispersion and wetting of the clay particles in the hydrophobic polymer matrix such as PP. A pseudo-MFI measurement proposed that the PP/organoclay nanocomposites could be 3D printed at the temperature range of 220 - 240 ^{o}C using a conventional FFF 3D printer.

For ***PP/graphene nanocomposites***, the mechanical tests show that the Young's modulus increases with graphene loading, whereas the elongation at break decreases. The graphene exfoliation seems to be playing an important role on the mechanical performance of the nanocomposites.

This study demonstrated one of the active attempts to print GO-based composite using FFF 3D printing process directly. The procedure used for fabrication of ABS/GO, PP/organoclay nanocomposites and PP/graphene nanocomposite, as well as testing protocol can be further used as a standard method for the development of new composites filaments for Fused Deposition Modeling (FDM) 3D printing.

3. Publication

3.1 **Aumnate, C.**; Pongwisuthiruchte, A.; Pattananuwat, P.; Potiyaraj, P. Fabrication of ABS/Graphene Oxide Composite Filament for Fused Filament Fabrication (FFF) 3D Printing. *Advances in Materials Science and Engineering*. 2018, https://doi.org/10.1155/2018/2830437.

3.2 **Aumnate, C**. ; Limpanart, S. ; Soatthiyanon, N. ; Khunton, S. PP/organoclay nanocomposites for fused filament fabrication (FFF) 3D printing. *eXPRESS Polymer Letters* **2019**, 13(10) , pp. 898- 909. , https://doi.org/10.3144/expresspolymlett.2019.78.

3.3 **Aumnate, C**; Rudolph, N.; Sarmadi, M. Recycling of polypropylene/polyethylene blendds: Effect of chain structure on the crystallization behaviors. *Polymers* 2019, 11(9), 1456, https://doi.org/10.3390/polym11091456

4. Additional Activities

4.1 **Oral presentation** in Macro 2018, Australia, Topic: "Fabrication of ABS/graphene Oxide Composite Filament for Fused Filament Fabrication (FFF) 3D Printing"

5. **Problems -**

6. **Comments and Suggestions -**

7. **Future work**

Reference

[1] S. Nazarpour and S. R. Waite, *Graphene Technology*. 2016.

[2] J. Zhang, H. Yang, G. Shen, P. Cheng, J. Zhang, and S. Guo, "Reduction of graphene oxide vial-ascorbic acid," *Chem. Commun.*, vol. 46, no. 7, pp. 1112–1114, 2010.

[3] S. Chen, J. Lu, and J. Feng, "3D-Printable ABS Blends with Improved Scratch Resistance and Balanced Mechanical Performance," *Ind. Eng. Chem. Res.*, vol. 57, pp. 3923–3931, 2018.

[4] X. Wei *et al.*, "3D Printable Graphene Composite," *Sci. Rep.*, vol. 5, no. 1, pp. 1–7, 2015.

[5] "https://en.wikipedia.org/wiki/Xylene." .

[6] "https://en.wikipedia.org/wiki/Toluene." .

[7] ASTM International, "Astm D1238 − 13," *ASTM Int.*, no. August, pp. 1–16, 2013.

[8] T. Pfeifer, C. Koch, L. Van Hulle, G. A. M. Capote, and P. Natalie, "Optimization of the FDM Additive Manufacturing Process," in *SPE ANTEC™ Indianapolis 2016*, 2016, pp. 22–29.

[9] T. A. Osswald and N. Rudolph, *Polymer Rheology Fundamental and Applications*. Munich: Hanser Publishers, 2015.

[10] A. Venkataraman, N; Rangarajan, S; Matthewson, M J; Harper, B; Safari, A; Danforth, S C; G. Wu; Langrana, N; Guceri, S; Yardimci, "Feedstock material property - process relationships in fused deposition of ceramics (FDC)," *Rapid Prototyp. J.*, vol. 6, no. 4, pp. 244–252, 2000.

[11] L. A. Al-Hariri, B. Leonhardt, M. Nowotarski, J. Magi, and K. Chambliss, "Carbon Nanotubes and Graphene as Additives in 3D Printing," in *INTECH*, 2016, pp. 227–251.

[12] L. Du, M. Namvari, and F. J. Stadler, "Large amplitude oscillatory shear behavior of graphene derivative/polidimethylsiloxane nanocomposites," *Rheol. Acta*, vol. 57, pp. 429–443, 2018.

[13] G. M. Shin, J. Y. Park, and Y. C. Kim, "GO Dispersion and Mechanical Properties of 70PC/30ABS/GO Composites according to Fabrication Methods," *Polym.*, vol. 41, no. 3, pp. 452–459, 2017.

[14] American Society for Testing and Material (ASTM), "Standard Test Method for Tensile Properties of Plastics (D638-14)," 2014.

[15] R. Sharma, R. Singh, R. Penna, and F. Fraternali, "Investigations for mechanical properties of Hap, PVC and PP based 3D porous structures obtained through biocompatible FDM filaments," *Compos. Part B*, vol. 132, pp. 237–243, 2018.

[16] V. Panwar and K. Pal, "An optimal reduction technique for rGO/ABS composites having high-end dynamic properties based on Cole-Cole plot, degree of entanglement and C-factor," *Compos. Part B*, vol. 114, pp. 46–57, 2017.

[17] S. Limpanart *et al.*, "Effect of the surfactant coverage on the preparation of polystyrene-clay nanocomposites prepared by melt intercalation," *Mater. Lett.*, vol. 59, no. 18, pp. 2292–2295, 2005.

[18] G. Colombe, S. Gree, O. Lhost, M. Dupire, M. Rosenthal, and D. A. Ivanov, "Correlation between mechanical properties and orientation of the crystalline and mesomorphic phases in isotactic polypropylene fibers," *Polymer (Guildf).*, vol. 52, no. 24, pp. 5630–5643, 2011.

[19] T. A. Osswald and G. Menges, *Materials Science of Polymers for Engineers*. Munich Vienna New York, 1996.

[20] G. Lamberti, "Isotactic polypropylene crystallization: Analysis and modeling," *Eur. Polym. J.*, vol. 47, no. 5, pp. 1097–1112, 2011.

[21] A. Durmus, A. Kasgoz, and C. W. Macosko, "Linear low density polyethylene (LLDPE)/clay nanocomposites. Part I: Structural characterization and quantifying clay dispersion by melt rheology," *Polymer (Guildf).*, vol. 48, no. 15, pp. 4492–4502, 2007.

[22] M. Abdel-Goad, "Rheological characterization of melt compounded polypropylene/clay nanocomposites," *Compos. Part B Eng.*, vol. 42, no. 5, pp. 1044–1047, 2011.

[23] M. Abdel-Goad, "Rheological characterization of melt compounded polypropylene/clay nanocomposites," *Compos. Part B Eng.*, vol. 42, no. 5, pp. 1044–1047, 2011.

[24] T. Pfeifer, C. Koch, L. Van Hulle, G. A. Mazzei, and N. Rudolph, "Optimization of the FDM Additve Manufacturing Process," *Proc. ANTEC 2016*, pp. 22–29, 2016.

[25] C. Aumnate, A. Pongwisuthiruchte, P. Pattananuwat, and P. Potiyaraj, "Fabrication of ABS / Graphene Oxide Composite Filament for Fused Filament Fabrication (FFF) 3D Printing," *Adv. Mater. Sci. Eng.*, vol. 2018, 2018.

[26] X. Wang, M. Jiang, Z. Zhou, J. Gou, and D. Hui, "3D printing of polymer matrix composites: A review and prospective," *Compos. Part B Eng.*, vol. 110, pp. 442–458, 2017.

[27] T. A. Osswald, G. Menges, and G. Manges, *Materials Science of Polymers for Engineers*, 3rd ed. Munich Vienna New York: Hanser Publishers, 2013.

[28] C. Aumnate, S. Limpanart, N. Soatthiyanon, and S. Khunton,

"PP/organoclay nanocomposites for fused filament fabrication (FFF) 3D printing," *Express Polym. Lett.*, vol. 13, no. 10, pp. 898–909, 2019.

[29] C. Spicker, N. Rudolph, I. Kühnert, and C. Aumnate, "The use of rheological behavior to monitor the processing and service life properties of recycled polypropylene," *Food Packag. Shelf Life*, vol. 19, pp. 174–183, Mar. 2019.

[30] A. P. Bafana *et al.*, "Polypropylene nanocomposites reinforced with low weight percent graphene nanoplatelets," *Compos. Part B Eng.*, vol. 109, pp. 101–107, 2017.

Appendix

A1. Aumnate, C.; Pongwisuthiruchte, A.; Pattananuwat, P.; Potiyaraj, P. Fabrication of ABS/Graphene Oxide Composite Filament for Fused Filament Fabrication (FFF) 3D Printing. *Advances in Materials Science and Engineering*. 2018, https://doi.org/10.1155/2018/2830437.

A2. Aumnate, C.; Limpanart, S.; Soatthiyanon, N.; Khunton, S. PP/organoclay nanocomposites for fused filament fabrication (FFF) 3D printing. *eXPRESS Polymer Letters* **2019**, 13(10), pp. 898-909., https://doi.org/10.3144/expresspolymlett.2019.78.

A3. Aumnate, C.; Rudolph, N.; Sarmadi, M. Recycling of polypropylene/polyethylene blends: Effect of chain structure on the crystallization behaviors. *Polymers* 2019, 11(9), 1456, https://doi.org/10.3390/polym11091456

Hindawi
Advances in Materials Science and Engineering
Volume 2018, Article ID 2830437, 9 pages
https://doi.org/10.1155/2018/2830437

Research Article

Fabrication of ABS/Graphene Oxide Composite Filament for Fused Filament Fabrication (FFF) 3D Printing

C. Aumnate[1], **A. Pongwisuthiruchte**[2,3], **P. Pattananuwat**[2,3] and **P. Potiyaraj**[1,2,3]

[1]*Metallurgy and Materials Science Research Institute, Chulalongkorn University, Bangkok, Thailand*
[2]*Department of Materials Science, Faculty of Science, Chulalongkorn University, Bangkok, Thailand*
[3]*Center of Excellence on Petrochemical and Materials Technology, Chulalongkorn University, Bangkok, Thailand*

Correspondence should be addressed to C. Aumnate; chuanchom.a@chula.ac.th

Received 6 August 2018; Revised 26 September 2018; Accepted 8 October 2018; Published 6 November 2018

Academic Editor: Amit Bandyopadhyay

Additive manufacturing, the so-called three-dimensional (3D) printing, is a revolutionary emerging technology. Fused filament fabrication (FFF) is the most used 3D printing technology in which the melted filament is extruded through the nozzle and builds up layer by layer onto the build platform. The layers are then fused together and solidified into final parts. Graphene-based materials have been positively incorporated into polymers for innovative applications, such as for the mechanical, thermal, and electrical enhancement. However, to reach optimum properties, the graphene fillers are necessary to be well dispersed in polymers matrix. This study aims to emphasise the interest of producing ABS/graphene oxide (GO) composites for 3D printing application. The ABS/GO composite filaments were produced using dry mixing and solvent mixing methods before further melt extruded to investigate the proper way to disperse GO into ABS matrix. The ABS/GO composite filament with 2 wt.% of GO, prepared from the solvent mixing method, was successfully printed into a 3D model. By adding GO, the tensile strength and Young's modulus of ABS can be enhanced. However, the ABS/GO composite filament that was prepared via the dry mixing method failed to print. This could be attributed to the aggregation of GO, leading to the die clogging and failure of the printing process.

1. Introduction

Numerous 3D printing technologies are now accessible, such as stereolithography apparatus (SLA), selective laser sintering (SLS), laminated object manufacturing (LOM), and fused filament fabrication (FFF). The FFF is considered to be the most commonly used and well-recognized technology for making functional prototypes. In the FFF technique, a thermoplastic filament is melted and extruded through the nozzle, building up layer by layer onto the platform or build plate. The layers are then fused together and solidified into final products. Consequently, the quality of the printed parts can be controlled by adjusting the printing parameters, such as layer height, printing temperature, printing speed, and printing orientation [1–6]. 3D printed polymers are used in various areas, for example, in automotive, architectural, and even in medical fields. Due to the relatively simple design, capability, and affordability of the FFF process, it has gained significant attention in both industry and academic research [5]. However, the usable materials are limited to thermoplastic polymers with appropriate melt viscosity. As a result, the melt viscosity should be adequate to allow extrusion, at the same time, suitable to provide structural supports [4, 6]. Even though the 3D printing technologies have attracted much attention over the past years, most of the published studies focused on the printing of pure polymer materials. The 3D printed polymer products are now used as conceptual prototypes rather than functional components because of their shortage in strength and limited functionality. Thus, there are recently extensive studies on developing printable polymer composites with improving the performance and gaining excellent functionalities [7–9]. For example, Bandyopadhyay et al. [2] used the FFF technique to fabricate the polymer/ceramic composites with controlled phase structures, which are not possible with the conventional fabrication techniques.

Polymer/nanofiller composites have been considerably investigated due to their broad applications. However, they have many drawbacks regarding the agglomeration or nonuniform dispersion of reinforcements or fillers. Also, the voids generated during the composite filaments fabrication can lead to the properties' defection. In general, the addition of nanofillers results in enhancing the mechanical, electrical, thermal, and optical properties of the matrix. Likewise, GO delivers relatively high mechanical strength, thermal conductivity, and electrical properties [8, 10, 11]. If the GO sheets are well dispersed in the polymer matrix, they can form a highly oriented microstructure or cocontinuous networks in the polymer, resulting in the mechanical, thermal, and electrical properties improvement [12]. Graphene-based composite is still challenged due to its poor dispersity, which may be caused by various reasons such as restacking of the GO, weak interfacial bonding, and incompatibility with polymer matrix [10, 13]. Pinto et al. [10] incorporated a small amount (0.2 to 1 wt.%) of graphene oxide (GO) and graphene nanoplatelets (GNP) into poly (lactic acid), PLA, to produce composite films with improved mechanical performance and oxygen and nitrogen permeability. Wang et al. [14] reported that the tensile strength of the PVA/GO composite nanofibers increased by 42 times with addition of only a slight loading of GO (0.02 wt.%). Lin et al. [15] fabricated polyethylene/graphene oxide nanocomposites by the melt blending technique using polyethylene-grafted graphene oxide as a compatibilizer. Even though a relatively good dispersion of graphene oxide in the polyethylene matrix was evidenced, the improvement of mechanical properties was still limited. The resulted graphene-based composites can be suitable for various applications such as architectural applications like patio roofs, windows, and trim [16].

There are three typical methods for graphene-based polymer composite fabrication methods, including in situ polymerization, melt compounding, and solvent blending. The critical challenge for efficiently reinforcing the graphene-based polymer composite is the good dispersion of graphene fillers, which is significantly influenced by the fabrication techniques. Even though many reports stated that the melt extrusion or melt-compounding process is the most typically used methods, the GO cannot be homogeneously dispersed in the polymer matrix. Due to the high surface area of GO, it is tough for the molten polymer to cover the two sides of the fragile GO sheets effectively. As a result, the stack or agglomeration of GO sheets can be observed [10, 11].

Zhang et al. [17] fabricated the flexible circuits based on reduced GO (r-GO) using the FFF 3D printing technique. They reported that the orientation of r-GO occurred during the extrusion process contributed to enhancing the conductivity of the 3D printed composite parts. Moreover, Dul et al. [18] successfully prepared the ABS/GNP composite for the FFF process using the melt compounding method. The presence of GNP led to the reduction in the coefficient of thermal dilation and improved the stability under long-lasting loads for the 3D printed parts. However, it has been spotted that the polymer/graphene-based material composites prepared via the solution mixing method provided better electrical properties than those fabricated by melt extrusion due to the better dispersion of graphene-based materials in polymer solution [16, 19].

Acrylonitrile butadiene styrene (ABS) is one of the most used materials in the FFF process [20]. The relatively low glass transition temperature (T_g) and excellent processing properties of ABS led to the ease of filament extrusion and 3D printing. Moreover, it is an amorphous polymer, which means there is no crystallite. Accordingly, the shrinkage ratio during the cooling process is small, offering the high printing accuracy and the dimensional constancy. All of the characteristics stated above make ABS as an outstanding material for FFF 3D printing. Incorporation of graphene-based materials will potentially enlarge the applications and functionalities of the 3D printed ABS, in particular, some practical applications such as auto parts, conceptual prototypes, and jigs. However, the use of ABS/graphene-based composites in 3D printing application is still rarely demonstrated. Wei et al. [13] successfully demonstrated one of the first attempts to 3D print ABS/graphene composites using solution-based process. However, there was no report regarding the property investigation for such 3D printed composites.

To produce a good-quality filament for the FFF process, critical melt extrusion process parameters need to be examined. This study aims to accomplish good-quality composite filament from ABS/GO composites. The ABS/GO composites are prepared via solution mixing and dry mixing methods, followed by melt extrusion to achieve the good GO dispersion. The processability of ABS/GO composites is further investigated in terms of thermal properties and rheological properties. Also, 3D objects are printed to explore the printability of the prepared ABS/GO filament.

2. Materials and Methods

2.1. Preparation of Graphene Oxide (GO). The GO was prepared using Hummers' method. Concentrated H_2SO_4 was added to a mixture of graphite flakes (1 wt.% equiv.) and $NaNO_3$ (0.5 wt.% equiv.). Then, the mixture was cooled to 0°C, and $KMnO_4$ (3 wt.% equiv.) was added slowly in portions to keep the reaction temperature below 20°C. After that, the reaction was warmed to 35°C and stirred for 30 minutes, at which time water was added slowly to produce a sizable exothermic reaction to 98°C. The external heating was also introduced to maintain the reaction temperature at 98°C for 15 minutes. Then the heat was removed, and the reaction was cooled down in a water bath for 10 minutes. From this step, additional water (420 ml) and 30% H_2O_2 (3 ml) were added, and then the mixture was cooled down to room temperature, followed by multiple washing, and dispersed in water.

2.2. Preparation of ABS/GO Composite. The dispersed GO in water was washed and replaced by DMF to obtain a homogeneous GO/DMF dispersion with 2 wt.% of GO in DMF. The ABS was then dissolved in DMF to get 10 wt.% of ABS in DMF. Then, the GO/DMF dispersion and ABS/DMF solution were mixed and sonicated for 2 hours. The mixture

was then dried to obtain ABS/GO composite with 20 wt.% GO.

2.3. Preparation of ABS/GO Composite Filament

2.3.1. Solution Mixing. In this method, the ABS gets dissolved, and the GO is dispersed in DMF. Then, the dispersed GO and ABS solution is mixed. The ABS/GO composite is obtained after solvent evaporation, which further combined with pure ABS and extruded to produce ABS/GO filament for FFF 3D printing.

2.3.2. Dry Mixing. ABS is mixed mechanically with GO powder and then is melt compounded using the twin-screw extruder to avoid the use of the solvent system. This method is widely used for preparing thermoplastic nanocomposite.

For the filament extrusion process, the ABS/GO composite with 20 wt.% of GO content was diluted to 4 wt.% of GO by mixing with the neat ABS granules. The mixture was then melted and extruded using the twin-screw extruder. The extrusion temperatures ranged from 160°C to 210°C from the hopper to the die. Thus, the 1.75 mm diameter filament was produced and collected for the 3D printing test. Figure 1 demonstrates the equipment setup for preparing the ABS/GO filament by the melt extrusion process.

2.4. Fabrication of 3D Printed Parts. An open source 3D printer, WANHAO Duplicator 6, was used to fabricate the 3D specimens. A tensile test specimen was designed using CAD software based on ASTM D638-10 [21]. The FFF printing parameters were optimized and are listed in Table 1. It is noted that the same printing parameters were used for both pure ABS and ABS/GO composite filaments.

2.5. Characterization

2.5.1. X-Ray Diffraction (XRD) Analysis. The X-ray diffraction (XRD) of graphene-based materials was performed using an X-ray diffractometer (Bruker AXS Model D8 Discover). All samples were scanned over the range $2\theta = 2–50^{\circ}$, and measurements were recorded at every 0.02° interval.

2.5.2. Differential Scanning Calorimetry (DSC). The measurements were carried out using a Netzsch DSC 3500 Sirius, under the nitrogen atmosphere. The samples were heated from room temperature to 250°C. After an isothermal step for 2 minutes, the samples were cooled down to 30°C and finally heated up to 250°C after another isothermal step for 2 min. A scanning temperature ramp of 10 K/min was used for all dynamic steps.

2.5.3. Thermogravimetric Analysis (TGA). The measurements were carried out using a Netzsch STA 2500. The samples were heated from room temperature to 600°C, under the nitrogen atmosphere. A scanning temperature ramp of 10 K/min was used for the dynamic steps.

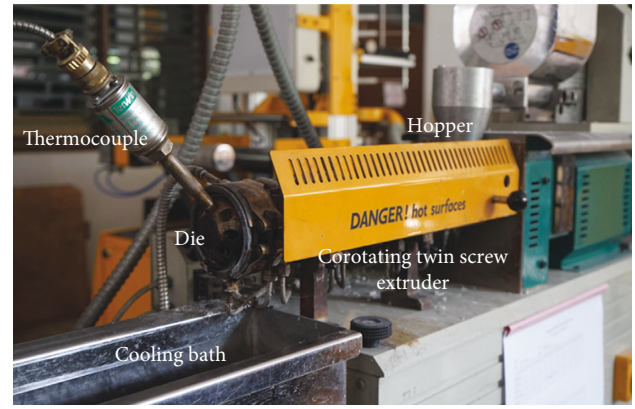

Figure 1: Melt extrusion process setup for ABS/GO composite filament fabrication.

Table 1: Parameters used for the FFF 3D printing of ABS and ABS/GO composites.

Parameters	Value
Print nozzle diameter (mm)	0.4
Nozzle temperature (°C)	220
Bed temperature (°C)	100
Layer height (mm)	0.1
Print infill (%)	100
Print speed (mm/s)	20

2.5.4. Melt Flow Rate. The melt flow rate (MFR) is a common rheological measurement in which the molten polymer is pushed through a capillary die under a specific load, and the mass of extruded polymer is measured and reported in the unit of the extruded mass/10 minutes. The MFR measurements were carried out according to ASTM D1238 standard (Procedure A), at a temperature range of 220–240°C with an applied load of 2.16 kg [22].

A pseudo-MFR measurement was performed using the FFF 3D printer with the nozzle diameter of 0.4 mm in order to determine the proper printing temperature. The extruded material through the nozzle in a 30-second time frame was weighed as a function of temperature.

2.5.5. Rheology Test. The linear viscoelasticity responses of the materials were measured using a parallel plate rheometer (ARES G2000). A frequency sweep between 0.0628 and 628 rad/s was performed at a temperature of 210°C. Based on the result of the strain sweep test, a constant strain was fixed as 5% where the linear viscoelastic behavior maintained. Also, the steady shear measurements were conducted at 220°C, from the shear rate range of 0.01 to 1000 s^{-1}. The two parallel plates were set up at 1 mm gap for all measurements.

2.5.6. Tensile Test. To study the mechanical properties, the tensile test specimens were printed based on ASTM D638 Type-V geometry [23]. The crosshead speed was set as 5 mm/min. Ultimate tensile strength, Young's modulus, and elongation at break were evaluated as an average value of at least three replicates.

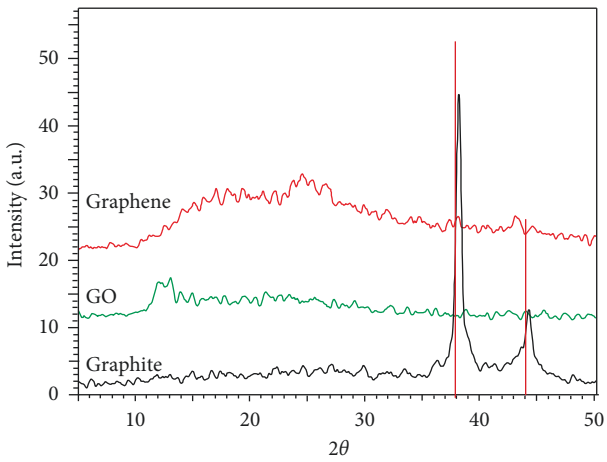

Figure 2: XRD diagram of graphite, graphene, and graphene oxide (GO).

3. Results and Discussion

Recently graphene/polymer composite has been fabricated by introducing graphene flakes into a conventional polymer that can be used for FFF printing applications. However, the apparent graphene aggregation and the phase separation between graphene and polymer matrixes are significant problems. In this work, graphene oxide (GO) was used to improve the graphene's dispersion in the ABS matrix.

3.1. X-Ray Diffraction (XRD) Analysis. In this study, GO was obtained by the oxidation of graphite regarding Hummers' method. Figure 2 shows the XRD patterns of the graphite, graphene, and obtained GO.

According to Bragg's law ($n\lambda = 2d \sin\theta$), the value of D spacing depended on the θ value. The diffraction peak of graphite was observed at $2\theta = 36.7^{\circ}$ with D spacing around 0.11 nm. The diffraction peak for graphene was shifted to $2\theta = 25$ with D spacing around 0.35 nm as compared to those of graphite, while the GO revealed the diffraction peak at $2\theta = 12.9^{\circ}$ with D spacing of 0.67 nm. The shifts of the diffraction peak and the increase of the D spacing value attributed to the oxygen functional group between planes of GO sheets. The interactions of the oxygen functional group between GO interlayers led to an increase in the D spacing value, while the θ value decreased. In other words, in the absence of the oxygen functional group, the θ value increases, while the D spacing value decreases.

3.2. Thermal Properties. Figure 3 shows the representative DSC curves of ABS, ABS/GO (dry mixing), and ABS/GO (solvent mixing) composite filaments. In general, the variation in the melting temperature (T_m) indicated the change in crystal structures of material. T_m of nanocomposites could be changed upon filler loading. ABS has no exact melting point because of its amorphous characteristic. However, no significant difference between T_g of the neat ABS filament and the ABS/GO composite filaments from both dry mixing and solvent mixing methods was found. The glass transition

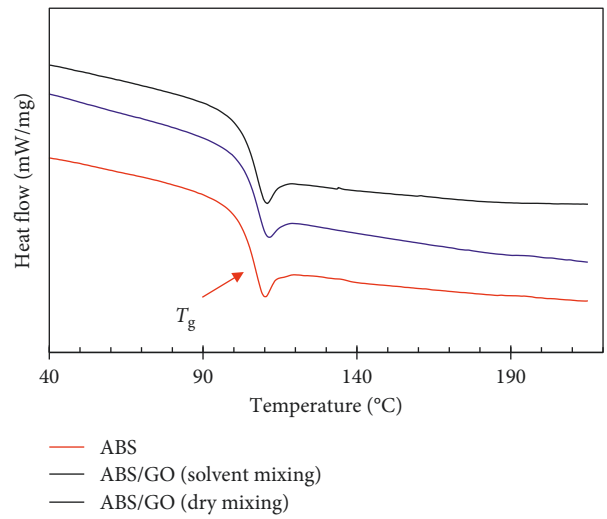

Figure 3: Melting temperature of the ABS filament, ABS/GO (solvent mixing), and ABS/GO (dry mixing) composite filaments from the DSC second heating scan.

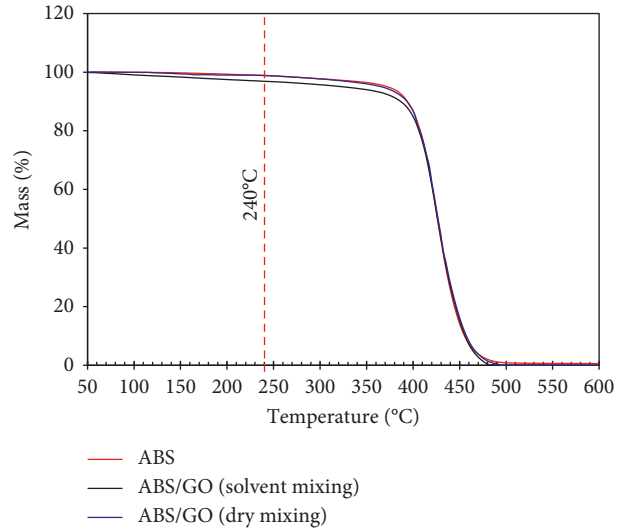

Figure 4: TGA thermogram of the ABS filament, ABS/GO (solvent mixing), and ABS/GO (dry mixing) composite filaments.

temperatures (T_g) were observed at 105.72°C, 104.77°C, and 105.69°C for ABS, ABS/GO (dry mixing), and ABS/GO (solvent mixing) filaments, respectively. The maintained T_g subsequently revealed the thermal stability of the ABS/GO composite even though the composite experienced the solvent system before the extrusion process. Furthermore, the ABS/GO composite could be softened and possibly 3D printed using the same temperature setup used for the pure and conventional ABS filaments.

3.3. Thermal Stability. To explore the effect of GO on thermal stability of the ABS and ABS/GO composite filaments, thermal gravimetric analysis (TGA) was conducted. Figure 4 shows the TGA thermogram of neat ABS and ABS/GO composite (2 wt.% GO) filaments. All materials

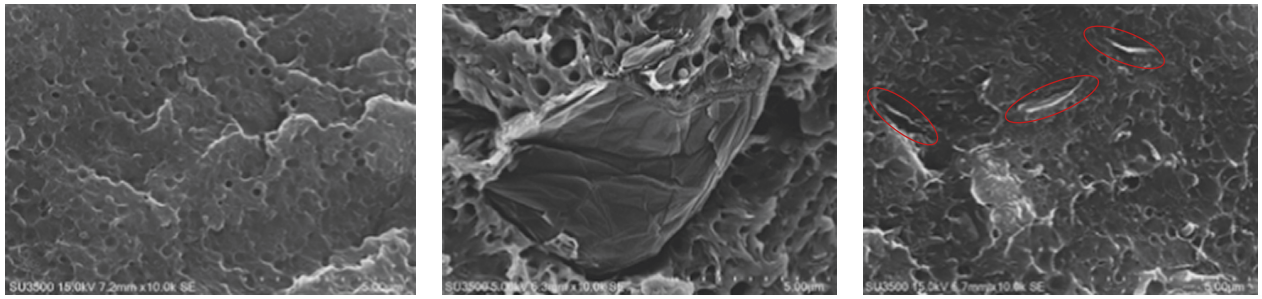

(a) (b) (c)

Figure 5: SEM images of (a) ABS, (b) ABS/GO (dry mixing), and (c) ABS/GO (solvent mixing) composite filaments.

started to decompose at the temperature around 400°C, which was higher than the typical temperature for 3D printing the conventional ABS filament (220–240°C). At 240°C, the highest temperature used for the 3D printing the conventional ABS filament, the ABS/GO (solvent mixing) showed a more mass drop (~3%) as compared to the pure ABS (~1.3%) and ABS/GO (dry mixing). These results could be due to the volatile compounds and the solvent molecules that might still be trapped in the composite filaments.

3.4. Morphology. The alternative performance of graphene-based nanofiller-reinforced composites depends on the dispersion and distribution of graphene-based materials in the polymer matrix and the interfacial bonding between these two phases [16]. The microstructures of the cryo-fractured sections of ABS, ABS/GO (dry mixing), and ABS/GO (solvent mixing) on cross section are shown in Figure 5. Pure ABS showed a denser microstructure, while ABS/GO demonstrated a higher-porous surface with the presence of dispersed GO flakes embedded in the ABS matrix.

For ABS/GO, GO flakes with the dimensions around 10 μm were noticed for the ABS/GO (dry mixing), while they ranged from 1–3 μm for the ABS/GO (solvent mixing). The smaller size and the more uniform distribution of GO were the critical keys for enhancing the mechanical behavior and for the thermal diffusivity of the composite.

3.5. Flowability. The flowability of the ABS/GO composite was investigated via the melt flow rate (MFR) measurement. The MFR represented the flowability of the material and was inversely proportional to its viscosity. It could be used to evaluate how the presence of GO affected the processability of the ABS/GO composite. As shown in Figure 6, the MFR values of both ABS and ABS/GO composite filaments increased with the temperatures, which meant the materials flew easier upon the temperature increased. The MFR values of the ABS/GO were lower than those of the pure ABS filament at all measured temperatures, which might be attributed to the solid GO flakes that restricted the mobility and disturbed the flowability of the ABS chains.

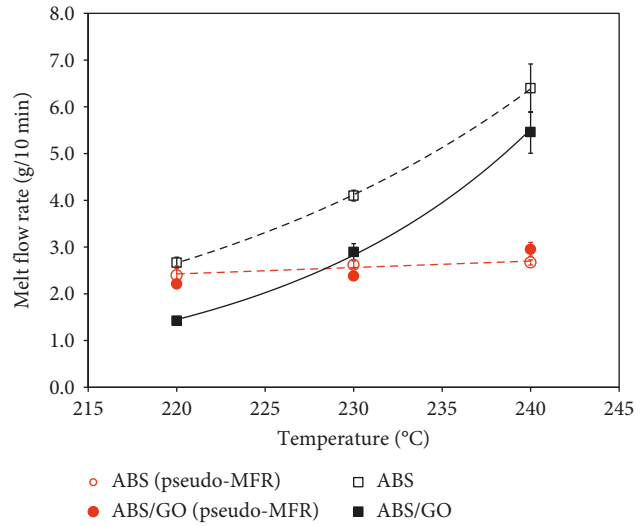

Figure 6: Melt flow rate (MFR) of the ABS filament and the ABS/GO composite filament dependent on temperature (220–240°C). Black color represents the results from the conventional MRF measurement, and red represents the results from the pseudo-MFR measurement using the 3D printer.

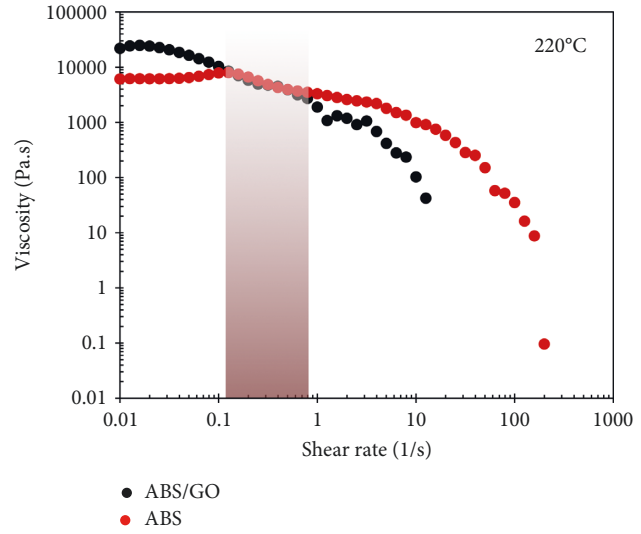

Figure 7: Shear rate dependence of viscosity for ABS and ABS/GO composite filaments.

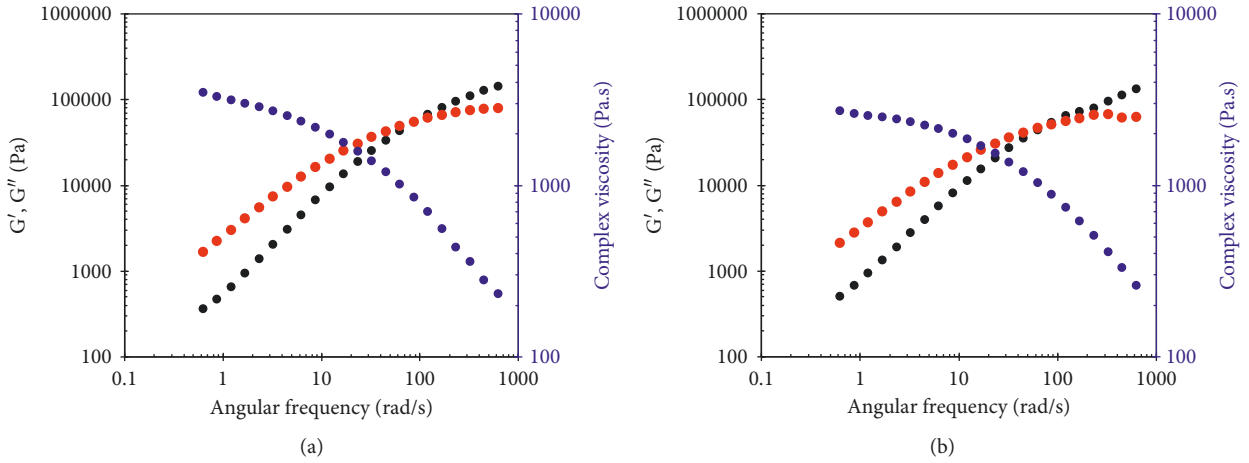

Figure 8: Rheological properties from the dynamic frequency sweep test: (a) ABS filament; (b) ABS/GO composite filament.

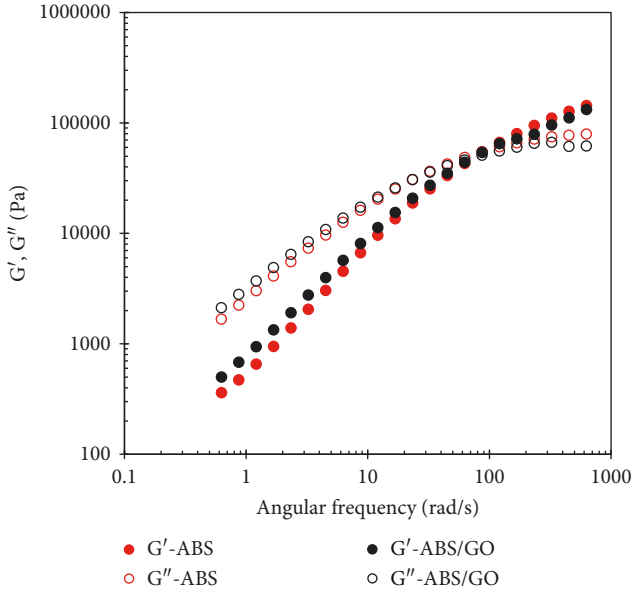

Figure 9: Storage modulus (G′) and loss modulus (G″) versus the angular frequency for ABS filament and ABS/GO composite filament.

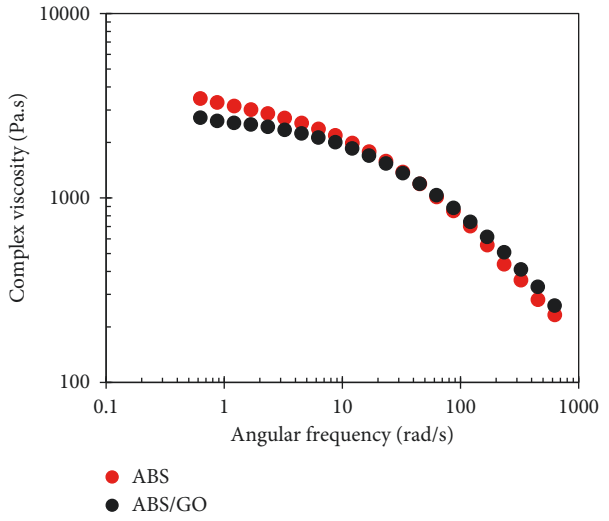

Figure 10: Complex viscosity versus the angular frequency for the ABS filament and the ABS/GO composite filament.

For FFF 3D printing processes, knowing the extrusion temperatures and flowability of the printed materials led to the more accuracy and precision of the printing process. The MFR information can be used as a guideline for setting up the printing parameters [24]. In this study, a pseudo-MFR measurement was conducted by measuring the extruded mass of the filaments through the printer nozzle. The pure ABS and ABS/GO filaments displayed clear plateau values at all temperatures (Figure 6). As a result, the edge of the plateau reflected the lower bound of acceptable temperature for the corresponded extrusion rate. Theoretically, below this temperature, the mass of polymer extruded cannot be accurately achieved at the given feed rate.

On the contrary, extruding at a higher temperature than the lower bound is undesirable since it would lead to slower solidification of the extruded bead on the printed part. It was

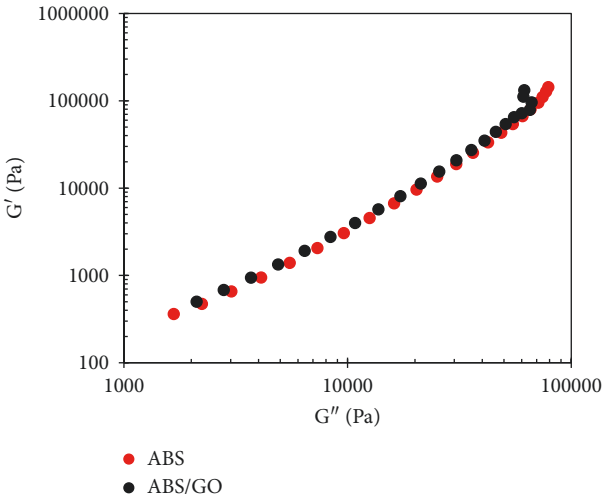

Figure 11: G′ versus G″ plot for (red) ABS filament and (black) ABS/GO composite filament.

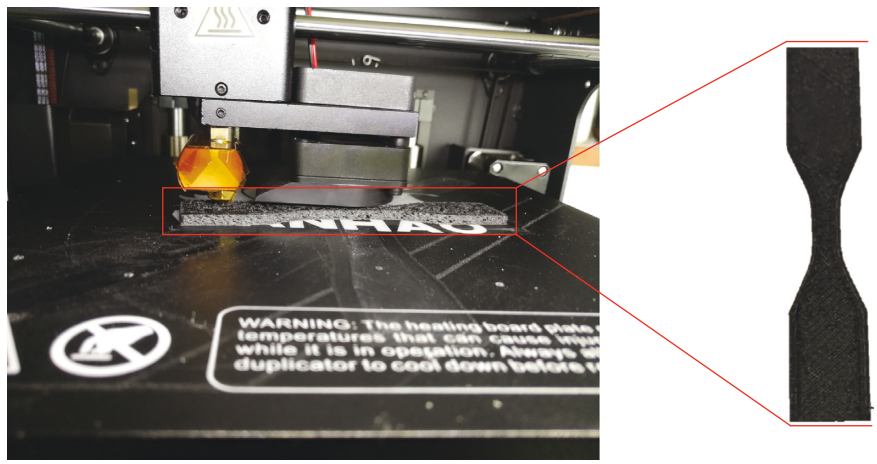

Figure 12: FFF 3D printed specimen from the ABS/GO composite filament.

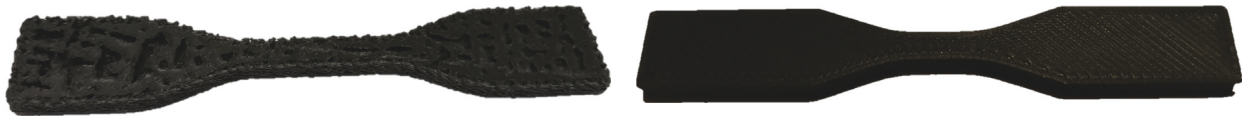

(a) (b)

Figure 13: FFF 3D printed specimen from (a) ABS/GO (dry mixing) and (b) ABS/GO (solvent mixing) composite filaments.

found that the ABS/GO composite filament exhibited the similar behavior as compared to the pure ABS. Thus, ABS/GO could be printed using the same temperature range (220–240°C) used for the pure or conventional ABS filaments.

3.6. Rheological Properties. The average shear rate in typical twin-screw extrusion ranges between 1 and 1,000 s^{-1} [25, 26]. For the FFF 3D printer, the shear rates in the nozzle are commonly in the range of 0.1–200 s^{-1} [27]. Figure 7 shows the shear rate dependence of viscosity for ABS and ABS/GO at 220°C. At the shear rate of 0.1 to 1 s^{-1}, ABS and ABS/GO filaments showed almost similar viscosity values, which confirmed that ABS/GO could be 3D printed with the same temperature setup for pure ABS. Incorporating with the MFR results, it was concluded that ABS/GO and pure ABS could be 3D printed using the same printing parameters (nozzle temperature and print speed).

Interfacial interaction between GO and ABS is a crucial role for enhancing the mechanical performance of the composite. Generally, the opposition between particle-particle interaction and particle-polymer interaction can be used to determine the particle dispersion or aggregation in nanocomposites. Thus, rheological behavior becomes a useful tool to evaluate the dispersion and distribution of the GO in ABS. Because the rheological behaviors deliver the relation between molecular structure and mesoscale properties (such as phase structure and filler dispersion), at the same time, providing the processing properties [28, 29]. From the dynamic frequency sweep measurements, it was noticed that the rheological behaviors of ABS and ABS/GO were almost similar as shown in Figures 8–10, respectively.

Figure 9 presents the storage and loss moduli of ABS and ABS/GO filaments. Only a small deviation of the G′ and G″ values was observed between ABS and ABS/GO filaments. Even though the increase in complex viscosities at low frequencies due to the effect of GO fillers was found, the complex viscosities of ABS and ABS/GO filament remained almost the same values at higher rates as shown in Figure 10. This is again confirmed that the GO loading did not affect the viscosity or flowability of the ABS.

Furthermore, we created the G′-G″ plot for predicting the dispersion of GO in ABS as presented in Figure 11. The G′-G″ patterns of pure ABS and ABS/GO were close together, suggested the well distribution of GO in the composite.

3.7. FFF 3D Printability. Figures 12 and 13 present the WANHAO Duplicator 6, the 3D printer based on the FFF principle, and the printed ABS/GO tensile specimens, respectively. With the same printing conditions used for pure ABS, the ABS/GO composite has been successfully printed. However, the clogged nozzle was sometimes observed, which further led to the print failure (Figure 13(a)).

3.9. Mechanical Properties. The tensile properties at the room temperature of ABS and ABS/GO were investigated and presented in Figure 14. From the typical stress-strain tensile curves and corresponding statistical data, the elongation at the break value decreased with the GO loading. The

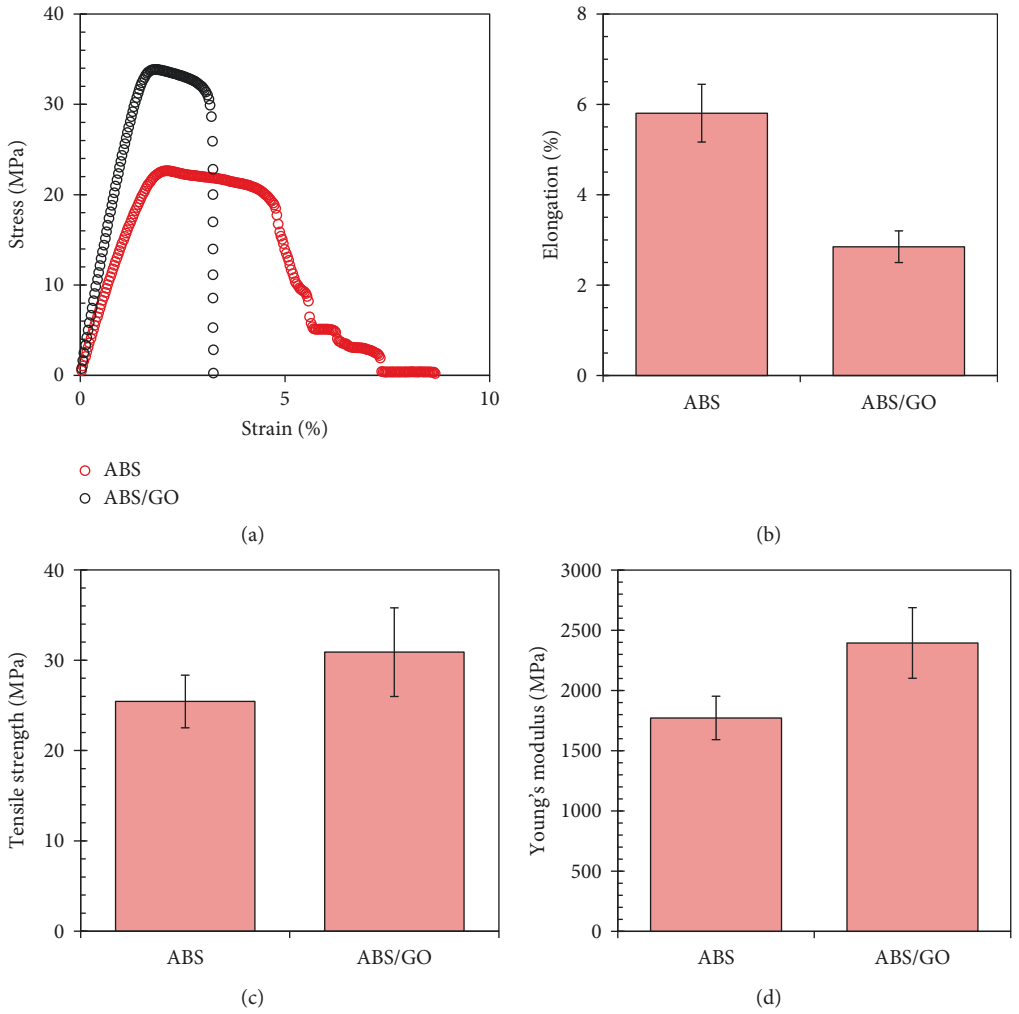

Figure 14: Typical stress-strain curves (a), value of elongation at break (b), tensile strength (c), and Young's modulus (d) of ABS and ABS/GO printed specimens.

elongation at the break value of pure ABS was determined as 5.8%, while the value of ABS/GO composite was 2.9%. However, by adding 2 wt.% GO, the tensile strength and Young's modulus of ABS were enhanced. This might be due to the interlayer crosslinks of GO sheets under loads, leading to the ordering of the hierarchical structures which results in the great significant enhancement of the mechanical properties [30].

4. Conclusion

A new 3D printing filament from ABS/GO composite was successfully prepared by solution mixing and followed by melted extrusion using a twin-screw extruder. The solvent system improved the GO dispersion capability in the ABS matrix and had no significant effect on the thermal properties of the ABS/GO composite. However, the aggregation of GO could lead to the die clogging and failure of the extrusion process. The tensile strength and Young's modulus of ABS were enhanced naturally by GO. Besides, the elongation at break decreased and needed to be further improved. Improving mechanical properties verified the feasibility of 3D printed ABS/GO for potential use in engineering applications.

Our study demonstrated one of the active attempts to print GO-based composite using FFF 3D printing process directly. However, the printed part quality, functionalities, and applications based on the printed ABS/GO composite needed to be further exploited.

Data Availability

The data used to support the findings of this study are available from the corresponding author upon request.

Conflicts of Interest

The authors declare that they have no conflicts of interest.

Acknowledgments

We thank Sami Briti from Polytech Montpellier, France, for helping in the preparation of graphene oxide (GO).

Additionally, we thankfully acknowledge the financial support from grants for Development of New Faculty Staff, Ratchadaphiseksomphot Endowment Fund, Chulalongkorn University, and the Thailand Research Fund (TRG6180009).

References

[1] S. Hertle, M. Drexler, and D. Drummer, "Additive manufacturing of poly(propylene) by means of melt extrusion," *Macromolecular Materials and Engineering*, vol. 301, no. 12, pp. 1482–1493, 2016.

[2] A. Bandyopadhyay, F. Janas, and R. Van Weeren, "Processing of piezocomposites by fused deposition technique," in *Proceedings of Tenth IEEE International Symposium on Applications of Ferroelectrics*, pp. 999–1002, East Brunswick, NJ, USA, August 1996.

[3] T. F. McNulty, F. Mohammadi, A. Bandyopadhyay, D. J. Shanefield, S. C. Danforth, and A. Safari, "Development of a binder formulation for fused deposition of ceramics," *Rapid Prototyping Journal*, vol. 4, no. 4, pp. 144–150, 1998.

[4] X. Wang, M. Jiang, Z. Zhou, J. Gou, and D. Hui, "3D printing of polymer matrix composites: a review and prospective," *Composites Part B: Engineering*, vol. 110, pp. 442–458, 2017.

[5] J. F. Christ, N. Aliheidari, A. Ameli, and P. Pötschke, "3D printed highly elastic strain sensors of multiwalled carbon nanotube/thermoplastic polyurethane nanocomposites," *Materials and Design*, vol. 131, pp. 394–401, 2017.

[6] J. Zhang, Y. Yang, F. Fu, F. You, X. Dong, and M. Dai, "2017_Zhang_resistivity and its anisotropy characterization of 3D printed acrylonitrile butadiene styrene copolymer-carbon black composites," *Applied Sciences*, vol. 7, no. 1, p. 20, 2017.

[7] R. Singh, G. Sandhu, R. Penna, and I. Farina, "Investigations for thermal and electrical conductivity of ABS-graphene blended prototypes," *Materials*, vol. 10, no. 8, p. 881, 2017.

[8] U. Kalsoom, P. N. Nesterenko, and B. Paull, "Recent developments in 3D printable composite materials," *RSC Advances*, vol. 6, no. 65, pp. 60355–60371, 2016.

[9] S. J. Kalita, S. Bose, H. L. Hosick, and A. Bandyopadhyay, "Development of controlled porosity polymer-ceramic composite scaffolds via fused deposition modeling," *Materials Science and Engineering: C*, vol. 23, no. 5, pp. 611–620, 2003.

[10] A. M. Pinto, J. Cabral, D. A. P. Tanaka, A. M. Mendes, and F. D. Magalhaes, "Effect of incorporation of graphene oxide and graphene nanoplatelets on mechanical and gas permeability properties of poly(lactic acid) films," *Polymer International*, vol. 62, no. 1, pp. 33–40, 2012.

[11] B. E. Yamamoto, A. Z. Trimble, B. Minei, and M. N. G. Nejhad, "Development of multifunctional nanocomposites with 3-D printing additive manufacturing and low grapene loading," *Journal of Thermoplastic Composite Materials*, pp. 1–26, 2018.

[12] H. Kim and C. W. Macosko, "Processing-property relationships of polycarbonate/graphene composites," *Polymer*, vol. 50, no. 15, pp. 3797–3809, 2009.

[13] X. Wei, D. Li, W. Jiang et al., "3D printable graphene composite," *Scientific Reports*, vol. 5, no. 1, pp. 1–7, 2015.

[14] C. Wang, Y. Li, G. Ding, X. Xie, and M. Jiang, "Preparation and characterization of graphene oxide/poly(vinyl alcohol) composite nanofibers via electrospinning," *Journal of Applied Polymer Science*, vol. 127, no. 4, pp. 3026–3032, 2013.

[15] X. Lin, X. Shen, Q. Zheng et al., "Fabrication of highly-aligned, conductive, and strong graphene," *ACS Nano*, vol. 6, no. 12, pp. 10708–10719, 2012.

[16] V. Panwar and K. Pal, "An optimal reduction technique for rGO/ABS composites having high-end dynamic properties based on Cole-Cole plot, degree of entanglement and C-factor," *Composites Part B: Engineering*, vol. 114, pp. 46–57, 2017.

[17] D. Zhang, B. Chi, B. Li et al., "Fabrication of highly conductive graphene flexible circuits by 3D printing," *Synthetic Metals*, vol. 217, pp. 79–86, 2016.

[18] S. Dul, L. Fambri, and A. Pegoretti, "Fused deposition modelling with ABS-graphene nanocomposites," *Composites Part A: Applied Science and Manufacturing*, vol. 85, pp. 181–191, 2016.

[19] V. Panwar and K. Pal, "Dynamic performance of an amorphous polymer composite under controlled loading of reduced graphene oxide based on entanglement of filler with polymer chains," *Journal of Polymer Research*, vol. 25, no. 2, 2018.

[20] S. Chen, J. Lu, and J. Feng, "3D-Printable ABS blends with improved scratch resistance and balanced mechanical performance," *Industrial and Engineering Chemistry Research*, vol. 57, no. 11, pp. 3923–3931, 2018.

[21] E. A. Papon and A. Haque, "Tensile properties, void contents, dispersion and fracture behaviour of 3D printed carbon nanofiber reinforced composites," *Journal of Reinforced Plastics and Composites*, vol. 37, no. 6, pp. 381–395, 2018.

[22] ASTM International, *ASTM D1238–13*, ASTM Int., West Conshohocken, PA, USA, 2013.

[23] American Society for Testing and Material (ASTM), *Standard Test Method for Tensile Properties of Plastics (D638-14)*, ASTM Int., West Conshohocken, PA, USA, 2014.

[24] T. Pfeifer, C. Koch, L. Van Hulle, G. A. M. Capote, and P. Natalie, "Optimization of the FDM additive manufacturing process," in *Proceedings of SPE ANTEC Indianapolis*, pp. 22–29, Indianapolis, IN, USA, May 2016.

[25] T. A. Osswald and N. Rudolph, *Polymer Rheology Fundamental and Applications*, Hanser Publishers, Munich, Germany, 2015.

[26] N. Venkataraman, S. Rangarajan, M. J. Matthewson et al., "Feedstock material property-process relationships in fused deposition of ceramics (FDC)," *Rapid Prototyping Journal*, vol. 6, no. 4, pp. 244–253, 2000.

[27] L. A. Al-Hariri, B. Leonhardt, M. Nowotarski, J. Magi, and K. Chambliss, *Carbon Nanotubes and Graphene as Additives in 3D Printing*, INTECH, London, UK, 2016.

[28] L. Du, M. Namvari, and F. J. Stadler, "Large amplitude oscillatory shear behavior of graphene derivative/polidimethylsiloxane nanocomposites," *Rheologica Acta*, vol. 57, no. 5, pp. 429–443, 2018.

[29] G. M. Shin, J. Y. Park, and Y. C. Kim, "GO dispersion and mechanical properties of 70PC/30ABS/GO composites according to fabrication methods," *Polymer Korea*, vol. 41, no. 3, pp. 452–459, 2017.

[30] R. Sharma, R. Singh, R. Penna, and F. Fraternali, "Investigations for mechanical properties of Hap, PVC and PP based 3D porous structures obtained through biocompatible FDM filaments," *Composites Part B: Engineering*, vol. 132, pp. 237–243, 2018.

eXPRESS Polymer Letters Vol.13, No.10 (2019) 898–909
Available online at www.expresspolymlett.com
https://doi.org/10.3144/expresspolymlett.2019.78

PP/organoclay nanocomposites for fused filament fabrication (FFF) 3D printing

C. Aumnate[*], *S. Limpanart, N. Soatthiyanon, S. Khunton*

Metallurgy and Materials Science Research Institute, Chulalongkorn University, Soi Chula 12, Phayathai Rd., Pathumwan, 10330 Bangkok, Thailand

Received 25 February 2019; accepted in revised form 23 May 2019

Abstract. 3D printing has attracted a lot of attention over the past three decades. In particular the Fuse Filament Fabrication (FFF) technique, general materials require low shrinkage during cooling and viscous behavior during extrusion through a nozzle. Semi-crystalline thermoplastics and their composites are of the relevance of new materials for 3D printing. However, the crystalline structures, for instance, may have a favorable impact on their printability. In this study, polypropylene/organoclay nanocomposites were prepared by melt extrusion using a twin-screw extruder. The effects of organoclay on the thermal, rheological and morphological properties were studied to evaluate the possibility of using the polypropylene/organoclay nanocomposites as the FFF 3D printing feedstock. Dioctadecyl dimethyl ammonium chloride (D18) was successfully used to modify the clay surfaces, providing a good dispersity and wettability of organoclay in the PP matrix.

Keywords: *polymer composites, polypropylene; organoclay, 3D printing, fused filament fabrication (FFF)*

1. Introduction

3D printing technologies have been introduced to serve the highly particular needs of model creating and rapid prototyping [1]. However, it has not gained enough vitality to be commercialized until recently. 3D printing becomes more affordable through a fused filament fabrication (FFF) process since it offers advantages, including low cost, high speed, and simplicity as compared to other 3D printing techniques. Another advantage is the potential of printing diverse materials simultaneously. Multiple extrusion nozzles with the loading of different materials can be set up in FFF printers, so printed parts can be multifunctional with designed composition [2, 3]. Conversely, one common drawback of FFF printing is that the composite materials have to be in a filament form to enable the extrusion process. It is difficult to disperse reinforcements homogeneously and remove the voids formed during the manufacturing of composite filaments. Thus, the usable material is limited to amorphous thermoplastic polymers with suitable melt viscosity to allow the good dispersion of the reinforcements. Also, the melt viscosity should be appropriate to provide structural support and low enough to enable extrusion. The general materials require low shrinkage during cooling and viscous behavior during extrusion through a nozzle. Therefore, this brings about the most exclusive use of amorphous thermoplastics in FFF. Thermoplastic polymer materials such as acrylonitrile butadiene styrene (ABS), polylactic acid (PLA), polyamide (PA) and polycarbonate (PC) could be processed by 3D printing technology. However, most of the 3D printed polymer products are still now used as conceptual prototypes rather than functional components, due to the intrinsically limited mechanical properties and functionalities of printed pure polymer parts. Accordingly, there is a critical need to develop printable polymer composites, including

[*]Corresponding author, e-mail: Chuanchom.a@chula.ac.th

high precision, cost-effective and customized geometry. Semi-crystalline thermoplastic is one of the new relevance materials for 3D printing. However, the crystalline structure, for example, may effect mechanical properties, chemical resistance positively and may have a favorable effect on the end-use properties for various applications [4, 5].

Nanocomposites are multiphase solid materials where one of the phases has a dimension of <100 nm. The nanofillers can be in various forms such as particles, sheets (exfoliated clay stacks) or fibers. Nanoclay is one of the most commonly used nanofiller in particular for the fuel tank and fuel line components for cars [6]. Polypropylene-based composites are generally used in automotive applications to manufacture the part that may need to involve the compressive impact loading under a wide range of temperatures such as bumpers [7].

Polypropylene (PP)/clay nanocomposites find applications where excellent mechanical properties, low permeability to gases or flame resistance are essential service specifications at low clay content [3, 5]. The development of PP/clay nanocomposites poses particular challenges because of the hydrophobicity of PP. Thus, the hydrophilic clays tend to form agglomerates during mixing with PP. This is due to the van der Waals attraction between clay particles. It is well-known that the dispersion of nanoclay in the polymer matrix depends on the surface peeling, followed by polymer chains diffusion into the nanoclay galleries [8]. The methods commonly employed to facilitate intercalation/exfoliation of the clay and maximize its interfacial contact with the polymer matrix include adding compatibilizers such as maleic anhydride grafted polymer; dimethyl maleate grafted polymer, as well as the surface modifications/treatments [6, 8–13]. This can significantly affect the matrix morphology and usually leads to proper clay intercalation instead of exfoliation [10, 11, 14]. Moreover, the cationic modification is commonly performed in an aqueous medium in which clay swell easily to produce organophilic clays. Among the methods, quaternary ammonium salts are frequently used. In such a case, the microstructural characterization concerning matrix morphology and clay dispersion, which affects the end properties of the composites, becomes crucial to understand. Melt compounding using twin-screw extruders allows the required high stress to break up the tactoid structure of the clays and to promote intercalation/exfoliation [15]. In addition, twin-screw extruders are widely used in industry, and the process is straightforward. Accordingly, thermal and rheological properties of the composites have attracted much interest [4, 15]. The properties of composites are dependent on different factors such as the size, shape and nature of the filler particles, interactions between their constituents, orientation, dispersion and distribution of the particles in the matrix and notably the filling level [16]. This study focuses on the development of polymer nanocomposite filaments for the FFF 3D printing process, using PP and organoclay. The typical melt extrusion process used in polymer processing technologies is performed to prepare the PP/organoclay nanocomposites. The thermal, rheological, morphological and tensile properties of the nanocomposites are investigated to evaluate a possibility of using PP/organoclay composites as FFF 3D printing feedstock. Such PP/organocomposites may have applications in structural, electrical/electronic and automotive fields.

2. Experimental

2.1. Materials

Sodium-bentonite clay was supplied by Thai Nippon Chemical Co. Ltd., Thailand. The surfactant used in this study was a mixture of dioctadecyl dimethyl ammonium chloride salts with alkyl chain length of 14 (4%), 16 (32%), and 18 (58%), which will be referred to as D18 throughout the study. The surfactant was purchased from Thai Specialty Chemical Co., Ltd., Thailand. Polypropylene (PP) powder (MFI = 19.8 g/10 min) was obtained from HMC Polymer co., Ltd., Thailand.

2.2. Organoclay preparation

400 g of Na-bentonite were added to 20 ml of deionized water and stirred vigorously for 3 h. Various amounts of D18 were then added in portions (Table 1) as coupling agent. The reaction mixture was heated at 70 °C for 1 h. The mixture suspension was finally filtered, washed and dried at 80 °C for at least 12 h and then ground to fine powder.

Table 1. Organoclay modified with different D18 concentrations.

Organoclay	Dioctadecyl dimethyl ammonium chloride (D18) [mmol/g Clay]
BAD05	0.50
BAD10	0.10
BAD15	0.15

2.3. PP/organoclay composites preparation

Polypropylene (PP) pellets were ground into powder form. PP powder with 30 wt% of organoclay (Table 1) was extruded first as a master batch using a co-rotating twin-screw extruder. The extrusion temperature profiles ramped from 180 up to 220 °C (from the hopper to the die). The amount of the organoclay used in all the nanocomposites was kept constant as 3 wt% concerning total PP, according to the good mechanical performance improvement resulting from our previous study [17]. Thus, the PP/organoclay master batch was then diluted to obtain 3 wt% of organoclay using the same melt extrusion parameters.

2.4. Characterization

2.4.1. X-ray diffraction (XRD)

The X-ray diffraction (XRD) of organoclay was performed using an X-ray diffractometer (Bruker AXS Model D8 Discover). All samples were scanned over the range $2\theta = 2–10°$ and the measurements were recorded at every 0.02° interval.

2.4.2. Differential scanning calorimetry

The measurements were carried out using a DSC 3500 Sirius, under nitrogen atmosphere. The samples were heated from room temperature to 280 °C. After an isothermal step for 2 min, the samples were cooled down to 30 °C and finally heated up to 280 °C after another isothermal step for 2 min. Scanning temperature ramps of 10 K/min were used for all dynamic steps. A heat of fusion for a 100% crystalline PP of 205 J/g [4] was used to calculate the degree of crystallization. For isothermal analysis, all materials were quenched from 230 °C to an isothermal temperature (125 °C).

2.4.3. Rheology test

First, dynamic strain sweep tests were performed using a rheometer (Germini 2000, TA instrument) equipped with 25 mm diameter parallel plates. The dynamic strain sweep test was conducted from the strain values of 0.1–100% with the frequency of 0.628 rad/s to investigate the linear regime for all samples. After that, the linear viscoelasticity responses of the materials were measured with the frequency sweep tests between 0.628 and 628 rad/s at a temperature of 210 °C. A constant strain of 2% (which is in the linear regime for all samples) was used, and the gap between the two plates was set to 1 mm. After applying the Cox-Merz rule, the complex viscosity could be determined as a function of the shear rate.

2.4.4. Scanning electron microscopy (SEM)

For the examination of the organoclay dispersion in the PP matrix, the PP/organoclay nanocomposite filaments were mounted in resin. They were then metallographically ground using emery paper and polished on diamond pads. The samples were examined using a JEOL JSM-IT500HR scanning electron microscope (SEM) at an accelerating voltage of 10 kV. For imaging, backscattered electrons were used to enhance the contrast of the specimen images, compared with secondary electrons.

Furthermore, the cryo-fracture surfaces of the PP/organoclay nanocomposite filament were also studied using a Hitachi SU3500 scanning electron microscope at an accelerating voltage of 15 kV. Prior to investigation, all samples were sputter coated with gold.

2.4.5. Transmission electron microscopy (TEM)

All PP/organoclay nanocomposite samples were investigated using the transmission electron microscope (TEM), (JEOL 2010 with an acceleration voltage of 200 kV) to verify the dispersion of organoclay in the PP matrix. The PP/organoclay nanocomposite filaments were prepared as a 90 nm thick slice using a microtome with a diamond knife in liquid nitrogen. The slices were then imaged in the TEM.

2.4.6. Tensile tests

To obtain the mechanical properties, the tensile tests were carried out according to ASTM D638 [18]. The specimens were printed based on Type-V geometry. The crosshead speed was set to 5 mm/min. Ultimate tensile strength; Young's modulus and elongation at break were evaluated as an average value of at least five replicates.

3. Results and discussion

3.1. X-ray diffraction

The XRD analysis allows estimating the distance between the clay layers according to Bragg's law [15] as shown in Equation (1):

$$2d\sin\theta = n\lambda \tag{1}$$

where d represents the spacing between diffraction lattice planes, θ is the diffraction angle of the beam

on these planes, n is a positive integer representing the diffraction order, and λ corresponds to the wavelength of the X-ray radiation used in the diffraction experiment. Based on the interaction force of the polymer/organoclay, three types of nanocomposite morphologies could be generated, including intercalation, exfoliation and phase-separation.

The intercalated morphology resulted in a displacement of the peaks associated with the basal distance toward angles' lower values, corresponding to a distance between the most critical sheets. Exfoliated morphology resulted in the absence of diffraction peak because of a much too large spacing between the layers, or the nanocomposite does not present ordering anymore [19, 20].

Figure 1 presents the XRD patterns of the unmodified clay, organoclay modified with different D18 contents as well as PP and PP/organoclay nanocomposites, respectively, from the region of 2θ between 2 to 10°. For the clay modified with the series of different D18 loading, the peak intensity was increased with increasing the D18 content. Besides, the peaks tended to shift toward the lower angle values (see Figure 1a). These results indicated that there exists a difference in the clay microstructure after organically modified the clay surface with D18. The similar results were also found in the case of the PP/organoclay nanocomposites as depicted in Figure 1b. There was no peak observed for the neat PP observed in the interesting region. For the PP/organoclay composites,

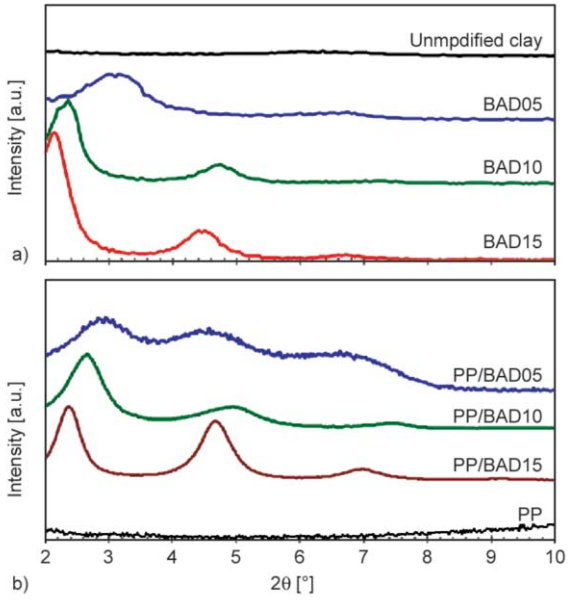

Figure 1. XRD patterns of (a) unmodified clay and organoclay modified with different D18 contents and (b) neat PP and PP/organoclay nanocomposites.

the examined diffraction peaks shifted toward lower angle values as the D18 contents increased. The peak of PP/BAD05 observed at the 2θ value of 3.0°, corresponded to 37.2 Å d-spacing. With increasing the D18 contents, the broader distribution of the d-spacing value was also observed. The d-spacing values were 33.3 Å (2θ = 2.7°) and 29.8 Å (2θ = 2.4°) for for PP/BAD10 and PP/ BAD15, respectively. PP is nonpolar and does not interact perfectly with clay platelets. However, due to the high shear during the melt extrusion process as well as the addition of the coupling agent, the combination of intercalation and exfoliation could be achieved in the composites despite the non-polarity of PP. The lower angle values revealed intercalation while the larger d-spacing values suggested exfoliation developed in the PP/organoclay nanocomposites, which allowed peeling of the clay platlets.

From our previous study, the D18 molecules can be either packed as an island of interdigitating monolayers or an island of highly tilted bilayers on the clay surface, leading to the increase in d-spacing value [17]. For the small loading of D18 (PP/BAD05), even though the stacking of the organoclay has not completely disappeared, the peaks have slightly broadened. It is possible that the clay surface has not yet fully covered with the D18 molecules, leaving the empty space around the island where the hydrate water-Na^+ is located, resulting in a less ordered structure.

3.2. Thermal properties

In FFF 3D printing, temperatures of the nozzle are crucial parameters to print the composite filaments without major structural flaws smoothly. Thus, thermal properties of such composite filament were carefully assessed with standard techniques, differential scanning calorimetry (DSC). The printable materials need to be heated above the glass transition temperature (T_g) or the melting temperature (T_m) to get softened the composites. However, if the temperature is set too high, it could degrade the polymer ingredients. Therefore, before 3D printing, T_g or T_m of the materials is the first and most vital parameter to be determined.

Figure 2 shows the representative DSC curves of the PP and the PP/organoclay nanocomposites. In general, the variation in the melting temperature (T_m) indicates the change of crystal structures of material. The T_m of nanocomposites could be changed upon

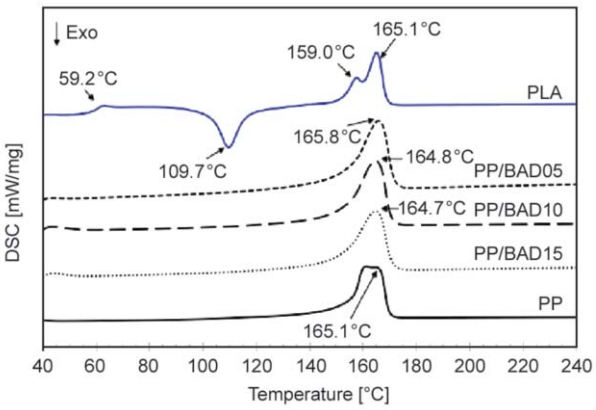

Figure 2. Melting temperatures of PP and PP/organoclay nanocomposites in comparison with PLA, the conventional material used for FFF 3D printing.

filler loading. However, there is no significant difference between Tm for the PP and the PP/organoclay nanocomposites. Since the amount of organoclay loading in all of the PP/organoclay nanocomposites in this study were kept constant at 3wt%, this justified that the concentration of D18 does not considerably affect the thermal stability of the PP.

A relatively broad melting peak at 165 °C is characteristic of the α-phase of iPP [21]. In comparison with the conventional PLA filament, the PP and the PP/organoclay nanocomposites could be softened at the nearly same temperature (T_m ~165 °C). It could be implied that the PP and the PP nanocomposites could be possibly 3D printed using the same temperature setup for the conventional PLA filament. Hence, the developed PP and PP/organoclay nanocomposite filaments can be 3D printed using the conventional FDM 3D printers.

Figure 3 shows the crystallization temperature (T_c) for the PP and the PP/organoclay nanocomposites. The

Table 2. Differential scanning calorimetry results of neat PP and PP/organoclay nanocomposites.

Samples	T_m [°C]	T_c [°C]	X_c^* [%]	$T_{m\,(start)}$ [°C]	$T_{c\,(start)}$ [°C]	ΔH_c [J/g]	ΔH_m [J/g]
PP	165.1	110.8	46.8	155.4	114.9	99.4	96.0
PP/BAD05	165.8	118.9	35.6	154.4	122.8	73.0	73.0
PP/BAD10	164.8	114.4	33.4	153.6	118.8	69.6	68.4
PP/BAD15	164.7	113.9	30.0	152.5	118.9	58.6	61.6

*Heat of fusion, ΔH_m for 100% crystalline PP = 205.0 J/g [18].

crystallization temperatures of all the PP/organoclay nanocomposites were found to be higher than that of pure PP. The PP/BAD10 and PP/BAD15 presented a nearly similar crystallization behavior whereas the PP/BAD05 showed the highest crystallization temperature. The shifts of both the onset and peak toward higher temperatures for all the PP/organoclay nanocomposites were observed as compared to pure PP. This clearly illustrates that the crystallization of PP significantly affected by both the presence of D18 and the clay. These effects on the crystallization were in agreement with the importance of the spherulite size reduction. Organoclay acted as nucleating sites and induced crystallization of the PP matrix. The degree of crystallization for materials with short molecules was high since they could crystallize faster and more accessible [22]. As shown in Table 2, the degree of crystallinity decreased with increasing the D18 content. The addition of D18 delayed the crystallization process as shown in Figure 4.

When the higher content of D18 was added into the nanocomposites, the crystallization behavior tended to be much more similar to the PP, in agreement again with the weaker reductions in spherulite size compared to the pure PP. However, for the small

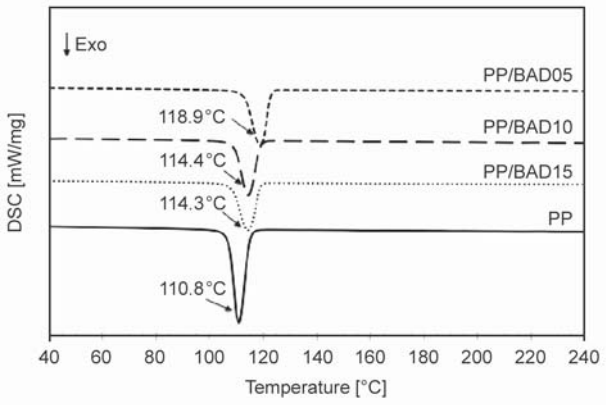

Figure 3. Crystallization temperature of PP and its composites; PP/BAD05, PP/BAD10 and PP/BAD15.

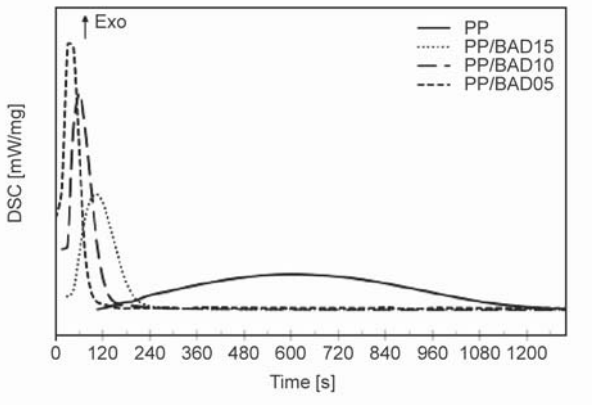

Figure 4. Isothermal segments of the crystallization process at 125 °C of PP its composites; PP/BAD05, PP/BAD10 and PP/BAD15.

amount of D18 (PP/BAD05), the significant shift of T_m to the higher temperature was observed, indicating the substantial reduction in spherulite size as well as the faster crystallization of the composite. These results thus suggested that the amount of D18 played an essential role in the crystallization behavior and also the degree of crystallinity. Furthermore, the enthalpy tended to drop with an increase in D18 content. This phenomenon may be also attributed to a decrease of the thermodynamically stable alpha phase content in favor of a mesomorphic structure [23].

3.3. Rheological behaviors

The viscosity of the polymer melt usually plays an important role in the processability of materials. Understanding rheological properties is of great importance to achieve an overview of the material's structures and also the determination of processing conditions for real polymer processing, such as extrusion and injection molding. The crucial challenge is to find the optimum balance between improvements in properties, at the same time being able to process the materials. Polymer composites are mainly processed under high temperatures and high shear rates. There are several drawbacks resulted from mixing hard particles with polymers, principally due to the considerable difference in densities. Adding solid particles into a molten polymer changes the viscoelastic behavior, the viscosity and the elasticity of the system.

The dynamic strain sweep test was first applied to the neat PP and PP/organoclay nanocomposites to determine the linear viscoelastic region. Figure 5 presents the storage modulus (G'), which is a sensitive rheological function related to the structural changes of the nanocomposites [12]. Storage modulus (G') of all samples exhibits a linear region (Newtonian plateau) at low strain and the non-linear region at high strain amplitudes. The addition of organoclay increased the plateau modulus. The transition point, which appeared at the deviation region from the linear to non-linear viscoelastic behavior, is defined as a critical strain (γ_c). It was observed that the critical strain (γ_c) for the PP/organoclay nanocomposites varies with the D18 content. However, at the strain less than 10%, all samples exhibit linear viscoelastic behavior. Therefore, all further rheological measurements in this study were done in the linear regime at 2% strain.

Frequency sweep tests for the PP/organoclay nanocomposites in the linear viscoelastic domain are shown in Figure 6. The storage modulus (G') was increased by the incorporation of the organoclay into the PP matrix. The enhancement in the dynamic modulus was significant, in particular, at low frequencies regime. Also, G' becomes nearly independent on the frequency at low frequencies, which is an evidence of the exfoliation or partial exfoliation [11]. It can be explained that the diffusion of the organoclay molecules is favored by making the galleries chemically compatible with the PP matrix. The compatibility occurs by exchanging interlayers inorganic clay cations with D18 cations. Therefore, layer distance (gallery distance) of organoclay increases due to the modifier. With the same loading of organoclay, G' value is molder with higher D18 content. This reflects the less effective development of the physical interaction between the PP chains and the layer of organoclay at higher D18 content.

Figure 7 shows the variation of the complex viscosity for the neat PP, PP/BAD05, PP/BAD10, and PP/BAD15 nanocomposites. It was well established that

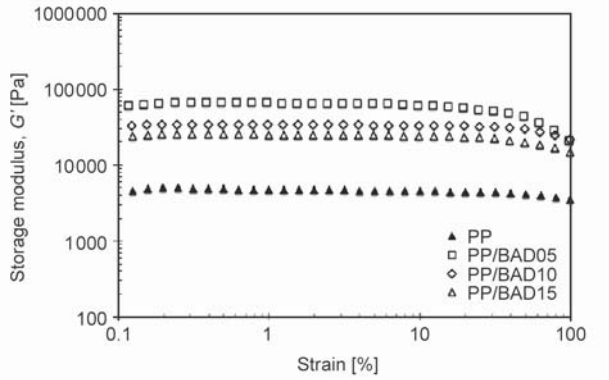

Figure 5. Storage modulus (G') versus strain (γ) curves for neat PP and its organoclay nanocomposites at the temperature of 230 °C.

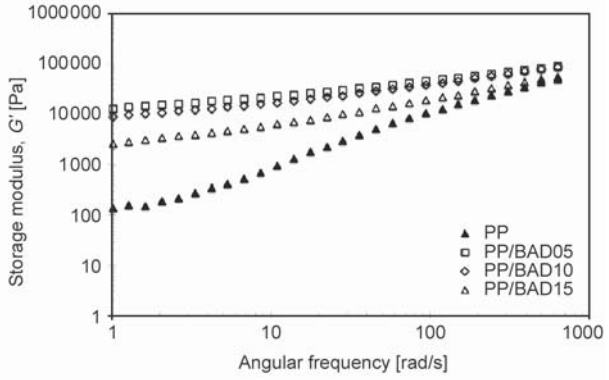

Figure 6. Frequency variations of the storage modulus, G' curves for neat PP and its organoclay nanocomposites at the temperature of 230 °C.

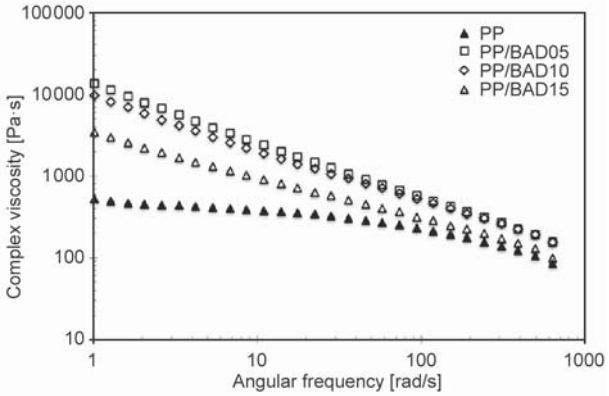

Figure 7. Complex viscosity curves for neat PP and its organoclay nanocomposites at the temperature of 230 °C.

the addition of nanofillers into the polymer matrix increased the viscosity of the system. When solid particles were added into a polymer matrix, they might disturb the flow lines and restricted the mobility of the polymer chains. The increase of the viscosity values also proves the physical network-like structure developed in the PP/organoclay nanocomposites. Furthermore, it should be noted that all the PP/organoclay nanocomposites exhibited shear-thinning behavior for the complex viscosity without any plateau region at low frequencies. Pronounced shear thinning has also been reflected the nanodispersion which is another evidence of the exfoliation morphology [11].

Also, by applying the Cox-Merz rule, Figure 8 presents the shear viscosity of the PP and its nanocomposites. The average shear rate in the typical co-rotating twin-screw ranges between 1 and 1000 s^{-1} [24]. For the FFF 3D printer, the relatively low shear rate is expected near the liquefier entrance and the print nozzle. Shear rates in the nozzle are commonly in the range of 100–200 s^{-1} [25]. Table 3 illustrates the

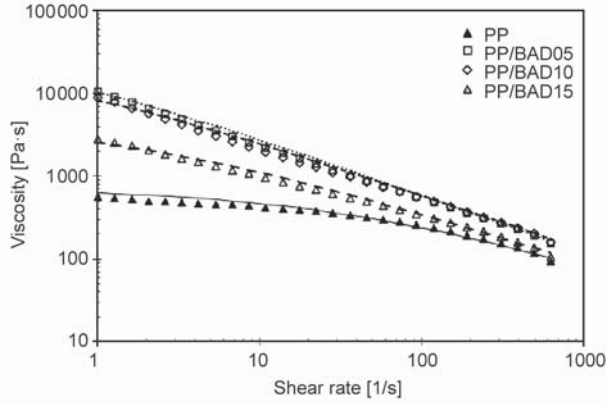

Figure 8. Shear viscosity (applied Cox-Merz rule) curves for neat PP and its organoclay nanocomposites at the temperature of 230 °C.

Table 3. Shear thinning exponent and viscosities of neat PP and PP/organoclay composites.

Samples	η at 100 s^{-1}	η at 200 s^{-1}	η at 1000 s^{-1}
PP	235.56	176.42	80.73
PP/BAD05	581.77	360.43	117.64
PP/BAD10	578.87	369.49	128.98
PP/BAD15	339.90	230.17	90.50

viscosities of the PP and the PP/organoclay nanocomposites at the shear rate of 100, 200 and 1000 s^{-1}. As expected, PP/BAD15, the nanocomposites with the highest degree of D18 loading displayed the lowest viscosity among the PP/organoclay nanocomposites at all shear rates. This can be attributed to the effect of the shorter molecule of D18, which flow easier than the longer molecules, PP. Addition of D18 led to the improvement of the flowability of the nanocomposites. However, incorporating with the G' and XRD results, the capability of the exfoliation and intercalation of the PP/organoclay nanocomposites could be improved by modifying clay with the coupling agent, D18. The less amount of D18 resulted in the higher degree of exfoliation/intercalation.

Figure 9 shows a Cole-Cole plot of the storage modulus G' versus the loss modulus G'' for the neat PP and its organoclay nanocomposites at 230 °C. It was proposed that the logG'-logG'' should be similar if the microstructure does not alter [26]. The logG'-logG'' curve can also be used to elucidate structure differences of polymer materials at a fixed conditions such as a fixed temperature. The increase of G' at a given G'' indicated that the microstructure of the composites changed significantly with the addition of organoclay. Also, the organoclay modified with higher

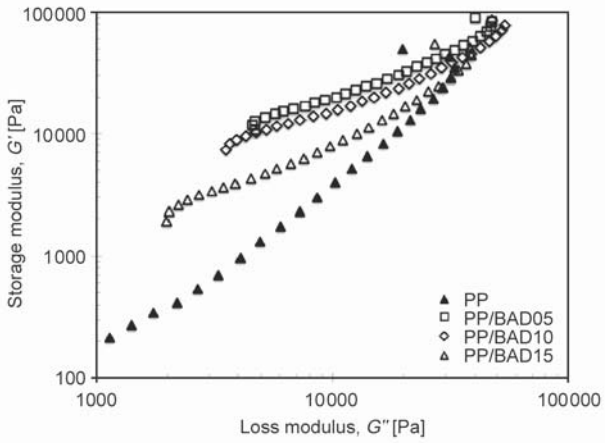

Figure 9. Storage modulus (G') as a function of loss modulus (G'') of neat PP and its organoclay nanocomposites at the temperature of 230 °C.

D18 content resulted in the less structural deviation as compared to the neat PP.

3.4. Morphology

The homogeneity of organoclay dispersion directly affected the composite's printing ability and other physical properties. The dispersion of organoclay in the PP matrix was investigated via the polished surfaces of the PP/organoclay composites as shown in Figure 10. It is seen that the smaller size of the organoclay is found for the case of more substantial D18 loading content.

Figure 11 shows the SEM images for fracture surface of the PP/clay composites filaments. With low D18 content, the PP/BAD05, the matrix coverage was not sufficient. It can be seen from many voids appeared as some evidences of the organoclay pull-out from the PP matrix. This indicated the weak interfacial bonding between the organoclay and the PP matrix. With increasing the D18 content, the matrix coverage was improved. This could be explained by the fact that the high mobility of the low molecular weight coupling agent, D18, allowed the PP matrix to interact actively with a large number of clay platelets during compounding.

The morphology of the PP/organoclay nanocomposites reported in this section were in good agreement with the rheological properties, confirming the capability of dispersion as well as the consequent formation of interfacial adhesion between the modified clay and the PP matrix.

3.5. 3D printing optimization

3.5.1. Nozzle temperature

For FFF 3D printing, with the extrusion temperature known, the accuracy of machine's motions can be explored [27, 28]. Figure 12 shows the extruded mass as a function of temperature for the PP/BAD05 in comparison with the conventional PLA filament.

Both materials tended to display a plateau at the temperatures higher than 220 °C. The edge of the plateau region is considered the lower bound of acceptable

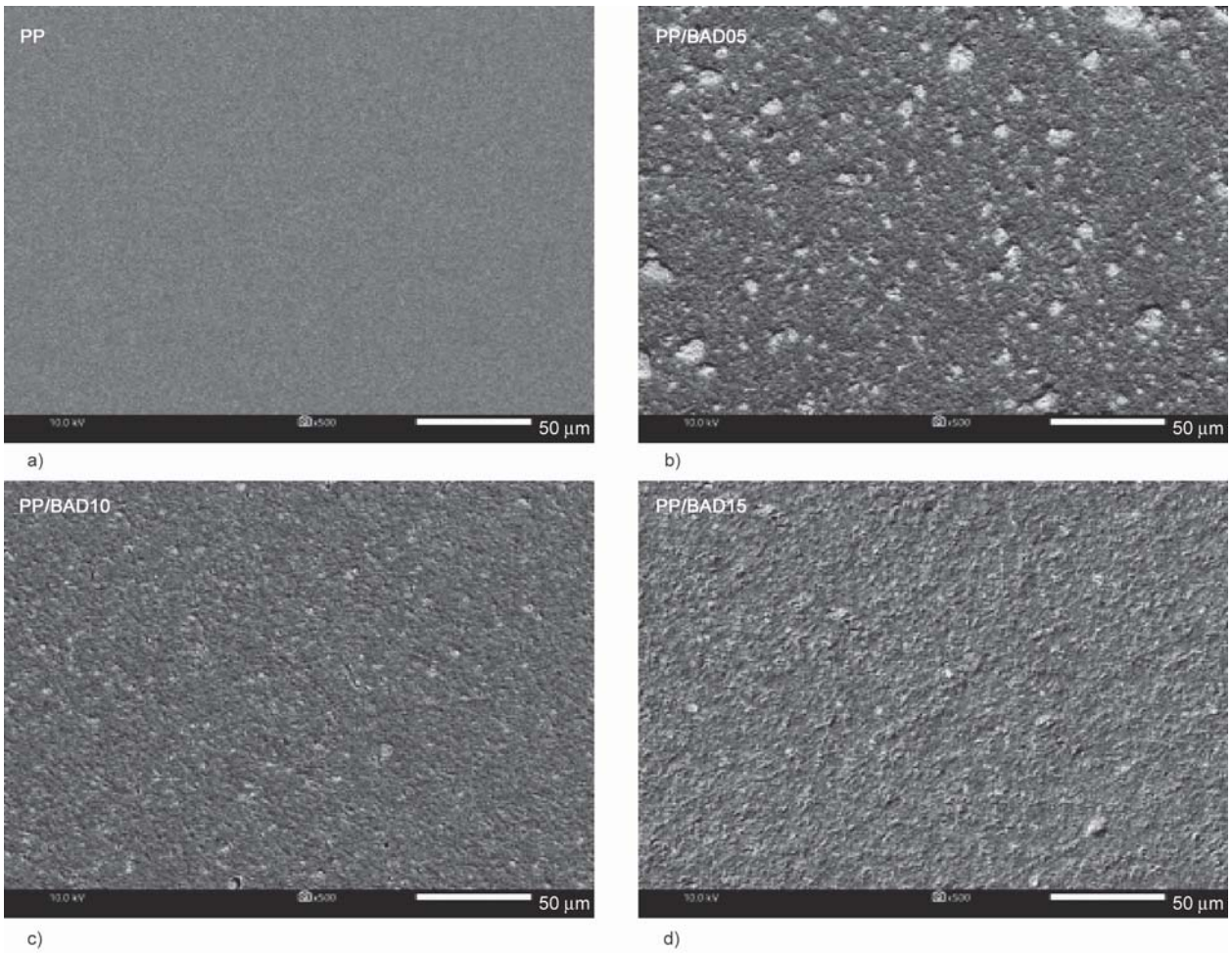

Figure 10. SEM images of polished surfaces for neat PP and its organoclay nanocomposites at 500× magnification. a) PP, b) PP/BAD05, c) PP/BAD10, d) PP/BAD15.

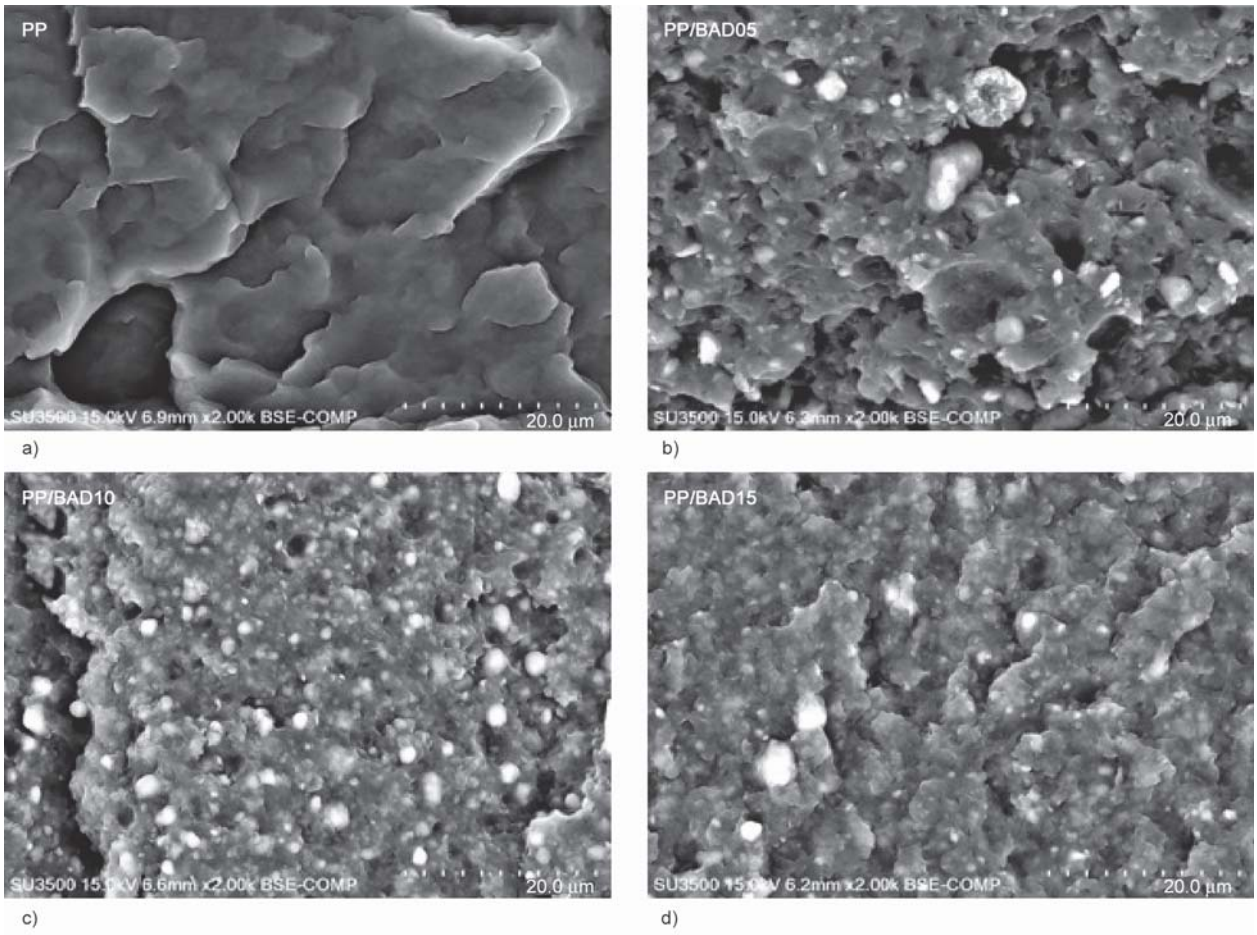

Figure 11. SEM images of fracture surfaces for neat PP and its organoclay nanocomposites at 2000× magnification. a) PP, b) PP/BAD05, c) PP/BAD10, d) PP/BAD15.

temperatures for the extrusion rate. Below this temperature, the theoretical amount of polymer extruded cannot be accurately achieved at the given feed rate. Furthermore, extruding at the higher temperature than this lower bound would cause the slower solidification of the extruded bead on the printed part. From the results, it could be concluded that PP/BAD05 could be 3D printed at the temperature range of 220–240 °C.

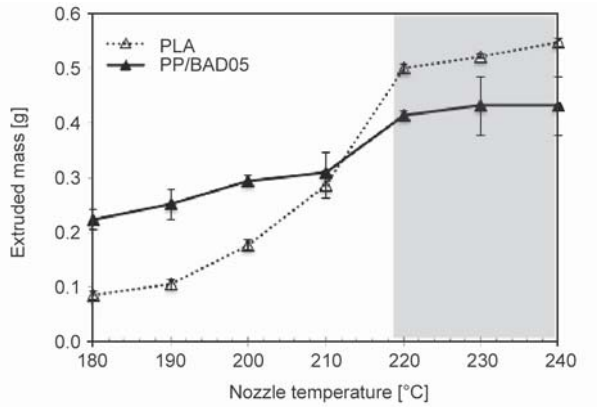

Figure 12. Extruded mass as a function of nozzle temperatures for PP/BAD05 and PLA filaments.

3.5.2. Tensile properties

In this study, an open source 3D printer, WANHAO Duplicator 6, was used to 3D print the tensile test specimens based on ASTM D638-14 [18]. It is noted that all prepared PP/organoclay nanocomposites can be 3D printed using the same printing parameters listed in Table 4. However, the neat PP cannot be successfully 3D printed because of its semi-crystalline characteristic, which leads to the high shrinkage and warpage during printing.

The tensile properties at room temperature of the PP/BAD05 and PP/BAD15 were shown in Figure 13.

Table 4. Parameters used for 3D printing of PP/organoclay nanocomposites.

Parameters		Value
Print nozzle diameter	[mm]	0.4
Nozzle temperature	[°C]	220
Bed temperature	[°C]	110
Layer height	[mm]	0.2
Print infill	[%]	30
Print speed	[mm·s^{-1}]	20

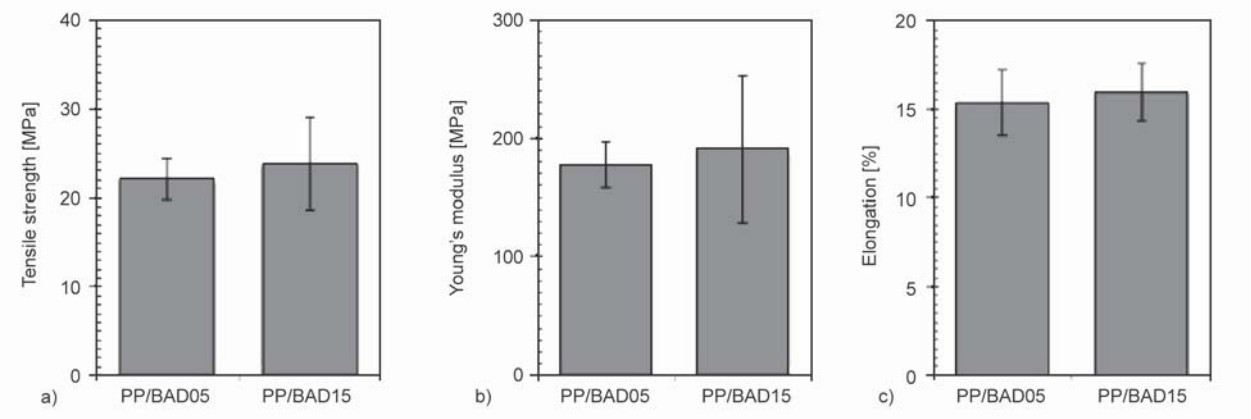

Figure 13. Tensile strength, Young's modulus and Elongation at break of PP/BAD05 and PP/BAD15 printed specimens. a) Tensile strength, b) Young's modulus, c) elongation at break.

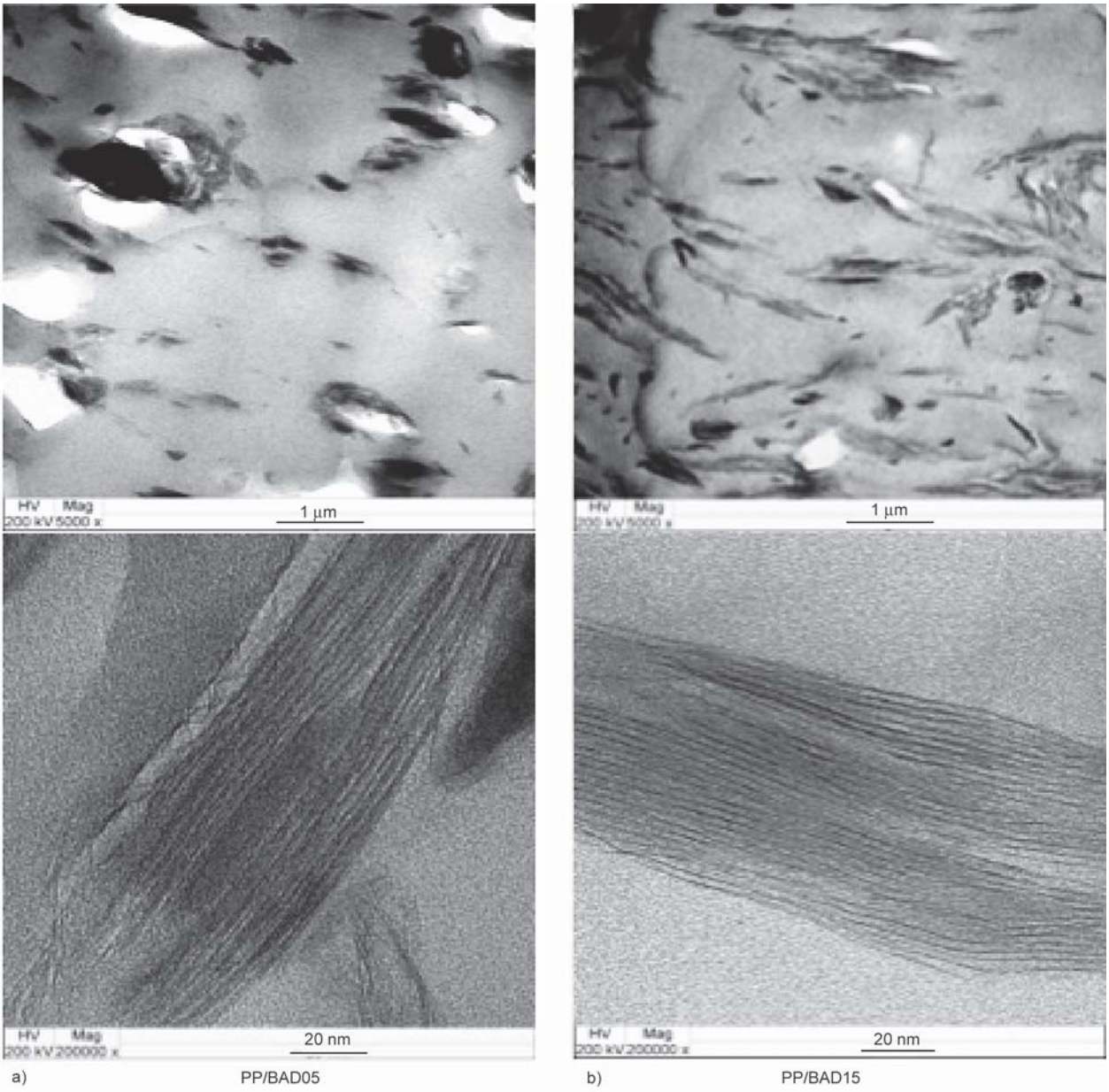

Figure 14. TEM images of the 3D printed (a) PP/BAD05 and (b) PP/BAD15 at 5000× (top) and 200 000× (bottom) magnifications.

The tensile strength, Young's modulus as well as the elongation at break of the PP/BAD15 were marginally higher than those of the PP/BAD05. This could be attributed to the better dispersion of the organoclay (BAD15) in the PP matrix. These results were in good agreement with the rheological behaviors and SEM results.

3.5.3. Organoclay dispersion

To verify the dispersion of the organoclay and its microstructure in the PP matrix, the TEM images of the printed PP/BAD05 and PP/BAD15 were presented in Figure 14. At the same magnification (5000×), the organoclay modified with higher D18 content (PP/BAD15) showed a smaller size and better dispersion in the PP matrix than the PP/BAD05. Both the PP/BAD05 and the PP/BAD15 seem to a combination of exfoliation and intercalation morphologies as anticipated by the XRD analysis. However, it is observed that the PP/BAD15 sample has larger clay tactoids which correspond to the more likely intercalated morphology [12].

4. Conclusions

In this study, a new PP/organoclay nanocomposite filament was first-time successfully prepared by the melt intercalation method using a twin-screw extruder and 3D printed into the three-dimensional shape. The linear viscoelasticity responses of the PP/organoclay nanocomposites showed the significant effect of the clay addition. D18 was successfully used to modify the clay surfaces, providing a better dispersion and wetting of the clay particles in the hydrophobic polymer matrix such as PP. A shift of the (0 0 1) plane peak to lower angle, indicated the more intercalation capability, while the larger *d*-spacing values suggested exfoliation developed in the PP/organoclay composites. Combining the XRD results, the rheological behavior and the TEM results together, it can be concluded that the PP/organoclay nanocomposites prepared in this study have mixed intercalated/exfoliated microstructure. A pseudo-MFI measurement proposed that the PP/organoclay nanocomposites could be 3D printed at the temperature range of 220–240 °C using a conventional FFF 3D printer. The results of this study can be further used for facilitating the development of engineering materials based on semicrystalline polymers from plastic industries.

Acknowledgements

We thankfully acknowledge the financial support from Grants for Development of New Faculty Staff, Ratchadaphiseksomphot Endowment Fund, Chulalongkorn University and The Thailand Research Fund (TRG6180009).

References

[1] Ligon S. C., Liska R., Stampfl J., Gurr M., Mülhaupt R.: Polymers for 3D printing and customized additive manufacturing. Chemical Reviews, **117**, 10212–10290 (2017). https://doi.org/10.1021/acs.chemrev.7b00074

[2] Wei X., Li D., Jiang W., Gu Z., Wang X., Zhang Z., Sun Z.: 3D printable graphene composite. Scientific Reports, **5**, 11181/1–11181/7 (2015). https://doi.org/10.1038/srep11181

[3] Wang L., Gardner D. J.: Effect of fused layer modeling (FLM) processing parameters on impact strength of cellular polypropylene. Polymer, **113**, 74–80 (2017). https://doi.org/10.1016/j.polymer.2017.02.055

[4] Ehrenstein G. W., Riede G., Trawiel P.: Thermal analysis of plastics. Hanser, München (2004).

[5] Sharma S. K., Nayak S. K.: Surface modified clay/polypropylene (PP) nanocomposites: Effect on physico-mechanical, thermal and morphological properties. Polymer Degradation and Stability, **94**, 132–138 (2009). https://doi.org/10.1016/j.polymdegradstab.2008.09.004

[6] Kumar V., Singh A.: Polypropylene clay nanocomposites. Reviews in Chemical Engineering, **29**, 439–448 (2013). https://doi.org/10.1515/revce-2013-0014

[7] Wang K., Bahlouli N., Addiego F., Ahzi S.: Elastic and yield behaviors of recycled polypropylene-based composites: Experimental and modeling study. Composites Part B: Engineering, **99**, 132–153 (2016). https://doi.org/10.1016/j.compositesb.2016.06.033

[8] Morajane D., Shinha Ray S., Bandyopadhyay J., Ojijo V.: Impact of melt-processing strategy on structural and mechanical properties: Clay-containing polypropylene nanocomposites. in 'Processing of polymer-based nanocomposites' (ed.: Sinha Ray S.) Springer, Basel, Vol 277, 127–154 (2018). https://doi.org/10.1007/978-3-319-97779-9_5

[9] Badji A. M., Ly E. H. B., Ndiaye D., Diallo A. K., Kebe N., Verney V.: The effect of poly-ethylene-co-glycidyl methacrylate efficiency and clay platelets on thermal and rheological properties of wood polyethylene composites. Advances in Chemical Engineering and Science, **6**, 436–455 (2016). https://doi.org/10.4236/aces.2016.64040

[10] Hong C. K., Kim M-J., Oh S. H., Lee Y-S., Nah C.: Effects of polypropylene-*g*-(maleic anhydride/styrene) compatibilizer on mechanical and rheological properties of polypropylene/clay nanocomposites. Journal of Industrial and Engineering Chemistry, **14**, 236–242 (2008). https://doi.org/10.1016/j.jiec.2007.11.001

[11] Abdel-Goad M.: Rheological characterization of melt compounded polypropylene/clay nanocomposites. Composites Part B: Engineering, **42**, 1044–1047 (2011). https://doi.org/10.1016/j.compositesb.2011.03.025

[12] Durmus A., Kasgoz A., Macosko C. W.: Linear low density polyethylene (LLDPE)/clay nanocomposites. Part I: Structural characterization and quantifying clay dispersion by melt rheology. Polymer, **48**, 4492–4502 (2007). https://doi.org/10.1016/j.polymer.2007.05.074

[13] Xie S., Harkin-Jones E., Shen Y., Hornsby P., McAfee M., McNally T., Patel R., Benkreira H., Coates P.: Quantitative characterization of clay dispersion in polypropylene-clay nanocomposites by combined transmission electron microscopy and optical microscopy. Materials Letters, **64**, 185–188 (2010). https://doi.org/10.1016/j.matlet.2009.10.042

[14] Abbasi F., Tavakoli A., Aghjeh M. K. R.: Rheology, morphology, and mechanical properties of reactive compatibilized polypropylene/polystyrene blends via Friedel–Crafts alkylation reaction in the presence of clay. Journal of Vinyl and Additive Technology, **24**, 18–26 (2018). https://doi.org/10.1002/vnl.21522

[15] Zdiri K., Elamri A., Hamdaoui M.: Advances in thermal and mechanical behaviors of PP/clay nanocomposites. Polymer-Plastics Technology and Engineering, **56**, 824–840 (2017). https://doi.org/10.1080/03602559.2016.1233282

[16] Rueda M. M., Auscher M-C., Fulchiron R., Périé T., Martin G., Sonntag P., Cassagnau P.: Rheology and applications of highly filled polymers: A review of current understanding. Progress in Polymer Science, **66**, 22–53 (2017). https://doi.org/10.1016/j.progpolymsci.2016.12.007

[17] Limpanart S., Khunthon S., Taepaiboon P., Supaphol P., Srikhirin T., Udomkichdecha W., Boontongkong Y.: Effect of the surfactant coverage on the preparation of polystyrene–clay nanocomposites prepared by melt intercalation. Materials Letters, **59**, 2292–2295 (2005). https://doi.org/10.1016/j.matlet.2005.03.006

[18] ASTM D638-14: Standard test method for tensile propertyies of plastics (2014).

[19] Ghaemi N., Madaeni S. S., Alizadeh A., Rajabi H., Daraei P.: Preparation, characterization and performance of polyethersulfone/organically modified montmorillonite nanocomposite membranes in removal of pesticides. Journal of Membrane Science, **382**, 135–147 (2011). https://doi.org/10.1016/j.memsci.2011.08.004

[20] Alexandre M., Dubois P.: Polymer-layered silicate nanocomposites: Preparation, properties and uses of a new class of materials. Materials Science and Engineering R: Reports, **28**, 1–63 (2000). https://doi.org/10.1016/S0927-796X(00)00012-7

[21] Colombe G., Gree S., Lhost O., Dupire M., Rosenthal M., Ivanov D. A.: Correlation between mechanical properties and orientation of the crystalline and mesomorphic phases in isotactic polypropylene fibers. Polymer, **52**, 5630–5643 (2011). https://doi.org/10.1016/j.polymer.2011.09.035

[22] Osswald T. A., Menges G.: Materials science of polymers for engineers. Hanser, Munich (2003).

[23] Lamberti G.: Isotactic polypropylene crystallization: Analysis and modeling. European Polymer Journal, **47**, 1097–1112 (2011). https://doi.org/10.1016/j.eurpolymj.2011.02.005

[24] Osswald T. A., Rudolph N.: Polymer rheology fundamental and applications. Hanser Publishers, Munich (2015)

[25] Venkataraman N., Rangarajan S., Matthewson M. J., Harper B., Safari A., Danforth S. C., Wu G., Langrana N., Guceri S., Yardimci A.: Feedstock material property – Process relationships in fused deposition of ceramics (FDC). Rapid Prototyping Journal, **6**, 244–252 (2000). https://doi.org/10.1108/13552540010373344

[26] Chen R-Y., Zou W., Zhang H-C., Zhang G-Z., Yang Z-T., Jin G., Qu J-P.: Thermal behavior, dynamic mechanical properties and rheological properties of poly(butylene succinate) composites filled with nanometer calcium carbonate. Polymer Testing, **42**, 160–167 (2015). https://doi.org/10.1016/j.polymertesting.2015.01.015

[27] Pfeifer T., Koch C., van Hulle L., Mazzei G. A., Rudolph N.: Optimization of the FDM additive manufacturing process. in 'Proceedings of ANTEC. Indianapolis, USA', 22–29 (2016).

[28] Aumnate C., Pongwisuthiruchte A., Pattananuwat P., Potiyaraj P.: Fabrication of ABS/graphene oxide composite filament for fused filament fabrication (FFF) 3D printing. Advances in Materials Science and Engineering, **2018**, 2830437/1–2830437/9 (2018). https://doi.org/10.1155/2018/2830437

polymers

MDPI

Article

Recycling of Polypropylene/Polyethylene Blends: Effect of Chain Structure on the Crystallization Behaviors

Chuanchom Aumnate [1,*], Natalie Rudolph [2] and Majid Sarmadi [3]

[1] Metallurgy and Material Sciences Research Institute, Chulalongkorn University, Bangkok 10330, Thailand
[2] AREVO, Inc., Milpitas, CA 95035, USA
[3] Textile Science, Department of Design Studies and Materials Science Graduate Program, University of Wisconsin-Madison, Madison, WI 53706, USA
* Correspondence: Chuanchom.a@chula.ac.th; Tel.: +662-218-8126

Received: 17 August 2019; Accepted: 5 September 2019; Published: 6 September 2019

Abstract: The combination of high-density polyethylene (HDPE), low-density polyethylene (LDPE) and polypropylene (PP) is frequently found in polymer waste streams. Because of their similar density, they cannot be easily separated from each other in the recycling stream. Blending of PP/ polyethylenes (PEs) in different ratios possibly eliminate the sorting process used in the regular recycling process. PP has fascinating properties such as excellent processability and chemical resistance. However, insufficient flexibility limits its use for specific applications. Blending of PP with relative flexible PEs might improve its flexibility. This is a unique approach for recycling or upcycling, which aims to maintain or improve the properties of recycled materials. The effects of the branched-chain structures of PEs on the crystallization behavior and the related mechanical properties of such blends were investigated. The overall kinetics of crystallization of PP was significantly influenced by the presence of PEs with different branched-chain structures. The presence of LDPE was found to decrease the overall crystallization rate while the addition of HDPE accelerated the crystallization process of the blends. No negative effect on the mechanical performance and the related crystallinity was observed within the studied parameter range.

Keywords: polymer blends and alloys; recycling; crystallization; crystal structure; kinetics

1. Introduction

Plastics are used daily in some applications. A considerable amount of plastic is used in disposable products. The amount of plastic consumed has been growing steadily due to desirable properties such as low density, high strength, ease of manufacturing and low cost. As a result, both industry and private households generate more and more plastic waste. The most prominent concerns are single-use plastic items such as packaging, bags and containers. Unfortunately, appropriate waste management strategies are not developing at the same rate as the increasing levels of plastic wastes. A significant amount of waste does not reach proper disposal sites, instead of littering the landscape, and blowing or washing into the sea, which leads to severe environmental problems. Polyolefins, which have excellent recycling properties, make up over 50% of the non-recycled plastic (high-density polyethylene, HDPE, low-density polyethylene, LDPE and polypropylene, PP). This has motivated the interest in plastic reuse and recycling [1–3].

Polyethylenes (PEs) are the most common plastic. Their primary uses are in packaging including plastic bags, plastic films and bottles. PEs are classified according to their polymerization method, density and branching. There are several types of PEs, but the most common use is the high-density polyethylene (HDPE) and the low-density polyethylene (LDPE). HDPE has between five and ten short

branches every 1000 carbon atoms. LDPE has the same number of branches as HDPE; however, they are much longer and are usually branched themselves [4–6]. Polypropylene (PP) is a linear hydrocarbon polymer with an intermediate level of crystallinity between LDPE and HDPE. Similar to PE in many properties, the presence of the methyl group attached to every other backbone carbon atom can alter the properties in some ways. The tertiary carbon atom can provide a site for oxidation. As a result, PP is less stable than PE. The orientation of each methyl group relative to the adjacent methyl groups has a strong effect on the polymer's ability to form crystals [7]. Due to its desirable physical properties such as high tensile strength, high stiffness and high chemical resistance, polypropylene (PP) has been widely used as packaging material, for instance as margarine and yogurt containers, bottle caps and microwavable food. However, it shows weak impact strength at low temperatures and is susceptible to environmental stress cracking [8,9]. LDPE waste mostly results from bags and packaging films. Owing to its low mechanical properties and easy processability it is recycled as garbage bags. One possibility to develop alternative applications is blending it with other materials to improve the low mechanical performance of recycled LDPE.

The combination of PP and PEs is frequently found in polymer waste streams. Because of their similar density, PP and PEs cannot be easily separated from each other in the recycling stream [10]. Blends of PP and PEs have become a subject of great economic and research interest, not only to improve the processing and mechanical properties of PP but also to some extent to expand opportunities to recycle these mixed plastics [11–15] Since the 1980s, a considerable amount of work has been focused on the study of mechanical properties of mixed PP and PEs. The effectiveness of blending mainly depends on the miscibility or immiscibility of the blended components. PP and HDPE as well as PP and LDPE are generally considered immiscible in any blending ratio and show a remarkable phase separation during cooling and crystallization, which reflects the end-properties of such blends. In polymer blends, the crystallization process may have a significant influence on its morphological features, thermal and mechanical properties.

Semi-crystalline polymers, PP and PEs, consist of crystallites of different lamellar thickness and degree of perfection. Crystallization kinetics in such polymer blends are very complex in relation to the different crystallization behavior of the two components. These include the production of primary nuclei, formation and spreading of surface nuclei, and inter-diffusion of crystallizable and non-crystallizable chains at the advancing front of the growing crystal [16–18]. In general, depending on the nucleation, there are two types of crystallization: heterogeneous and homogeneous crystallization. The crystal fraction in a polymer is a function of both the nucleation rate and the growth rate of the spherulite in the sample. The factors influencing the changes in primary nucleation in polymer blends can be divided into two groups. (i) The properties of the minor phase polymer in the blend, including miscibility, glass transition temperature, ability to crystallize, the temperature range in which crystallization is possible and surface tension of the polymer melt and (ii) the blending/mixing processes. For such blends in which dispersed polymer can crystallize, the size of its inclusions, controlled by the parameters of the mixing process, is one of the most critical factors determining the crystallization kinetics of the blend. For example, the non-equilibrium molecular structure of the PP/LDPE blend can be observed as a result of the strange process of PP crystallization [12]. Accordingly, the crystallization in blends of PP with LDPE and HDPE has been studied. PP has a high degree of crystallinity due to its regular chain structure. Galeski et al. [19] examined the morphology of an isotactic PP (iPP)/LDPE blend and revealed that the LDPE occlusions introduced substantial changes in the internal structure of the iPP spherulites. From a polarizing micrograph, it was seen that the LDPE droplets hindered the spherulite-growing front, causing distinct concavities. The influence of crystallization of a dispersed polymer in the matrix crystallization can probably explain the decrease of spherulite size in nonisothermically crystallized samples of the blends reported for iPP with LDPE [20], and iPP with HDPE [21]. During fast nonisothermal crystallization, a simultaneous crystallization of both components is also possible. Already crystallized inclusions of a dispersed polymer accelerate the crystallization of the matrix acting as nucleating agent and induce the formation of additional

spherulites. Finally, the average spherulite radius in those blends becomes smaller than in plain iPP crystallized under the same condition [22]. Razavi-Nouri et al. [23] studied the morphology of PP/linear low-density PE (LLDPE) blends and found that the nucleation densities of the PP spherulites decreased in the presence of the LLDPE. Moreover, LLDPE remained as discrete droplets dispersed throughout the PP spherulites, which indicated the immiscibility of these two components. In the case of PE/PE blends, molten PEs of different type chain structures usually are immiscible. The spherulites of PE with higher T_m, are encapsulated by those of the other PE during crystallization. Thus, once cooled below the crystallization point of one component, the blends' morphology is fixed within the crystalline structure.

The physical properties of PP and PEs are too similar to enable the detection of such phase separation, which governs the mechanical properties of the end product directly. Likewise, the phase behaviors of PP/PEs blends, are not entirely understood yet. However, the crystallization behavior plays an essential role in determining the crystal structure as well as the phase morphology, which further affects the end-use properties, especially mechanical performance. In this study, the influences of different chain structures PEs on the crystallization behaviors of PP/PEs blends as well as effects on the tensile properties are investigated. The crystallization behaviors, including the kinetics of crystallization as well as the crystal morphology, were studied using the differential scanning calorimetry (DSC) and the polarized optical microscopy techniques, respectively. The gel permeation chromatography (GPC) technique was used to measure the molecular weight and molecular weight distribution of the materials. Also, the blend morphology was analyzed via the scanning electron microscopy (SEM). Thus, the correlation between the crystallization behaviors and the tensile properties of PP/PEs blends were addressed. Furthermore, the effects of the recycling process on the chain structures, crystallization behaviors, as well as the tensile properties of recycled PP/PEs blends, are discussed.

2. Materials and Methods

2.1. Materials

The polymers chosen for this study have substantial differences in processing behavior and end-use properties. We selected the commercial virgin resins which are commonly used for packaging applications including Low-density polyethylene, LDPE (DOW LDPE 132I, Dow Chemical Company, Chicago, IL, USA), high-density polyethylene, HDPE (Marlex HXM 50100, Chevron Phillips Chemical, Woodlands, TX, USA) and polypropylene, PP (FHR Polypropylene P9G1Z-047, Flint Hills Resources, Longview, TX, USA).

The manufacturing scrap of recycled LDPE (Bapolene®1072, Bamberger Polymers, Inc., Itasca, IL, USA), injection molding grade used for food packaging) and regrind PP (Inspire ®6025N, Braskem, Philadelphia, PA, USA), used for blown film and thermoforming of packaging containers) were supplied by PLACON (Fitchburg, WI, USA). Incorporated together with virgin material of both grades were selected as representatives for recycled materials.

2.2. Sample Preparation

All materials were processed using a Leistritz (Somerville, NJ, USA) ZSE18HPe laboratory, modular, intermeshing, co-rotating twin-screw extruder and subsequently pelletized with the appropriate downstream equipment (a water-through, blown-air drier and a rotary cutter). The extrusion temperature profile was in a range of 180–220 °C from the hopper to die and the screw speed of 100 rpm. The PP/LDPE and PP/HDPE blends were prepared with the weight ratio of 100/0, 75/25, 50/50, 25/75 and 0/100, respectively.

For the mechanical properties' measurement, the PP/LDPE and PP/HDPE blends were prepared as the tensile bars according to ASTM D638-14 using a Type 1. All specimens were injection molded using an Allrounder 320S injection molding machine of the ARBURG GmbH and Co. KG, Loßburg-Germany with a clamping force of 500 kN. This machine is equipped with a screw of 25 mm diameter and an effective screw length (L/D ratio) of 24. The mold temperature is set at 25 °C.

3. Characterization

3.1. Melt Flow Rate (MFR) Measurements

The melt flow rate (MFR) is a good technique to determine the effects of reprocessing since it is an indirect measurement of the melt viscosity of materials. It also indicates the changes in molecular weight and is widely used in the thermoplastic industry. The MFR measurements were carried out in an extrusion plastometer Series 4000 according to the ASTM D1238-10, using procedure A [24].

3.2. Differential Scanning Calorimetry (DSC)

The melting and crystallization behavior of PP, LDPE, HDPE and their blends were determined using a DSC (214 Polyma, NETZSCH Group, Selb, Germany) under nitrogen atmosphere. For crystallization and melting temperature measurement, PP, LDPE, HDPE and their blends were melted at 200 °C, held isothermal for 2 min, then cooled to −35 °C and heated to 200 °C again with the scanning temperature rate of 5 K/min. For isothermal analysis, all blends and pure polymers were quenched from 200 °C to an isothermal temperature between 100 to 125 °C.

For the analysis of the crystallization kinetics, the Thermokinetics software (Version 3.1, Selb, Germany) from NETZSCH Group was used (Model: n-Dimensional nucleation (Avrami–Erofeev)).

According to the rule of mixtures, the crystallinity of PP/LDPE blends was determined from the melting enthalpy (ΔH_m) [25]. The actual melting enthalpy of a blend is related to the enthalpy of the individual polymer and to their weight fraction w in the blends:

$$\Delta H_i = \frac{\Delta H_{m(i)}}{w_{(i)}} \tag{1}$$

thus,

$$\Delta H_{PP/LDPE} = \left(\frac{\Delta H_{m(PP)}}{w_{(PP)}} + \frac{\Delta H_{m(LDPE)}}{w_{(LDPE)}} \right) \tag{2}$$

The degree of crystallinity, χ, of PP, LDPE and their blends was calculated using the following equation;

$$\chi = \frac{\Delta H_i}{\Delta H_0} \times 100 \tag{3}$$

where ΔH_0 is the specific heat of melting of completely crystalline materials, $\Delta H_0 =$ 205 J/g, and 293 J/g for PP and PEs, respectively [6].

However, in PP/PEs blends, the resultant morphologies are not only attributed to thermodynamic factors but also to kinetic ones during subsequent crystallization. The crystallization kinetics are described in terms of the Avrami equation (Equation (4)), a common tool to describe overall isothermal crystallization (including nucleation and growth of spherulites). It can be also written as:

$$ln(-ln(1 - X(t))) = ln\, k(T) + n\, ln\, t \tag{4}$$

When applied for DSC analysis, it is assumed that the differential area under the crystallization curve with time corresponds to the dynamic changes in the conversion of mass from the melt phase to the solid phase. The relative crystal conversion $X(t)$ as a function of time was calculated by the following equation:

$$X(t) = \frac{X_t}{X_\infty} \tag{5}$$

where $X(t)$ is the released heat until time t and t_∞ is the total released heat by crystallization.

The Avrami index, n, is a complex exponent, which is related to the dimensionality of the growing crystals and to the time dependence of nucleation. While the crystallization rate coefficient, k, is the overall crystallization growth rate constant and related to the nucleation type, crystal growth and

crystallization temperature. Based on these two values, the crystallization half-time, $t_{1/2}$, which is a representation of the crystallization rate, can be evaluated from:

$$k = \frac{\ln 2}{(t_{1/2})^n}. \quad (6)$$

In this study, the crystallization kinetics of all materials were calculated based on the Avrami model using the Thermokinetics software.

3.3. Polarized Optical Microscopy

The phase transformation of PP, LDPE, HDPE and their blends was investigated using an Olympus IX71 polarising optical microscope (Melville, NY, USA) equipped with a 50× objective and a hot-stage. All samples were prepared as 10 µm thick films using a microtome. The films were heated between a glass slide and coverslip to 200 °C and kept for 2 min. Subsequently, the samples were quenched to an isothermal temperature between the crystallization temperatures for PP (125 °C) and LDPE (100 °C).

3.4. Tensile Tests

The tests were carried out according to ASTM D638-14 [26] using a Type 1 tensile bar on an Instron 5960 Dual Column Tabletop tensile test machine (Norwood, Massachusetts) with a 30 kN load cell. The crosshead was moved with a constant velocity of 500 mm/min until the specimen broke in the gauge section. The strength and the strain of the sample were determined based on the maximum force and the elongation of the tensile bar. At least five measurements were taken for each material.

3.5. Gel Permeation Chromatography (GPC) Analysis

The analyses were performed using a PL GPC220, equipped with DAWn Heleos-II, detector from Wyatt Technology (Santa Barbara, California). The two PLgel Olexis separating column with 300 mm × 7.5 mm, Agilent Technologies were employed. All measurements were performed with 1,2,4 trichlorobenzol stabilized with 0.1% BHT at the flow rate of 1 ml/min and the measurement temperature of 150 °C.

3.6. Scanning Electron Microscope (SEM) Analysis

The cryo-fracture surfaces of the PP/PEs blends were studied using the LEO 1530 scanning electron microscope (SEM, White Plains, NY, USA) at an accelerating voltage of 5 kV. All fractured samples were etched with sulfuric acid at 80 °C for 2 h. Prior to investigation, all samples were sputter-coated with gold.

4. Results and Discussion

4.1. Melting and Crystallization Temperatures

According to the data available in the literature as well as the one presented in this study, PP, LDPE and HDPE crystallize separately, and both polymers can have a mutual effect on the process of crystallization, and the morphology of the blends [12].

Figure 1a shows the DSC heating curves of PP, LDPE and their blends at different compositions. The two endothermic peaks in the temperature range corresponding to the melting temperature of the individual polymers. The melting temperature of PP and LDPE does not significantly depend on the composition of the blends. As shown in Figure 1b, the crystallization temperature of LDPE in PP/LDPE blends remarkably shifts to higher temperature relative to the crystallization peak of pure LDPE and remains almost constant in all blend compositions. However, the crystallization temperature of PP in PP/LDPE blend with 75 wt % of LDPE content shifts to lower temperatures, which indicates a reduction in the perfection of the formed crystallites.

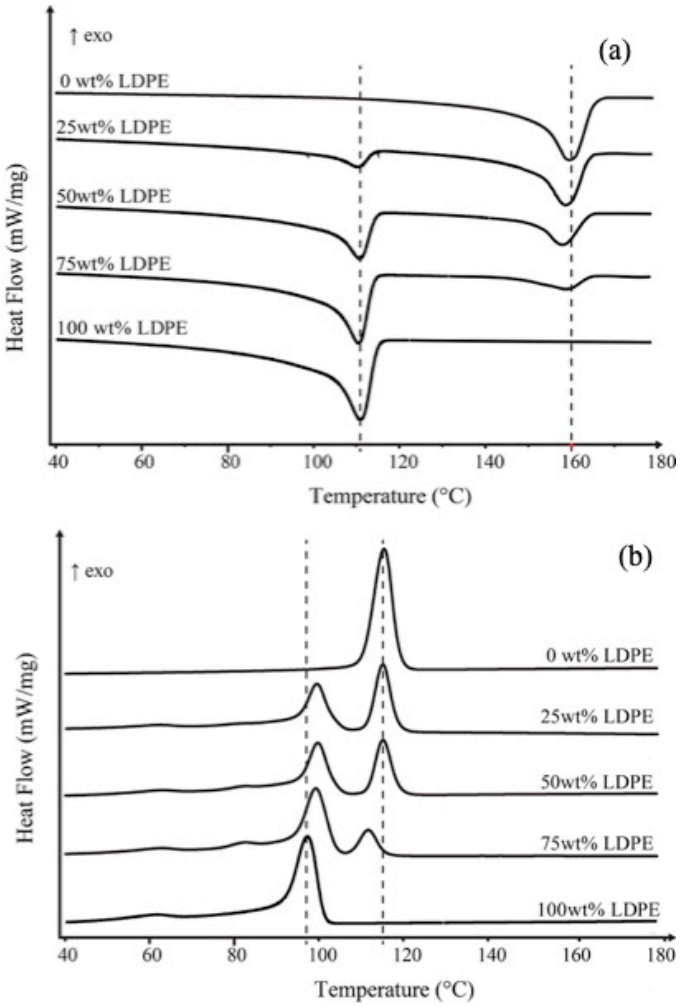

Figure 1. (**a**) Melting temperature (T_m) from the 2nd heating scan and (**b**) crystallization temperature (T_c) of polypropylene (PP), low-density polyethylene (LDPE) and their blends at different compositions.

For PP/HDPE blend, the T_m of HDPE in all blend compositions remains almost constant temperatures relative to that of pure HDPE (~131 °C) as shown in Figure 2a. However, the crystallization behavior of PP/HDPE blends is complex compared with the melting behavior. As shown in Figure 2b, the crystallization peak of blends shifts to the higher temperature, which is close to the crystallization temperature (T_c) of HDPE. Even though PP/HDPE blend systems seem to show only one T_c, however, the bimodal behavior is more pronounced at higher HDPE loading blend (75 wt % HDPE). The bimodal crystallization behavior could be associated with partially miscible behavior. Also, a single crystallization peak of the blend with small HDPE loading could be postulated that the PP was miscible with HDPE at elevated fraction and temperature. A single crystallization peak may be due to a very close crystallization temperature of the individual polymers; 116.2 °C for PP and 117.6 °C for HDPE. Also, the one crystallization peak possibly implies co-crystallization of the materials, which leads to miscibility and compatibility of the blends.

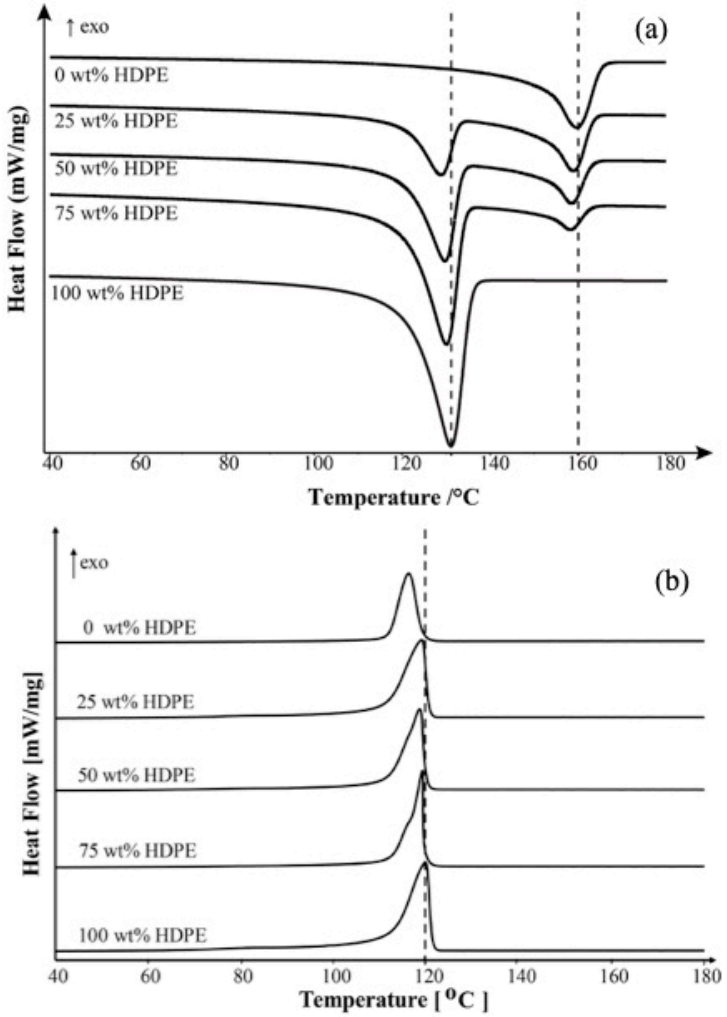

Figure 2. (**a**) Melting temperature (T_m) from the 2nd heating scan and (**b**) crystallization temperature (T_c) of PP, high-density polyethylene (HDPE) and their blends at different compositions.

4.2. Crystallinity

Figure 3a presents the crystallinity of PP/LDPE blends both total and separately in the blends. It can be seen that the crystallinity of PP and LDPE in the blends varies depending on their composition. In the case of high viscosity polymers, the increase of LDPE (lower viscosity) content decreases the degree of crystallinity of the blend. Concerning an individual component, it is seen that the crystallinities of both LDPE and PP in the blends exhibit an almost linear relationship with its concentration.

Similarly, Figure 3b presents the total crystallinity of PP/HDPE blends both total and separately in the blends. The more linear structure of HDPE results in more crystallinity compared to those of PP. The larger the HDPE contents, the higher crystallinity of the blends. Remarkably, a drop of the total crystallinity of PP/HDPE blends appears when the blend contains 75 wt % HDPE, which could be related to the deviation in crystallization behavior as well as the crystal structure of the blend.

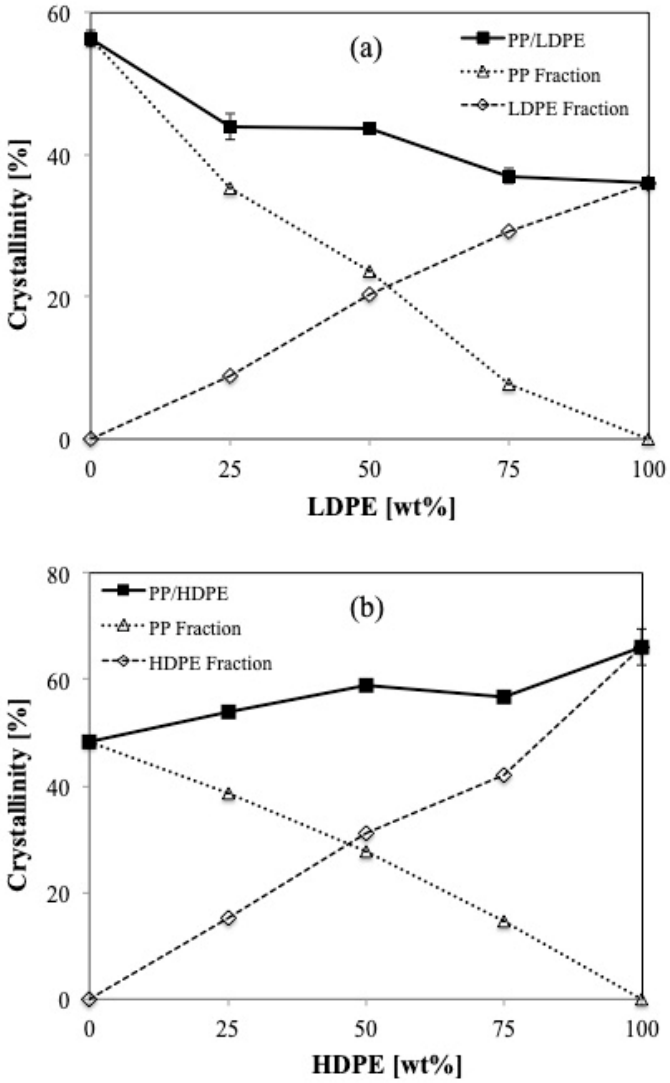

Figure 3. % Crystallinity of (**a**) PP/LDPE blends and (**b**) PP/HDPE blends at different blend compositions.

4.3. Crystal Structures

The crystal structures and morphology of PP, LDPE, HDPE and their blends were captured using the polarized optical microscope. From the DSC results, it is known that PP starts crystallizing at 125 °C while LDPE and HDPE begin at 100 and 124 °C, respectively.

PP is a semi-crystalline thermoplastic polymer with a high degree of crystallinity due to its regular chain structure. In general, PP can crystallize in a wide range of spherulite dimensions (from 10–50 μm to 280–370 μm) depending on the crystallization conditions as well as the presence of nucleating agent [27,28]. LDPE and HDPE crystals, in general, consist of ethylene units in a chain fold structure. Thus, the segment length of an ethylene unit can limit the lamella thickness. From this study, it is visible that LDPE crystals are much smaller in size compared to PP crystals. The crystal sizes are about 25 and 100 μm in diameter for LDPE crystals and PP crystals, respectively. However, the crystal sizes of HDPE are much smaller than those of PP and LDPE as can be observed in Figure 4.

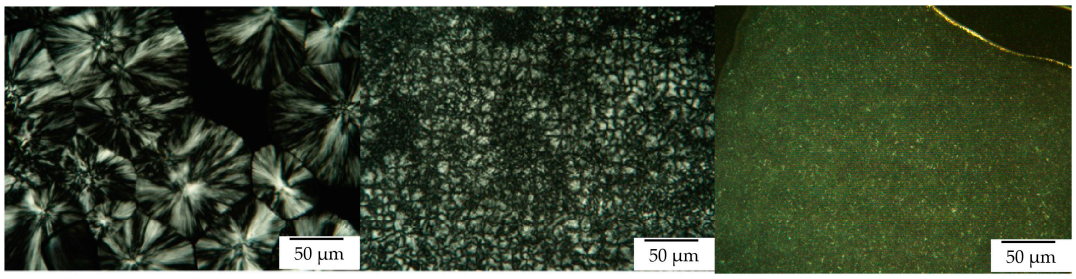

Figure 4. Polarizing optical microscopy of (**a**) LDPE after isothermal crystallization at 100 °C for 20 min, and (**b**) PP after isothermal crystallization at 125 °C for 20 min and (**c**) HDPE after isothermal crystallization at 124 °C.

In this study, each blend was crystallized isothermally at 125 °C, where PP could crystallize. Figure 5 shows the nucleation and growth process of PP/LDPE blends during the isothermal crystallization at 125 °C from 4 to 20 min. The spherulites of PP in blends were not as sharp as in the virgin PP, but they could still be readily distinguished. During crystallization, the PP in the blend crystallizes at almost the same rate as pure PP. A larger LDPE content resulted in a reduction of the average spherulite size of PP. Possibly, PP should be somewhat soluble in the melted LDPE, which seems to be consuming the remaining PP dissolved in the matrix, preventing bridging growth [29]. This can also be concluded from the shifting of T_c of PP to a lower temperature with more substantial LDPE contents.

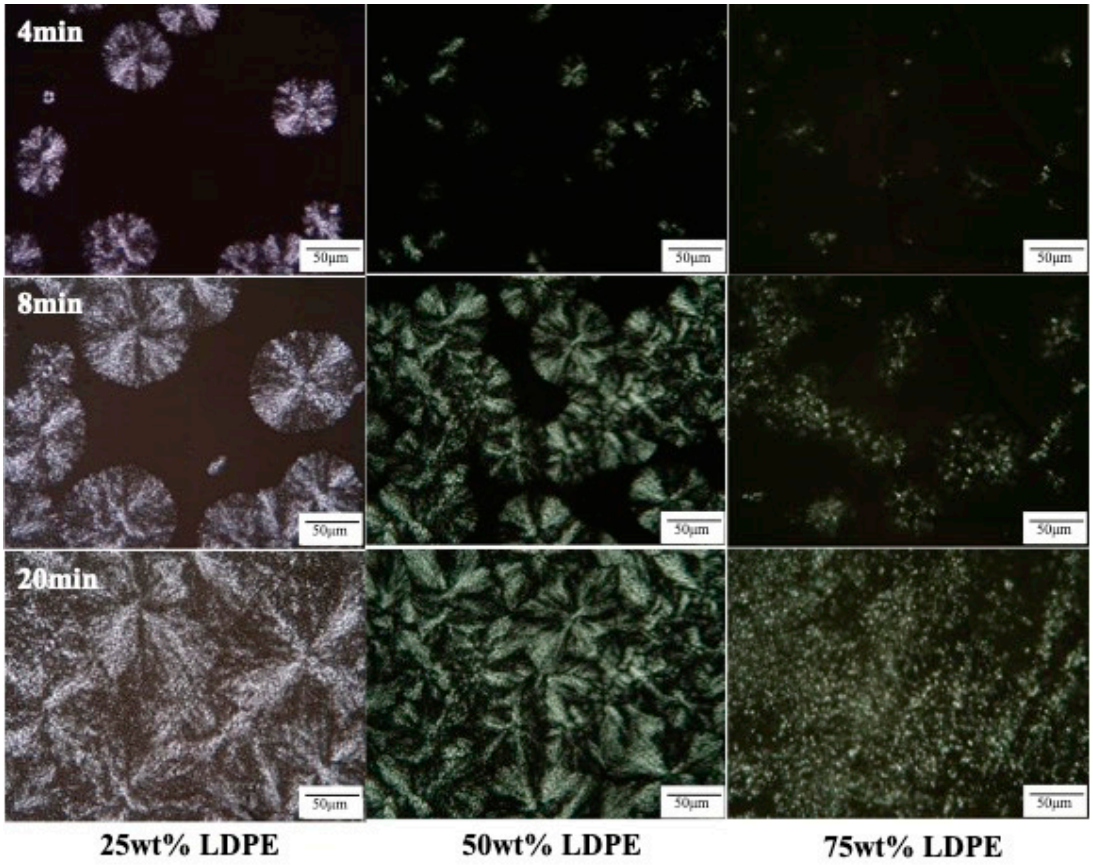

Figure 5. Polarizing optical microscopy of the nucleation and growth process of PP/LDPE blends containing 25 wt % LDPE, 50 wt % LDPE and 75 wt % LDPE during isothermal crystallization at 125 °C.

The crystallization rate of PP was found to be slightly slower at larger LDPE contents. As can be seen from Figure 5 at 4 min, the PP spherulite in the 75 wt % LDPE blend developed slower than that of PP spherulites in the 50 wt % LDPE and 75 wt % LDPE blends, respectively. Even though the PP crystals in the blend of 25 wt % LDPE nucleated faster than that of the blend with 50 wt % LDPE, it should be noted that once the PP crystals in the blend of 50 wt % LDPE were nucleated, they grew faster. This can be seen at 8 min. Some crystals nucleated at a much lower rate and then grew faster afterward.

In contrast, the opposite effects are found for PP/HDPE blends. The larger the HDPE contents, the faster the crystallization rate as can be seen in Figure 6. Since the crystallization temperatures of PP and HDPE overlap, both PP and HDPE could crystallize, increasing the crystallization rate. The overall crystallization rates are accelerated as the higher HDPE contents are loading.

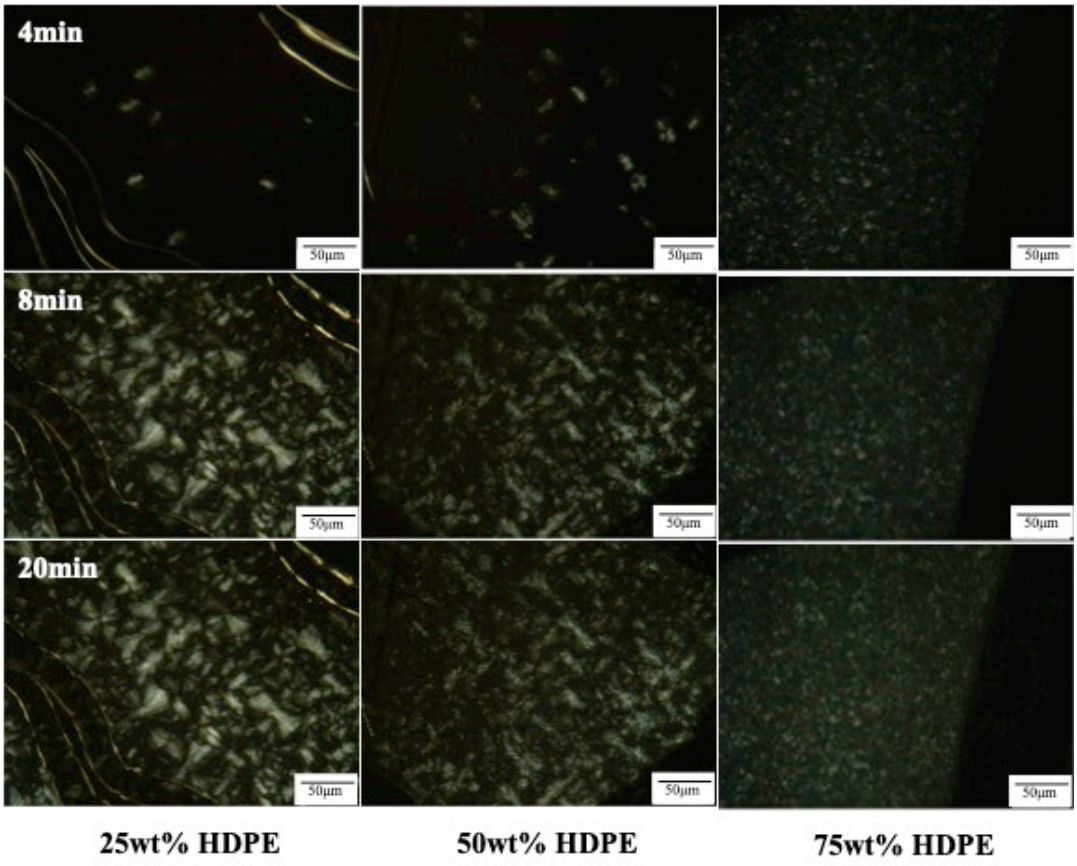

Figure 6. Polarizing optical microscopy of the nucleation and growth process of PP/HDPE blends containing 25 wt % HDPE, 50 wt % HDPE and 75 wt % HDPE during isothermal crystallization at 125 °C.

4.4. Crystallization Kinetics

Figure 7a shows the crystallization behaviors, and Figure 7b shows the comparison of crystalline fraction development in PP/LDPE and PP/HDPE at the same concentration of LDPE and HDPE (25 wt %), respectively. The solid line represents the crystalline fraction of pure PP at the same isothermal crystallization process.

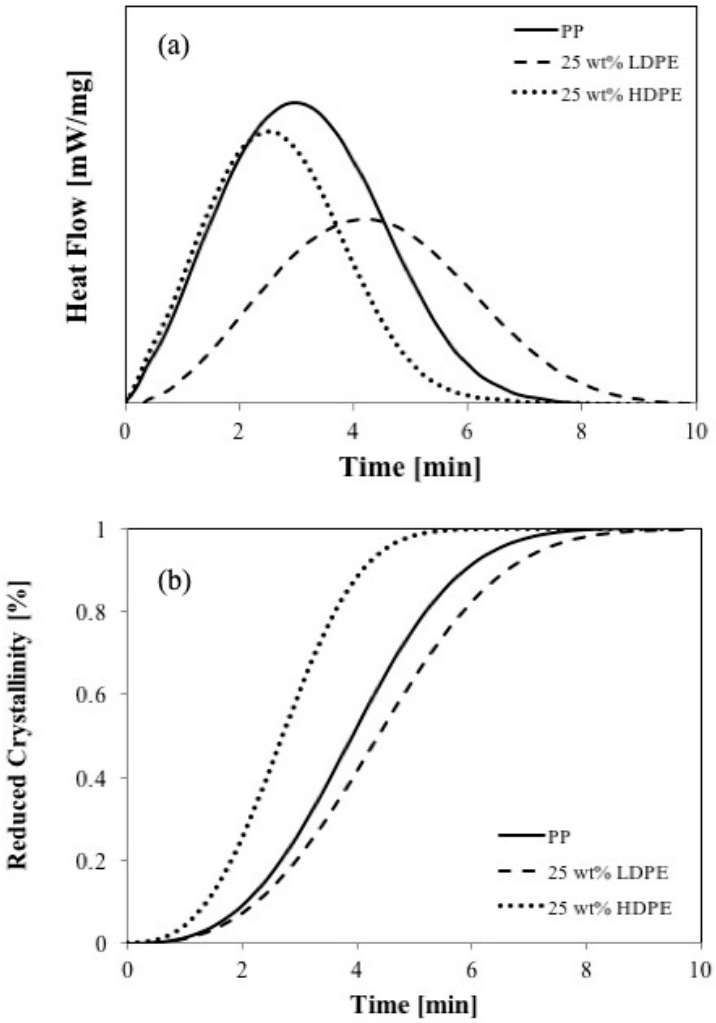

Figure 7. (**a**) Differential scanning calorimetry (DSC) crystallization curves and (**b**) reduced crystallinity obtained at 125 °C for PP (solid line), PP/LDPE containing 25 wt % of LDPE (dash line) and PP/HDPE blends containing 25 wt % of HDPE (dot line).

Based on the Avrami equation, the values of the Avrami exponent, n, varied slightly but they were all close to 2, indicating that the crystallization process was heterogeneous and took place within two dimensions. The growth of spherulites was confined in two dimensions although initial nucleation and crystallization may take place in three dimensions because the specimens were 10 μm in thickness and were sandwiched between glass slides and coverslips. The most dramatic increase in the Avrami index, n, can be obtained by increasing the LDPE content since the morphology can also be significantly altered by confinement effects or interference from the LDPE melt. The growing PP spherulites may occlude the droplets of LDPE. Theoretically, the difference in interfacial energy decides whether the droplets of LDPE were engulfed or rejected by the growing PP spherulites [28]. The crystallization kinetic parameters of all blends are shown in Table 1.

Table 1. Avrami index (n), overall crystallization rate constant (k), and crystallization half-time obtained during isothermal crystallization of PP, LDPE, HDPE and their blend at isothermal crystallization temperatures (125 °C) at the cooling rate of 25 K/min.

Materials	MFR [g/10 min]	Half-Time, $t_{1/2}$ [min]	n [-]	k [min^{-1}]
PP (0 wt % LDPE)	0.66	3.24	2.42	0.2655
PP/LDPE (25 wt % LDPE)	0.71	4.58	2.73	0.1908
PP/LDPE (50 wt % LDPE)	0.89	4.68	2.65	0.1862
PP/LDPE (75 wt % LDPE)	0.91	N/A	N/A	N/A
LDPE (100 wt % LDPE)	0.72	N/A	N/A	N/A
PP/HDPE (25 wt % HDPE)	0.45	2.73	2.36	0.3143
PP/HDPE (50 wt % HDPE)	0.32	2.27	2.54	0.3808
PP/HDPE (75 wt % HDPE)	0.23	N/A	N/A	N/A
HDPE (100 wt % HDPE)	0.15	N/A	N/A	N/A

From the crystallization behavior studies, which include the kinetics of crystallization as well as the crystal morphology from the optical microscope, we found that the overall crystallization rate of PP was sharply reduced by the addition of LDPE, the more branched structure. However, the opposite results were found for the case of linear chain HDPE. Consequently, the branched-chain structure seems to affect the nuclei density. However, from this study, it can be said that both nucleation and diffusion processes controlled the overall crystallization rate.

The MFR seems to affect the crystallization haft-time, as shown in Table 1. The addition of LDPE and HDPE into PP showed different effects on the MFR of the blends. The MFR of PP/HDPE blends decreased with increasing the HDPE content, and all blend compositions have the MFR within the limits of the pure components; PP and HDPE. Surprisingly, the MFR of PP/LDPE increased with increasing LDPE loading, which is even higher than the MFR of the pure components; LDPE and PP. It is possible that LDPE acts as a plasticizer for the PP molecules and enhances the mobility and diffusion of PP in the blends.

4.5. Effect of Recycling Process

Due to the large differences in structure and behavior, for recycled materials, the results presented in this study will be limited to PP, LDPE and their blends. Some results of PP/HDPE blends will be shown to confirm the applicability of methods or results where appropriate. Thus, the manufacturing scraps of recycled LDPE (Bapolene®1072) and regrind PP (Inspire ®6025N), which will be called as LDPE1 and PP1 were selected as representatives.

Figure 8 shows the comparison of isothermal crystallization behavior of virgin material (vPP1, solid line) and recycled material (rPP1, dash line) at 139 °C. It is seen that the crystallization behavior of recycled PP deviates from that of the virgin material. The broader shape indicates that rPP1 needs more time to crystallize and that the crystal geometry could be different.

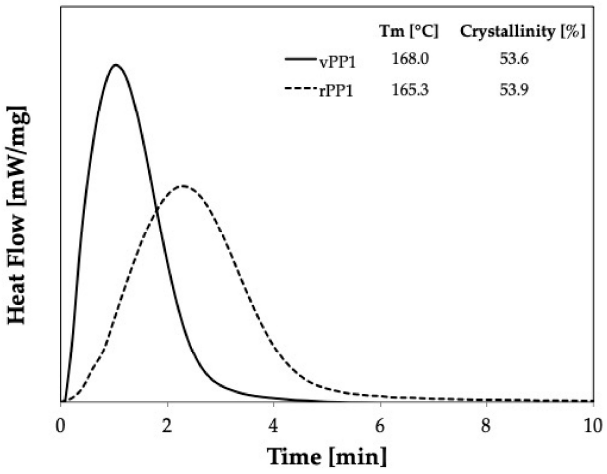

Figure 8. Crystallization curves obtained at 139 °C for virgin material (vPP1), and recycled material (rPP1).

Figure 9 shows the isothermal crystallization curves for vPP1, and vPP1/vLDPE1 blends at 139 °C, a temperature at which the only vPP1 can crystallize. These results imply a delay in the crystallization and the imperfection of the crystal formation in the recycled blends.

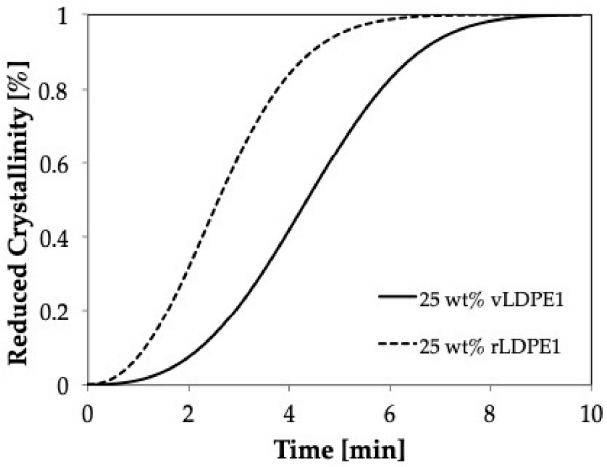

Figure 9. Crystallinity obtained at 139 °C for virgin material (vPP1/vLDPE1) and recycled material (rPP1/rLDPE1) blends containing 25 wt % of vLDPE1 and rLDPE1, respectively.

The effect of recycling process on the crystallization behavior of PP/LDPE blends is shown in Figure 9. The recycled blend (dash line) shows a higher rate of crystallization compared to that of the virgin blend (solid line), which may be caused by the shorter polymeric chain resulting from the degradation during the recycling process [14]. Furthermore, the recycling process affects the shape of the crystals (rPP1), which become more spherical. The smaller the value of k and the higher the half-time value, the slower is the rate of crystallization.

It can be seen that the recycling process resulted in the broader of the crystallization peak. Moreover, the nucleation of rPP1 is much slower than that of vPP1, as reported in Table 2. Furthermore, a significant decrease in M_w of virgin PP1 (vPP1) from 481,000 to 354,150 g/mol for recycled PP1 (rPP1) was observed. Recycled PP1 (rPP1) is the regrind material received out of the production stream, resulting from the dilution of 70% recyclate with 30% virgin material. Thus, the properties can be influenced by highly degraded fractions, which have shorter polymer chains than the virgin material. The shorter chains have a lower molecular weight and thus, affect the mechanical performance of the

material. The observed lowering in the molecular weight (M_w) indicates that chain scission occurred during the recycling process. The lower polydispersity index shows that the chain scission was mostly affecting the longest chains, while the lower limit was not affected. Thus, the molecular chain of rPP1 is shorter, and the molecular weight distribution is narrower, leading to the smaller k value and lowering the crystallization rate as shown in the increasing of the crystallization half-time.

Table 2. Weight average molecular weight (M_w), molecular weight distribution (M_w/M_n) and kinetic parameters for the isothermal crystallization of vPP1 and rPP1 at 139 °C at the cooling rate of 25 K/min.

Materials	MFR [g/10min]	M_w [g/mol]	M_w/M_n	Crystallization Temperature [°C]	Half-Time, $t_{1/2}$ [min]	n [-]	k [min^{-1}]
vPP1	2.76	414,933	3.15	139	1.52	1.93	0.5436
rPP1	6.10	333,467	2.46	139	2.21	2.24	0.3844

From the crystallization behavior studies, which include the kinetics of crystallization as well as the crystal morphology from the optical microscope, it is clearly shown that the overall crystallization rate of PP was strongly reduced by the addition of LDPE for both the high-viscosity system (PP/LDPE and PP/HDPE) and low-viscosity system (vPP1/vLDPE1). Furthermore, consistent behavior was observed in the blend system of recycled material (rPP1/rLDPE1). It can be concluded that the reduction in the overall rate is attributed to a decrease in the nucleation density. The decrease in nucleation density was found predominantly caused by the nuclei migration from PP to PE, which was in turn caused by an interfacial energy difference [19].

In general, polymer degradation during processing operations can cause changes in molecular weight and molecular weight distribution in polymers. The MFI indicates changes in molecular weight but is rather insensitive to changes in molecular parameters such as molecular weight distribution. In the case of viscosity, the sensitivity to molecular weight distribution changes is seen in the very low and very high shear rate ranges. MFI has been used to estimate the extent of thermal and shear degradation of polymeric material as it can be readily measured on a simple and inexpensive melt flow indexer. The recycled blend shows a higher MFI at the blend composition of less than 50 wt % of LDPE while the lower MFI can be observed at the high LDPE contents (>50 wt %). Therefore, it can be concluded that at small LDPE contents, the MFI of the matrix PP dominates the change in MFI of the blend. Vise Versa, at higher LDPE content, when the LDPE presents the matrix, the MFI of the blends are indeed governed by LDPE. The low-viscosity materials (high MFI) show a faster crystallization rate as well as shorter crystallization half-time compared to the high-viscosity materials.

4.6. Mechanical Properties

Figure 10a presents the stress-strain curves for PP, LDPE and their blends at different compositions. The tensile stress-strain curves are dependent on their composition. As expected, the elongation of PP was improved by adding the more ductile LDPE. The larger the content of LDPE, the higher is the strain at break. The same behaviors were observed for the PP/HDPE blends as shown in Figure 10b. The tensile strength, Young's modulus and maximum tensile stress for such PP/LDPE and PP/HDPE blends are depicted in Figure 10c–e, respectively. It can be seen that Young's modulus and the tensile strength of PP/LDPE and PP/HDPE blends followed the same trends. However, a distinct improvement in Young's modulus and tensile strength were found in PP/HDPE blend with 25 wt % of HDPE. One reason could be attributed to the co-crystallization of PP and HDPE (exhibit one crystallization peak), and the higher degree of crystallinity, which again results in an increased modulus.

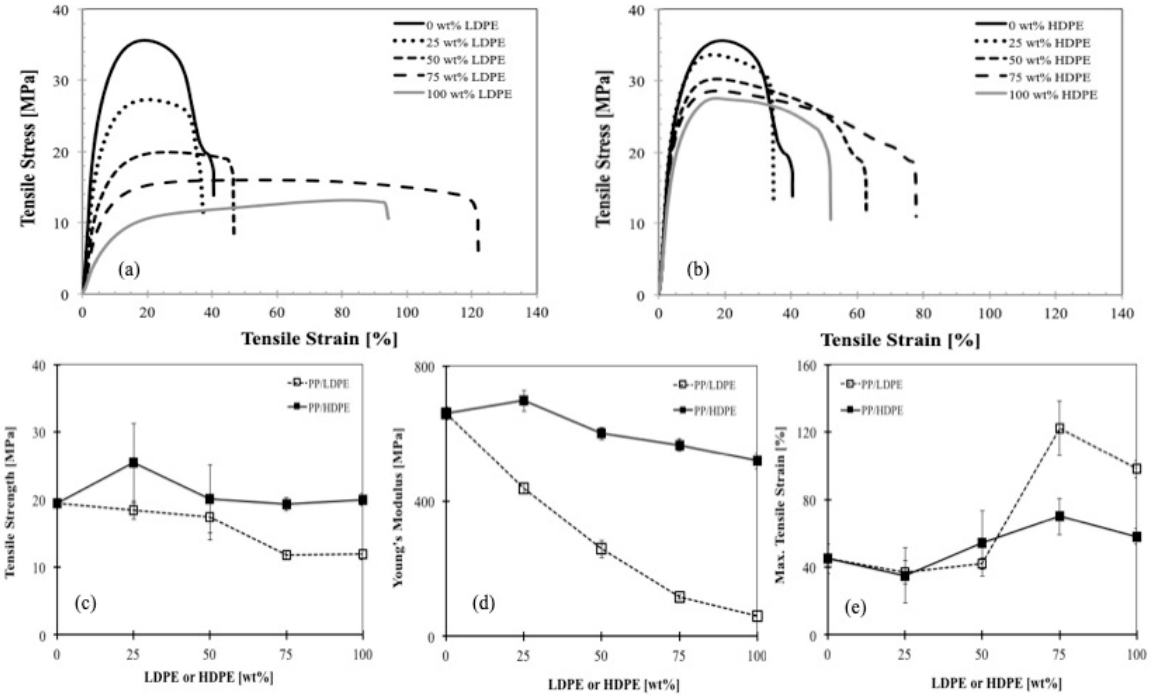

Figure 10. Tensile properties: (**a**) stress-strain curves of PP, LDPE and their blends at different compositions (u_0 = 500 mm/min), (**b**) stress-strain curves of PP, HDPE and their blends at different compositions (u_0 = 500 mm/min), (**c**) tensile stress, (**d**) Young's modulus and (**e**) tensile strain at maximum stress for PP/LDPE (dash line) and PP/HDPE (solid line) as a function of blend composition.

Figure 11 shows the tensile properties of the blends prepared from virgin materials (vPP1/vLDPE1), and recycled materials (rPP1/rLDPE1), respectively. The tensile properties of rPP1 show only a slight change compared to those of virgin material (vPP1/vLDPE1). These results indicate the potential for recycling the PP/LDPE blend with consistent mechanical performances.

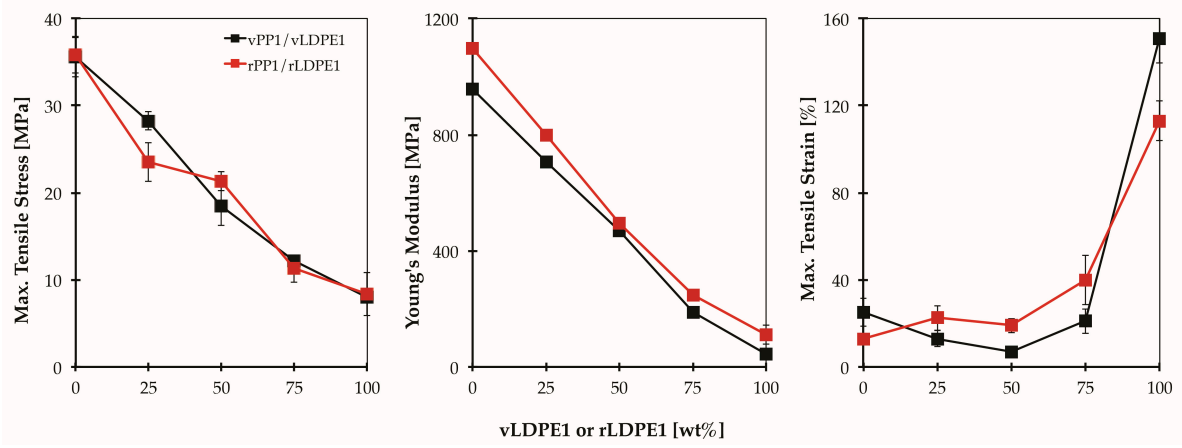

Figure 11. Tensile stress [MPa], Young's modulus [MPa] and tensile strain [%] for vPP1/vLDPE1 and rPP1/rLDPE1 as a function of blend composition.

4.7. Blend Morphology

Figure 12 presents the SEM micrographs for the low-viscosity blend (rPP1/rLDPE1, MFI ratio = 10) in comparison with the high-viscosity blend (PP/LDPE, MFI ratio = 1) of 75 wt % LDPE. It is seen that the polymer pairs with different viscosities and MFI ratios, in which related to the different chain

structures and degree of entanglement, developed different phase morphologies. The rPP1/rLDPE1 blend shows a droplet structure, small holes as well as droplets of material being dispersed in the matrix. However, sharp borders at the dispersed phase sites and no evidence of PP-LDPE interpenetration are observed. Since rLDPE1 has a much lower viscosity than rPP1 in this blend, holes and droplets may be attributed to LDPE particles, which are entirely surrounded by PP. The lack of interfacial adhesion between PP and LDPE phases leads to the decreasing in mechanical strength of the blend as presented in Figures 10 and 11.

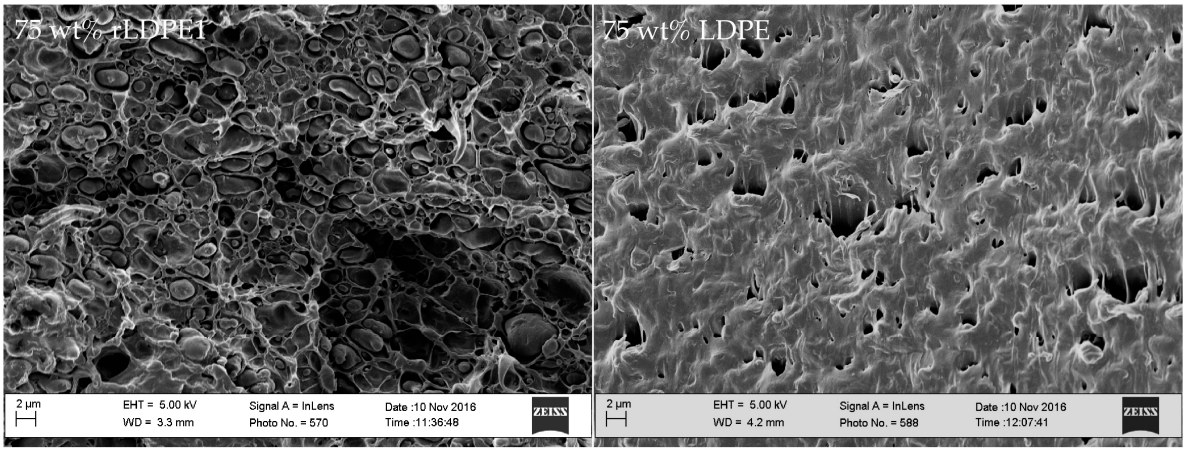

Figure 12. SEM images for vPP1/vLDPE1 (left) and PP/LDPE (right) at 25 wt % of LDPE composition, sulfuric etching at 80 °C for 2 h.

Polymer pairs and blend composition affect the results of the short-term tensile test. The higher maximum tensile stress of PP can be explained by the short rigid methyl group, which is attached to every second carbon atom of the polymer backbone. The methyl group restricts rotation of the chain, which results in a higher degree of crystallinity while producing a stronger and less flexible material. Thus, already a small content of this brittle material decreases the ability of elongation significantly, which is shown by the considerable drop of maximum tensile strain between 0 and 25 wt % LDPE. Such behavior can be also observed all blends.

The PP/LDPE in this study shows extremely improved tensile properties at 75 wt % LDPE content, which imply partial miscibility or partial compatibility of the blend. Similar behavior is also observed in PP/HDPE blend. Incorporating with the crystal structure results, it could be said that the PP/PEs blends showed a dynamic incompatible behavior that has been attributed to the different crystalline structures of the two components, PP and PEs. Even though it took longer time to crystallize, blends with 25 wt % of LDPE and HDPE crystallized with the large size of crystals. This could be causing a heterogeneous structure with weak interconnections, leading to modest maximum tensile strain values. As the LDPE and HDPE content increase, the blends getting crystallized into aggregates of smaller sizes in which well interconnections between the crystals, leading to the tensile strain enhancement. The PP/PEs blends with a high level of compatibility are expected to offer advantages for a wide range of applications, including the applications of the individual polymers.

5. Conclusions

The crystallization behavior studies, which include the kinetics of crystallization as well as the crystal morphology from the optical microscope, clearly showed that the addition of long branches LDPE strongly reduced the overall crystallization rate of PP. The reduction in the overall rate is mainly attributed to a decrease in the nucleation density. The decrease in nucleation density was found predominantly caused by the nuclei migration from PP to LDPE. Accordingly, the imperfection of PP crystals in the blends resulted from LDPE droplets engulfed in the PP spherulites, which can

also be observed from the shifting of T_c of PP to a lower temperature with larger LDPE contents. The crystallization rate of PP was found to be slightly slower at larger LDPE contents. Even though the PP crystals in the blend with 25 wt % LDPE nucleated faster than that of the blend with 50 wt % LDPE, it should be noted that once the PP crystals in the blend of 50 wt % LDPE were nucleated, they grew faster. This can be seen in the optical microscopic images for the isothermal crystallization at 8 min as well as the overall crystallization rate, which is represented in the form of reduced crystallinity versus time. Some crystals nucleated at a much lower rate and then grew faster afterward. However, in the case of PP/HDPE blend in which the crystallization temperatures overlap, resulting in an increase of the crystallization rate. Moreover, the more LDPE and HDPE contents, the smaller crystal sizes propagated in the blends. The Avrami coefficient, n, depends on the shape of the crystal: spherical (n = 3); disk-shaped (n = 2); rod-shaped (n = 1). This study shows that the shape of the crystal and the crystallization rates seemed to affect the tensile properties of the blends. These results are observed for the blends of PP and HDPE (short branched structure). The PP/HDPE blend with 75 wt % HDPE, which n = 1.69 and had a prolonged crystallization rate, showed a significantly improved on the elongation property. Accordingly, the slower crystallization rate resulted in the tensile properties improvement.

The mechanical properties are in good agreement with the crystallization study and show that PP/LDPE with 75 wt % LDPE and PP/HDPE with 75 wt % HDPE are partially compatible. Particularly the elongation at maximum strain is considerably improved while the tensile stress at break and Young's modulus are not lower than expected. Thus, the recycled PP/PEs blends can be expected to be able to serve in a wide range of application. This is depending on the degree of miscibility or compatibility, which is related to the desired properties of the products as well as the processability of the materials. According to this study, the properties of recycled PP/PE blend (rPP1/rLDPE1) remains unchanged until the composition of rLDPE1 reach 25 wt %, which means that rPP1/rLDPE1 can be used similarly as the pure recycled PP. For example, the recycled blends could be used again in injection molded or blow-molded applications to make bottles or containers. Furthermore, the outdoor decking, fencing and picnic tables can be manufactured from the recycled PP/PEs blends as well as pipe, films or sack bags.

Author Contributions: Conceptualization: C.A., N.R. and M.S.; methodology: C.A.; analysis: C.A.; writing—original draft: C.A.; writing—review and editing: C.A., N.R. and M.S.

Funding: This research was funded by the University of Wisconsin-Madison, USA, the grants for Development of New Faculty Staff, Ratchadaphiseksomphot Endowment Fund, Chulalongkorn University, Thailand and The Thailand Research Fund (TRG6180009).

Conflicts of Interest: The authors declare no conflict of interest.

References

1. Hamad, K.; Kaseem, M.; Deri, F. Recycling of waste from polymer materials: An overview of the recent works. *Polym. Degrad. Stab.* **2013**, *98*, 2801–2812. [CrossRef]
2. Chen, H.; Sundararaj, U.; Nandakumar, K.; Wetzel, M.D. Investigation of the Melting Mechanism in a Twin-Screw Extruder Using a Pulse Method and Online Measurement. *Ind. Eng. Chem. Res.* **2004**, *43*, 6822–6831. [CrossRef]
3. United States Environmental Protection Agency (EPA). *Advancing Sustainable Materials Management: Facts and Figures 2013 Assesing Trends in Material Generation, Recycling and Disposal in the United States*; United States Environmental Protection Agency (EPA): Washington, DC, USA, 2015.
4. Osswald, T.A.; Menges, G.; Manges, G. *Materials Science of Polymers for Engineers*, 3rd ed.; Hanser Publishers: Munich, Germany; Vienna, Austria; New York, NY, USA, 2012.
5. Osswald, T.A.; Rudolph, N. *Polymer Rheology*; Hanser Publishers: Munich, Germany, 2015.
6. Ehrenstein, G.W.; Riedel, G.; Trawiel, P.; Riede, G.; Trawiel, P. *Thermal Analysis of Plastics*; Hanser Gardner Publishers, Inc.: Cincinnati, OH, USA, 2004.
7. Ward, I.M. Polymers: Chemistry and Physics of Modern Materials. In *Contemporary Physics*, 3rd ed.; Cowie, J.M.G., Arrighi, V., Eds.; CRC Press: Boca Raton, FL, USA, 2009; Volume 50, p. 670. [CrossRef]

8. Utracki, L.A. *Commercial Polymer Blends*; Chapman & Hall: Londan, UK, 2000; ISBN 0412810204.
9. Van Eygen, E.; Laner, D.; Fellner, J. Circular economy of plastic packaging: Current practice and perspectives in Austria. *Waste Manag.* **2017**, *72*, 55–64. [CrossRef]
10. Yin, S.; Tuladhar, R.; Shi, F.; Shanks, R.A.; Combe, M.; Collister, T. Mechanical Reprocessing of Polyolefin Waste: A Review. *Polym. Eng. Sci.* **2015**, *55*, 2899–2909. [CrossRef]
11. Salih, S.E.; Hamood, A.F.; Alsabih, A.H. Comparison of the Characteristics of LDPE: PP and HDPE: PP Polymer Blends. *Mod. Appl. Sci.* **2013**, *7*, 33–42. [CrossRef]
12. Mastalygina, E.E.; Popov, A.A.; Kolesnikova, N.N.; Karpova, S.G. Morphology, thermal behavior and dynamic properties of the blends based on isotactic polypropylene and low-density polyethylene. *Int. J. Plast. Technol.* **2015**, *19*, 68–83. [CrossRef]
13. Rudolph, N.; Kiesel, R.; Aumnate, C. *Understanding Plastic Recycling*; Hanser Publishers: Munich, Germany, 2017.
14. Spicker, C.; Rudolph, N.; Kühnert, I.; Aumnate, C. The use of rheological behavior to monitor the processing and service life properties of recycled polypropylene. *Food Packag. Shelf Life* **2019**, *19*, 174–183. [CrossRef]
15. Eagan, J.M.; Xu, J.; Di Girolamo, R.; Thurber, C.M.; Macosko, C.W.; Lapointe, A.M.; Bates, F.S.; Coates, G.W. Combining polyethylene and polypropylene: Enhanced performance with PE/iPP multiblock polymers. *Science* **2017**, *355*, 814–816. [CrossRef]
16. Tien, N.-D.; Prud'homme, R.E. Crystallization Behavior of Miscible Semicrystalline Immiscible Polymer Blends. In *Crystallization in Multiphase Polymer Systems*; Elsevier Inc.: Amsterdam, The Netherlands, 2018; pp. 181–212.
17. Mofokeng, T.G.; Ray, S.S.; Ojijo, V. Influence of Selectively Localised Nanoclay Particles on Non-Isothermal Crystallisation and Degradation Behaviour of PP/LDPE Blend Composites. *Polymers* **2018**, *10*, 245. [CrossRef]
18. Lin, J.-H.; Pan, Y.-J.; Liu, C.-F.; Huang, C.-L.; Hsieh, C.-T.; Chen, C.-K.; Lin, Z.-I.; Lou, C.-W. Preparation and Compatibility Evaluation of Polypropylene/High Density Polyethylene Polyblends. *Materials* **2015**, *8*, 8850–8859. [CrossRef]
19. Galeski, A.; Bartczak, Z.; Pracella, M. Spherulite nucleation in polypropylene blends with low density polyethylene. *Polymers* **1984**, *25*, 1323–1326. [CrossRef]
20. Teh, J.W. Structure and Properties of Polyethylene-Polypropylene Blend. *J. Appl. Polym. Sci.* **1983**, *28*, 605–618. [CrossRef]
21. Lovinger, A.J.; Williams, M.L.; Telephone, B. Tensile Properties and Morphology of Blends of Polyethylene and Polypropylene. *J. Appl. Polym. Sci.* **1980**, *25*, 1703–1713. [CrossRef]
22. Zhang, Z.; Yu, F.; Zhang, H. Isothermal and Non-Isothermal Crystallization Studies of Long Chain Branched Polypropylene Containing Poly(ethylene-co-octene) under Quiescent and Shear Conditions. *Polymers* **2017**, *9*, 236. [CrossRef]
23. Razavi-nouri, M.; Hay, J.N. Isothermal crystallization and spherulite nucleation in blends of polypropylene with metallocene-prepared polyethylene. *Polym. Int.* **2006**, *55*, 6–11. [CrossRef]
24. ASTM International. Astm D1238−13. *ASTM Int.* **2013**, 1–16. [CrossRef]
25. Lu, X.; Weiss, R.A. Relationship between the glass transition temperature and the interaction parameter of miscible binary polymer blends. *Macromolecules* **1992**, *25*, 3242–3246. [CrossRef]
26. American Society for Testing and Material (ASTM). Standard Test Method for Tensile Properties of Plastics (D638-14). *Annu. Book ASTM Stand.* **2009**, 1–17.
27. Lee, J.H.; Lee, S.-G.; Choi, K.-Y. Crystallization and Melting Behavior of Nylon 66/Poly (ether imide) Blends. *Polym. J.* **1998**, *30*, 531–537. [CrossRef]
28. Li, J.; Shanks, R.; Long, Y. Miscibility and crystallisation of polypropylene–linear low density polyethylene blends. *Polymers* **2001**, *42*, 1941–1951. [CrossRef]
29. Strapasson, R.; Amico, S.; Pereira, M.; Sydenstricker, T.; Pereira, M.F. Tensile and impact behavior of polypropylene/low density polyethylene blends. *Polym. Test.* **2005**, *24*, 468–473. [CrossRef]

โครงการ **Fabrication of Graphene/PP composites filaments for Fused Deposition Modeling (FDM) 3D Printing**

โดย ดร.ชวนชม อ่วมเนตร
สังกัด สถาบันวิจัยโลหะและวัสดุ จุฬาลงกรณ์มหาวิทยาลัย

Output บทความตีพิมพ์ในวารสารวิชาการระดับนานาติ จำนวน 3 เรื่อง

(1) **Chuanchom Aumnate**, Aphiwat Pongwisuthiruchte, Prasit Pattananuwat and Pranut Potiyaraj. “Fabrication of ABS/Graphene Oxide Composite Filament for Fused Filament Fabrication (FFF) 3D Printing” *Advances in Materials Science and Engineering* 2018 (2018): Article ID 2830437.

(อยู่ในฐานข้อมูล ISI, Impact Factor: 1.399: Q2)

(2) **Chuanchom Aumnate**, Sarintorn Limpanart, Niphaphun Soatthiyanon and Srichalai Khunton. “PP/organoclay nanocomposites for fused filament fabrication (FFF) 3D printing” *eXPRESS Polymer Letters* 13(10) (2019): 898-909.

(อยู่ในฐานข้อมูล Scopus, Impact Factor: 2.875: Q1)

(3) **Chuanchom Aumnate**, Natalie Rudolph and Majid Sarmadi. “Recycling of Polypropylene/ Polyethylene Blends: Effect of Chain Structure on the Crystallization Behaviors” *Polymers* 11 (2019): 1456.

(อยู่ในฐานข้อมูล ISI, Impact Factor: 3.164: Q1)

Hindawi
Advances in Materials Science and Engineering
Volume 2018, Article ID 2830437, 9 pages
https://doi.org/10.1155/2018/2830437

Research Article

Fabrication of ABS/Graphene Oxide Composite Filament for Fused Filament Fabrication (FFF) 3D Printing

C. Aumnate[1], **A. Pongwisuthiruchte**[2,3], **P. Pattananuwat**[2,3] and **P. Potiyaraj**[1,2,3]

[1]*Metallurgy and Materials Science Research Institute, Chulalongkorn University, Bangkok, Thailand*
[2]*Department of Materials Science, Faculty of Science, Chulalongkorn University, Bangkok, Thailand*
[3]*Center of Excellence on Petrochemical and Materials Technology, Chulalongkorn University, Bangkok, Thailand*

Correspondence should be addressed to C. Aumnate; chuanchom.a@chula.ac.th

Received 6 August 2018; Revised 26 September 2018; Accepted 8 October 2018; Published 6 November 2018

Academic Editor: Amit Bandyopadhyay

Additive manufacturing, the so-called three-dimensional (3D) printing, is a revolutionary emerging technology. Fused filament fabrication (FFF) is the most used 3D printing technology in which the melted filament is extruded through the nozzle and builds up layer by layer onto the build platform. The layers are then fused together and solidified into final parts. Graphene-based materials have been positively incorporated into polymers for innovative applications, such as for the mechanical, thermal, and electrical enhancement. However, to reach optimum properties, the graphene fillers are necessary to be well dispersed in polymers matrix. This study aims to emphasise the interest of producing ABS/graphene oxide (GO) composites for 3D printing application. The ABS/GO composite filaments were produced using dry mixing and solvent mixing methods before further melt extruded to investigate the proper way to disperse GO into ABS matrix. The ABS/GO composite filament with 2 wt.% of GO, prepared from the solvent mixing method, was successfully printed into a 3D model. By adding GO, the tensile strength and Young's modulus of ABS can be enhanced. However, the ABS/GO composite filament that was prepared via the dry mixing method failed to print. This could be attributed to the aggregation of GO, leading to the die clogging and failure of the printing process.

1. Introduction

Numerous 3D printing technologies are now accessible, such as stereolithography apparatus (SLA), selective laser sintering (SLS), laminated object manufacturing (LOM), and fused filament fabrication (FFF). The FFF is considered to be the most commonly used and well-recognized technology for making functional prototypes. In the FFF technique, a thermoplastic filament is melted and extruded through the nozzle, building up layer by layer onto the platform or build plate. The layers are then fused together and solidified into final products. Consequently, the quality of the printed parts can be controlled by adjusting the printing parameters, such as layer height, printing temperature, printing speed, and printing orientation [1–6]. 3D printed polymers are used in various areas, for example, in automotive, architectural, and even in medical fields. Due to the relatively simple design, capability, and affordability of the FFF process, it has gained significant attention in both industry and academic research [5]. However, the usable materials are limited to thermoplastic polymers with appropriate melt viscosity. As a result, the melt viscosity should be adequate to allow extrusion, at the same time, suitable to provide structural supports [4, 6]. Even though the 3D printing technologies have attracted much attention over the past years, most of the published studies focused on the printing of pure polymer materials. The 3D printed polymer products are now used as conceptual prototypes rather than functional components because of their shortage in strength and limited functionality. Thus, there are recently extensive studies on developing printable polymer composites with improving the performance and gaining excellent functionalities [7–9]. For example, Bandyopadhyay et al. [2] used the FFF technique to fabricate the polymer/ceramic composites with controlled phase structures, which are not possible with the conventional fabrication techniques.

Polymer/nanofiller composites have been considerably investigated due to their broad applications. However, they have many drawbacks regarding the agglomeration or nonuniform dispersion of reinforcements or fillers. Also, the voids generated during the composite filaments fabrication can lead to the properties' defection. In general, the addition of nanofillers results in enhancing the mechanical, electrical, thermal, and optical properties of the matrix. Likewise, GO delivers relatively high mechanical strength, thermal conductivity, and electrical properties [8, 10, 11]. If the GO sheets are well dispersed in the polymer matrix, they can form a highly oriented microstructure or cocontinuous networks in the polymer, resulting in the mechanical, thermal, and electrical properties improvement [12]. Graphene-based composite is still challenged due to its poor dispersity, which may be caused by various reasons such as restacking of the GO, weak interfacial bonding, and incompatibility with polymer matrix [10, 13]. Pinto et al. [10] incorporated a small amount (0.2 to 1 wt.%) of graphene oxide (GO) and graphene nanoplatelets (GNP) into poly (lactic acid), PLA, to produce composite films with improved mechanical performance and oxygen and nitrogen permeability. Wang et al. [14] reported that the tensile strength of the PVA/GO composite nanofibers increased by 42 times with addition of only a slight loading of GO (0.02 wt.%). Lin et al. [15] fabricated polyethylene/graphene oxide nanocomposites by the melt blending technique using polyethylene-grafted graphene oxide as a compatibilizer. Even though a relatively good dispersion of graphene oxide in the polyethylene matrix was evidenced, the improvement of mechanical properties was still limited. The resulted graphene-based composites can be suitable for various applications such as architectural applications like patio roofs, windows, and trim [16].

There are three typical methods for graphene-based polymer composite fabrication methods, including in situ polymerization, melt compounding, and solvent blending. The critical challenge for efficiently reinforcing the graphene-based polymer composite is the good dispersion of graphene fillers, which is significantly influenced by the fabrication techniques. Even though many reports stated that the melt extrusion or melt-compounding process is the most typically used methods, the GO cannot be homogeneously dispersed in the polymer matrix. Due to the high surface area of GO, it is tough for the molten polymer to cover the two sides of the fragile GO sheets effectively. As a result, the stack or agglomeration of GO sheets can be observed [10, 11].

Zhang et al. [17] fabricated the flexible circuits based on reduced GO (r-GO) using the FFF 3D printing technique. They reported that the orientation of r-GO occurred during the extrusion process contributed to enhancing the conductivity of the 3D printed composite parts. Moreover, Dul et al. [18] successfully prepared the ABS/GNP composite for the FFF process using the melt compounding method. The presence of GNP led to the reduction in the coefficient of thermal dilation and improved the stability under long-lasting loads for the 3D printed parts. However, it has been spotted that the polymer/graphene-based material composites prepared via the solution mixing method provided better electrical properties than those fabricated by melt extrusion due to the better dispersion of graphene-based materials in polymer solution [16, 19].

Acrylonitrile butadiene styrene (ABS) is one of the most used materials in the FFF process [20]. The relatively low glass transition temperature (T_g) and excellent processing properties of ABS led to the ease of filament extrusion and 3D printing. Moreover, it is an amorphous polymer, which means there is no crystallite. Accordingly, the shrinkage ratio during the cooling process is small, offering the high printing accuracy and the dimensional constancy. All of the characteristics stated above make ABS as an outstanding material for FFF 3D printing. Incorporation of graphene-based materials will potentially enlarge the applications and functionalities of the 3D printed ABS, in particular, some practical applications such as auto parts, conceptual prototypes, and jigs. However, the use of ABS/graphene-based composites in 3D printing application is still rarely demonstrated. Wei et al. [13] successfully demonstrated one of the first attempts to 3D print ABS/graphene composites using solution-based process. However, there was no report regarding the property investigation for such 3D printed composites.

To produce a good-quality filament for the FFF process, critical melt extrusion process parameters need to be examined. This study aims to accomplish good-quality composite filament from ABS/GO composites. The ABS/GO composites are prepared via solution mixing and dry mixing methods, followed by melt extrusion to achieve the good GO dispersion. The processability of ABS/GO composites is further investigated in terms of thermal properties and rheological properties. Also, 3D objects are printed to explore the printability of the prepared ABS/GO filament.

2. Materials and Methods

2.1. Preparation of Graphene Oxide (GO). The GO was prepared using Hummers' method. Concentrated H_2SO_4 was added to a mixture of graphite flakes (1 wt.% equiv.) and $NaNO_3$ (0.5 wt.% equiv.). Then, the mixture was cooled to 0°C, and $KMnO_4$ (3 wt.% equiv.) was added slowly in portions to keep the reaction temperature below 20°C. After that, the reaction was warmed to 35°C and stirred for 30 minutes, at which time water was added slowly to produce a sizable exothermic reaction to 98°C. The external heating was also introduced to maintain the reaction temperature at 98°C for 15 minutes. Then the heat was removed, and the reaction was cooled down in a water bath for 10 minutes. From this step, additional water (420 ml) and 30% H_2O_2 (3 ml) were added, and then the mixture was cooled down to room temperature, followed by multiple washing, and dispersed in water.

2.2. Preparation of ABS/GO Composite. The dispersed GO in water was washed and replaced by DMF to obtain a homogeneous GO/DMF dispersion with 2 wt.% of GO in DMF. The ABS was then dissolved in DMF to get 10 wt.% of ABS in DMF. Then, the GO/DMF dispersion and ABS/DMF solution were mixed and sonicated for 2 hours. The mixture

was then dried to obtain ABS/GO composite with 20 wt.% GO.

2.3. Preparation of ABS/GO Composite Filament

2.3.1. Solution Mixing. In this method, the ABS gets dissolved, and the GO is dispersed in DMF. Then, the dispersed GO and ABS solution is mixed. The ABS/GO composite is obtained after solvent evaporation, which further combined with pure ABS and extruded to produce ABS/GO filament for FFF 3D printing.

2.3.2. Dry Mixing. ABS is mixed mechanically with GO powder and then is melt compounded using the twin-screw extruder to avoid the use of the solvent system. This method is widely used for preparing thermoplastic nanocomposite.

For the filament extrusion process, the ABS/GO composite with 20 wt.% of GO content was diluted to 4 wt.% of GO by mixing with the neat ABS granules. The mixture was then melted and extruded using the twin-screw extruder. The extrusion temperatures ranged from 160°C to 210°C from the hopper to the die. Thus, the 1.75 mm diameter filament was produced and collected for the 3D printing test. Figure 1 demonstrates the equipment setup for preparing the ABS/GO filament by the melt extrusion process.

2.4. Fabrication of 3D Printed Parts. An open source 3D printer, WANHAO Duplicator 6, was used to fabricate the 3D specimens. A tensile test specimen was designed using CAD software based on ASTM D638-10 [21]. The FFF printing parameters were optimized and are listed in Table 1. It is noted that the same printing parameters were used for both pure ABS and ABS/GO composite filaments.

2.5. Characterization

2.5.1. X-Ray Diffraction (XRD) Analysis. The X-ray diffraction (XRD) of graphene-based materials was performed using an X-ray diffractometer (Bruker AXS Model D8 Discover). All samples were scanned over the range $2\theta = 2–50^{\circ}$, and measurements were recorded at every 0.02° interval.

2.5.2. Differential Scanning Calorimetry (DSC). The measurements were carried out using a Netzsch DSC 3500 Sirius, under the nitrogen atmosphere. The samples were heated from room temperature to 250°C. After an isothermal step for 2 minutes, the samples were cooled down to 30°C and finally heated up to 250°C after another isothermal step for 2 min. A scanning temperature ramp of 10 K/min was used for all dynamic steps.

2.5.3. Thermogravimetric Analysis (TGA). The measurements were carried out using a Netzsch STA 2500. The samples were heated from room temperature to 600°C, under the nitrogen atmosphere. A scanning temperature ramp of 10 K/min was used for the dynamic steps.

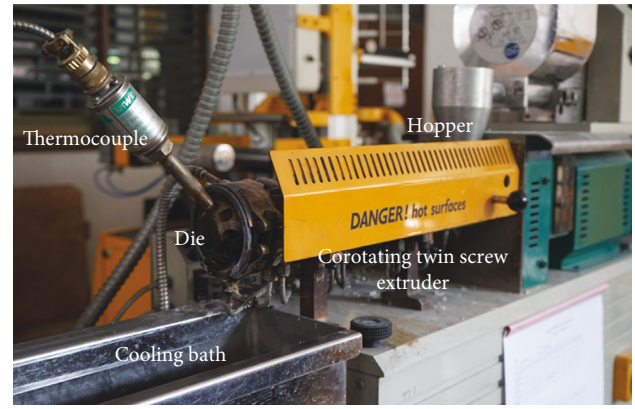

Figure 1: Melt extrusion process setup for ABS/GO composite filament fabrication.

Table 1: Parameters used for the FFF 3D printing of ABS and ABS/GO composites.

Parameters	Value
Print nozzle diameter (mm)	0.4
Nozzle temperature (°C)	220
Bed temperature (°C)	100
Layer height (mm)	0.1
Print infill (%)	100
Print speed (mm/s)	20

2.5.4. Melt Flow Rate. The melt flow rate (MFR) is a common rheological measurement in which the molten polymer is pushed through a capillary die under a specific load, and the mass of extruded polymer is measured and reported in the unit of the extruded mass/10 minutes. The MFR measurements were carried out according to ASTM D1238 standard (Procedure A), at a temperature range of 220–240°C with an applied load of 2.16 kg [22].

A pseudo-MFR measurement was performed using the FFF 3D printer with the nozzle diameter of 0.4 mm in order to determine the proper printing temperature. The extruded material through the nozzle in a 30-second time frame was weighed as a function of temperature.

2.5.5. Rheology Test. The linear viscoelasticity responses of the materials were measured using a parallel plate rheometer (ARES G2000). A frequency sweep between 0.0628 and 628 rad/s was performed at a temperature of 210°C. Based on the result of the strain sweep test, a constant strain was fixed as 5% where the linear viscoelastic behavior maintained. Also, the steady shear measurements were conducted at 220°C, from the shear rate range of 0.01 to 1000 s^{-1}. The two parallel plates were set up at 1 mm gap for all measurements.

2.5.6. Tensile Test. To study the mechanical properties, the tensile test specimens were printed based on ASTM D638 Type-V geometry [23]. The crosshead speed was set as 5 mm/min. Ultimate tensile strength, Young's modulus, and elongation at break were evaluated as an average value of at least three replicates.

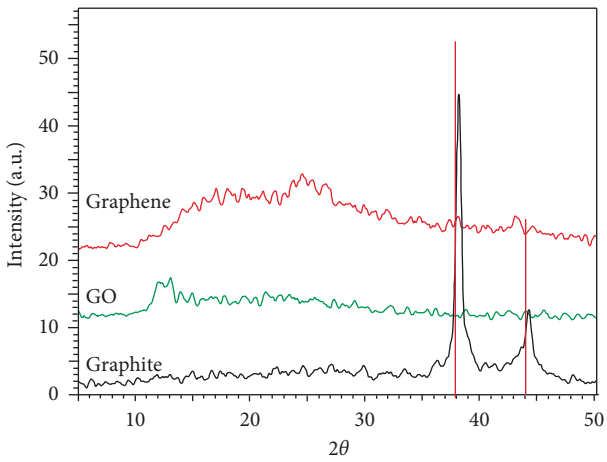

Figure 2: XRD diagram of graphite, graphene, and graphene oxide (GO).

3. Results and Discussion

Recently graphene/polymer composite has been fabricated by introducing graphene flakes into a conventional polymer that can be used for FFF printing applications. However, the apparent graphene aggregation and the phase separation between graphene and polymer matrixes are significant problems. In this work, graphene oxide (GO) was used to improve the graphene's dispersion in the ABS matrix.

3.1. X-Ray Diffraction (XRD) Analysis. In this study, GO was obtained by the oxidation of graphite regarding Hummers' method. Figure 2 shows the XRD patterns of the graphite, graphene, and obtained GO.

According to Bragg's law ($n\lambda = 2d \sin\theta$), the value of D spacing depended on the θ value. The diffraction peak of graphite was observed at $2\theta = 36.7^{\circ}$ with D spacing around 0.11 nm. The diffraction peak for graphene was shifted to $2\theta = 25$ with D spacing around 0.35 nm as compared to those of graphite, while the GO revealed the diffraction peak at $2\theta = 12.9^{\circ}$ with D spacing of 0.67 nm. The shifts of the diffraction peak and the increase of the D spacing value attributed to the oxygen functional group between planes of GO sheets. The interactions of the oxygen functional group between GO interlayers led to an increase in the D spacing value, while the θ value decreased. In other words, in the absence of the oxygen functional group, the θ value increases, while the D spacing value decreases.

3.2. Thermal Properties. Figure 3 shows the representative DSC curves of ABS, ABS/GO (dry mixing), and ABS/GO (solvent mixing) composite filaments. In general, the variation in the melting temperature (T_m) indicated the change in crystal structures of material. T_m of nanocomposites could be changed upon filler loading. ABS has no exact melting point because of its amorphous characteristic. However, no significant difference between T_g of the neat ABS filament and the ABS/GO composite filaments from both dry mixing and solvent mixing methods was found. The glass transition

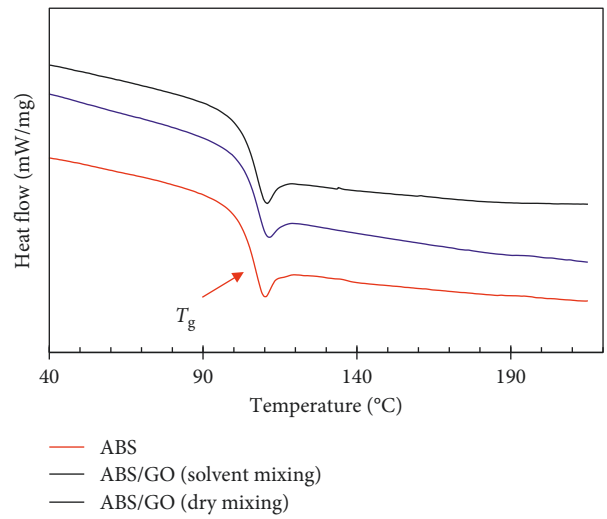

Figure 3: Melting temperature of the ABS filament, ABS/GO (solvent mixing), and ABS/GO (dry mixing) composite filaments from the DSC second heating scan.

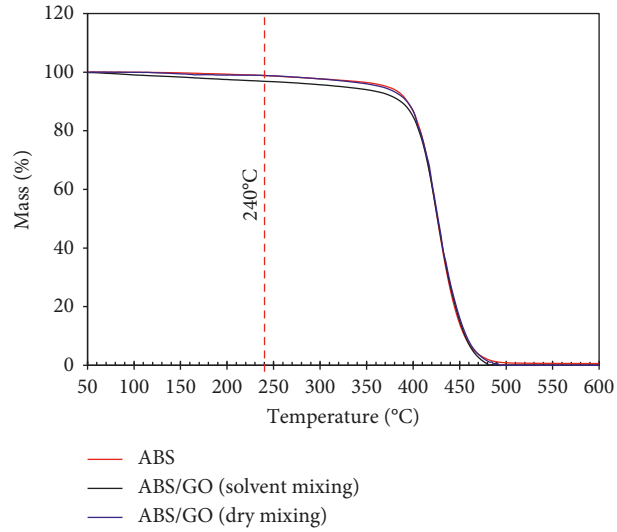

Figure 4: TGA thermogram of the ABS filament, ABS/GO (solvent mixing), and ABS/GO (dry mixing) composite filaments.

temperatures (T_g) were observed at 105.72°C, 104.77°C, and 105.69°C for ABS, ABS/GO (dry mixing), and ABS/GO (solvent mixing) filaments, respectively. The maintained T_g subsequently revealed the thermal stability of the ABS/GO composite even though the composite experienced the solvent system before the extrusion process. Furthermore, the ABS/GO composite could be softened and possibly 3D printed using the same temperature setup used for the pure and conventional ABS filaments.

3.3. Thermal Stability. To explore the effect of GO on thermal stability of the ABS and ABS/GO composite filaments, thermal gravimetric analysis (TGA) was conducted. Figure 4 shows the TGA thermogram of neat ABS and ABS/GO composite (2 wt.% GO) filaments. All materials

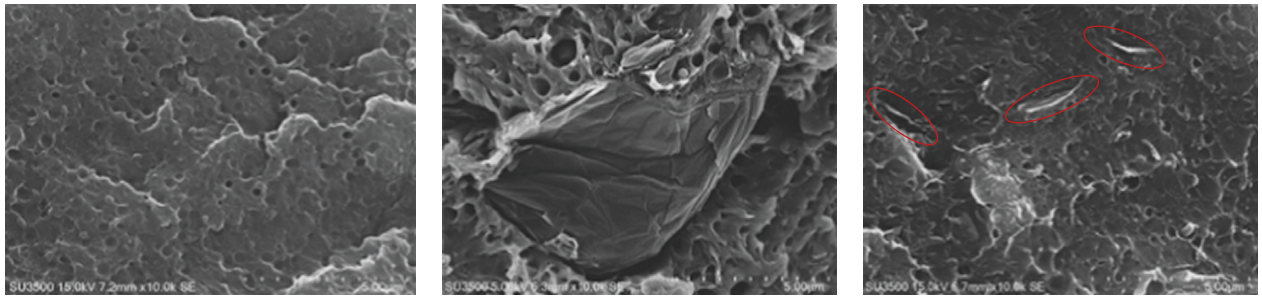

(a) (b) (c)

Figure 5: SEM images of (a) ABS, (b) ABS/GO (dry mixing), and (c) ABS/GO (solvent mixing) composite filaments.

started to decompose at the temperature around 400°C, which was higher than the typical temperature for 3D printing the conventional ABS filament (220–240°C). At 240°C, the highest temperature used for the 3D printing the conventional ABS filament, the ABS/GO (solvent mixing) showed a more mass drop (~3%) as compared to the pure ABS (~1.3%) and ABS/GO (dry mixing). These results could be due to the volatile compounds and the solvent molecules that might still be trapped in the composite filaments.

3.4. Morphology. The alternative performance of graphene-based nanofiller-reinforced composites depends on the dispersion and distribution of graphene-based materials in the polymer matrix and the interfacial bonding between these two phases [16]. The microstructures of the cryo-fractured sections of ABS, ABS/GO (dry mixing), and ABS/GO (solvent mixing) on cross section are shown in Figure 5. Pure ABS showed a denser microstructure, while ABS/GO demonstrated a higher-porous surface with the presence of dispersed GO flakes embedded in the ABS matrix.

For ABS/GO, GO flakes with the dimensions around 10 μm were noticed for the ABS/GO (dry mixing), while they ranged from 1–3 μm for the ABS/GO (solvent mixing). The smaller size and the more uniform distribution of GO were the critical keys for enhancing the mechanical behavior and for the thermal diffusivity of the composite.

3.5. Flowability. The flowability of the ABS/GO composite was investigated via the melt flow rate (MFR) measurement. The MFR represented the flowability of the material and was inversely proportional to its viscosity. It could be used to evaluate how the presence of GO affected the processability of the ABS/GO composite. As shown in Figure 6, the MFR values of both ABS and ABS/GO composite filaments increased with the temperatures, which meant the materials flew easier upon the temperature increased. The MFR values of the ABS/GO were lower than those of the pure ABS filament at all measured temperatures, which might be attributed to the solid GO flakes that restricted the mobility and disturbed the flowability of the ABS chains.

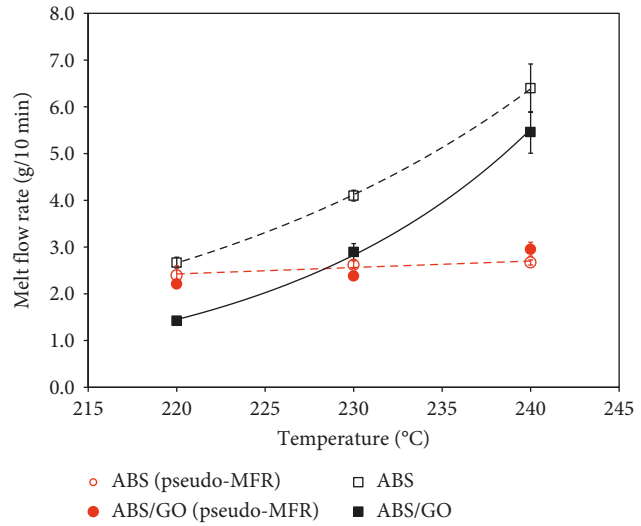

Figure 6: Melt flow rate (MFR) of the ABS filament and the ABS/GO composite filament dependent on temperature (220–240°C). Black color represents the results from the conventional MRF measurement, and red represents the results from the pseudo-MFR measurement using the 3D printer.

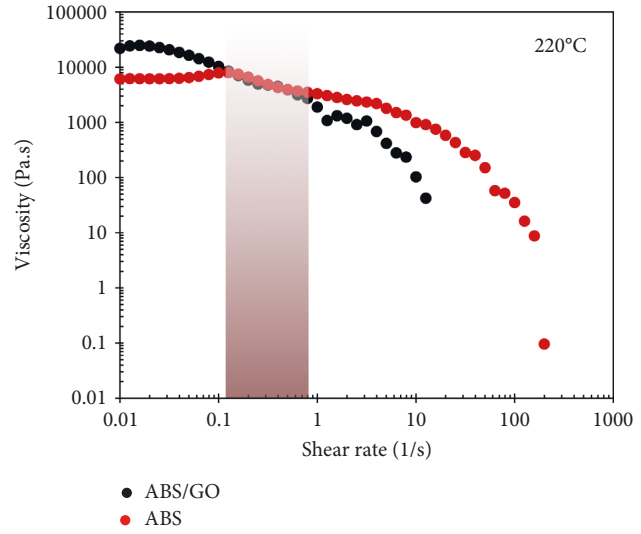

Figure 7: Shear rate dependence of viscosity for ABS and ABS/GO composite filaments.

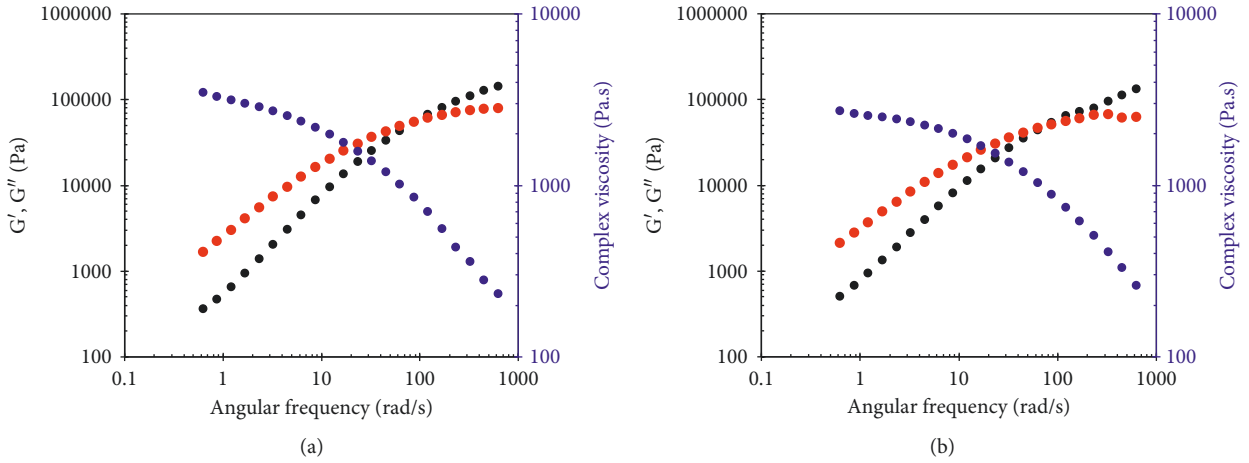

Figure 8: Rheological properties from the dynamic frequency sweep test: (a) ABS filament; (b) ABS/GO composite filament.

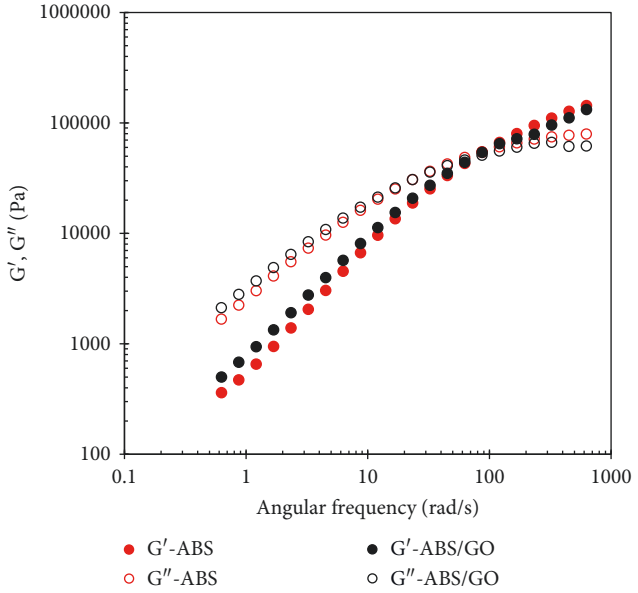

Figure 9: Storage modulus (G′) and loss modulus (G″) versus the angular frequency for ABS filament and ABS/GO composite filament.

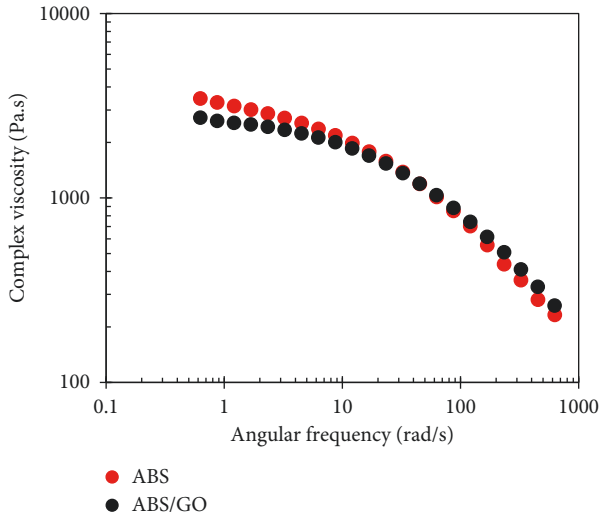

Figure 10: Complex viscosity versus the angular frequency for the ABS filament and the ABS/GO composite filament.

For FFF 3D printing processes, knowing the extrusion temperatures and flowability of the printed materials led to the more accuracy and precision of the printing process. The MFR information can be used as a guideline for setting up the printing parameters [24]. In this study, a pseudo-MFR measurement was conducted by measuring the extruded mass of the filaments through the printer nozzle. The pure ABS and ABS/GO filaments displayed clear plateau values at all temperatures (Figure 6). As a result, the edge of the plateau reflected the lower bound of acceptable temperature for the corresponded extrusion rate. Theoretically, below this temperature, the mass of polymer extruded cannot be accurately achieved at the given feed rate.

On the contrary, extruding at a higher temperature than the lower bound is undesirable since it would lead to slower solidification of the extruded bead on the printed part. It was

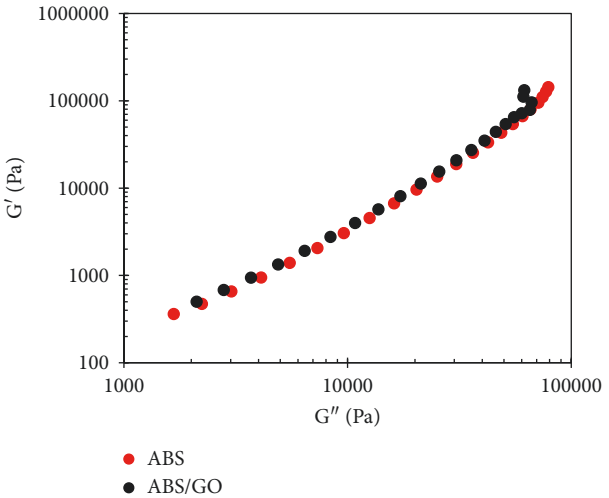

Figure 11: G′ versus G″ plot for (red) ABS filament and (black) ABS/GO composite filament.

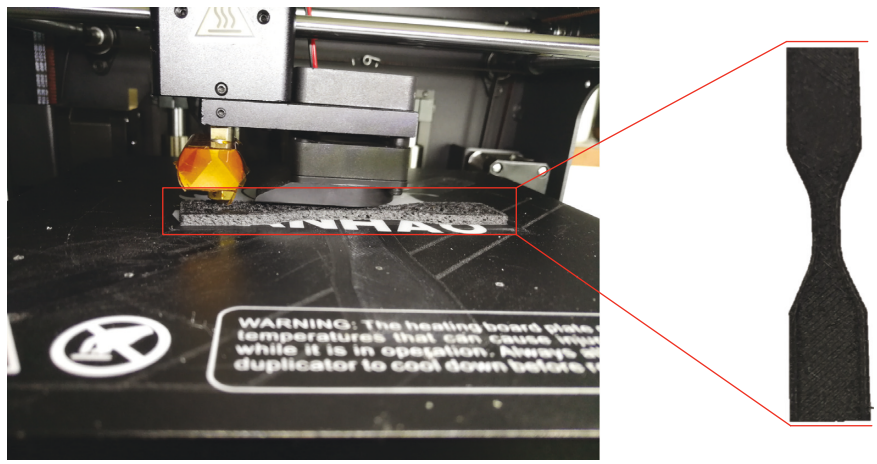

Figure 12: FFF 3D printed specimen from the ABS/GO composite filament.

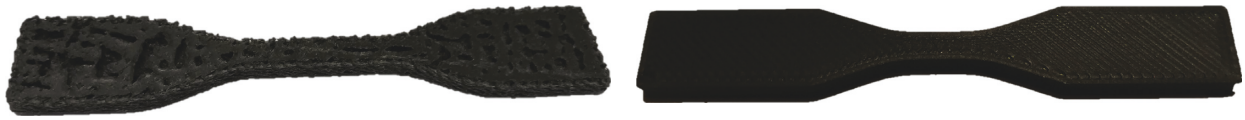

(a) (b)

Figure 13: FFF 3D printed specimen from (a) ABS/GO (dry mixing) and (b) ABS/GO (solvent mixing) composite filaments.

found that the ABS/GO composite filament exhibited the similar behavior as compared to the pure ABS. Thus, ABS/GO could be printed using the same temperature range (220–240°C) used for the pure or conventional ABS filaments.

3.6. Rheological Properties. The average shear rate in typical twin-screw extrusion ranges between 1 and 1,000 s^{-1} [25, 26]. For the FFF 3D printer, the shear rates in the nozzle are commonly in the range of 0.1–200 s^{-1} [27]. Figure 7 shows the shear rate dependence of viscosity for ABS and ABS/GO at 220°C. At the shear rate of 0.1 to 1 s^{-1}, ABS and ABS/GO filaments showed almost similar viscosity values, which confirmed that ABS/GO could be 3D printed with the same temperature setup for pure ABS. Incorporating with the MFR results, it was concluded that ABS/GO and pure ABS could be 3D printed using the same printing parameters (nozzle temperature and print speed).

Interfacial interaction between GO and ABS is a crucial role for enhancing the mechanical performance of the composite. Generally, the opposition between particle-particle interaction and particle-polymer interaction can be used to determine the particle dispersion or aggregation in nanocomposites. Thus, rheological behavior becomes a useful tool to evaluate the dispersion and distribution of the GO in ABS. Because the rheological behaviors deliver the relation between molecular structure and mesoscale properties (such as phase structure and filler dispersion), at the same time, providing the processing properties [28, 29]. From the dynamic frequency sweep measurements, it was noticed that the rheological behaviors of ABS and ABS/GO were almost similar as shown in Figures 8–10, respectively.

Figure 9 presents the storage and loss moduli of ABS and ABS/GO filaments. Only a small deviation of the G′ and G″ values was observed between ABS and ABS/GO filaments. Even though the increase in complex viscosities at low frequencies due to the effect of GO fillers was found, the complex viscosities of ABS and ABS/GO filament remained almost the same values at higher rates as shown in Figure 10. This is again confirmed that the GO loading did not affect the viscosity or flowability of the ABS.

Furthermore, we created the G′-G″ plot for predicting the dispersion of GO in ABS as presented in Figure 11. The G′-G″ patterns of pure ABS and ABS/GO were close together, suggested the well distribution of GO in the composite.

3.7. FFF 3D Printability. Figures 12 and 13 present the WANHAO Duplicator 6, the 3D printer based on the FFF principle, and the printed ABS/GO tensile specimens, respectively. With the same printing conditions used for pure ABS, the ABS/GO composite has been successfully printed. However, the clogged nozzle was sometimes observed, which further led to the print failure (Figure 13(a)).

3.9. Mechanical Properties. The tensile properties at the room temperature of ABS and ABS/GO were investigated and presented in Figure 14. From the typical stress-strain tensile curves and corresponding statistical data, the elongation at the break value decreased with the GO loading. The

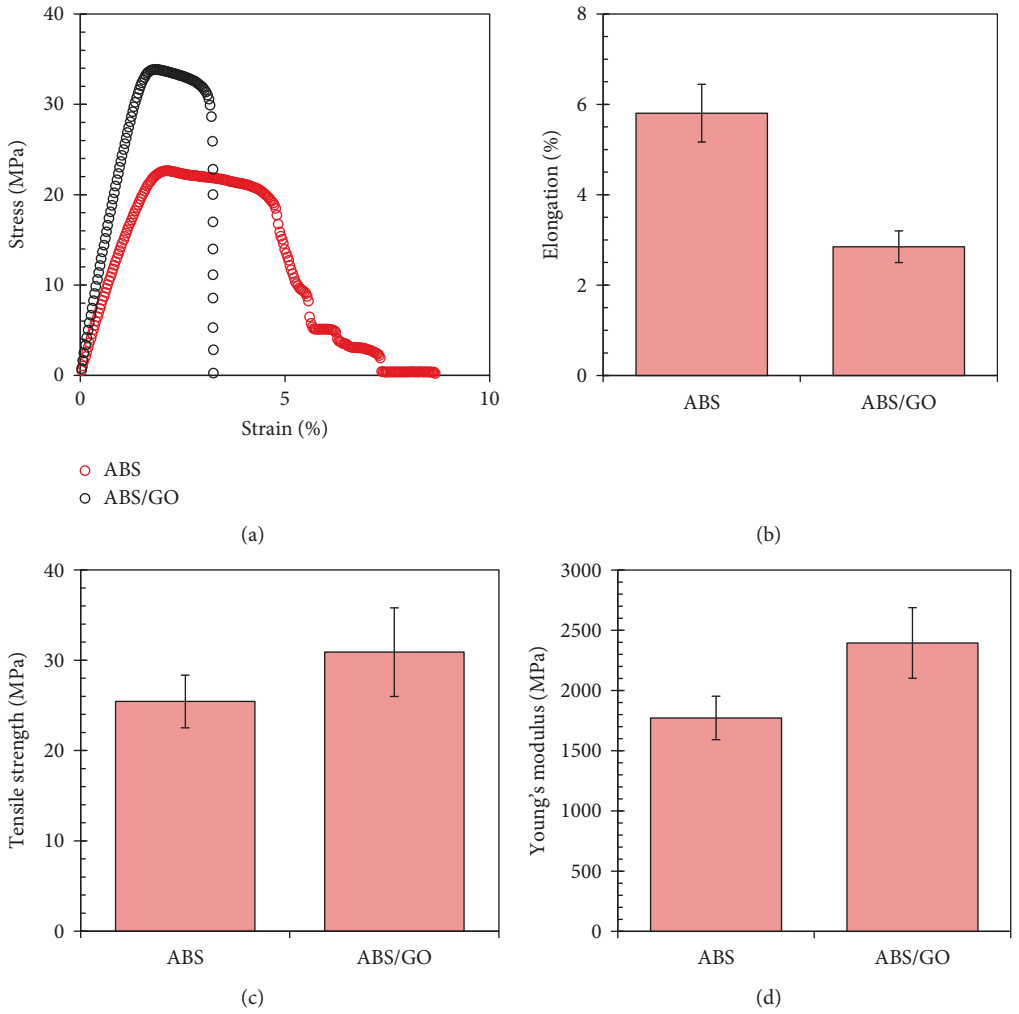

Figure 14: Typical stress-strain curves (a), value of elongation at break (b), tensile strength (c), and Young's modulus (d) of ABS and ABS/GO printed specimens.

elongation at the break value of pure ABS was determined as 5.8%, while the value of ABS/GO composite was 2.9%. However, by adding 2 wt.% GO, the tensile strength and Young's modulus of ABS were enhanced. This might be due to the interlayer crosslinks of GO sheets under loads, leading to the ordering of the hierarchical structures which results in the great significant enhancement of the mechanical properties [30].

4. Conclusion

A new 3D printing filament from ABS/GO composite was successfully prepared by solution mixing and followed by melted extrusion using a twin-screw extruder. The solvent system improved the GO dispersion capability in the ABS matrix and had no significant effect on the thermal properties of the ABS/GO composite. However, the aggregation of GO could lead to the die clogging and failure of the extrusion process. The tensile strength and Young's modulus of ABS were enhanced naturally by GO. Besides, the elongation at break decreased and needed to be further improved. Improving mechanical properties verified the feasibility of 3D printed ABS/GO for potential use in engineering applications.

Our study demonstrated one of the active attempts to print GO-based composite using FFF 3D printing process directly. However, the printed part quality, functionalities, and applications based on the printed ABS/GO composite needed to be further exploited.

Data Availability

The data used to support the findings of this study are available from the corresponding author upon request.

Conflicts of Interest

The authors declare that they have no conflicts of interest.

Acknowledgments

We thank Sami Briti from Polytech Montpellier, France, for helping in the preparation of graphene oxide (GO).

Additionally, we thankfully acknowledge the financial support from grants for Development of New Faculty Staff, Ratchadaphiseksomphot Endowment Fund, Chulalongkorn University, and the Thailand Research Fund (TRG6180009).

References

[1] S. Hertle, M. Drexler, and D. Drummer, "Additive manufacturing of poly(propylene) by means of melt extrusion," *Macromolecular Materials and Engineering*, vol. 301, no. 12, pp. 1482–1493, 2016.

[2] A. Bandyopadhyay, F. Janas, and R. Van Weeren, "Processing of piezocomposites by fused deposition technique," in *Proceedings of Tenth IEEE International Symposium on Applications of Ferroelectrics*, pp. 999–1002, East Brunswick, NJ, USA, August 1996.

[3] T. F. McNulty, F. Mohammadi, A. Bandyopadhyay, D. J. Shanefield, S. C. Danforth, and A. Safari, "Development of a binder formulation for fused deposition of ceramics," *Rapid Prototyping Journal*, vol. 4, no. 4, pp. 144–150, 1998.

[4] X. Wang, M. Jiang, Z. Zhou, J. Gou, and D. Hui, "3D printing of polymer matrix composites: a review and prospective," *Composites Part B: Engineering*, vol. 110, pp. 442–458, 2017.

[5] J. F. Christ, N. Aliheidari, A. Ameli, and P. Pötschke, "3D printed highly elastic strain sensors of multiwalled carbon nanotube/thermoplastic polyurethane nanocomposites," *Materials and Design*, vol. 131, pp. 394–401, 2017.

[6] J. Zhang, Y. Yang, F. Fu, F. You, X. Dong, and M. Dai, "2017_Zhang_resistivity and its anisotropy characterization of 3D printed acrylonitrile butadiene styrene copolymer-carbon black composites," *Applied Sciences*, vol. 7, no. 1, p. 20, 2017.

[7] R. Singh, G. Sandhu, R. Penna, and I. Farina, "Investigations for thermal and electrical conductivity of ABS-graphene blended prototypes," *Materials*, vol. 10, no. 8, p. 881, 2017.

[8] U. Kalsoom, P. N. Nesterenko, and B. Paull, "Recent developments in 3D printable composite materials," *RSC Advances*, vol. 6, no. 65, pp. 60355–60371, 2016.

[9] S. J. Kalita, S. Bose, H. L. Hosick, and A. Bandyopadhyay, "Development of controlled porosity polymer-ceramic composite scaffolds via fused deposition modeling," *Materials Science and Engineering: C*, vol. 23, no. 5, pp. 611–620, 2003.

[10] A. M. Pinto, J. Cabral, D. A. P. Tanaka, A. M. Mendes, and F. D. Magalhaes, "Effect of incorporation of graphene oxide and graphene nanoplatelets on mechanical and gas permeability properties of poly(lactic acid) films," *Polymer International*, vol. 62, no. 1, pp. 33–40, 2012.

[11] B. E. Yamamoto, A. Z. Trimble, B. Minei, and M. N. G. Nejhad, "Development of multifunctional nanocomposites with 3-D printing additive manufacturing and low grapene loading," *Journal of Thermoplastic Composite Materials*, pp. 1–26, 2018.

[12] H. Kim and C. W. Macosko, "Processing-property relationships of polycarbonate/graphene composites," *Polymer*, vol. 50, no. 15, pp. 3797–3809, 2009.

[13] X. Wei, D. Li, W. Jiang et al., "3D printable graphene composite," *Scientific Reports*, vol. 5, no. 1, pp. 1–7, 2015.

[14] C. Wang, Y. Li, G. Ding, X. Xie, and M. Jiang, "Preparation and characterization of graphene oxide/poly(vinyl alcohol) composite nanofibers via electrospinning," *Journal of Applied Polymer Science*, vol. 127, no. 4, pp. 3026–3032, 2013.

[15] X. Lin, X. Shen, Q. Zheng et al., "Fabrication of highly-aligned, conductive, and strong graphene," *ACS Nano*, vol. 6, no. 12, pp. 10708–10719, 2012.

[16] V. Panwar and K. Pal, "An optimal reduction technique for rGO/ABS composites having high-end dynamic properties based on Cole-Cole plot, degree of entanglement and C-factor," *Composites Part B: Engineering*, vol. 114, pp. 46–57, 2017.

[17] D. Zhang, B. Chi, B. Li et al., "Fabrication of highly conductive graphene flexible circuits by 3D printing," *Synthetic Metals*, vol. 217, pp. 79–86, 2016.

[18] S. Dul, L. Fambri, and A. Pegoretti, "Fused deposition modelling with ABS-graphene nanocomposites," *Composites Part A: Applied Science and Manufacturing*, vol. 85, pp. 181–191, 2016.

[19] V. Panwar and K. Pal, "Dynamic performance of an amorphous polymer composite under controlled loading of reduced graphene oxide based on entanglement of filler with polymer chains," *Journal of Polymer Research*, vol. 25, no. 2, 2018.

[20] S. Chen, J. Lu, and J. Feng, "3D-Printable ABS blends with improved scratch resistance and balanced mechanical performance," *Industrial and Engineering Chemistry Research*, vol. 57, no. 11, pp. 3923–3931, 2018.

[21] E. A. Papon and A. Haque, "Tensile properties, void contents, dispersion and fracture behaviour of 3D printed carbon nanofiber reinforced composites," *Journal of Reinforced Plastics and Composites*, vol. 37, no. 6, pp. 381–395, 2018.

[22] ASTM International, *ASTM D1238–13*, ASTM Int., West Conshohocken, PA, USA, 2013.

[23] American Society for Testing and Material (ASTM), *Standard Test Method for Tensile Properties of Plastics (D638-14)*, ASTM Int., West Conshohocken, PA, USA, 2014.

[24] T. Pfeifer, C. Koch, L. Van Hulle, G. A. M. Capote, and P. Natalie, "Optimization of the FDM additive manufacturing process," in *Proceedings of SPE ANTEC Indianapolis*, pp. 22–29, Indianapolis, IN, USA, May 2016.

[25] T. A. Osswald and N. Rudolph, *Polymer Rheology Fundamental and Applications*, Hanser Publishers, Munich, Germany, 2015.

[26] N. Venkataraman, S. Rangarajan, M. J. Matthewson et al., "Feedstock material property-process relationships in fused deposition of ceramics (FDC)," *Rapid Prototyping Journal*, vol. 6, no. 4, pp. 244–253, 2000.

[27] L. A. Al-Hariri, B. Leonhardt, M. Nowotarski, J. Magi, and K. Chambliss, *Carbon Nanotubes and Graphene as Additives in 3D Printing*, INTECH, London, UK, 2016.

[28] L. Du, M. Namvari, and F. J. Stadler, "Large amplitude oscillatory shear behavior of graphene derivative/polidimethylsiloxane nanocomposites," *Rheologica Acta*, vol. 57, no. 5, pp. 429–443, 2018.

[29] G. M. Shin, J. Y. Park, and Y. C. Kim, "GO dispersion and mechanical properties of 70PC/30ABS/GO composites according to fabrication methods," *Polymer Korea*, vol. 41, no. 3, pp. 452–459, 2017.

[30] R. Sharma, R. Singh, R. Penna, and F. Fraternali, "Investigations for mechanical properties of Hap, PVC and PP based 3D porous structures obtained through biocompatible FDM filaments," *Composites Part B: Engineering*, vol. 132, pp. 237–243, 2018.

eXPRESS Polymer Letters Vol.13, No.10 (2019) 898–909
Available online at www.expresspolymlett.com
https://doi.org/10.3144/expresspolymlett.2019.78

PP/organoclay nanocomposites for fused filament fabrication (FFF) 3D printing

C. Aumnate[*], *S. Limpanart, N. Soatthiyanon, S. Khunton*

Metallurgy and Materials Science Research Institute, Chulalongkorn University, Soi Chula 12, Phayathai Rd., Pathumwan, 10330 Bangkok, Thailand

Received 25 February 2019; accepted in revised form 23 May 2019

Abstract. 3D printing has attracted a lot of attention over the past three decades. In particular the Fuse Filament Fabrication (FFF) technique, general materials require low shrinkage during cooling and viscous behavior during extrusion through a nozzle. Semi-crystalline thermoplastics and their composites are of the relevance of new materials for 3D printing. However, the crystalline structures, for instance, may have a favorable impact on their printability. In this study, polypropylene/organoclay nanocomposites were prepared by melt extrusion using a twin-screw extruder. The effects of organoclay on the thermal, rheological and morphological properties were studied to evaluate the possibility of using the polypropylene/organoclay nanocomposites as the FFF 3D printing feedstock. Dioctadecyl dimethyl ammonium chloride (D18) was successfully used to modify the clay surfaces, providing a good dispersity and wettability of organoclay in the PP matrix.

Keywords: *polymer composites, polypropylene; organoclay, 3D printing, fused filament fabrication (FFF)*

1. Introduction

3D printing technologies have been introduced to serve the highly particular needs of model creating and rapid prototyping [1]. However, it has not gained enough vitality to be commercialized until recently. 3D printing becomes more affordable through a fused filament fabrication (FFF) process since it offers advantages, including low cost, high speed, and simplicity as compared to other 3D printing techniques. Another advantage is the potential of printing diverse materials simultaneously. Multiple extrusion nozzles with the loading of different materials can be set up in FFF printers, so printed parts can be multifunctional with designed composition [2, 3]. Conversely, one common drawback of FFF printing is that the composite materials have to be in a filament form to enable the extrusion process. It is difficult to disperse reinforcements homogeneously and remove the voids formed during the manufacturing of composite filaments. Thus, the usable material is limited to amorphous thermoplastic polymers with suitable melt viscosity to allow the good dispersion of the reinforcements. Also, the melt viscosity should be appropriate to provide structural support and low enough to enable extrusion. The general materials require low shrinkage during cooling and viscous behavior during extrusion through a nozzle. Therefore, this brings about the most exclusive use of amorphous thermoplastics in FFF. Thermoplastic polymer materials such as acrylonitrile butadiene styrene (ABS), polylactic acid (PLA), polyamide (PA) and polycarbonate (PC) could be processed by 3D printing technology. However, most of the 3D printed polymer products are still now used as conceptual prototypes rather than functional components, due to the intrinsically limited mechanical properties and functionalities of printed pure polymer parts. Accordingly, there is a critical need to develop printable polymer composites, including

[*]Corresponding author, e-mail: Chuanchom.a@chula.ac.th

high precision, cost-effective and customized geometry. Semi-crystalline thermoplastic is one of the new relevance materials for 3D printing. However, the crystalline structure, for example, may effect mechanical properties, chemical resistance positively and may have a favorable effect on the end-use properties for various applications [4, 5].

Nanocomposites are multiphase solid materials where one of the phases has a dimension of <100 nm. The nanofillers can be in various forms such as particles, sheets (exfoliated clay stacks) or fibers. Nanoclay is one of the most commonly used nanofiller in particular for the fuel tank and fuel line components for cars [6]. Polypropylene-based composites are generally used in automotive applications to manufacture the part that may need to involve the compressive impact loading under a wide range of temperatures such as bumpers [7].

Polypropylene (PP)/clay nanocomposites find applications where excellent mechanical properties, low permeability to gases or flame resistance are essential service specifications at low clay content [3, 5]. The development of PP/clay nanocomposites poses particular challenges because of the hydrophobicity of PP. Thus, the hydrophilic clays tend to form agglomerates during mixing with PP. This is due to the van der Waals attraction between clay particles. It is well-known that the dispersion of nanoclay in the polymer matrix depends on the surface peeling, followed by polymer chains diffusion into the nanoclay galleries [8]. The methods commonly employed to facilitate intercalation/exfoliation of the clay and maximize its interfacial contact with the polymer matrix include adding compatibilizers such as maleic anhydride grafted polymer; dimethyl maleate grafted polymer, as well as the surface modifications/treatments [6, 8–13]. This can significantly affect the matrix morphology and usually leads to proper clay intercalation instead of exfoliation [10, 11, 14]. Moreover, the cationic modification is commonly performed in an aqueous medium in which clay swell easily to produce organophilic clays. Among the methods, quaternary ammonium salts are frequently used. In such a case, the microstructural characterization concerning matrix morphology and clay dispersion, which affects the end properties of the composites, becomes crucial to understand. Melt compounding using twin-screw extruders allows the required high stress to break up the tactoid structure of the clays and to promote intercalation/exfoliation [15]. In addition, twin-screw extruders are widely used in industry, and the process is straightforward. Accordingly, thermal and rheological properties of the composites have attracted much interest [4, 15]. The properties of composites are dependent on different factors such as the size, shape and nature of the filler particles, interactions between their constituents, orientation, dispersion and distribution of the particles in the matrix and notably the filling level [16]. This study focuses on the development of polymer nanocomposite filaments for the FFF 3D printing process, using PP and organoclay. The typical melt extrusion process used in polymer processing technologies is performed to prepare the PP/organoclay nanocomposites. The thermal, rheological, morphological and tensile properties of the nanocomposites are investigated to evaluate a possibility of using PP/organoclay composites as FFF 3D printing feedstock. Such PP/organocomposites may have applications in structural, electrical/electronic and automotive fields.

2. Experimental

2.1. Materials

Sodium-bentonite clay was supplied by Thai Nippon Chemical Co. Ltd., Thailand. The surfactant used in this study was a mixture of dioctadecyl dimethyl ammonium chloride salts with alkyl chain length of 14 (4%), 16 (32%), and 18 (58%), which will be referred to as D18 throughout the study. The surfactant was purchased from Thai Specialty Chemical Co., Ltd., Thailand. Polypropylene (PP) powder (MFI = 19.8 g/10 min) was obtained from HMC Polymer co., Ltd., Thailand.

2.2. Organoclay preparation

400 g of Na-bentonite were added to 20 ml of deionized water and stirred vigorously for 3 h. Various amounts of D18 were then added in portions (Table 1) as coupling agent. The reaction mixture was heated at 70 °C for 1 h. The mixture suspension was finally filtered, washed and dried at 80 °C for at least 12 h and then ground to fine powder.

Table 1. Organoclay modified with different D18 concentrations.

Organoclay	Dioctadecyl dimethyl ammonium chloride (D18) [mmol/g Clay]
BAD05	0.50
BAD10	0.10
BAD15	0.15

2.3. PP/organoclay composites preparation

Polypropylene (PP) pellets were ground into powder form. PP powder with 30 wt% of organoclay (Table 1) was extruded first as a master batch using a co-rotating twin-screw extruder. The extrusion temperature profiles ramped from 180 up to 220 °C (from the hopper to the die). The amount of the organoclay used in all the nanocomposites was kept constant as 3 wt% concerning total PP, according to the good mechanical performance improvement resulting from our previous study [17]. Thus, the PP/organoclay master batch was then diluted to obtain 3 wt% of organoclay using the same melt extrusion parameters.

2.4. Characterization

2.4.1. X-ray diffraction (XRD)

The X-ray diffraction (XRD) of organoclay was performed using an X-ray diffractometer (Bruker AXS Model D8 Discover). All samples were scanned over the range $2\theta = 2–10°$ and the measurements were recorded at every 0.02° interval.

2.4.2. Differential scanning calorimetry

The measurements were carried out using a DSC 3500 Sirius, under nitrogen atmosphere. The samples were heated from room temperature to 280 °C. After an isothermal step for 2 min, the samples were cooled down to 30 °C and finally heated up to 280 °C after another isothermal step for 2 min. Scanning temperature ramps of 10 K/min were used for all dynamic steps. A heat of fusion for a 100% crystalline PP of 205 J/g [4] was used to calculate the degree of crystallization. For isothermal analysis, all materials were quenched from 230 °C to an isothermal temperature (125 °C).

2.4.3. Rheology test

First, dynamic strain sweep tests were performed using a rheometer (Germini 2000, TA instrument) equipped with 25 mm diameter parallel plates. The dynamic strain sweep test was conducted from the strain values of 0.1–100% with the frequency of 0.628 rad/s to investigate the linear regime for all samples. After that, the linear viscoelasticity responses of the materials were measured with the frequency sweep tests between 0.628 and 628 rad/s at a temperature of 210 °C. A constant strain of 2% (which is in the linear regime for all samples) was used, and the gap between the two plates was set to 1 mm. After applying the Cox-Merz rule, the complex viscosity could be determined as a function of the shear rate.

2.4.4. Scanning electron microscopy (SEM)

For the examination of the organoclay dispersion in the PP matrix, the PP/organoclay nanocomposite filaments were mounted in resin. They were then metallographically ground using emery paper and polished on diamond pads. The samples were examined using a JEOL JSM-IT500HR scanning electron microscope (SEM) at an accelerating voltage of 10 kV. For imaging, backscattered electrons were used to enhance the contrast of the specimen images, compared with secondary electrons.

Furthermore, the cryo-fracture surfaces of the PP/organoclay nanocomposite filament were also studied using a Hitachi SU3500 scanning electron microscope at an accelerating voltage of 15 kV. Prior to investigation, all samples were sputter coated with gold.

2.4.5. Transmission electron microscopy (TEM)

All PP/organoclay nanocomposite samples were investigated using the transmission electron microscope (TEM), (JEOL 2010 with an acceleration voltage of 200 kV) to verify the dispersion of organoclay in the PP matrix. The PP/organoclay nanocomposite filaments were prepared as a 90 nm thick slice using a microtome with a diamond knife in liquid nitrogen. The slices were then imaged in the TEM.

2.4.6. Tensile tests

To obtain the mechanical properties, the tensile tests were carried out according to ASTM D638 [18]. The specimens were printed based on Type-V geometry. The crosshead speed was set to 5 mm/min. Ultimate tensile strength; Young's modulus and elongation at break were evaluated as an average value of at least five replicates.

3. Results and discussion

3.1. X-ray diffraction

The XRD analysis allows estimating the distance between the clay layers according to Bragg's law [15] as shown in Equation (1):

$$2d\sin\theta = n\lambda \tag{1}$$

where d represents the spacing between diffraction lattice planes, θ is the diffraction angle of the beam

on these planes, n is a positive integer representing the diffraction order, and λ corresponds to the wavelength of the X-ray radiation used in the diffraction experiment. Based on the interaction force of the polymer/organoclay, three types of nanocomposite morphologies could be generated, including intercalation, exfoliation and phase-separation.

The intercalated morphology resulted in a displacement of the peaks associated with the basal distance toward angles' lower values, corresponding to a distance between the most critical sheets. Exfoliated morphology resulted in the absence of diffraction peak because of a much too large spacing between the layers, or the nanocomposite does not present ordering anymore [19, 20].

Figure 1 presents the XRD patterns of the unmodified clay, organoclay modified with different D18 contents as well as PP and PP/organoclay nanocomposites, respectively, from the region of 2θ between 2 to 10°. For the clay modified with the series of different D18 loading, the peak intensity was increased with increasing the D18 content. Besides, the peaks tended to shift toward the lower angle values (see Figure 1a). These results indicated that there exists a difference in the clay microstructure after organically modified the clay surface with D18. The similar results were also found in the case of the PP/organoclay nanocomposites as depicted in Figure 1b. There was no peak observed for the neat PP observed in the interesting region. For the PP/organoclay composites,

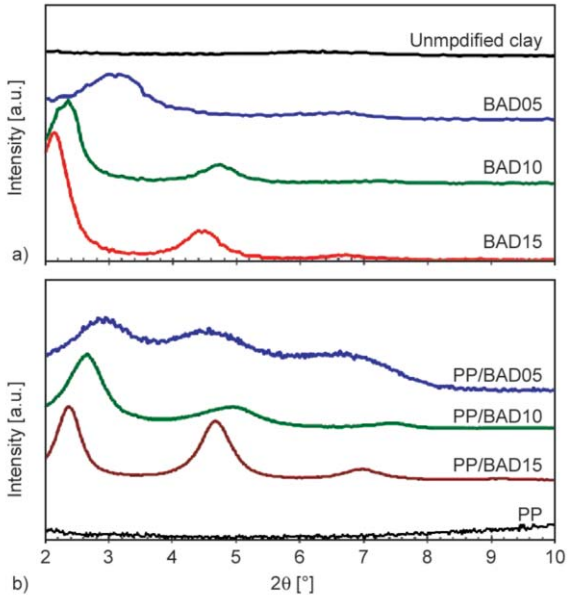

Figure 1. XRD patterns of (a) unmodified clay and organoclay modified with different D18 contents and (b) neat PP and PP/organoclay nanocomposites.

the examined diffraction peaks shifted toward lower angle values as the D18 contents increased. The peak of PP/BAD05 observed at the 2θ value of 3.0°, corresponded to 37.2 Å d-spacing. With increasing the D18 contents, the broader distribution of the d-spacing value was also observed. The d-spacing values were 33.3 Å (2θ = 2.7°) and 29.8 Å (2θ = 2.4°) for for PP/BAD10 and PP/ BAD15, respectively. PP is nonpolar and does not interact perfectly with clay platelets. However, due to the high shear during the melt extrusion process as well as the addition of the coupling agent, the combination of intercalation and exfoliation could be achieved in the composites despite the non-polarity of PP. The lower angle values revealed intercalation while the larger d-spacing values suggested exfoliation developed in the PP/organoclay nanocomposites, which allowed peeling of the clay platlets.

From our previous study, the D18 molecules can be either packed as an island of interdigitating monolayers or an island of highly tilted bilayers on the clay surface, leading to the increase in d-spacing value [17]. For the small loading of D18 (PP/BAD05), even though the stacking of the organoclay has not completely disappeared, the peaks have slightly broadened. It is possible that the clay surface has not yet fully covered with the D18 molecules, leaving the empty space around the island where the hydrate water-Na^+ is located, resulting in a less ordered structure.

3.2. Thermal properties

In FFF 3D printing, temperatures of the nozzle are crucial parameters to print the composite filaments without major structural flaws smoothly. Thus, thermal properties of such composite filament were carefully assessed with standard techniques, differential scanning calorimetry (DSC). The printable materials need to be heated above the glass transition temperature (T_g) or the melting temperature (T_m) to get softened the composites. However, if the temperature is set too high, it could degrade the polymer ingredients. Therefore, before 3D printing, T_g or T_m of the materials is the first and most vital parameter to be determined.

Figure 2 shows the representative DSC curves of the PP and the PP/organoclay nanocomposites. In general, the variation in the melting temperature (T_m) indicates the change of crystal structures of material. The T_m of nanocomposites could be changed upon

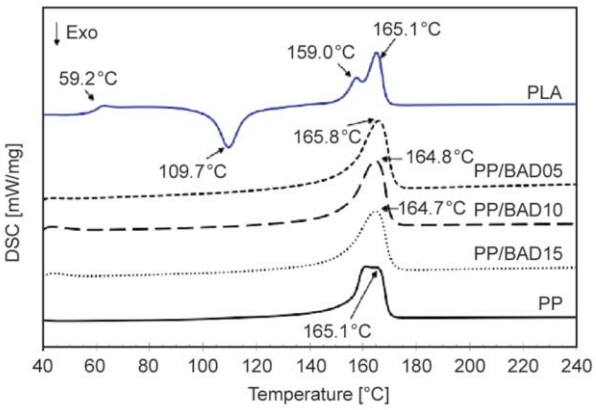

Figure 2. Melting temperatures of PP and PP/organoclay nanocomposites in comparison with PLA, the conventional material used for FFF 3D printing.

filler loading. However, there is no significant difference between Tm for the PP and the PP/organoclay nanocomposites. Since the amount of organoclay loading in all of the PP/organoclay nanocomposites in this study were kept constant at 3wt%, this justified that the concentration of D18 does not considerably affect the thermal stability of the PP.

A relatively broad melting peak at 165 °C is characteristic of the α-phase of iPP [21]. In comparison with the conventional PLA filament, the PP and the PP/organoclay nanocomposites could be softened at the nearly same temperature (T_m ~165 °C). It could be implied that the PP and the PP nanocomposites could be possibly 3D printed using the same temperature setup for the conventional PLA filament. Hence, the developed PP and PP/organoclay nanocomposite filaments can be 3D printed using the conventional FDM 3D printers.

Figure 3 shows the crystallization temperature (T_c) for the PP and the PP/organoclay nanocomposites. The

Table 2. Differential scanning calorimetry results of neat PP and PP/organoclay nanocomposites.

Samples	T_m [°C]	T_c [°C]	X_c^* [%]	$T_{m\,(start)}$ [°C]	$T_{c\,(start)}$ [°C]	ΔH_c [J/g]	ΔH_m [J/g]
PP	165.1	110.8	46.8	155.4	114.9	99.4	96.0
PP/BAD05	165.8	118.9	35.6	154.4	122.8	73.0	73.0
PP/BAD10	164.8	114.4	33.4	153.6	118.8	69.6	68.4
PP/BAD15	164.7	113.9	30.0	152.5	118.9	58.6	61.6

*Heat of fusion, ΔH_m for 100% crystalline PP = 205.0 J/g [18].

crystallization temperatures of all the PP/organoclay nanocomposites were found to be higher than that of pure PP. The PP/BAD10 and PP/BAD15 presented a nearly similar crystallization behavior whereas the PP/BAD05 showed the highest crystallization temperature. The shifts of both the onset and peak toward higher temperatures for all the PP/organoclay nanocomposites were observed as compared to pure PP. This clearly illustrates that the crystallization of PP significantly affected by both the presence of D18 and the clay. These effects on the crystallization were in agreement with the importance of the spherulite size reduction. Organoclay acted as nucleating sites and induced crystallization of the PP matrix. The degree of crystallization for materials with short molecules was high since they could crystallize faster and more accessible [22]. As shown in Table 2, the degree of crystallinity decreased with increasing the D18 content. The addition of D18 delayed the crystallization process as shown in Figure 4.

When the higher content of D18 was added into the nanocomposites, the crystallization behavior tended to be much more similar to the PP, in agreement again with the weaker reductions in spherulite size compared to the pure PP. However, for the small

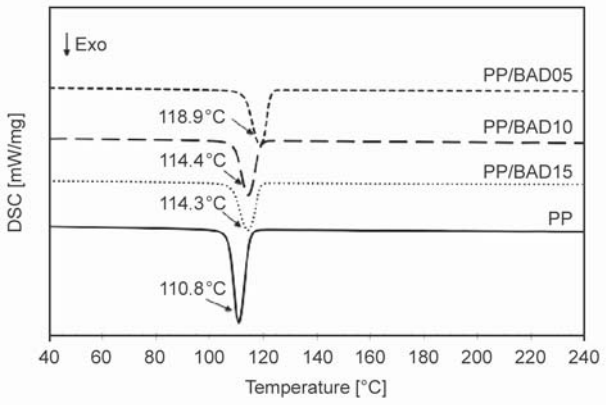

Figure 3. Crystallization temperature of PP and its composites; PP/BAD05, PP/BAD10 and PP/BAD15.

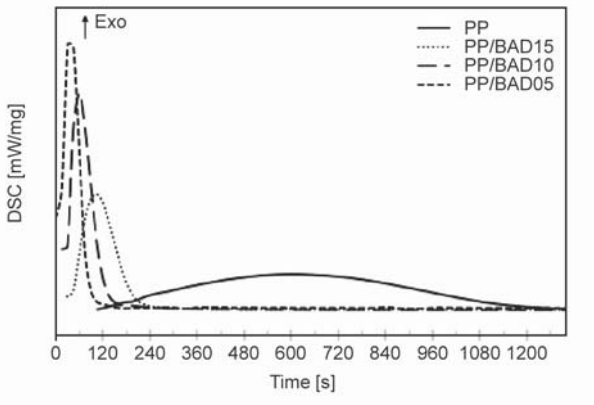

Figure 4. Isothermal segments of the crystallization process at 125 °C of PP its composites; PP/BAD05, PP/BAD10 and PP/BAD15.

amount of D18 (PP/BAD05), the significant shift of T_m to the higher temperature was observed, indicating the substantial reduction in spherulite size as well as the faster crystallization of the composite. These results thus suggested that the amount of D18 played an essential role in the crystallization behavior and also the degree of crystallinity. Furthermore, the enthalpy tended to drop with an increase in D18 content. This phenomenon may be also attributed to a decrease of the thermodynamically stable alpha phase content in favor of a mesomorphic structure [23].

3.3. Rheological behaviors

The viscosity of the polymer melt usually plays an important role in the processability of materials. Understanding rheological properties is of great importance to achieve an overview of the material's structures and also the determination of processing conditions for real polymer processing, such as extrusion and injection molding. The crucial challenge is to find the optimum balance between improvements in properties, at the same time being able to process the materials. Polymer composites are mainly processed under high temperatures and high shear rates. There are several drawbacks resulted from mixing hard particles with polymers, principally due to the considerable difference in densities. Adding solid particles into a molten polymer changes the viscoelastic behavior, the viscosity and the elasticity of the system.

The dynamic strain sweep test was first applied to the neat PP and PP/organoclay nanocomposites to determine the linear viscoelastic region. Figure 5 presents the storage modulus (G'), which is a sensitive rheological function related to the structural changes of the nanocomposites [12]. Storage modulus (G') of all samples exhibits a linear region (Newtonian plateau) at low strain and the non-linear region at high strain amplitudes. The addition of organoclay increased the plateau modulus. The transition point, which appeared at the deviation region from the linear to non-linear viscoelastic behavior, is defined as a critical strain (γ_c). It was observed that the critical strain (γ_c) for the PP/organoclay nanocomposites varies with the D18 content. However, at the strain less than 10%, all samples exhibit linear viscoelastic behavior. Therefore, all further rheological measurements in this study were done in the linear regime at 2% strain.

Frequency sweep tests for the PP/organoclay nanocomposites in the linear viscoelastic domain are shown in Figure 6. The storage modulus (G') was increased by the incorporation of the organoclay into the PP matrix. The enhancement in the dynamic modulus was significant, in particular, at low frequencies regime. Also, G' becomes nearly independent on the frequency at low frequencies, which is an evidence of the exfoliation or partial exfoliation [11]. It can be explained that the diffusion of the organoclay molecules is favored by making the galleries chemically compatible with the PP matrix. The compatibility occurs by exchanging interlayers inorganic clay cations with D18 cations. Therefore, layer distance (gallery distance) of organoclay increases due to the modifier. With the same loading of organoclay, G' value is molder with higher D18 content. This reflects the less effective development of the physical interaction between the PP chains and the layer of organoclay at higher D18 content.

Figure 7 shows the variation of the complex viscosity for the neat PP, PP/BAD05, PP/BAD10, and PP/BAD15 nanocomposites. It was well established that

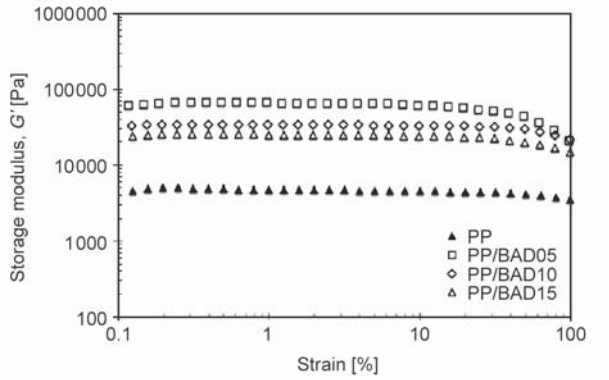

Figure 5. Storage modulus (G') versus strain (γ) curves for neat PP and its organoclay nanocomposites at the temperature of 230 °C.

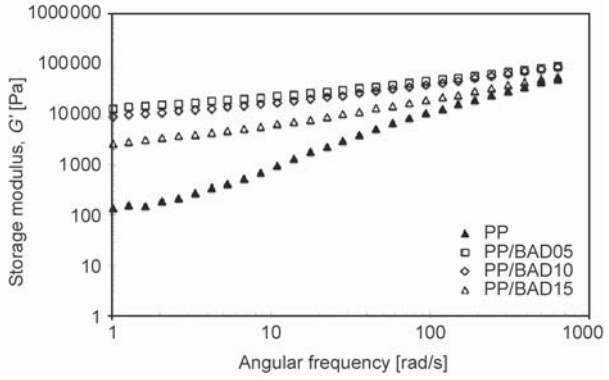

Figure 6. Frequency variations of the storage modulus, G' curves for neat PP and its organoclay nanocomposites at the temperature of 230 °C.

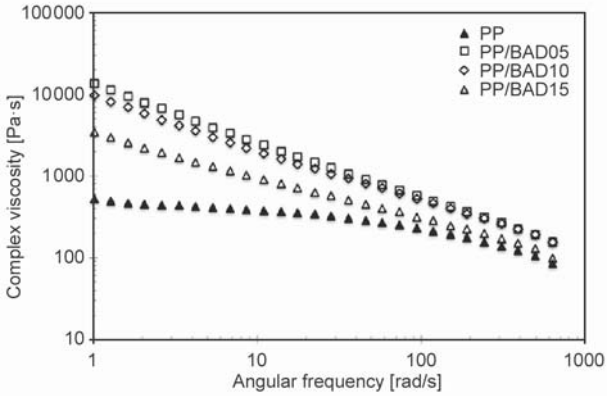

Figure 7. Complex viscosity curves for neat PP and its organoclay nanocomposites at the temperature of 230 °C.

the addition of nanofillers into the polymer matrix increased the viscosity of the system. When solid particles were added into a polymer matrix, they might disturb the flow lines and restricted the mobility of the polymer chains. The increase of the viscosity values also proves the physical network-like structure developed in the PP/organoclay nanocomposites. Furthermore, it should be noted that all the PP/organoclay nanocomposites exhibited shear-thinning behavior for the complex viscosity without any plateau region at low frequencies. Pronounced shear thinning has also been reflected the nanodispersion which is another evidence of the exfoliation morphology [11].

Also, by applying the Cox-Merz rule, Figure 8 presents the shear viscosity of the PP and its nanocomposites. The average shear rate in the typical co-rotating twin-screw ranges between 1 and 1000 s^{-1} [24]. For the FFF 3D printer, the relatively low shear rate is expected near the liquefier entrance and the print nozzle. Shear rates in the nozzle are commonly in the range of 100–200 s^{-1} [25]. Table 3 illustrates the

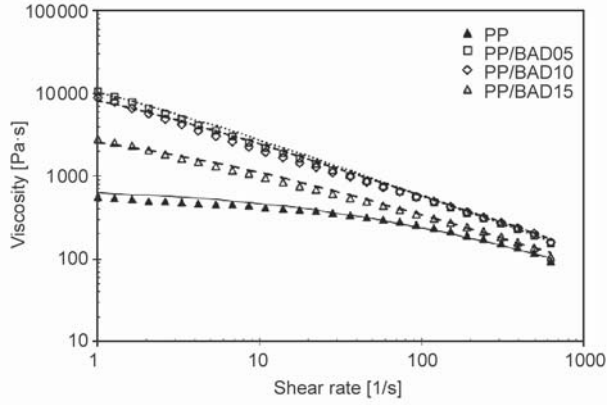

Figure 8. Shear viscosity (applied Cox-Merz rule) curves for neat PP and its organoclay nanocomposites at the temperature of 230 °C.

Table 3. Shear thinning exponent and viscosities of neat PP and PP/organoclay composites.

Samples	η at 100 s^{-1}	η at 200 s^{-1}	η at 1000 s^{-1}
PP	235.56	176.42	80.73
PP/BAD05	581.77	360.43	117.64
PP/BAD10	578.87	369.49	128.98
PP/BAD15	339.90	230.17	90.50

viscosities of the PP and the PP/organoclay nanocomposites at the shear rate of 100, 200 and 1000 s^{-1}. As expected, PP/BAD15, the nanocomposites with the highest degree of D18 loading displayed the lowest viscosity among the PP/organoclay nanocomposites at all shear rates. This can be attributed to the effect of the shorter molecule of D18, which flow easier than the longer molecules, PP. Addition of D18 led to the improvement of the flowability of the nanocomposites. However, incorporating with the G' and XRD results, the capability of the exfoliation and intercalation of the PP/organoclay nanocomposites could be improved by modifying clay with the coupling agent, D18. The less amount of D18 resulted in the higher degree of exfoliation/intercalation.

Figure 9 shows a Cole-Cole plot of the storage modulus G' versus the loss modulus G'' for the neat PP and its organoclay nanocomposites at 230 °C. It was proposed that the logG'-logG'' should be similar if the microstructure does not alter [26]. The logG'-logG'' curve can also be used to elucidate structure differences of polymer materials at a fixed conditions such as a fixed temperature. The increase of G' at a given G'' indicated that the microstructure of the composites changed significantly with the addition of organoclay. Also, the organoclay modified with higher

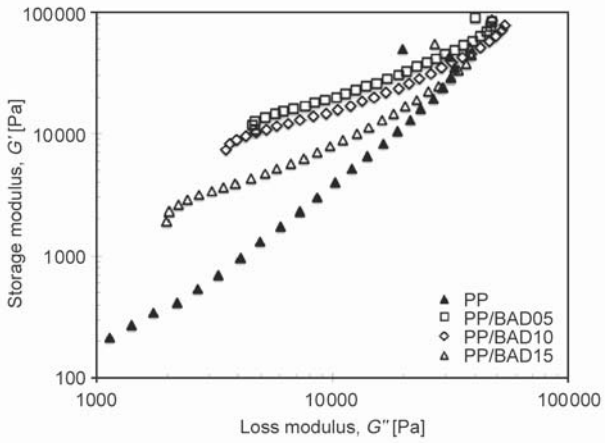

Figure 9. Storage modulus (G') as a function of loss modulus (G'') of neat PP and its organoclay nanocomposites at the temperature of 230 °C.

D18 content resulted in the less structural deviation as compared to the neat PP.

3.4. Morphology

The homogeneity of organoclay dispersion directly affected the composite's printing ability and other physical properties. The dispersion of organoclay in the PP matrix was investigated via the polished surfaces of the PP/organoclay composites as shown in Figure 10. It is seen that the smaller size of the organoclay is found for the case of more substantial D18 loading content.

Figure 11 shows the SEM images for fracture surface of the PP/clay composites filaments. With low D18 content, the PP/BAD05, the matrix coverage was not sufficient. It can be seen from many voids appeared as some evidences of the organoclay pull-out from the PP matrix. This indicated the weak interfacial bonding between the organoclay and the PP matrix. With increasing the D18 content, the matrix coverage was improved. This could be explained by the fact that the high mobility of the low molecular weight coupling agent, D18, allowed the PP matrix to interact actively with a large number of clay platelets during compounding.

The morphology of the PP/organoclay nanocomposites reported in this section were in good agreement with the rheological properties, confirming the capability of dispersion as well as the consequent formation of interfacial adhesion between the modified clay and the PP matrix.

3.5. 3D printing optimization

3.5.1. Nozzle temperature

For FFF 3D printing, with the extrusion temperature known, the accuracy of machine's motions can be explored [27, 28]. Figure 12 shows the extruded mass as a function of temperature for the PP/BAD05 in comparison with the conventional PLA filament.

Both materials tended to display a plateau at the temperatures higher than 220 °C. The edge of the plateau region is considered the lower bound of acceptable

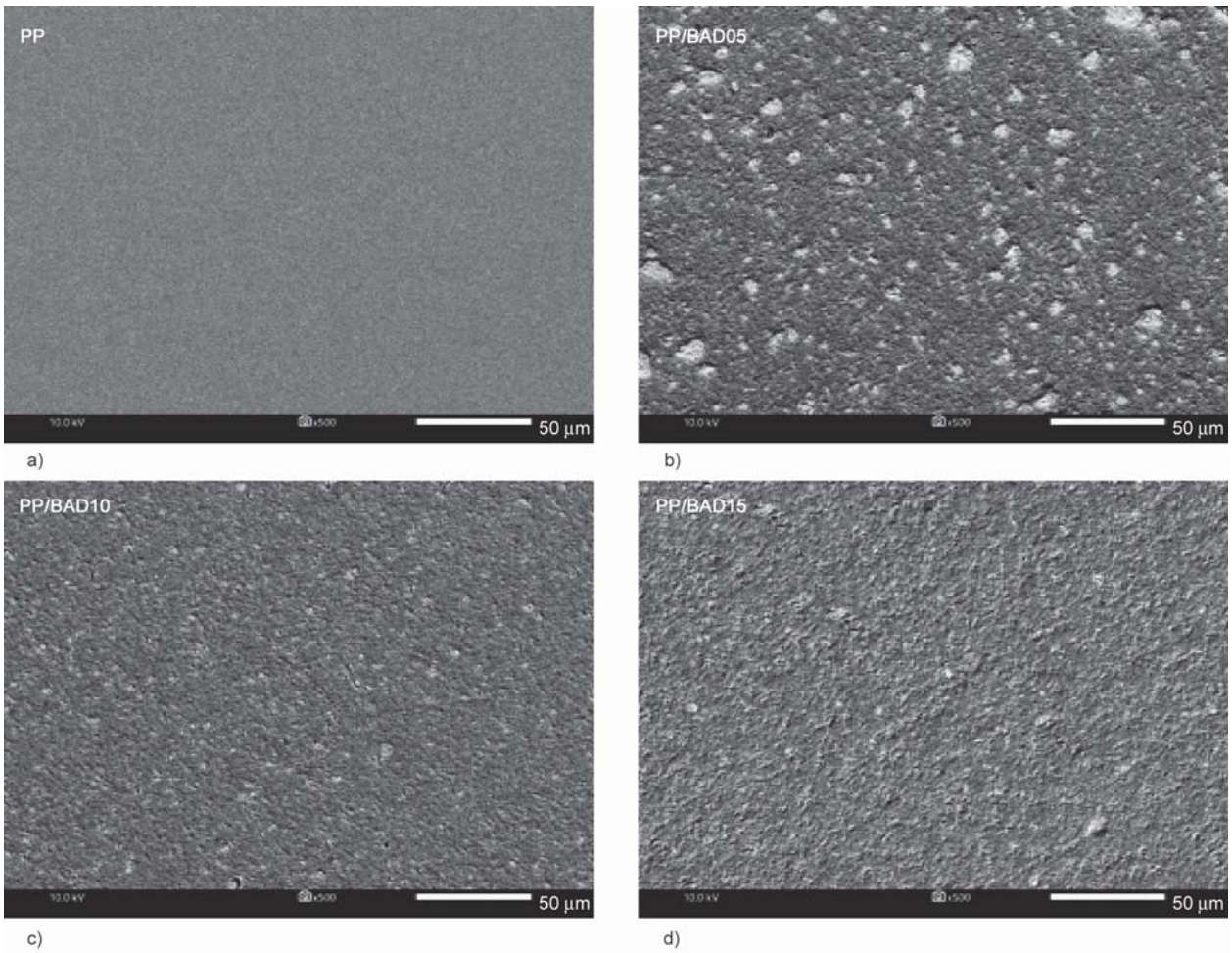

Figure 10. SEM images of polished surfaces for neat PP and its organoclay nanocomposites at 500× magnification. a) PP, b) PP/BAD05, c) PP/BAD10, d) PP/BAD15.

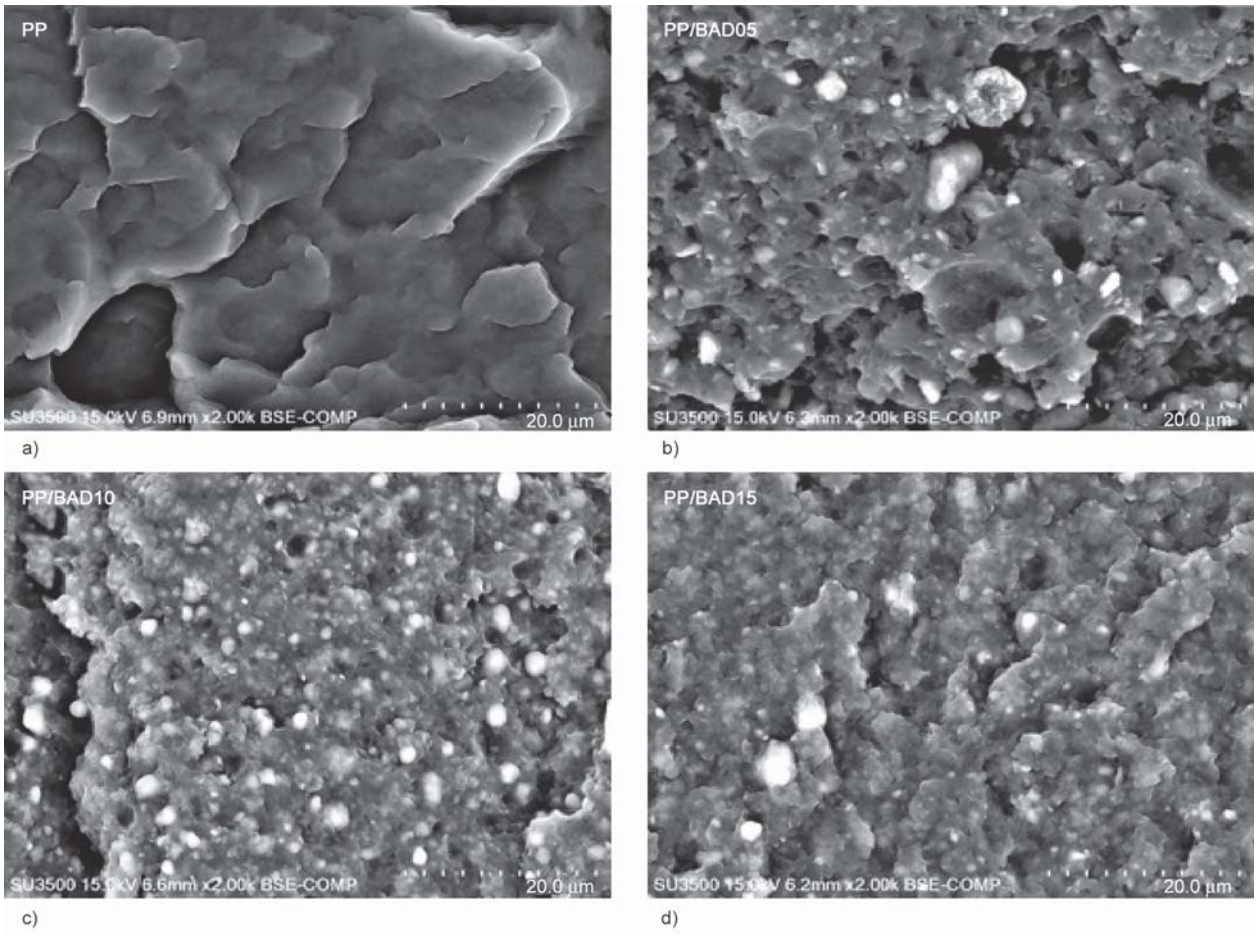

Figure 11. SEM images of fracture surfaces for neat PP and its organoclay nanocomposites at 2000× magnification. a) PP, b) PP/BAD05, c) PP/BAD10, d) PP/BAD15.

temperatures for the extrusion rate. Below this temperature, the theoretical amount of polymer extruded cannot be accurately achieved at the given feed rate. Furthermore, extruding at the higher temperature than this lower bound would cause the slower solidification of the extruded bead on the printed part. From the results, it could be concluded that PP/BAD05 could be 3D printed at the temperature range of 220–240 °C.

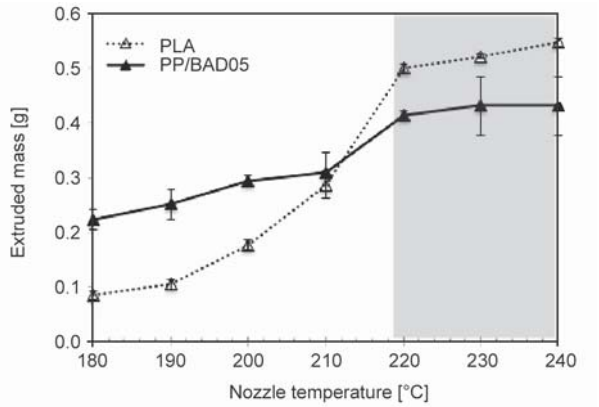

Figure 12. Extruded mass as a function of nozzle temperatures for PP/BAD05 and PLA filaments.

3.5.2. Tensile properties

In this study, an open source 3D printer, WANHAO Duplicator 6, was used to 3D print the tensile test specimens based on ASTM D638-14 [18]. It is noted that all prepared PP/organoclay nanocomposites can be 3D printed using the same printing parameters listed in Table 4. However, the neat PP cannot be successfully 3D printed because of its semi-crystalline characteristic, which leads to the high shrinkage and warpage during printing.

The tensile properties at room temperature of the PP/BAD05 and PP/BAD15 were shown in Figure 13.

Table 4. Parameters used for 3D printing of PP/organoclay nanocomposites.

Parameters		Value
Print nozzle diameter	[mm]	0.4
Nozzle temperature	[°C]	220
Bed temperature	[°C]	110
Layer height	[mm]	0.2
Print infill	[%]	30
Print speed	[mm·s^{-1}]	20

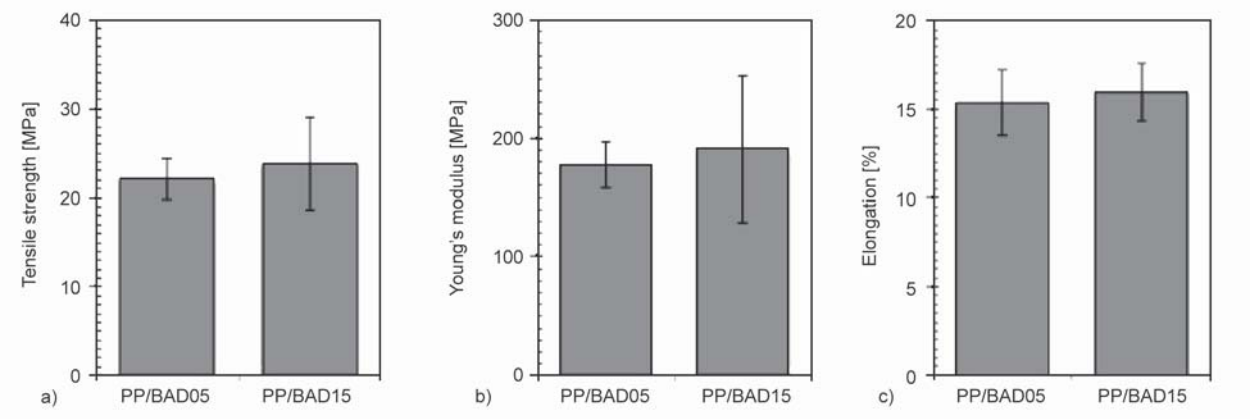

Figure 13. Tensile strength, Young's modulus and Elongation at break of PP/BAD05 and PP/BAD15 printed specimens. a) Tensile strength, b) Young's modulus, c) elongation at break.

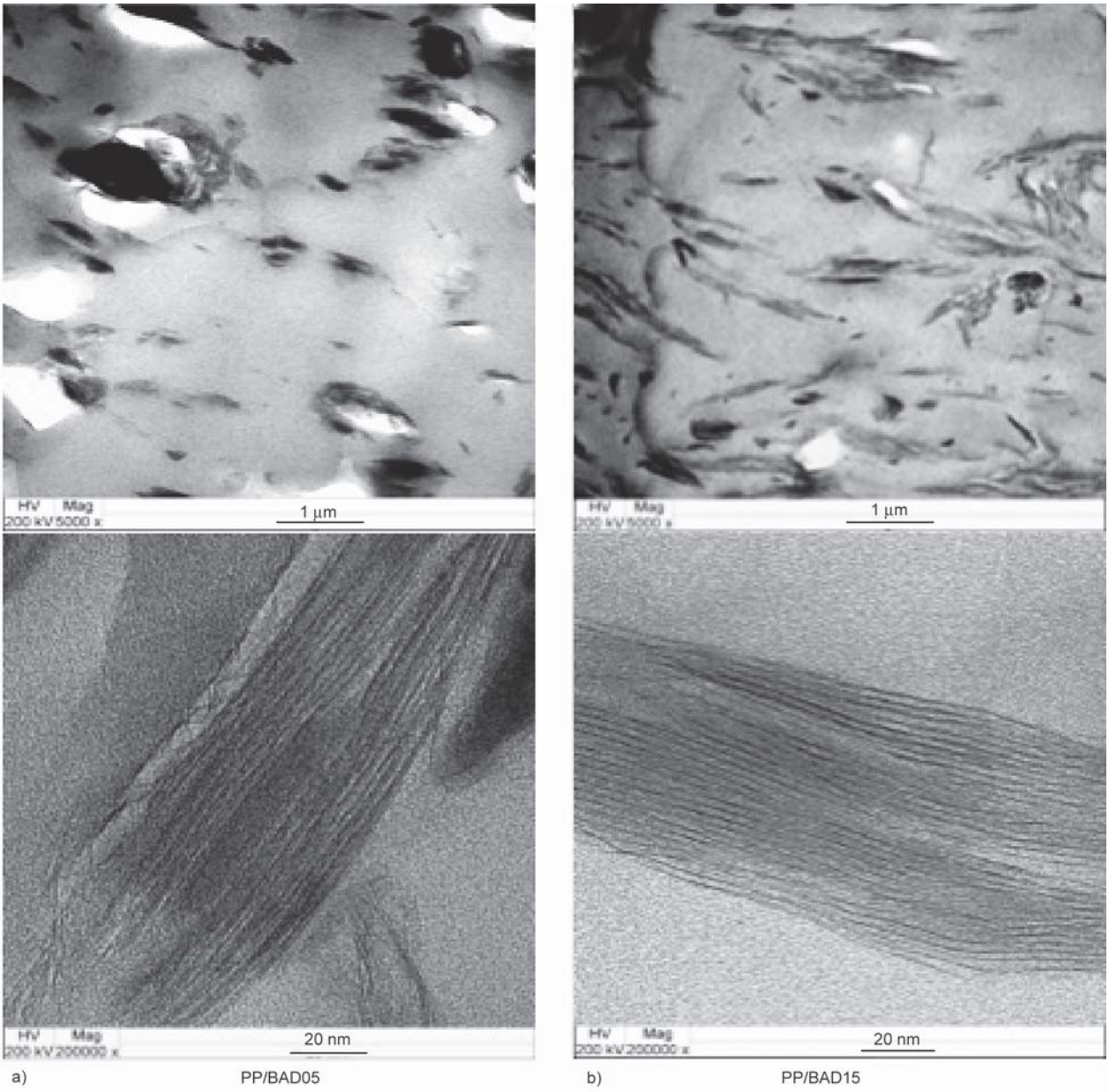

Figure 14. TEM images of the 3D printed (a) PP/BAD05 and (b) PP/BAD15 at 5000× (top) and 200 000× (bottom) magnifications.

The tensile strength, Young's modulus as well as the elongation at break of the PP/BAD15 were marginally higher than those of the PP/BAD05. This could be attributed to the better dispersion of the organoclay (BAD15) in the PP matrix. These results were in good agreement with the rheological behaviors and SEM results.

3.5.3. Organoclay dispersion

To verify the dispersion of the organoclay and its microstructure in the PP matrix, the TEM images of the printed PP/BAD05 and PP/BAD15 were presented in Figure 14. At the same magnification (5000×), the organoclay modified with higher D18 content (PP/BAD15) showed a smaller size and better dispersion in the PP matrix than the PP/BAD05. Both the PP/BAD05 and the PP/BAD15 seem to a combination of exfoliation and intercalation morphologies as anticipated by the XRD analysis. However, it is observed that the PP/BAD15 sample has larger clay tactoids which correspond to the more likely intercalated morphology [12].

4. Conclusions

In this study, a new PP/organoclay nanocomposite filament was first-time successfully prepared by the melt intercalation method using a twin-screw extruder and 3D printed into the three-dimensional shape. The linear viscoelasticity responses of the PP/organoclay nanocomposites showed the significant effect of the clay addition. D18 was successfully used to modify the clay surfaces, providing a better dispersion and wetting of the clay particles in the hydrophobic polymer matrix such as PP. A shift of the (0 0 1) plane peak to lower angle, indicated the more intercalation capability, while the larger *d*-spacing values suggested exfoliation developed in the PP/organoclay composites. Combining the XRD results, the rheological behavior and the TEM results together, it can be concluded that the PP/organoclay nanocomposites prepared in this study have mixed intercalated/exfoliated microstructure. A pseudo-MFI measurement proposed that the PP/organoclay nanocomposites could be 3D printed at the temperature range of 220–240 °C using a conventional FFF 3D printer. The results of this study can be further used for facilitating the development of engineering materials based on semicrystalline polymers from plastic industries.

Acknowledgements

We thankfully acknowledge the financial support from Grants for Development of New Faculty Staff, Ratchadaphiseksomphot Endowment Fund, Chulalongkorn University and The Thailand Research Fund (TRG6180009).

References

[1] Ligon S. C., Liska R., Stampfl J., Gurr M., Mülhaupt R.: Polymers for 3D printing and customized additive manufacturing. Chemical Reviews, **117**, 10212–10290 (2017). https://doi.org/10.1021/acs.chemrev.7b00074

[2] Wei X., Li D., Jiang W., Gu Z., Wang X., Zhang Z., Sun Z.: 3D printable graphene composite. Scientific Reports, **5**, 11181/1–11181/7 (2015). https://doi.org/10.1038/srep11181

[3] Wang L., Gardner D. J.: Effect of fused layer modeling (FLM) processing parameters on impact strength of cellular polypropylene. Polymer, **113**, 74–80 (2017). https://doi.org/10.1016/j.polymer.2017.02.055

[4] Ehrenstein G. W., Riede G., Trawiel P.: Thermal analysis of plastics. Hanser, München (2004).

[5] Sharma S. K., Nayak S. K.: Surface modified clay/polypropylene (PP) nanocomposites: Effect on physico-mechanical, thermal and morphological properties. Polymer Degradation and Stability, **94**, 132–138 (2009). https://doi.org/10.1016/j.polymdegradstab.2008.09.004

[6] Kumar V., Singh A.: Polypropylene clay nanocomposites. Reviews in Chemical Engineering, **29**, 439–448 (2013). https://doi.org/10.1515/revce-2013-0014

[7] Wang K., Bahlouli N., Addiego F., Ahzi S.: Elastic and yield behaviors of recycled polypropylene-based composites: Experimental and modeling study. Composites Part B: Engineering, **99**, 132–153 (2016). https://doi.org/10.1016/j.compositesb.2016.06.033

[8] Morajane D., Shinha Ray S., Bandyopadhyay J., Ojijo V.: Impact of melt-processing strategy on structural and mechanical properties: Clay-containing polypropylene nanocomposites. in 'Processing of polymer-based nanocomposites' (ed.: Sinha Ray S.) Springer, Basel, Vol 277, 127–154 (2018). https://doi.org/10.1007/978-3-319-97779-9_5

[9] Badji A. M., Ly E. H. B., Ndiaye D., Diallo A. K., Kebe N., Verney V.: The effect of poly-ethylene-co-glycidyl methacrylate efficiency and clay platelets on thermal and rheological properties of wood polyethylene composites. Advances in Chemical Engineering and Science, **6**, 436–455 (2016). https://doi.org/10.4236/aces.2016.64040

[10] Hong C. K., Kim M-J., Oh S. H., Lee Y-S., Nah C.: Effects of polypropylene-*g*-(maleic anhydride/styrene) compatibilizer on mechanical and rheological properties of polypropylene/clay nanocomposites. Journal of Industrial and Engineering Chemistry, **14**, 236–242 (2008). https://doi.org/10.1016/j.jiec.2007.11.001

[11] Abdel-Goad M.: Rheological characterization of melt compounded polypropylene/clay nanocomposites. Composites Part B: Engineering, **42**, 1044–1047 (2011). https://doi.org/10.1016/j.compositesb.2011.03.025

[12] Durmus A., Kasgoz A., Macosko C. W.: Linear low density polyethylene (LLDPE)/clay nanocomposites. Part I: Structural characterization and quantifying clay dispersion by melt rheology. Polymer, **48**, 4492–4502 (2007). https://doi.org/10.1016/j.polymer.2007.05.074

[13] Xie S., Harkin-Jones E., Shen Y., Hornsby P., McAfee M., McNally T., Patel R., Benkreira H., Coates P.: Quantitative characterization of clay dispersion in polypropylene-clay nanocomposites by combined transmission electron microscopy and optical microscopy. Materials Letters, **64**, 185–188 (2010). https://doi.org/10.1016/j.matlet.2009.10.042

[14] Abbasi F., Tavakoli A., Aghjeh M. K. R.: Rheology, morphology, and mechanical properties of reactive compatibilized polypropylene/polystyrene blends via Friedel–Crafts alkylation reaction in the presence of clay. Journal of Vinyl and Additive Technology, **24**, 18–26 (2018). https://doi.org/10.1002/vnl.21522

[15] Zdiri K., Elamri A., Hamdaoui M.: Advances in thermal and mechanical behaviors of PP/clay nanocomposites. Polymer-Plastics Technology and Engineering, **56**, 824–840 (2017). https://doi.org/10.1080/03602559.2016.1233282

[16] Rueda M. M., Auscher M-C., Fulchiron R., Périé T., Martin G., Sonntag P., Cassagnau P.: Rheology and applications of highly filled polymers: A review of current understanding. Progress in Polymer Science, **66**, 22–53 (2017). https://doi.org/10.1016/j.progpolymsci.2016.12.007

[17] Limpanart S., Khunthon S., Taepaiboon P., Supaphol P., Srikhirin T., Udomkichdecha W., Boontongkong Y.: Effect of the surfactant coverage on the preparation of polystyrene–clay nanocomposites prepared by melt intercalation. Materials Letters, **59**, 2292–2295 (2005). https://doi.org/10.1016/j.matlet.2005.03.006

[18] ASTM D638-14: Standard test method for tensile propertyies of plastics (2014).

[19] Ghaemi N., Madaeni S. S., Alizadeh A., Rajabi H., Daraei P.: Preparation, characterization and performance of polyethersulfone/organically modified montmorillonite nanocomposite membranes in removal of pesticides. Journal of Membrane Science, **382**, 135–147 (2011). https://doi.org/10.1016/j.memsci.2011.08.004

[20] Alexandre M., Dubois P.: Polymer-layered silicate nanocomposites: Preparation, properties and uses of a new class of materials. Materials Science and Engineering R: Reports, **28**, 1–63 (2000). https://doi.org/10.1016/S0927-796X(00)00012-7

[21] Colombe G., Gree S., Lhost O., Dupire M., Rosenthal M., Ivanov D. A.: Correlation between mechanical properties and orientation of the crystalline and mesomorphic phases in isotactic polypropylene fibers. Polymer, **52**, 5630–5643 (2011). https://doi.org/10.1016/j.polymer.2011.09.035

[22] Osswald T. A., Menges G.: Materials science of polymers for engineers. Hanser, Munich (2003).

[23] Lamberti G.: Isotactic polypropylene crystallization: Analysis and modeling. European Polymer Journal, **47**, 1097–1112 (2011). https://doi.org/10.1016/j.eurpolymj.2011.02.005

[24] Osswald T. A., Rudolph N.: Polymer rheology fundamental and applications. Hanser Publishers, Munich (2015)

[25] Venkataraman N., Rangarajan S., Matthewson M. J., Harper B., Safari A., Danforth S. C., Wu G., Langrana N., Guceri S., Yardimci A.: Feedstock material property – Process relationships in fused deposition of ceramics (FDC). Rapid Prototyping Journal, **6**, 244–252 (2000). https://doi.org/10.1108/13552540010373344

[26] Chen R-Y., Zou W., Zhang H-C., Zhang G-Z., Yang Z-T., Jin G., Qu J-P.: Thermal behavior, dynamic mechanical properties and rheological properties of poly(butylene succinate) composites filled with nanometer calcium carbonate. Polymer Testing, **42**, 160–167 (2015). https://doi.org/10.1016/j.polymertesting.2015.01.015

[27] Pfeifer T., Koch C., van Hulle L., Mazzei G. A., Rudolph N.: Optimization of the FDM additive manufacturing process. in 'Proceedings of ANTEC. Indianapolis, USA', 22–29 (2016).

[28] Aumnate C., Pongwisuthiruchte A., Pattananuwat P., Potiyaraj P.: Fabrication of ABS/graphene oxide composite filament for fused filament fabrication (FFF) 3D printing. Advances in Materials Science and Engineering, **2018**, 2830437/1–2830437/9 (2018). https://doi.org/10.1155/2018/2830437

polymers

MDPI

Article

Recycling of Polypropylene/Polyethylene Blends: Effect of Chain Structure on the Crystallization Behaviors

Chuanchom Aumnate [1,*], Natalie Rudolph [2] and Majid Sarmadi [3]

[1] Metallurgy and Material Sciences Research Institute, Chulalongkorn University, Bangkok 10330, Thailand
[2] AREVO, Inc., Milpitas, CA 95035, USA
[3] Textile Science, Department of Design Studies and Materials Science Graduate Program, University of Wisconsin-Madison, Madison, WI 53706, USA
* Correspondence: Chuanchom.a@chula.ac.th; Tel.: +662-218-8126

Received: 17 August 2019; Accepted: 5 September 2019; Published: 6 September 2019

Abstract: The combination of high-density polyethylene (HDPE), low-density polyethylene (LDPE) and polypropylene (PP) is frequently found in polymer waste streams. Because of their similar density, they cannot be easily separated from each other in the recycling stream. Blending of PP/ polyethylenes (PEs) in different ratios possibly eliminate the sorting process used in the regular recycling process. PP has fascinating properties such as excellent processability and chemical resistance. However, insufficient flexibility limits its use for specific applications. Blending of PP with relative flexible PEs might improve its flexibility. This is a unique approach for recycling or upcycling, which aims to maintain or improve the properties of recycled materials. The effects of the branched-chain structures of PEs on the crystallization behavior and the related mechanical properties of such blends were investigated. The overall kinetics of crystallization of PP was significantly influenced by the presence of PEs with different branched-chain structures. The presence of LDPE was found to decrease the overall crystallization rate while the addition of HDPE accelerated the crystallization process of the blends. No negative effect on the mechanical performance and the related crystallinity was observed within the studied parameter range.

Keywords: polymer blends and alloys; recycling; crystallization; crystal structure; kinetics

1. Introduction

Plastics are used daily in some applications. A considerable amount of plastic is used in disposable products. The amount of plastic consumed has been growing steadily due to desirable properties such as low density, high strength, ease of manufacturing and low cost. As a result, both industry and private households generate more and more plastic waste. The most prominent concerns are single-use plastic items such as packaging, bags and containers. Unfortunately, appropriate waste management strategies are not developing at the same rate as the increasing levels of plastic wastes. A significant amount of waste does not reach proper disposal sites, instead of littering the landscape, and blowing or washing into the sea, which leads to severe environmental problems. Polyolefins, which have excellent recycling properties, make up over 50% of the non-recycled plastic (high-density polyethylene, HDPE, low-density polyethylene, LDPE and polypropylene, PP). This has motivated the interest in plastic reuse and recycling [1–3].

Polyethylenes (PEs) are the most common plastic. Their primary uses are in packaging including plastic bags, plastic films and bottles. PEs are classified according to their polymerization method, density and branching. There are several types of PEs, but the most common use is the high-density polyethylene (HDPE) and the low-density polyethylene (LDPE). HDPE has between five and ten short

branches every 1000 carbon atoms. LDPE has the same number of branches as HDPE; however, they are much longer and are usually branched themselves [4–6]. Polypropylene (PP) is a linear hydrocarbon polymer with an intermediate level of crystallinity between LDPE and HDPE. Similar to PE in many properties, the presence of the methyl group attached to every other backbone carbon atom can alter the properties in some ways. The tertiary carbon atom can provide a site for oxidation. As a result, PP is less stable than PE. The orientation of each methyl group relative to the adjacent methyl groups has a strong effect on the polymer's ability to form crystals [7]. Due to its desirable physical properties such as high tensile strength, high stiffness and high chemical resistance, polypropylene (PP) has been widely used as packaging material, for instance as margarine and yogurt containers, bottle caps and microwavable food. However, it shows weak impact strength at low temperatures and is susceptible to environmental stress cracking [8,9]. LDPE waste mostly results from bags and packaging films. Owing to its low mechanical properties and easy processability it is recycled as garbage bags. One possibility to develop alternative applications is blending it with other materials to improve the low mechanical performance of recycled LDPE.

The combination of PP and PEs is frequently found in polymer waste streams. Because of their similar density, PP and PEs cannot be easily separated from each other in the recycling stream [10]. Blends of PP and PEs have become a subject of great economic and research interest, not only to improve the processing and mechanical properties of PP but also to some extent to expand opportunities to recycle these mixed plastics [11–15] Since the 1980s, a considerable amount of work has been focused on the study of mechanical properties of mixed PP and PEs. The effectiveness of blending mainly depends on the miscibility or immiscibility of the blended components. PP and HDPE as well as PP and LDPE are generally considered immiscible in any blending ratio and show a remarkable phase separation during cooling and crystallization, which reflects the end-properties of such blends. In polymer blends, the crystallization process may have a significant influence on its morphological features, thermal and mechanical properties.

Semi-crystalline polymers, PP and PEs, consist of crystallites of different lamellar thickness and degree of perfection. Crystallization kinetics in such polymer blends are very complex in relation to the different crystallization behavior of the two components. These include the production of primary nuclei, formation and spreading of surface nuclei, and inter-diffusion of crystallizable and non-crystallizable chains at the advancing front of the growing crystal [16–18]. In general, depending on the nucleation, there are two types of crystallization: heterogeneous and homogeneous crystallization. The crystal fraction in a polymer is a function of both the nucleation rate and the growth rate of the spherulite in the sample. The factors influencing the changes in primary nucleation in polymer blends can be divided into two groups. (i) The properties of the minor phase polymer in the blend, including miscibility, glass transition temperature, ability to crystallize, the temperature range in which crystallization is possible and surface tension of the polymer melt and (ii) the blending/mixing processes. For such blends in which dispersed polymer can crystallize, the size of its inclusions, controlled by the parameters of the mixing process, is one of the most critical factors determining the crystallization kinetics of the blend. For example, the non-equilibrium molecular structure of the PP/LDPE blend can be observed as a result of the strange process of PP crystallization [12]. Accordingly, the crystallization in blends of PP with LDPE and HDPE has been studied. PP has a high degree of crystallinity due to its regular chain structure. Galeski et al. [19] examined the morphology of an isotactic PP (iPP)/LDPE blend and revealed that the LDPE occlusions introduced substantial changes in the internal structure of the iPP spherulites. From a polarizing micrograph, it was seen that the LDPE droplets hindered the spherulite-growing front, causing distinct concavities. The influence of crystallization of a dispersed polymer in the matrix crystallization can probably explain the decrease of spherulite size in nonisothermically crystallized samples of the blends reported for iPP with LDPE [20], and iPP with HDPE [21]. During fast nonisothermal crystallization, a simultaneous crystallization of both components is also possible. Already crystallized inclusions of a dispersed polymer accelerate the crystallization of the matrix acting as nucleating agent and induce the formation of additional

spherulites. Finally, the average spherulite radius in those blends becomes smaller than in plain iPP crystallized under the same condition [22]. Razavi-Nouri et al. [23] studied the morphology of PP/linear low-density PE (LLDPE) blends and found that the nucleation densities of the PP spherulites decreased in the presence of the LLDPE. Moreover, LLDPE remained as discrete droplets dispersed throughout the PP spherulites, which indicated the immiscibility of these two components. In the case of PE/PE blends, molten PEs of different type chain structures usually are immiscible. The spherulites of PE with higher T_m, are encapsulated by those of the other PE during crystallization. Thus, once cooled below the crystallization point of one component, the blends' morphology is fixed within the crystalline structure.

The physical properties of PP and PEs are too similar to enable the detection of such phase separation, which governs the mechanical properties of the end product directly. Likewise, the phase behaviors of PP/PEs blends, are not entirely understood yet. However, the crystallization behavior plays an essential role in determining the crystal structure as well as the phase morphology, which further affects the end-use properties, especially mechanical performance. In this study, the influences of different chain structures PEs on the crystallization behaviors of PP/PEs blends as well as effects on the tensile properties are investigated. The crystallization behaviors, including the kinetics of crystallization as well as the crystal morphology, were studied using the differential scanning calorimetry (DSC) and the polarized optical microscopy techniques, respectively. The gel permeation chromatography (GPC) technique was used to measure the molecular weight and molecular weight distribution of the materials. Also, the blend morphology was analyzed via the scanning electron microscopy (SEM). Thus, the correlation between the crystallization behaviors and the tensile properties of PP/PEs blends were addressed. Furthermore, the effects of the recycling process on the chain structures, crystallization behaviors, as well as the tensile properties of recycled PP/PEs blends, are discussed.

2. Materials and Methods

2.1. Materials

The polymers chosen for this study have substantial differences in processing behavior and end-use properties. We selected the commercial virgin resins which are commonly used for packaging applications including Low-density polyethylene, LDPE (DOW LDPE 132I, Dow Chemical Company, Chicago, IL, USA), high-density polyethylene, HDPE (Marlex HXM 50100, Chevron Phillips Chemical, Woodlands, TX, USA) and polypropylene, PP (FHR Polypropylene P9G1Z-047, Flint Hills Resources, Longview, TX, USA).

The manufacturing scrap of recycled LDPE (Bapolene®1072, Bamberger Polymers, Inc., Itasca, IL, USA), injection molding grade used for food packaging) and regrind PP (Inspire ®6025N, Braskem, Philadelphia, PA, USA), used for blown film and thermoforming of packaging containers) were supplied by PLACON (Fitchburg, WI, USA). Incorporated together with virgin material of both grades were selected as representatives for recycled materials.

2.2. Sample Preparation

All materials were processed using a Leistritz (Somerville, NJ, USA) ZSE18HPe laboratory, modular, intermeshing, co-rotating twin-screw extruder and subsequently pelletized with the appropriate downstream equipment (a water-through, blown-air drier and a rotary cutter). The extrusion temperature profile was in a range of 180–220 °C from the hopper to die and the screw speed of 100 rpm. The PP/LDPE and PP/HDPE blends were prepared with the weight ratio of 100/0, 75/25, 50/50, 25/75 and 0/100, respectively.

For the mechanical properties' measurement, the PP/LDPE and PP/HDPE blends were prepared as the tensile bars according to ASTM D638-14 using a Type 1. All specimens were injection molded using an Allrounder 320S injection molding machine of the ARBURG GmbH and Co. KG, Loßburg-Germany with a clamping force of 500 kN. This machine is equipped with a screw of 25 mm diameter and an effective screw length (L/D ratio) of 24. The mold temperature is set at 25 °C.

3. Characterization

3.1. Melt Flow Rate (MFR) Measurements

The melt flow rate (MFR) is a good technique to determine the effects of reprocessing since it is an indirect measurement of the melt viscosity of materials. It also indicates the changes in molecular weight and is widely used in the thermoplastic industry. The MFR measurements were carried out in an extrusion plastometer Series 4000 according to the ASTM D1238-10, using procedure A [24].

3.2. Differential Scanning Calorimetry (DSC)

The melting and crystallization behavior of PP, LDPE, HDPE and their blends were determined using a DSC (214 Polyma, NETZSCH Group, Selb, Germany) under nitrogen atmosphere. For crystallization and melting temperature measurement, PP, LDPE, HDPE and their blends were melted at 200 °C, held isothermal for 2 min, then cooled to −35 °C and heated to 200 °C again with the scanning temperature rate of 5 K/min. For isothermal analysis, all blends and pure polymers were quenched from 200 °C to an isothermal temperature between 100 to 125 °C.

For the analysis of the crystallization kinetics, the Thermokinetics software (Version 3.1, Selb, Germany) from NETZSCH Group was used (Model: n-Dimensional nucleation (Avrami–Erofeev)).

According to the rule of mixtures, the crystallinity of PP/LDPE blends was determined from the melting enthalpy (ΔH_m) [25]. The actual melting enthalpy of a blend is related to the enthalpy of the individual polymer and to their weight fraction w in the blends:

$$\Delta H_i = \frac{\Delta H_{m(i)}}{w_{(i)}} \tag{1}$$

thus,

$$\Delta H_{PP/LDPE} = \left(\frac{\Delta H_{m(PP)}}{w_{(PP)}} + \frac{\Delta H_{m(LDPE)}}{w_{(LDPE)}} \right) \tag{2}$$

The degree of crystallinity, χ, of PP, LDPE and their blends was calculated using the following equation;

$$\chi = \frac{\Delta H_i}{\Delta H_0} \times 100 \tag{3}$$

where ΔH_0 is the specific heat of melting of completely crystalline materials, $\Delta H_0 =$ 205 J/g, and 293 J/g for PP and PEs, respectively [6].

However, in PP/PEs blends, the resultant morphologies are not only attributed to thermodynamic factors but also to kinetic ones during subsequent crystallization. The crystallization kinetics are described in terms of the Avrami equation (Equation (4)), a common tool to describe overall isothermal crystallization (including nucleation and growth of spherulites). It can be also written as:

$$ln(-ln(1 - X(t))) = ln\, k(T) + n\, ln\, t \tag{4}$$

When applied for DSC analysis, it is assumed that the differential area under the crystallization curve with time corresponds to the dynamic changes in the conversion of mass from the melt phase to the solid phase. The relative crystal conversion $X(t)$ as a function of time was calculated by the following equation:

$$X(t) = \frac{X_t}{X_\infty} \tag{5}$$

where $X(t)$ is the released heat until time t and t_∞ is the total released heat by crystallization.

The Avrami index, n, is a complex exponent, which is related to the dimensionality of the growing crystals and to the time dependence of nucleation. While the crystallization rate coefficient, k, is the overall crystallization growth rate constant and related to the nucleation type, crystal growth and

crystallization temperature. Based on these two values, the crystallization half-time, $t_{1/2}$, which is a representation of the crystallization rate, can be evaluated from:

$$k = \frac{\ln 2}{(t_{1/2})^n}. \quad (6)$$

In this study, the crystallization kinetics of all materials were calculated based on the Avrami model using the Thermokinetics software.

3.3. Polarized Optical Microscopy

The phase transformation of PP, LDPE, HDPE and their blends was investigated using an Olympus IX71 polarising optical microscope (Melville, NY, USA) equipped with a 50× objective and a hot-stage. All samples were prepared as 10 µm thick films using a microtome. The films were heated between a glass slide and coverslip to 200 °C and kept for 2 min. Subsequently, the samples were quenched to an isothermal temperature between the crystallization temperatures for PP (125 °C) and LDPE (100 °C).

3.4. Tensile Tests

The tests were carried out according to ASTM D638-14 [26] using a Type 1 tensile bar on an Instron 5960 Dual Column Tabletop tensile test machine (Norwood, Massachusetts) with a 30 kN load cell. The crosshead was moved with a constant velocity of 500 mm/min until the specimen broke in the gauge section. The strength and the strain of the sample were determined based on the maximum force and the elongation of the tensile bar. At least five measurements were taken for each material.

3.5. Gel Permeation Chromatography (GPC) Analysis

The analyses were performed using a PL GPC220, equipped with DAWn Heleos-II, detector from Wyatt Technology (Santa Barbara, California). The two PLgel Olexis separating column with 300 mm × 7.5 mm, Agilent Technologies were employed. All measurements were performed with 1,2,4 trichlorobenzol stabilized with 0.1% BHT at the flow rate of 1 ml/min and the measurement temperature of 150 °C.

3.6. Scanning Electron Microscope (SEM) Analysis

The cryo-fracture surfaces of the PP/PEs blends were studied using the LEO 1530 scanning electron microscope (SEM, White Plains, NY, USA) at an accelerating voltage of 5 kV. All fractured samples were etched with sulfuric acid at 80 °C for 2 h. Prior to investigation, all samples were sputter-coated with gold.

4. Results and Discussion

4.1. Melting and Crystallization Temperatures

According to the data available in the literature as well as the one presented in this study, PP, LDPE and HDPE crystallize separately, and both polymers can have a mutual effect on the process of crystallization, and the morphology of the blends [12].

Figure 1a shows the DSC heating curves of PP, LDPE and their blends at different compositions. The two endothermic peaks in the temperature range corresponding to the melting temperature of the individual polymers. The melting temperature of PP and LDPE does not significantly depend on the composition of the blends. As shown in Figure 1b, the crystallization temperature of LDPE in PP/LDPE blends remarkably shifts to higher temperature relative to the crystallization peak of pure LDPE and remains almost constant in all blend compositions. However, the crystallization temperature of PP in PP/LDPE blend with 75 wt % of LDPE content shifts to lower temperatures, which indicates a reduction in the perfection of the formed crystallites.

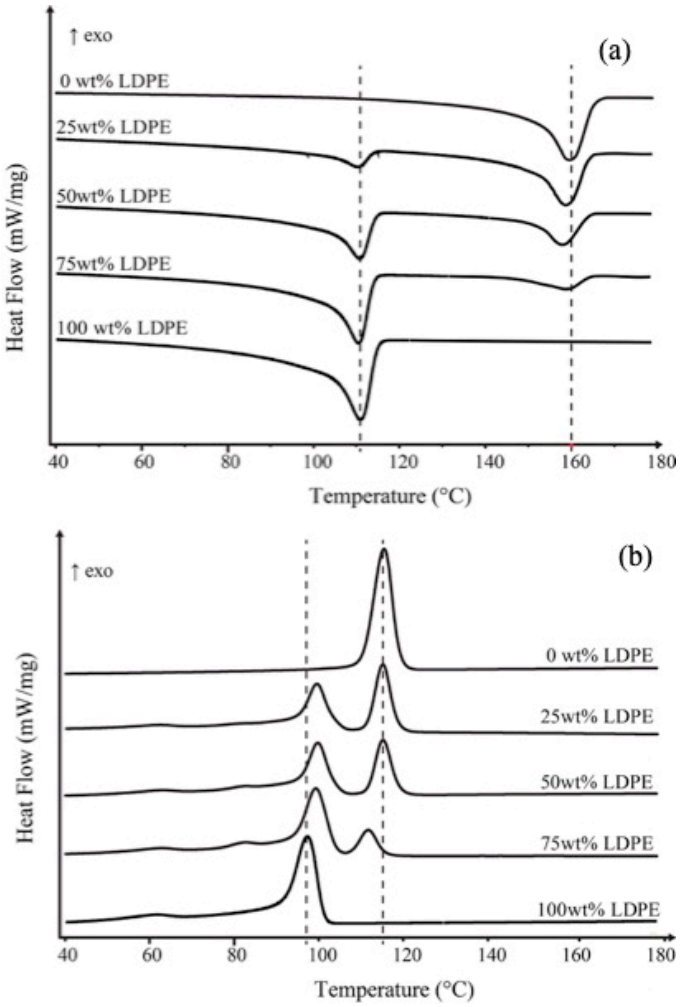

Figure 1. (**a**) Melting temperature (T_m) from the 2nd heating scan and (**b**) crystallization temperature (T_c) of polypropylene (PP), low-density polyethylene (LDPE) and their blends at different compositions.

For PP/HDPE blend, the T_m of HDPE in all blend compositions remains almost constant temperatures relative to that of pure HDPE (~131 °C) as shown in Figure 2a. However, the crystallization behavior of PP/HDPE blends is complex compared with the melting behavior. As shown in Figure 2b, the crystallization peak of blends shifts to the higher temperature, which is close to the crystallization temperature (T_c) of HDPE. Even though PP/HDPE blend systems seem to show only one T_c, however, the bimodal behavior is more pronounced at higher HDPE loading blend (75 wt % HDPE). The bimodal crystallization behavior could be associated with partially miscible behavior. Also, a single crystallization peak of the blend with small HDPE loading could be postulated that the PP was miscible with HDPE at elevated fraction and temperature. A single crystallization peak may be due to a very close crystallization temperature of the individual polymers; 116.2 °C for PP and 117.6 °C for HDPE. Also, the one crystallization peak possibly implies co-crystallization of the materials, which leads to miscibility and compatibility of the blends.

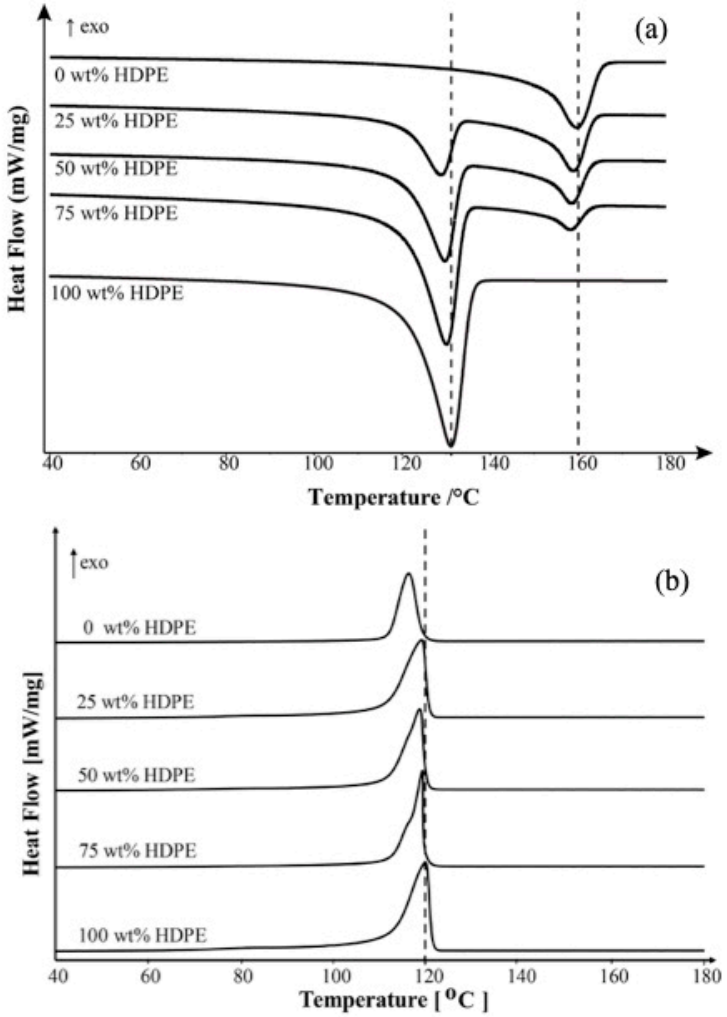

Figure 2. (**a**) Melting temperature (T_m) from the 2nd heating scan and (**b**) crystallization temperature (T_c) of PP, high-density polyethylene (HDPE) and their blends at different compositions.

4.2. Crystallinity

Figure 3a presents the crystallinity of PP/LDPE blends both total and separately in the blends. It can be seen that the crystallinity of PP and LDPE in the blends varies depending on their composition. In the case of high viscosity polymers, the increase of LDPE (lower viscosity) content decreases the degree of crystallinity of the blend. Concerning an individual component, it is seen that the crystallinities of both LDPE and PP in the blends exhibit an almost linear relationship with its concentration.

Similarly, Figure 3b presents the total crystallinity of PP/HDPE blends both total and separately in the blends. The more linear structure of HDPE results in more crystallinity compared to those of PP. The larger the HDPE contents, the higher crystallinity of the blends. Remarkably, a drop of the total crystallinity of PP/HDPE blends appears when the blend contains 75 wt % HDPE, which could be related to the deviation in crystallization behavior as well as the crystal structure of the blend.

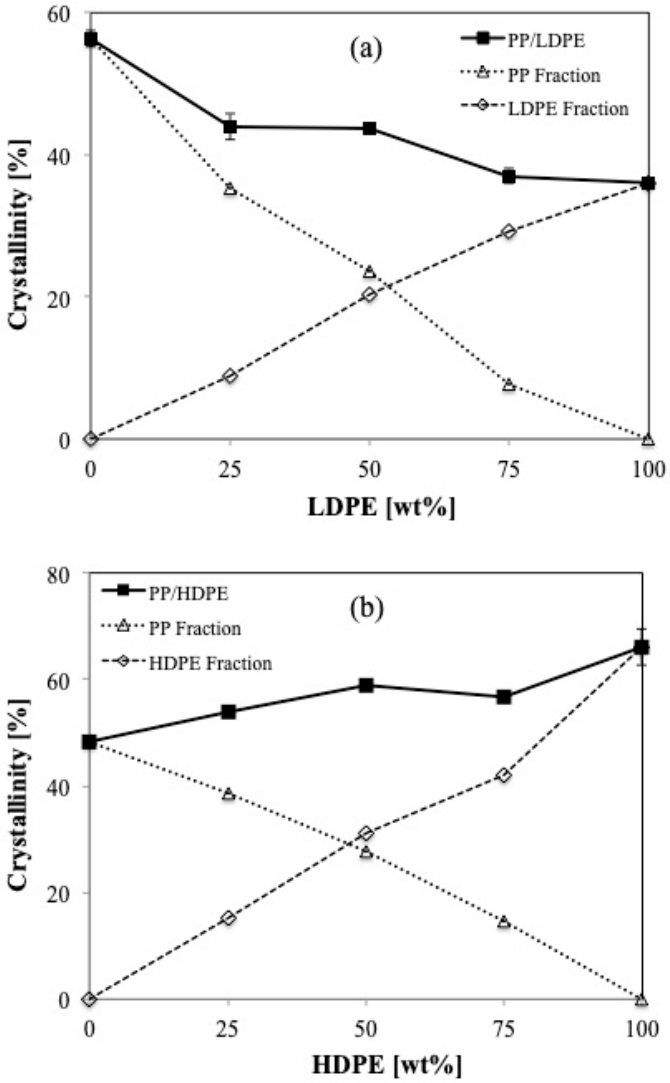

Figure 3. % Crystallinity of (**a**) PP/LDPE blends and (**b**) PP/HDPE blends at different blend compositions.

4.3. Crystal Structures

The crystal structures and morphology of PP, LDPE, HDPE and their blends were captured using the polarized optical microscope. From the DSC results, it is known that PP starts crystallizing at 125 °C while LDPE and HDPE begin at 100 and 124 °C, respectively.

PP is a semi-crystalline thermoplastic polymer with a high degree of crystallinity due to its regular chain structure. In general, PP can crystallize in a wide range of spherulite dimensions (from 10–50 μm to 280–370 μm) depending on the crystallization conditions as well as the presence of nucleating agent [27,28]. LDPE and HDPE crystals, in general, consist of ethylene units in a chain fold structure. Thus, the segment length of an ethylene unit can limit the lamella thickness. From this study, it is visible that LDPE crystals are much smaller in size compared to PP crystals. The crystal sizes are about 25 and 100 μm in diameter for LDPE crystals and PP crystals, respectively. However, the crystal sizes of HDPE are much smaller than those of PP and LDPE as can be observed in Figure 4.

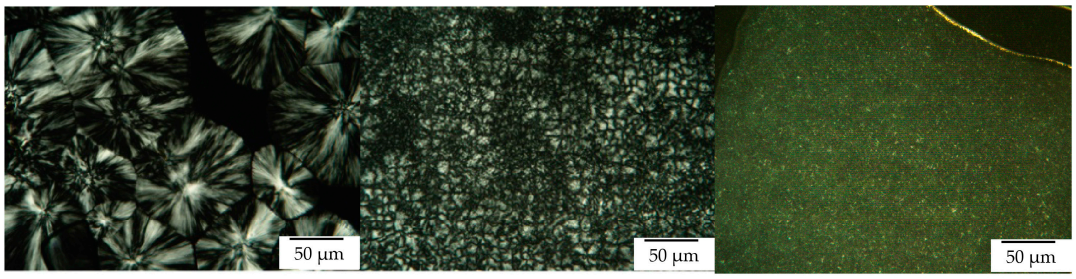

Figure 4. Polarizing optical microscopy of (**a**) LDPE after isothermal crystallization at 100 °C for 20 min, and (**b**) PP after isothermal crystallization at 125 °C for 20 min and (**c**) HDPE after isothermal crystallization at 124 °C.

In this study, each blend was crystallized isothermally at 125 °C, where PP could crystallize. Figure 5 shows the nucleation and growth process of PP/LDPE blends during the isothermal crystallization at 125 °C from 4 to 20 min. The spherulites of PP in blends were not as sharp as in the virgin PP, but they could still be readily distinguished. During crystallization, the PP in the blend crystallizes at almost the same rate as pure PP. A larger LDPE content resulted in a reduction of the average spherulite size of PP. Possibly, PP should be somewhat soluble in the melted LDPE, which seems to be consuming the remaining PP dissolved in the matrix, preventing bridging growth [29]. This can also be concluded from the shifting of T_c of PP to a lower temperature with more substantial LDPE contents.

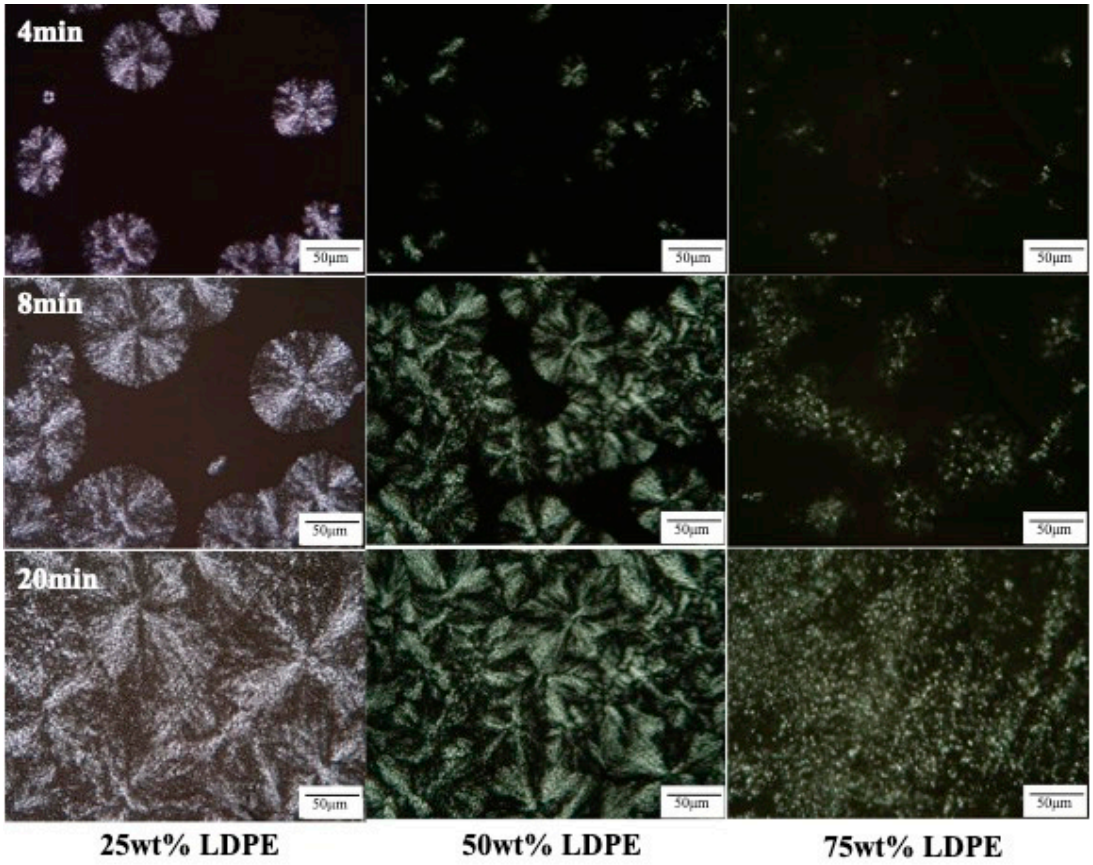

Figure 5. Polarizing optical microscopy of the nucleation and growth process of PP/LDPE blends containing 25 wt % LDPE, 50 wt % LDPE and 75 wt % LDPE during isothermal crystallization at 125 °C.

The crystallization rate of PP was found to be slightly slower at larger LDPE contents. As can be seen from Figure 5 at 4 min, the PP spherulite in the 75 wt % LDPE blend developed slower than that of PP spherulites in the 50 wt % LDPE and 75 wt % LDPE blends, respectively. Even though the PP crystals in the blend of 25 wt % LDPE nucleated faster than that of the blend with 50 wt % LDPE, it should be noted that once the PP crystals in the blend of 50 wt % LDPE were nucleated, they grew faster. This can be seen at 8 min. Some crystals nucleated at a much lower rate and then grew faster afterward.

In contrast, the opposite effects are found for PP/HDPE blends. The larger the HDPE contents, the faster the crystallization rate as can be seen in Figure 6. Since the crystallization temperatures of PP and HDPE overlap, both PP and HDPE could crystallize, increasing the crystallization rate. The overall crystallization rates are accelerated as the higher HDPE contents are loading.

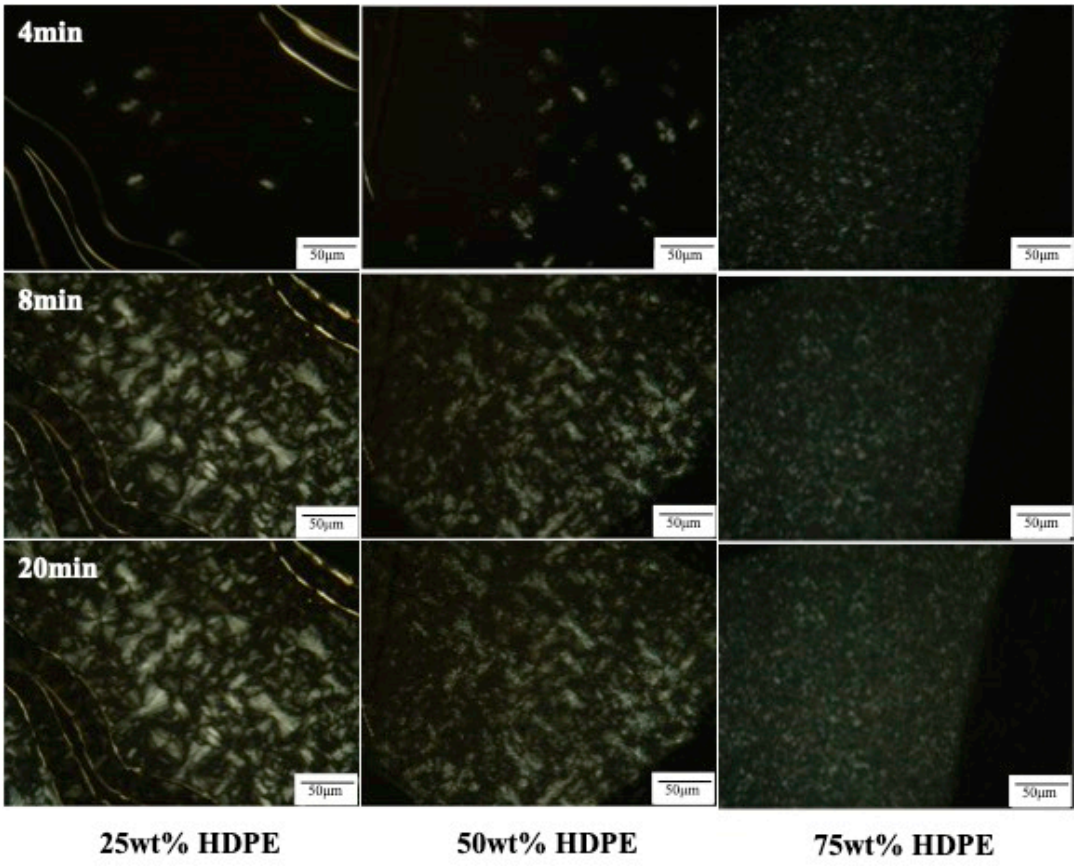

Figure 6. Polarizing optical microscopy of the nucleation and growth process of PP/HDPE blends containing 25 wt % HDPE, 50 wt % HDPE and 75 wt % HDPE during isothermal crystallization at 125 °C.

4.4. Crystallization Kinetics

Figure 7a shows the crystallization behaviors, and Figure 7b shows the comparison of crystalline fraction development in PP/LDPE and PP/HDPE at the same concentration of LDPE and HDPE (25 wt %), respectively. The solid line represents the crystalline fraction of pure PP at the same isothermal crystallization process.

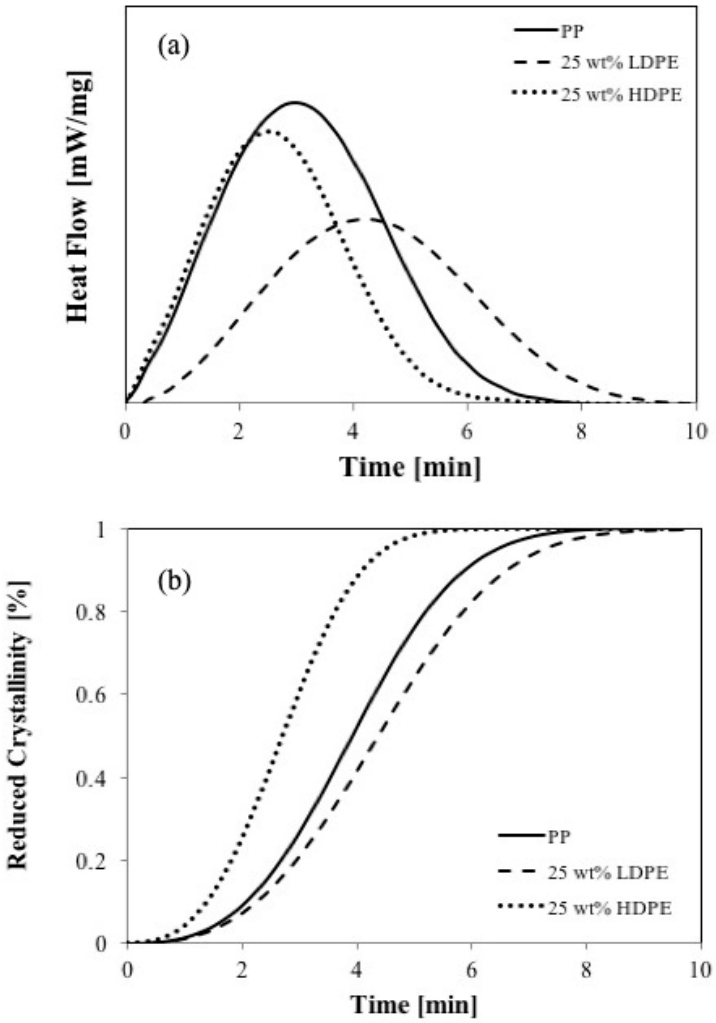

Figure 7. (**a**) Differential scanning calorimetry (DSC) crystallization curves and (**b**) reduced crystallinity obtained at 125 °C for PP (solid line), PP/LDPE containing 25 wt % of LDPE (dash line) and PP/HDPE blends containing 25 wt % of HDPE (dot line).

Based on the Avrami equation, the values of the Avrami exponent, n, varied slightly but they were all close to 2, indicating that the crystallization process was heterogeneous and took place within two dimensions. The growth of spherulites was confined in two dimensions although initial nucleation and crystallization may take place in three dimensions because the specimens were 10 μm in thickness and were sandwiched between glass slides and coverslips. The most dramatic increase in the Avrami index, n, can be obtained by increasing the LDPE content since the morphology can also be significantly altered by confinement effects or interference from the LDPE melt. The growing PP spherulites may occlude the droplets of LDPE. Theoretically, the difference in interfacial energy decides whether the droplets of LDPE were engulfed or rejected by the growing PP spherulites [28]. The crystallization kinetic parameters of all blends are shown in Table 1.

Table 1. Avrami index (n), overall crystallization rate constant (k), and crystallization half-time obtained during isothermal crystallization of PP, LDPE, HDPE and their blend at isothermal crystallization temperatures (125 °C) at the cooling rate of 25 K/min.

Materials	MFR [g/10 min]	Half-Time, $t_{1/2}$ [min]	n [-]	k [min^{-1}]
PP (0 wt % LDPE)	0.66	3.24	2.42	0.2655
PP/LDPE (25 wt % LDPE)	0.71	4.58	2.73	0.1908
PP/LDPE (50 wt % LDPE)	0.89	4.68	2.65	0.1862
PP/LDPE (75 wt % LDPE)	0.91	N/A	N/A	N/A
LDPE (100 wt % LDPE)	0.72	N/A	N/A	N/A
PP/HDPE (25 wt % HDPE)	0.45	2.73	2.36	0.3143
PP/HDPE (50 wt % HDPE)	0.32	2.27	2.54	0.3808
PP/HDPE (75 wt % HDPE)	0.23	N/A	N/A	N/A
HDPE (100 wt % HDPE)	0.15	N/A	N/A	N/A

From the crystallization behavior studies, which include the kinetics of crystallization as well as the crystal morphology from the optical microscope, we found that the overall crystallization rate of PP was sharply reduced by the addition of LDPE, the more branched structure. However, the opposite results were found for the case of linear chain HDPE. Consequently, the branched-chain structure seems to affect the nuclei density. However, from this study, it can be said that both nucleation and diffusion processes controlled the overall crystallization rate.

The MFR seems to affect the crystallization haft-time, as shown in Table 1. The addition of LDPE and HDPE into PP showed different effects on the MFR of the blends. The MFR of PP/HDPE blends decreased with increasing the HDPE content, and all blend compositions have the MFR within the limits of the pure components; PP and HDPE. Surprisingly, the MFR of PP/LDPE increased with increasing LDPE loading, which is even higher than the MFR of the pure components; LDPE and PP. It is possible that LDPE acts as a plasticizer for the PP molecules and enhances the mobility and diffusion of PP in the blends.

4.5. Effect of Recycling Process

Due to the large differences in structure and behavior, for recycled materials, the results presented in this study will be limited to PP, LDPE and their blends. Some results of PP/HDPE blends will be shown to confirm the applicability of methods or results where appropriate. Thus, the manufacturing scraps of recycled LDPE (Bapolene®1072) and regrind PP (Inspire ®6025N), which will be called as LDPE1 and PP1 were selected as representatives.

Figure 8 shows the comparison of isothermal crystallization behavior of virgin material (vPP1, solid line) and recycled material (rPP1, dash line) at 139 °C. It is seen that the crystallization behavior of recycled PP deviates from that of the virgin material. The broader shape indicates that rPP1 needs more time to crystallize and that the crystal geometry could be different.

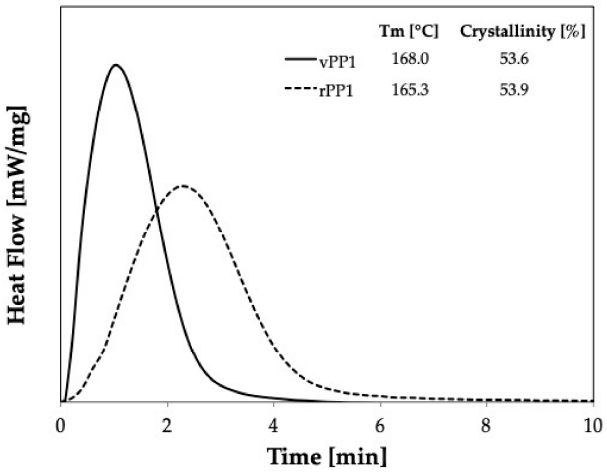

Figure 8. Crystallization curves obtained at 139 °C for virgin material (vPP1), and recycled material (rPP1).

Figure 9 shows the isothermal crystallization curves for vPP1, and vPP1/vLDPE1 blends at 139 °C, a temperature at which the only vPP1 can crystallize. These results imply a delay in the crystallization and the imperfection of the crystal formation in the recycled blends.

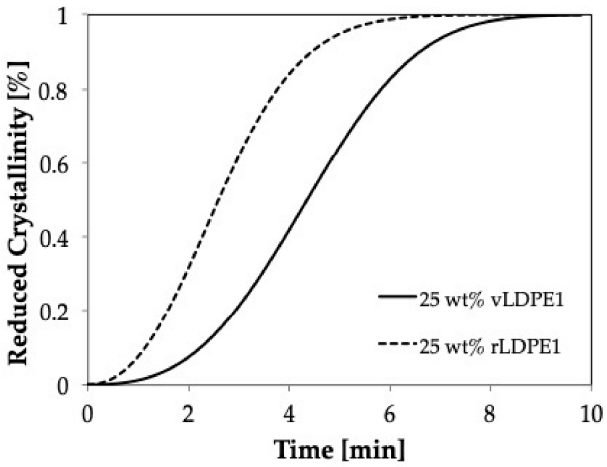

Figure 9. Crystallinity obtained at 139 °C for virgin material (vPP1/vLDPE1) and recycled material (rPP1/rLDPE1) blends containing 25 wt % of vLDPE1 and rLDPE1, respectively.

The effect of recycling process on the crystallization behavior of PP/LDPE blends is shown in Figure 9. The recycled blend (dash line) shows a higher rate of crystallization compared to that of the virgin blend (solid line), which may be caused by the shorter polymeric chain resulting from the degradation during the recycling process [14]. Furthermore, the recycling process affects the shape of the crystals (rPP1), which become more spherical. The smaller the value of k and the higher the half-time value, the slower is the rate of crystallization.

It can be seen that the recycling process resulted in the broader of the crystallization peak. Moreover, the nucleation of rPP1 is much slower than that of vPP1, as reported in Table 2. Furthermore, a significant decrease in M_w of virgin PP1 (vPP1) from 481,000 to 354,150 g/mol for recycled PP1 (rPP1) was observed. Recycled PP1 (rPP1) is the regrind material received out of the production stream, resulting from the dilution of 70% recyclate with 30% virgin material. Thus, the properties can be influenced by highly degraded fractions, which have shorter polymer chains than the virgin material. The shorter chains have a lower molecular weight and thus, affect the mechanical performance of the

material. The observed lowering in the molecular weight (M_w) indicates that chain scission occurred during the recycling process. The lower polydispersity index shows that the chain scission was mostly affecting the longest chains, while the lower limit was not affected. Thus, the molecular chain of rPP1 is shorter, and the molecular weight distribution is narrower, leading to the smaller k value and lowering the crystallization rate as shown in the increasing of the crystallization half-time.

Table 2. Weight average molecular weight (M_w), molecular weight distribution (M_w/M_n) and kinetic parameters for the isothermal crystallization of vPP1 and rPP1 at 139 °C at the cooling rate of 25 K/min.

Materials	MFR [g/10min]	M_w [g/mol]	M_w/M_n	Crystallization Temperature [°C]	Half-Time, $t_{1/2}$ [min]	n [-]	k [min^{-1}]
vPP1	2.76	414,933	3.15	139	1.52	1.93	0.5436
rPP1	6.10	333,467	2.46	139	2.21	2.24	0.3844

From the crystallization behavior studies, which include the kinetics of crystallization as well as the crystal morphology from the optical microscope, it is clearly shown that the overall crystallization rate of PP was strongly reduced by the addition of LDPE for both the high-viscosity system (PP/LDPE and PP/HDPE) and low-viscosity system (vPP1/vLDPE1). Furthermore, consistent behavior was observed in the blend system of recycled material (rPP1/rLDPE1). It can be concluded that the reduction in the overall rate is attributed to a decrease in the nucleation density. The decrease in nucleation density was found predominantly caused by the nuclei migration from PP to PE, which was in turn caused by an interfacial energy difference [19].

In general, polymer degradation during processing operations can cause changes in molecular weight and molecular weight distribution in polymers. The MFI indicates changes in molecular weight but is rather insensitive to changes in molecular parameters such as molecular weight distribution. In the case of viscosity, the sensitivity to molecular weight distribution changes is seen in the very low and very high shear rate ranges. MFI has been used to estimate the extent of thermal and shear degradation of polymeric material as it can be readily measured on a simple and inexpensive melt flow indexer. The recycled blend shows a higher MFI at the blend composition of less than 50 wt % of LDPE while the lower MFI can be observed at the high LDPE contents (>50 wt %). Therefore, it can be concluded that at small LDPE contents, the MFI of the matrix PP dominates the change in MFI of the blend. Vise Versa, at higher LDPE content, when the LDPE presents the matrix, the MFI of the blends are indeed governed by LDPE. The low-viscosity materials (high MFI) show a faster crystallization rate as well as shorter crystallization half-time compared to the high-viscosity materials.

4.6. Mechanical Properties

Figure 10a presents the stress-strain curves for PP, LDPE and their blends at different compositions. The tensile stress-strain curves are dependent on their composition. As expected, the elongation of PP was improved by adding the more ductile LDPE. The larger the content of LDPE, the higher is the strain at break. The same behaviors were observed for the PP/HDPE blends as shown in Figure 10b. The tensile strength, Young's modulus and maximum tensile stress for such PP/LDPE and PP/HDPE blends are depicted in Figure 10c–e, respectively. It can be seen that Young's modulus and the tensile strength of PP/LDPE and PP/HDPE blends followed the same trends. However, a distinct improvement in Young's modulus and tensile strength were found in PP/HDPE blend with 25 wt % of HDPE. One reason could be attributed to the co-crystallization of PP and HDPE (exhibit one crystallization peak), and the higher degree of crystallinity, which again results in an increased modulus.

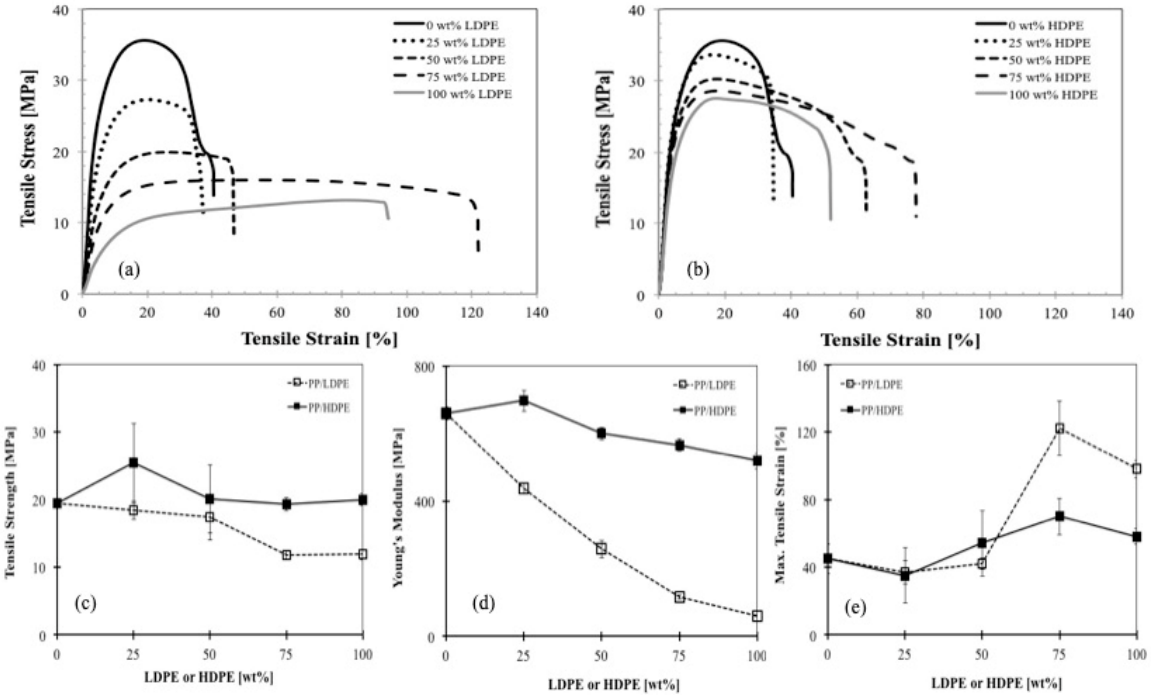

Figure 10. Tensile properties: (**a**) stress-strain curves of PP, LDPE and their blends at different compositions (u_0 = 500 mm/min), (**b**) stress-strain curves of PP, HDPE and their blends at different compositions (u_0 = 500 mm/min), (**c**) tensile stress, (**d**) Young's modulus and (**e**) tensile strain at maximum stress for PP/LDPE (dash line) and PP/HDPE (solid line) as a function of blend composition.

Figure 11 shows the tensile properties of the blends prepared from virgin materials (vPP1/vLDPE1), and recycled materials (rPP1/rLDPE1), respectively. The tensile properties of rPP1 show only a slight change compared to those of virgin material (vPP1/vLDPE1). These results indicate the potential for recycling the PP/LDPE blend with consistent mechanical performances.

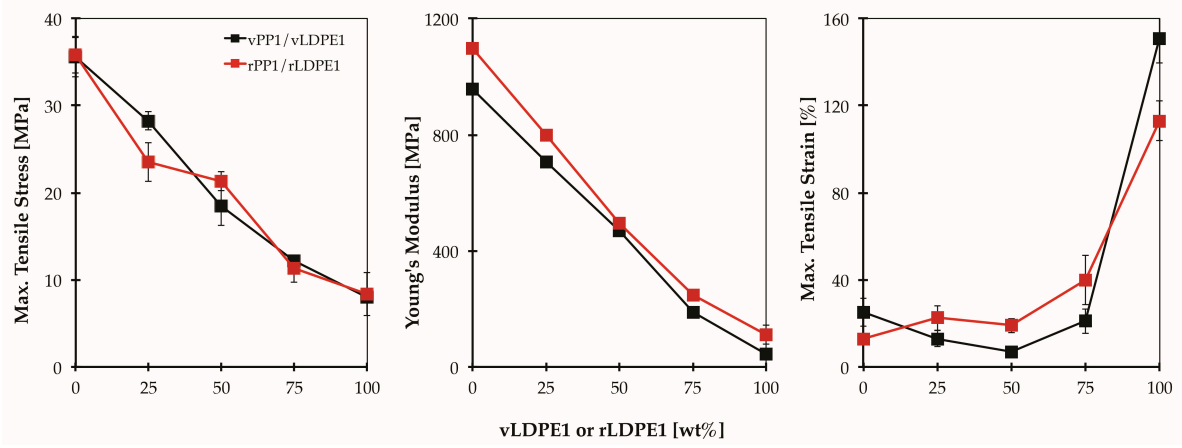

Figure 11. Tensile stress [MPa], Young's modulus [MPa] and tensile strain [%] for vPP1/vLDPE1 and rPP1/rLDPE1 as a function of blend composition.

4.7. Blend Morphology

Figure 12 presents the SEM micrographs for the low-viscosity blend (rPP1/rLDPE1, MFI ratio = 10) in comparison with the high-viscosity blend (PP/LDPE, MFI ratio = 1) of 75 wt % LDPE. It is seen that the polymer pairs with different viscosities and MFI ratios, in which related to the different chain

structures and degree of entanglement, developed different phase morphologies. The rPP1/rLDPE1 blend shows a droplet structure, small holes as well as droplets of material being dispersed in the matrix. However, sharp borders at the dispersed phase sites and no evidence of PP-LDPE interpenetration are observed. Since rLDPE1 has a much lower viscosity than rPP1 in this blend, holes and droplets may be attributed to LDPE particles, which are entirely surrounded by PP. The lack of interfacial adhesion between PP and LDPE phases leads to the decreasing in mechanical strength of the blend as presented in Figures 10 and 11.

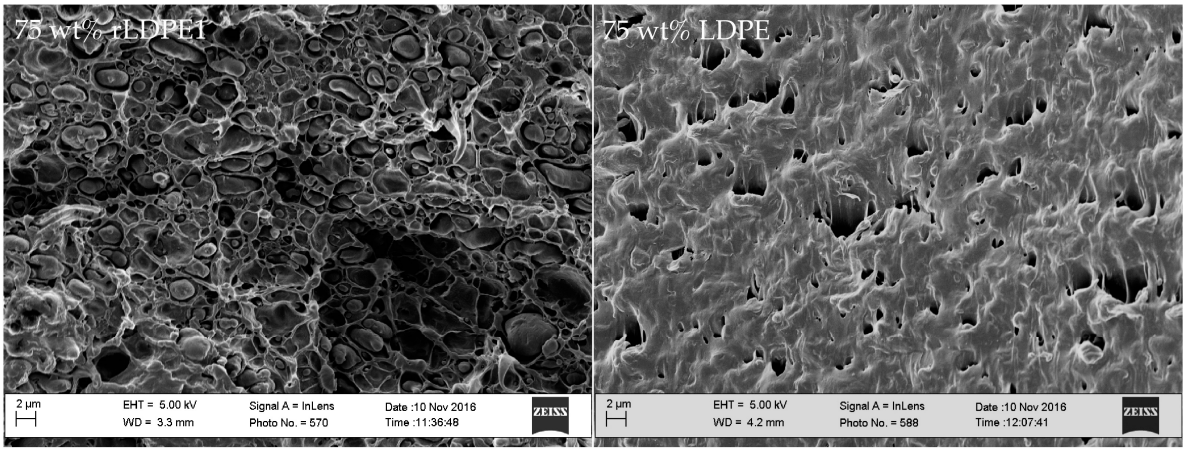

Figure 12. SEM images for vPP1/vLDPE1 (left) and PP/LDPE (right) at 25 wt % of LDPE composition, sulfuric etching at 80 °C for 2 h.

Polymer pairs and blend composition affect the results of the short-term tensile test. The higher maximum tensile stress of PP can be explained by the short rigid methyl group, which is attached to every second carbon atom of the polymer backbone. The methyl group restricts rotation of the chain, which results in a higher degree of crystallinity while producing a stronger and less flexible material. Thus, already a small content of this brittle material decreases the ability of elongation significantly, which is shown by the considerable drop of maximum tensile strain between 0 and 25 wt % LDPE. Such behavior can be also observed all blends.

The PP/LDPE in this study shows extremely improved tensile properties at 75 wt % LDPE content, which imply partial miscibility or partial compatibility of the blend. Similar behavior is also observed in PP/HDPE blend. Incorporating with the crystal structure results, it could be said that the PP/PEs blends showed a dynamic incompatible behavior that has been attributed to the different crystalline structures of the two components, PP and PEs. Even though it took longer time to crystallize, blends with 25 wt % of LDPE and HDPE crystallized with the large size of crystals. This could be causing a heterogeneous structure with weak interconnections, leading to modest maximum tensile strain values. As the LDPE and HDPE content increase, the blends getting crystallized into aggregates of smaller sizes in which well interconnections between the crystals, leading to the tensile strain enhancement. The PP/PEs blends with a high level of compatibility are expected to offer advantages for a wide range of applications, including the applications of the individual polymers.

5. Conclusions

The crystallization behavior studies, which include the kinetics of crystallization as well as the crystal morphology from the optical microscope, clearly showed that the addition of long branches LDPE strongly reduced the overall crystallization rate of PP. The reduction in the overall rate is mainly attributed to a decrease in the nucleation density. The decrease in nucleation density was found predominantly caused by the nuclei migration from PP to LDPE. Accordingly, the imperfection of PP crystals in the blends resulted from LDPE droplets engulfed in the PP spherulites, which can

also be observed from the shifting of T_c of PP to a lower temperature with larger LDPE contents. The crystallization rate of PP was found to be slightly slower at larger LDPE contents. Even though the PP crystals in the blend with 25 wt % LDPE nucleated faster than that of the blend with 50 wt % LDPE, it should be noted that once the PP crystals in the blend of 50 wt % LDPE were nucleated, they grew faster. This can be seen in the optical microscopic images for the isothermal crystallization at 8 min as well as the overall crystallization rate, which is represented in the form of reduced crystallinity versus time. Some crystals nucleated at a much lower rate and then grew faster afterward. However, in the case of PP/HDPE blend in which the crystallization temperatures overlap, resulting in an increase of the crystallization rate. Moreover, the more LDPE and HDPE contents, the smaller crystal sizes propagated in the blends. The Avrami coefficient, n, depends on the shape of the crystal: spherical (n = 3); disk-shaped (n = 2); rod-shaped (n = 1). This study shows that the shape of the crystal and the crystallization rates seemed to affect the tensile properties of the blends. These results are observed for the blends of PP and HDPE (short branched structure). The PP/HDPE blend with 75 wt % HDPE, which n = 1.69 and had a prolonged crystallization rate, showed a significantly improved on the elongation property. Accordingly, the slower crystallization rate resulted in the tensile properties improvement.

The mechanical properties are in good agreement with the crystallization study and show that PP/LDPE with 75 wt % LDPE and PP/HDPE with 75 wt % HDPE are partially compatible. Particularly the elongation at maximum strain is considerably improved while the tensile stress at break and Young's modulus are not lower than expected. Thus, the recycled PP/PEs blends can be expected to be able to serve in a wide range of application. This is depending on the degree of miscibility or compatibility, which is related to the desired properties of the products as well as the processability of the materials. According to this study, the properties of recycled PP/PE blend (rPP1/rLDPE1) remains unchanged until the composition of rLDPE1 reach 25 wt %, which means that rPP1/rLDPE1 can be used similarly as the pure recycled PP. For example, the recycled blends could be used again in injection molded or blow-molded applications to make bottles or containers. Furthermore, the outdoor decking, fencing and picnic tables can be manufactured from the recycled PP/PEs blends as well as pipe, films or sack bags.

Author Contributions: Conceptualization: C.A., N.R. and M.S.; methodology: C.A.; analysis: C.A.; writing—original draft: C.A.; writing—review and editing: C.A., N.R. and M.S.

Funding: This research was funded by the University of Wisconsin-Madison, USA, the grants for Development of New Faculty Staff, Ratchadaphiseksomphot Endowment Fund, Chulalongkorn University, Thailand and The Thailand Research Fund (TRG6180009).

Conflicts of Interest: The authors declare no conflict of interest.

References

1. Hamad, K.; Kaseem, M.; Deri, F. Recycling of waste from polymer materials: An overview of the recent works. *Polym. Degrad. Stab.* **2013**, *98*, 2801–2812. [CrossRef]
2. Chen, H.; Sundararaj, U.; Nandakumar, K.; Wetzel, M.D. Investigation of the Melting Mechanism in a Twin-Screw Extruder Using a Pulse Method and Online Measurement. *Ind. Eng. Chem. Res.* **2004**, *43*, 6822–6831. [CrossRef]
3. United States Environmental Protection Agency (EPA). *Advancing Sustainable Materials Management: Facts and Figures 2013 Assesing Trends in Material Generation, Recycling and Disposal in the United States*; United States Environmental Protection Agency (EPA): Washington, DC, USA, 2015.
4. Osswald, T.A.; Menges, G.; Manges, G. *Materials Science of Polymers for Engineers*, 3rd ed.; Hanser Publishers: Munich, Germany; Vienna, Austria; New York, NY, USA, 2012.
5. Osswald, T.A.; Rudolph, N. *Polymer Rheology*; Hanser Publishers: Munich, Germany, 2015.
6. Ehrenstein, G.W.; Riedel, G.; Trawiel, P.; Riede, G.; Trawiel, P. *Thermal Analysis of Plastics*; Hanser Gardner Publishers, Inc.: Cincinnati, OH, USA, 2004.
7. Ward, I.M. Polymers: Chemistry and Physics of Modern Materials. In *Contemporary Physics*, 3rd ed.; Cowie, J.M.G., Arrighi, V., Eds.; CRC Press: Boca Raton, FL, USA, 2009; Volume 50, p. 670. [CrossRef]

8. Utracki, L.A. *Commercial Polymer Blends*; Chapman & Hall: Londan, UK, 2000; ISBN 0412810204.
9. Van Eygen, E.; Laner, D.; Fellner, J. Circular economy of plastic packaging: Current practice and perspectives in Austria. *Waste Manag.* **2017**, *72*, 55–64. [CrossRef]
10. Yin, S.; Tuladhar, R.; Shi, F.; Shanks, R.A.; Combe, M.; Collister, T. Mechanical Reprocessing of Polyolefin Waste: A Review. *Polym. Eng. Sci.* **2015**, *55*, 2899–2909. [CrossRef]
11. Salih, S.E.; Hamood, A.F.; Alsabih, A.H. Comparison of the Characteristics of LDPE: PP and HDPE: PP Polymer Blends. *Mod. Appl. Sci.* **2013**, *7*, 33–42. [CrossRef]
12. Mastalygina, E.E.; Popov, A.A.; Kolesnikova, N.N.; Karpova, S.G. Morphology, thermal behavior and dynamic properties of the blends based on isotactic polypropylene and low-density polyethylene. *Int. J. Plast. Technol.* **2015**, *19*, 68–83. [CrossRef]
13. Rudolph, N.; Kiesel, R.; Aumnate, C. *Understanding Plastic Recycling*; Hanser Publishers: Munich, Germany, 2017.
14. Spicker, C.; Rudolph, N.; Kühnert, I.; Aumnate, C. The use of rheological behavior to monitor the processing and service life properties of recycled polypropylene. *Food Packag. Shelf Life* **2019**, *19*, 174–183. [CrossRef]
15. Eagan, J.M.; Xu, J.; Di Girolamo, R.; Thurber, C.M.; Macosko, C.W.; Lapointe, A.M.; Bates, F.S.; Coates, G.W. Combining polyethylene and polypropylene: Enhanced performance with PE/iPP multiblock polymers. *Science* **2017**, *355*, 814–816. [CrossRef]
16. Tien, N.-D.; Prud'homme, R.E. Crystallization Behavior of Miscible Semicrystalline Immiscible Polymer Blends. In *Crystallization in Multiphase Polymer Systems*; Elsevier Inc.: Amsterdam, The Netherlands, 2018; pp. 181–212.
17. Mofokeng, T.G.; Ray, S.S.; Ojijo, V. Influence of Selectively Localised Nanoclay Particles on Non-Isothermal Crystallisation and Degradation Behaviour of PP/LDPE Blend Composites. *Polymers* **2018**, *10*, 245. [CrossRef]
18. Lin, J.-H.; Pan, Y.-J.; Liu, C.-F.; Huang, C.-L.; Hsieh, C.-T.; Chen, C.-K.; Lin, Z.-I.; Lou, C.-W. Preparation and Compatibility Evaluation of Polypropylene/High Density Polyethylene Polyblends. *Materials* **2015**, *8*, 8850–8859. [CrossRef]
19. Galeski, A.; Bartczak, Z.; Pracella, M. Spherulite nucleation in polypropylene blends with low density polyethylene. *Polymers* **1984**, *25*, 1323–1326. [CrossRef]
20. Teh, J.W. Structure and Properties of Polyethylene-Polypropylene Blend. *J. Appl. Polym. Sci.* **1983**, *28*, 605–618. [CrossRef]
21. Lovinger, A.J.; Williams, M.L.; Telephone, B. Tensile Properties and Morphology of Blends of Polyethylene and Polypropylene. *J. Appl. Polym. Sci.* **1980**, *25*, 1703–1713. [CrossRef]
22. Zhang, Z.; Yu, F.; Zhang, H. Isothermal and Non-Isothermal Crystallization Studies of Long Chain Branched Polypropylene Containing Poly(ethylene-co-octene) under Quiescent and Shear Conditions. *Polymers* **2017**, *9*, 236. [CrossRef]
23. Razavi-nouri, M.; Hay, J.N. Isothermal crystallization and spherulite nucleation in blends of polypropylene with metallocene-prepared polyethylene. *Polym. Int.* **2006**, *55*, 6–11. [CrossRef]
24. ASTM International. Astm D1238−13. *ASTM Int.* **2013**, 1–16. [CrossRef]
25. Lu, X.; Weiss, R.A. Relationship between the glass transition temperature and the interaction parameter of miscible binary polymer blends. *Macromolecules* **1992**, *25*, 3242–3246. [CrossRef]
26. American Society for Testing and Material (ASTM). Standard Test Method for Tensile Properties of Plastics (D638-14). *Annu. Book ASTM Stand.* **2009**, 1–17.
27. Lee, J.H.; Lee, S.-G.; Choi, K.-Y. Crystallization and Melting Behavior of Nylon 66/Poly (ether imide) Blends. *Polym. J.* **1998**, *30*, 531–537. [CrossRef]
28. Li, J.; Shanks, R.; Long, Y. Miscibility and crystallisation of polypropylene–linear low density polyethylene blends. *Polymers* **2001**, *42*, 1941–1951. [CrossRef]
29. Strapasson, R.; Amico, S.; Pereira, M.; Sydenstricker, T.; Pereira, M.F. Tensile and impact behavior of polypropylene/low density polyethylene blends. *Polym. Test.* **2005**, *24*, 468–473. [CrossRef]